DESIGN AND ASSESSMENT OF SEISMIC PROTECTIVE SYSTEMS FOR NEAR-FIELD GROUND MOTIONS

By

ZHOU XU

A dissertation submitted to the Graduate Faculty in Engineering in partial fulfillment of the requirements for the degree of Doctor of Philosophy

The City University of New York

2007

UMI Number: 3245085

ProQuest Information and Learning Company
300 North Zeeb Road
P.O. Box 1346
Ann Arbor, MI 48106-1346

This Manuscript Has Been Read and Accepted for the Graduate Faculty in Engineering in Satisfaction of the Dissertation Requirement for the Degree of Doctor of Philosophy.

July 17, 2006

Date

Professor Anil K. Agrawal

Chair of Examining Committee

July 17, 2006

Date

Professor Mumtaz K. Kassir

Executive Officer

Professor Feng-Bao Lin

Professor Kolluru Subramaniam

Professor Thomas Price

Dr. Mohammed Ettouney, Weidlinger Associates

Supervisory Committee

THE CITY UNIVERSITY OF NEW YORK

ABSTRACT

by

Zhou Xu

Advisor: Professor Anil Kumar Agrawal

The objective of this research is to assess the effectiveness of existing seismic protective devices and design novel controllers for the protection of civil infrastructure systems against near-field ground motions.

The characteristics of near-field ground motions and their effects on linear and nonlinear structural systems are investigated to gain an understanding of the effect of the excitation properties on structural responses. The results indicate that the responses of these structures subjected to recorded near-field ground motions are controlled by the pulse components of these records represented by the frequency, shape, damping and amplitude. Near-field ground motions cause distinct strength and ductility demands, and energy dissipation requirements on structures. The response modification factor versus ductility (R-μ) relationships for pulse excitations are found to match the lower bound of the recorded ground motion results for low T_n/T_p (ratio of structure-excitation period) values and match the Newmark-Hall's relationship otherwise.

The performance of existing passive energy dissipation systems in protecting linear and nonlinear structures against near-field excitations is investigated. It is found that the effectiveness of these systems is related to the ratio of structure-excitation period, T_n/T_p, and the frequency contents of near-field excitations. Passive viscous damping is most

effective in reducing structural responses near resonance caused by dominant pulse effects; otherwise, it is only effective in reducing the responses caused by broadband frequency components. Yielding dampers are only effective in reducing responses caused by excitations having $T_p > T_n$ and they may amplify the structural responses otherwise.

In this study, optimal active and semi-active controllers are designed by incorporating a frequency-domain pulse filter into modern control algorithms. The results indicate that these controllers developed for the augmented structural systems have distinct advantages over many other existing methods and yield more significant base and superstructure response reductions with the same amount of control force. Systematic parametric studies demonstrate that these controllers are robust with respect to the variation of the characteristic filter parameters in a substantial range.

A hybrid controller utilizing the advantages of viscous damping and variable stiffness mechanisms is proposed for the control of flexible structures against long-period excitations. Analysis results indicate that this controller is capable of significantly reducing displacements caused by long-period pulse-type and near-field excitations for flexible structures through instantly adjusting damper parameters.

Both base-isolated building and bridge benchmark models are employed to investigate the effectiveness of the proposed control systems. Numerical analyses using the benchmark models demonstrate that the proposed control systems are very effective in reducing the responses caused by near-field ground motions and have much better overall performance than the sample controllers provided in the benchmark packages.

ACKNOWLEDGEMENTS

I would like to express my deepest appreciation to Professor Anil Kumar Agrawal, my mentor, for his guidance, support and encouragement during the period of my graduate studies at the City College of the City University of New York.

My sincere appreciation also goes to Professors John Fillos, Mumtaz Kassir, Michel Ghosn, Feng-Bao Lin, Kolluru Subramaniam and Thomas Price, for their encouragement and assistance during past years. In particular, I am thankful to Professor Michel Ghosn, Dr. Wanlong He and Dr. Ping Tan for their comments and suggestions.

Thanks also go to Dr. Mohammed Ettouney of Weidlinger Associates for his comments and suggestions on this dissertation.

Professor Jann N. Yang from the University of California Irvine and Professor Satish Najarajaiah at Rice University provided helpful guidance and suggestions.

Finally, I am indebted to my family for their unconditional love and support.

The research presented in this dissertation is jointly supported by the National Science Foundation grant number CMS-009985 and the Multidisciplinary Center for Earthquake Engineering through Earthquake Engineering Research Centers Program of the National Science Foundation, under award number EEC-9701471.

TABLE OF CONTENTS

LIST OF TABLES

LIST OF FIGURES

CHAPTER 1

INTRODUCTION

1.1 BACKGROUND INFORMATION

Significant research efforts have been made on protecting civil infrastructures from strong earthquakes and wind loads. The objectives of this type of research range from reliable operation and occupant comfort to human safety and structural survivability. Traditional design strategies increase structural strengths to resist dynamic loadings by relying on the inelastic deformation of structural components to dissipate seismic energy during extreme events. Recent developments in the areas of structural control, seismic isolation and supplemental damping devices provide alternative approaches to increase the structural survivability during unpredicted hazards using various types of energy dissipation devices, e.g., passive, semi-active, active as well as hybrid protective systems. Full-scale implementations of these systems have been made and are being increasingly pursued around the world. Effectiveness, reliability and other characteristics of these systems are being evaluated through large-scale testing and practical implementations in certain test structures.

Passive control systems, such as base isolation systems, passive energy dissipation systems, and tuned mass dampers, etc., are widely accepted by engineering community for mitigating structural responses. However, passive devices are unable to adjust themselves to varying loading conditions. Hence, the efficiency of these systems cannot

be assured if the actual excitations are much different from design excitations. Likewise, although active control systems are able to adjust themselves to environmental variations, their operations during strong earthquakes are not reliable due to the limitation of large external power requirement. On the other hand, semi-active systems have significant practical implementation potentials because of inherent reliability of passive systems and the versatility and adaptability of active systems at the same time, while only requiring battery-level power sources. Hybrid control systems may consist of both passive and active control devices and thus could at least offer the effectiveness of passive component in the case of active component malfunction during extreme events. Because of reliability of both semi-active and hybrid control systems, considerable attention has been paid to the research and implementation of these systems recently, most notably in Japan.

Due to the tremendous damage caused by 1994 Northridge and 1995 Kobe earthquakes, research on characteristics of near-field ground motions has been investigated extensively during last decade. Near field ground motions are characterized by pulse-like time histories with high velocity peaks and large ground displacement, which are much different from the far-field ground motions. Recent developments in documents such as ATC40 [Applied Technology Council (ATC) 1996], FEMA352 (FEMA 2000), FEMA356 (FEMA 2000), FEMA368 (FEMA 2000), and Uniform Building Code (UBC) [International Code of Building Officials (ICBO) 1997], allow for the design of structures located near known earthquake faults. However, the assessment of peak demands due to inelastic shaking is still carried out by methods used for far-field shaking and none of these documents explicitly consider the increase in inelastic demand on structural components due to near-fault ground motions. This approach may lead to a

significant under-prediction of inelastic demand. On the other hand, though seismic protective systems, e.g., base-isolation systems and passive energy dissipation systems, have been recommended by some of these documents for the rehabilitation and/or construction of structures [e.g., UBC97, FEMA 368 (2000), FEMA 356 (2000), FEMA274 (1997)]; design procedure for these systems still does not consider the characteristics of near-field ground motions, although it is well-known that near-source effects could considerably influence the performance of these systems. A systematic study on the performance of various seismic protective systems and the design of innovative control approaches considering near-field ground motions is imperative for the successful applications of these systems to achieve effective seismic mitigations.

1.2 RESEARCH OBJECTIVES

The objectives of this study are to investigate the effects of pulse-type ground motion characteristics on the performance of various seismic protective systems, and to design innovative active and semi-active systems considering the inherent pulse-like dynamics of these ground motions for protecting building and bridge structures.

It is well known that the performance of various seismic protective systems is significantly influenced by the characteristics of ground motions. However, this aspect has been studied mostly using recorded ground motions and a systematic study of why and how the performance changes has not been carried out. In this study, a continuous velocity pulse type model proposed by He (2003) has been used to carry out the proposed systematic study. The model has been demonstrated to be capable of effectively capturing the pulse-type behavior of near-field ground motions. Utilizing the analytical model as

well as recorded near-field ground motions, the spectrum and instantaneous response characteristics, including both the strength and energy quantities, of linear and nonlinear structures are thoroughly investigated to thoroughly understand the near-field ground motion effects on structures. The performance of various passive energy dissipation systems (e.g., linear and nonlinear viscous dampers, yielding and friction dampers) in protecting both linear and nonlinear structures against the pulse-type and recorded near-field excitations are evaluated and the reasons for performance variation of these protective systems during different types of ground motions are investigated in detail to quantify a relationship among pulse parameters, control system parameters and structural parameters.

Another main objective of this study is to develop innovative semi-active and active control approaches for protecting structures against near-field ground motions. Considering a major disadvantage of current seismic protective approaches of not including the dynamics of excitation in the design of controllers, both semi-active and active control laws are designed by incorporating the inherent dynamics associated with pulse-like behaviors in terms of augmented structural systems. The effectiveness, robustness, and advantages of the proposed control approaches are investigated by applying these approaches to different structural models and comparing the results with other conventional/competitive control approaches.

Novel control approaches proposed in this study can be divided into two categories. The first category is ground-motion-pulse based semi-active and active control approaches, in which controllers are designed for the augmented structural-excitation systems using H2-LQG algorithm. Applications of these controllers to base-isolated

building structures demonstrate that they are capable of reducing both the base and super-structure response quantities simultaneously and significantly. The second type of protective system proposed in this study is a stiffness based hybrid controller, which is designed for the control of flexible structures, including nonlinear and base-isolated structures, against long-period pulse-type excitations. Applications of the hybrid control system to nonlinear SDOF models and a nonlinear base-isolated bridge model show that this controller could effectively and significantly mitigate displacement (ductility) demand on these structures during long-period excitations.

1.3 OUTLINE OF THE DISSERTATION

This dissertation presents research work carried out towards the objectives mentioned above. The entire dissertation consists of nine chapters. Each of these chapters deals with separate but inherently integrated tasks. The outline of this dissertation is as the following:

Chapter 1, which is this chapter, presents the problem statement and the objectives of this research.

Chapter 2 presents the literature review. The state-of-the-art and the state-of-the-practice on the research and application of various seismic protective systems in civil engineering are reviewed critically. Also presented is the recent progress on near-field ground motion research.

Chapter 3 investigates the characteristics of pulse-type ground motions. Using the analytical pulse model and the Empirical Mode Decomposition (EMD) method, it is demonstrated that a recorded near-field ground motion could be decomposed into a

dominant pulse component and a series of broadband frequency components. The contributions of the dominant pulse component and the broadband frequency components to the full record and their effects on the responses of linear and nonlinear structures are investigated.

Chapter 4 systematically studies the performance of passive energy dissipation systems, including linear and nonlinear viscous dampers, yielding and friction dampers, in protecting linear structures against near-field ground motion type pulses. The pulse excitations are generated using the pulse-model and the results and conclusions are verified using recorded ground motions.

Chapter 5 deals with the effects of near-field ground motions on the behavior of nonlinear structures and the effectiveness of passive energy dissipation systems on nonlinear structures. The strength, ductility and energy response properties of nonlinear structures subjected to the pulse and recorded near-field ground motions are investigated followed by the investigation on the effectiveness of passive energy dissipation systems in mitigating inelastic dynamic responses. Both the strength-related and energy-related characteristics of controlled and uncontrolled structural systems are studied.

Chapter 6 presents the design of novel semi-active and active control systems for the control of structures against near-field ground motions. A frequency domain pulse filter based on the analytical pulse model is developed and incorporated in the design of novel controllers. The pulse filter contains the estimated information of major ground motion characteristics. Numerical results show that proposed semi-active and active controllers are significantly more effective than other types of controllers in protecting structures subjected to near-field ground motions.

Chapter 7 further evaluates the performance of the proposed semi-active and active controllers using a base-isolated building model developed for benchmark study of various control strategies. Using the prescribed near-field ground motions, the simulation results substantiate that the proposed controllers are superior to the sample controller provided as a part of the benchmark study and several other controllers in terms of more reductions in base and super-structure responses, simultaneously and significantly.

Chapter 8 presents a hybrid controller for the control of flexible structures subjected to long-period pulse-type excitations. The hybrid controller is based on a combination of viscous damping and optimal variable stiffness mechanisms. The controller design attempts to combine the advantages of both mechanisms with the consideration of structural and excitation properties. Characteristics of the hybrid controller are studied using nonlinear SDOF structures and its effectiveness is investigated using a benchmark base-isolated highway bridge model.

Chapter 9 presents conclusions of the research and recommends future work in the subject area.

CHAPTER 2

STATE-OF-THE-ART OF LITERATURE REVIEW ON STRUCTURAL CONTROL AND NEAR-FIELD GROUND MOTIONS

2.1 INTRODUCTION

Enormous progress has been made during last few decades in the research and development of structural control and seismic protective systems technologies to alleviate structural responses due to seismic and wind excitations [e.g., Soong (1990), Housner et al (1997), Soong & Dargush (1997), Symans and Constantinou (1999), Soong and Spencer (2002), Spencer and Nagarahaiah (2003), Connor (2003), Spencer and Yang (2004), Ou (2004)]. These control systems are usually classified into three groups, i.e., passive systems, active systems and semi-active systems, depending on control strategies adopted and the requirements on external power supply for the operation of control devices. Different devices may be used in combination as hybrid control systems in order to achieve better control effects. Full-scale applications of various control systems have been accomplished in many countries for both the retrofit of existing structures and new constructions [Spencer and Nagarahaiah (2003), Ou (2004)].

Most of the seismic protective systems that are currently in use and the structures to which they are applied were designed without considering the near-source effects of

excitations that these structures and protective systems may be subjected to during their life time. Recent research in earthquake engineering and structural control has began to pay more attentions to near-field ground motions, which are recorded in the vicinity of earthquake faults and are particularly destructive because of their impulsive long period components. Hence, in-depth research on characteristics of near-field ground motions and the effectiveness of various seismic protective systems during such ground motions is very imperative and necessary for the state-of-the-practice of these systems.

This chapter first reviews the developments and applications of various seismic protective or structural control technologies. Then, recent research and progress on near-field pulse-type ground motions and response mitigations for such type of ground motions are reviewed in detail.

2.2 REVIEW ON STRUCTURAL CONTROL SYSTEMS

During recent years, passive control systems have been widely employed in structural retrofit or new constructions for both wind and seismic applications. These systems are usually referred to as passive energy dissipation systems and may also include passive base-isolation systems and passive tuned mass damper systems [Soong and Spencer (2002), Spencer and Nagarahaiah (2003)]. Passive control devices utilize the motion of the structures to develop control forces and do not require external power supplies during their operation [Soong and Darguish (1997), Sadek et al (1996), Constantinou et al (1998)]. Widely used passive energy dissipation devices include metallic yielding dampers [e.g., Skinner et al (1975), Kelly et al (1972), Bergman and Goel (1987), Whittaker et al (1991), Xia and Hanson (1992), Tsai et al (1993, 1995),

Soong and Dargush(1997)], friction dampers [Pall et al (1982), Li and Reinhorn (1995)] and viscous dampers [Zhang et al (1989), Kasai et al (1993), Shen and Soong (1995), Makris and Constantinou (1991),Constantinou and Symans (1992), Makris et al (1993), Terenzi (1999), Perry et al (1993),and Lin and Chopra (2002)].

Figure 2.1, 2.2 and 2.3 show the configurations of viscous fluid dampers, visco-elastic dampers and metallic yielding dampers, respectively. It is noted that although passive devices can achieve stable performance during designed earthquakes, they are incapable of adjusting themselves in the cases of changing excitations. As a result, a passive system that works very well for one earthquake may not perform equally well during others.

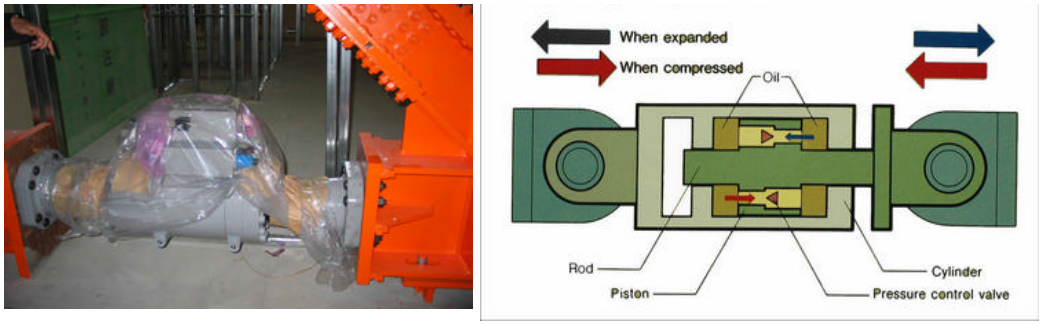

Figure 2.1: Configuration of a passive viscous fluid damper used in Japan and its operating principle (Courtesy of Kajima Corporation, Japan)

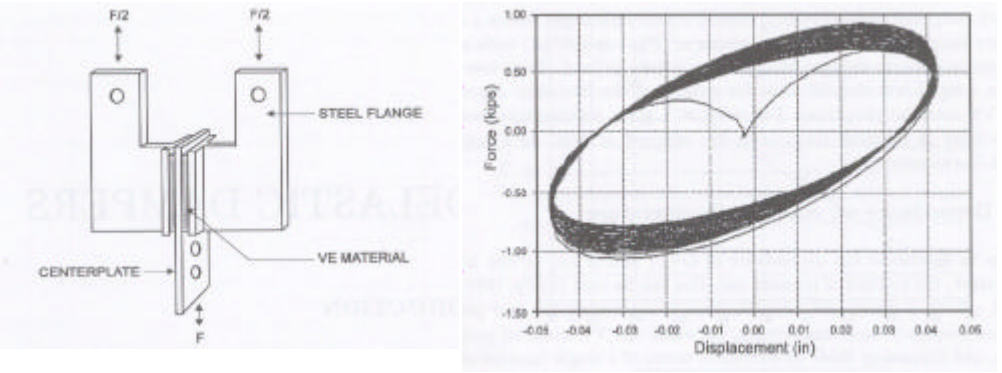

Figure 2.2: Configuration of a viscoelastic damper and its hysteretic loop (Shen and Soong 1995).

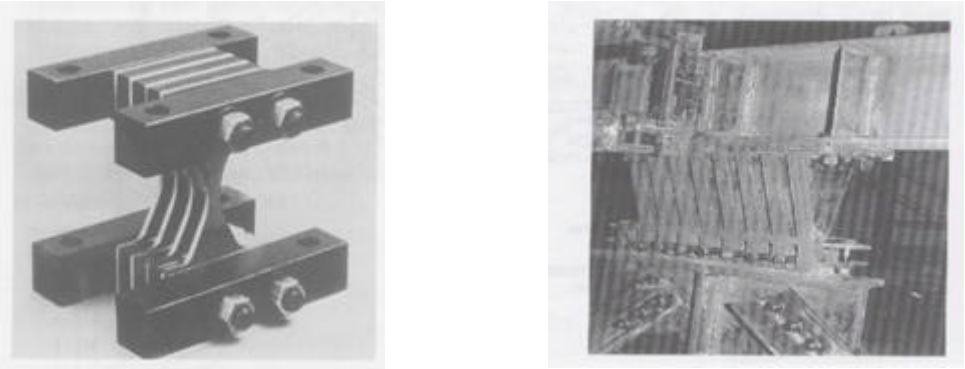

Figure 2.3: X-shaped (Soong and Dargush 1997) and triangular (Tsai et al 1993) Metallic Yielding Dampers.

In semi-active control systems, control forces in the devices are regulated through parametric control of device properties, e.g., size of orifice in fluid viscous dampers, normal force in semi-active friction dampers, current/voltage in MR dampers, etc., based on the feedback of structural responses and/or excitations [Symans and Constantinou (1999), Jalili (2002)]. These systems require battery-level external power sources for their operation. Semi-active control strategies could be realized either through directly applying friction-type restraints to passive devices [e.g., Reid controller (Reid 1956), sequential controller (Stammers and Sireteanu 1998), modulated homogenous friction controller (Inaudi 1997, He et al 2003) and visco-elastic friction controller (Chen and Chen 2000)], or by applying semi-active dissipative restraints to active control forces designed by various active control algorithms (e.g., H2-LQG, Sliding Mode Control, Fuzzy logic, H-infinity and Polynomial etc) [e.g., clipped optimal control (Dyke et al (1996a, 1996b), Dyke and Spencer 1997, Yoshioka et al 2002), friction restraints [Xu et al 2006]. Typical semi-active systems include the following devices:

- **Semi-Active Stiffness Damper (SASD)**. SASD consists of a cylinder-piston system with an on-off valve in the bypass pipe connecting two sides of the

cylinder filled by hydraulic oil [Yang et al (2000), Jabbari et al (2000), Agrawal et al (2003)], as shown in Figure 2.4. It can be operated in resetting or switching modes [Yang et al (2000), Agrawal et al (2003)]. Applications of SASD on different structures have been investigated, such as the benchmark cable-stayed bridge [Agrawal et al (2003)] and base-isolated benchmark building [Xu and Agrawal (2004), Xu et al (2005)].

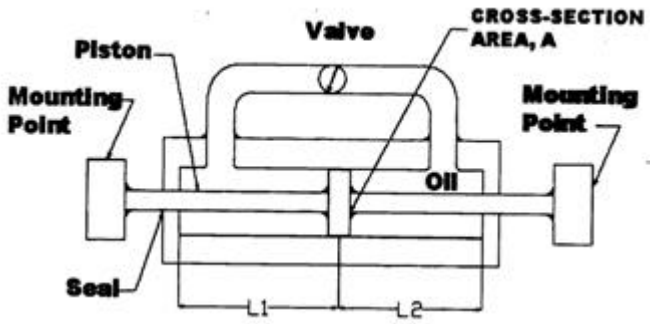

Figure 2.4: Schematic of semi-active stiffness damper

- **Active Variable System (AVS).** AVS is intrinsically a semi-active stiffness damper and was first proposed by Kobori et al (1993). It controls the stiffness of the structure through an on/off switch valve to lock or unlock stiffness braces of the damper to avert resonance condition during earthquakes (Figure 2.7a). Different control laws have been proposed to control the AVS system, such as Kamagata and Korobi (1994) and Yang et al 1996a). Yang et al (2000) has shown that an AVS system can be implemented using the semi-active stiffness damper (SASD) operating in the switching mode and the corresponding control law can be derived using the sliding mode control approach.

- **Semi-active variable orifice viscous dampers.** Variable viscous force of a semi-active variable orifice damper is achieved by using a controllable, variable orifice valve to alter the resistance to the flow of a conventional hydraulic fluid damper, which typically consists of a hydraulic cylinder containing a piston head separating the two sides of the cylinder (Figure 2.5). Feng and Shinozuka (1990) first proposed the concept of applying the variable-damping damper to bridge motion control. Kawashima et al (1992, 1993) presented the analytical and experimental study of semi-active fluid dampers for the control of highway bridges. Experimental work on semi-active orifice damper has been done by Kurata et al (1992), Sato et al (1996), Symans et al (1995) and Symans and Constantinou (1997a, 1997b).

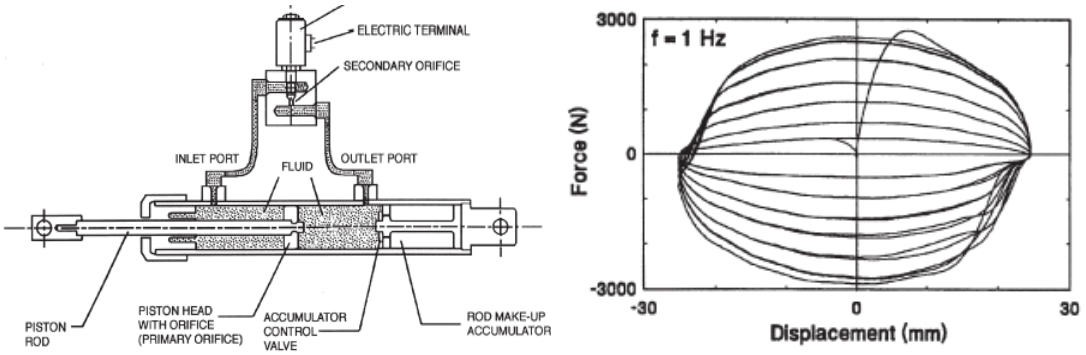

(a) Schematic (b) Hysteretic loops

Figure 2.5: Semi-active fluid viscous damper (Symans and Constantinou 1999)

- **Semi-active friction damper systems**. Utilizing forces generated by friction to dissipate vibration energy in a structural system is a well-established concept. Akbay and Aktan (1991, 1995) and Kannan et al (1995) proposed a variable-friction device that consists of a friction shaft rigidly connected to

the structural bracing. The force at the frictional interface is adjusted by allowing slippage in controlled amounts. Inaudi (1997) first proposed a modulated homogeneous damper. Chen and Chen (2000) proposed a visco-elastic semi-active friction damper. Agrawal and Yang (2000a, 2000b) proposed a semi-active electromagnetic friction damper (SAEMFD), which is based on regulating the friction force across the damper using an electromagnetic field. Recently, He et al (2003) introduced boundary layer to eliminate the acceleration spikes during the operation of friction dampers to allow continuous slippage in the damper. Their control law is a modified form of modulated homogeneous controller proposed by Inaudi (1997).

- **Electrorheological (ER) damper**. ER dampers typically consist of a hydraulic cylinder containing micron-sized dielectric particles suspended in ER fluids. The mechanical behavior of ER damper is determined by the external applied electric field and can be modeled by visco-plastic Bingham model (Shames and Cozzarelli 1992). In the presence of a strong electric field, the particles polarize and become aligned, thus offering an increased resistance to flow within a few milliseconds. As the applied electric field increases, the behavior of ER fluids changes from liquid state to solid state almost instantaneously and the damper then provides both damping and stiffness to the controlled structure [Makris et al (1996)]. Galvin et al (1993, 1996a, 1996b) tested a large-scale ER damper system consisting of a closed box containing nine interconnected rectangular plates and ER fluid, and developed an more accurate model for the ER damper by curve-fitting

method. Galvin et al (1996b) also investigated the behavior of small-scale ER walls. Ehrgott et al (1993) and Burton et al (1996) investigated the application of ER dampers in seismic control. Makris et al (1997) investigated the efficiency of ER dampers in protecting structures against near-field earthquakes.

- **Magnetorheological (MR) damper.** MR dampers use MR fluids to provide controllable devices for structural motion control. MR fluids typically consist of micron-sized, magnetically polarizable particles dispersed in a carrier medium such as mineral or silicone oil. When a magnetic field is applied to the fluids, particles change form and the fluids transform to plastic or semi-solid state in a few milliseconds. The operating temperature in these dampers can vary from -40 to $150\ ^0$C without any significant change in the yielding stress. It can be viewed as fail-safe device in that they become passive as a supplemental damping device should the control hardware malfunction [Spencer et al (1996, 1997), Dyke et al (1996a, 1996b), Carlson and Spencer (1996)]. Spencer et al (1997) developed a 14-parameter phenomenological model for a MR damper based on Bouc-wen model through experimental verification (Figure 2.6). Dyke et al (1996a, 1996b, 1997) tested the behavior of MR dampers through both numerical simulations and experimental verifications. Through clipped optimal control algorithm, MR dampers were also shown to be effective for smart base isolation systems [e.g., Spencer et al (2000), Ramallo et al (2000) and Yoshioka et al (2002)].

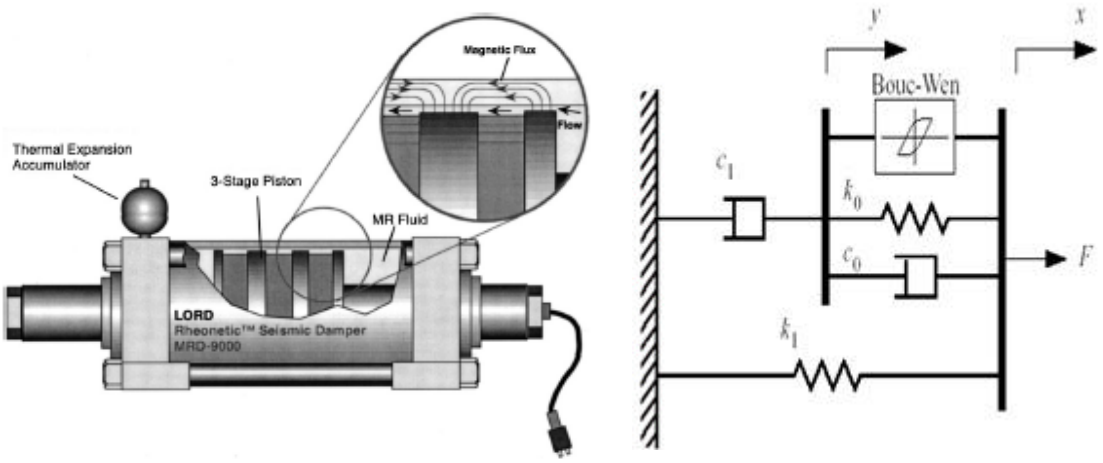

a) Schematic b) Phenomenological model

Figure 2.6: Schematic of MR damper and its phenomenological model (Spencer and Nagarajaiah 2003)

- **Semi-active tuned mass dampers (STMDs)**. STMDs offer distinct advantage over passive TMD through adjustment of damping and stiffness property of TMDs using a semi-active device [Hrovat et al (1983), Abe and Igusa (1996), Nagarajaiah and Varadarajan (2000)]. STMDs can also be based on controllable tuned sloshing dampers and controllable liquid column dampers, depending on the source of damping [Spencer and Nagarajaiah (2003)].

Active control systems are typically characterized as systems that require large external power supply [Soong (1990), Soong and Constantinou (1994)]. In active control systems, desired control forces are calculated by a control algorithm utilizing measured response quantities/excitations and then are applied to the structure through hydraulic actuators. Commonly used control algorithms employed in calculating feedback active control forces include LQG/H2/H_∞ control [Suhardjo et al (1990), Spencer et al (1993), Yang et al (1996b), Zhou et al (1996)], Sliding Mode Control [Utkin (1992), Yang et al

(1994, 1995a, 1995b, 1996c), Moon et al (2003), Wu (2003), Wu and Yang (2004)], optimal polynomial control [Agrawal and Yang (1995, 1996)], fuzzy logic and artificial neural network [Nagarajaiah (1994), Battaini et al (1999), Symans and Kelly (1999), Wang (1994), Brown and Harris (1994), Verbruggen and Babuska (1999)], etc. By definition, active control systems may add energy to structure systems and/or dissipate the input energy. An active control system has the distinct advantage of adjustability, i.e., it can adjust the control force according to the scale of structure responses and external excitations. However, since active control system can add energy to a structure, an active control system may become unstable or ineffective due to system uncertainties and measurement errors. In addition, since large power supply may be unavailable during strong earthquakes, an active control system is not a practical approach for seismically excited structures.

There have been several full scale applications of various types of control systems during last several decades. The first known proposal for seismically isolating a structure had appeared almost a century ago in Japan [Komodromos (2000)]. Currently, passive control systems have been adopted as a part of standard seismic retrofit practice around the world. The first full-scale implementation of semi-active control system in buildings was in Kajima Technical Research Institute in Tokyo, Japan, where an AVS system was applied to the three story building, as shown in Figure 2.7 [Kobori et al (1993)]. In USA, first full-scale implementation of an semi-active (variable) orifice damper was conducted in the Walnut Creek Bridge, on interstate highway I-35, as shown in Figure 2.8 [Patten (1998), Spencer and Nagarahaiah (2003)]. However, this application was targeted at reducing traffic induced vibration of the bridge. The first full-scale implementation of

MR dampers for buildings was in the Tokyo Museum of Emerging Science and Innovation building in Japan. Recently, MR dampers were used in the Dongting Lake Bridge in China to control wind-induced vibration of stay-cables of the bridge (Figure 2.9). Outstanding performance of MR dampers in reducing vibration of stay-cables of the Dongting Lake bridge has been demonstrated through numerous field observations.

Till 2002, more than 100 buildings and several bridges have been installed with passive energy dissipation systems in the U.S. [Soong and Spencer (2002)]. In China, more than 450 buildings have been built with seismic isolation systems till the end of 2000 [Zhou (2001)] and more than 50 buildings have been implemented with passive energy dissipations systems [Ou (2004)]. Moreover, over 40 buildings and 10 bridges, mostly in Japan, have been installed with feedback control strategies (e.g., hybrid, semi-active or active technology) [Spencer and Nagarajaiah (2003)].

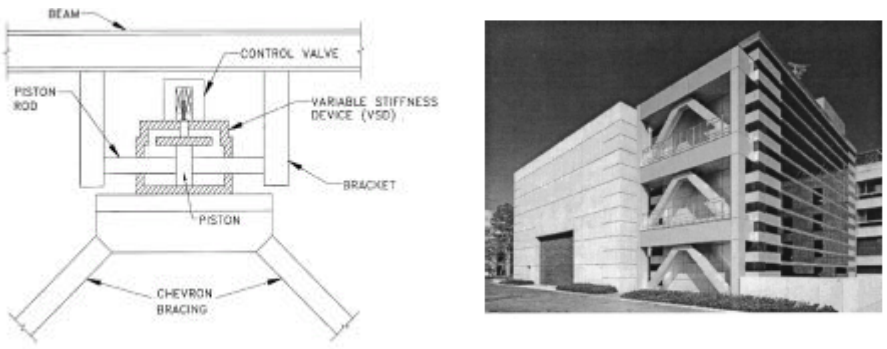

a) Schematic of the AVS (b) Building with the AVS

Figure 2.7: Active Variable System applied to the Kajima Technical Research Institute building (Kabori et al 1993)

a) Walnut Creek Bridge b)Variable orifice damper

Figure 2.8: First full-scale application of semi-active control in the U.S in Walnut Creek Bridge (Spencer and Nagarahaiah 2003).

a) Dongting Lake Bridge b) Damper configuration

Figure 2.9: First full-scale implementation of MR dampers for control of vibration of stay cables in Donting Lake Bridge in China.

2.3 NEAR-FIELD GROUND MOTIONS

Near-field (NF) ground motions are measured in the vicinity of an earthquake fault and they are responsible for causing extensive damages to structures during recent Northridge (1994), Kobe (1995), Turkey (1999) and Chi-Chi (1999) earthquakes. These ground motions are characterized by long-period pulses with high peak ground velocities and are being investigated intensively. It has been recognized that near-field ground motions are dominated by the source characteristics and vary significantly depending

upon the direction of rupture propagation: a structure in the near-fault region may experience a dynamic response that is twice or more than that of a similar structure located at same distance from the fault, even though the peak ground accelerations are almost the same. Seismic source directivity can overshadow the effects of soils on the ground motion as a result of propagation of the rupture along the fault, and fault-normal component can be several times stronger than its fault-parallel counterpart [Bertero et al (1978), Singh (1995), Somerville and Graves (1993), Somerville et al (1995, 1997, 1998), Erdik and Durukal (2001)].

The first seismological evidence of the near-field phenomenon was observed during 1952 Kern County, California earthquake by Benioff (1955)-although the first time that earthquake engineers linked the structural damage caused by earthquake to the impulsive character of near-fault earthquakes was after the 1971 San Fernando earthquake, CA [Singh (1995)]. In his pioneering work, Benioff (1955) found that the propagation of fault rupture as a moving source could lead to different types of ground motions at opposite ends of the ruptured area, with larger intensities of higher frequencies in the direction of propagation and smaller intensities of lower frequencies at opposite ends.

Malhotra (1999) showed that near-field pulse-like ground motions with high PGV/PGA ratio (PGV: Peak Ground Velocity, PGA: Peak Ground Acceleration) have wide acceleration-sensitive regions in their response spectra, which increases the base shear, inter-story drift and ductility demand on high-rise buildings. Huang (2001) studied the multimode structural response of tall buildings idealized as continuous shear-beam model subjected to ground motion velocities modeled by a set of three simple triangular-shaped piecewise pulses and another set of three sinusoidal pulses to include velocity

smoothness effects. The parameters of these velocity pulses are the peak ground velocity (PGV) and the pulse period. His results showed that the building responses are mostly dominated by its fundamental mode when the fundamental period of the structure is smaller than the pulse period, and it is dominated by higher mode contributions when the fundamental period is longer than the pulse period.

The pulse-type characteristics within NF ground motions cause large elastic displacements, and the inelastic displacement demands caused by these NF records may also be significantly larger than those estimated with displacement prediction techniques commonly used for far-fault records [Hall et al (1995), Bozorgnia and Mahin (1998), Alavi and Krawinkler (2001)]. Effectiveness of various control strategies in protecting bridge and building structures against near-field ground motions are also being investigated through benchmark studies. These benchmark models include linear and nonlinear building model developed by Spencer et al (1998a, 1998b) and Ohtori et al (2004), cable-stayed bridge model developed by Dyke et al (2003), wind-excited high-rise building model developed by Yang et al (2004), base-isolated building model developed by Narasimhan et al (2005) and Nagarajaiah and Narasimhan (2005), and base-isolated bridge model developed by Agrawal et al (2004). Among various control strategies, recent studies have shown that semi-active damping systems offer an effective and promising way in suppressing undesirable large displacement of base-isolated buildings subjected to NF ground motions [e.g., Yang and Agrawal (2002), He et al (2003), Agrawal et al (2005), Xu et al (2005), Wongprasert and Symans (2005a, b) and Madden et al (2002)].

Several analytical models have been proposed for the study of NF ground motions.

Makris (1997) and Makris and Chang (2000) classified velocity pulses in near-field ground motions into types A , B and Cn pulses to investigate the performance of various damping systems systematically. These pulses are represented by a unique set of closed-form functions. Type A is a half-cycle forward ground motion pulse; type B approximates a full-cycle forward-and-backward motion and type Cn approximates a ground motion pulse having *n* main pulses in its displacement time history. Alavi and Krawinkler (2001) have proposed three piecewise-linear equivalent velocity pulses and have investigated their suitability in lieu of recorded ground motions. Tirca et al (2003) have used the velocity pulse model of Alavi and Krawinkler (2001) to investigate the response of middle-rise steel frames with and without shear-link passive dampers. Their results show that response quantities are sensitive to the ratio of structural and pulse periods, and the structural strength. Menun and Fu (2002) have proposed a piecewise function with five parameters to represent velocity pulses observed in recorded ground motions. Mavroeidis and Papageorgiou (2004) have proposed an analytical model of ground motion pulses modeled by Gabor wavelet, which is essentially an amplitude modulated sinusoid.

Recently, He (2003) proposed an analytical model of ground motion velocity pulses to incorporate the dominant parameters of ground motions in the design of seismic protective systems. The model is continuous in nature and can be varied to generate various waveforms to represent different excitations. Characteristic parameters of a near-field ground motion can be obtained through curve-fitting analysis on the velocity history. Then, the displacement and acceleration could either be obtained through integrating or deriving the model velocity history, or be generated directly through the corresponding

mathematical expressions with the gained parameters. Validity of the pulse model has been demonstrated through comparison with numerous recorded ground motions, response spectra and performance of passive energy dissipation systems [He (2003), He and Agrawal (2005)].

Pulse models discussed above have been mainly used in the seismic analysis of structures in lieu of recorded ground motions. Incorporating ground motion characteristics in the design of protective systems, e.g., passive, semi-active and active systems, has also been investigated [Agrawal et al (2005, 2006), Xu et al (2005)]. Results have shown that active and semi-active systems designed for base-isolated buildings considering ground motion characteristics perform significantly better than those designed without considering ground motion characteristics.

CHAPTER 3

PULSE-TYPE GROUND MOTIONS

3.1 INTRODUCTION

Near-field ground motions are characterized by intense long-period pulses recorded in the vicinity of earthquake faults. After the 1994 Northridge (CA) and the 1995 Kobe (Japan) earthquakes, structural engineers started investigating correlations between structural damage and impulsive characteristics of these earthquakes [Hall et al (1995), Somerville et al (1997), Sakai and Kawashima (1997), Bozorgnia and Mahin (1998), Alavi and Krawinkler (1999)]. Long-period impulsive dynamic loads impose both large strength and ductility demand, especially on intermediate and long-period structures, such as high-rise and base-isolated buildings, and long-span cable-stayed bridges. As an example, an investigation after the 1994 Northridge earthquake demonstrated that a number of steel moment-frame buildings had experienced brittle fractures of beam-to-column connections, which did not behave as anticipated (i.e., damage would be limited to ductile yielding of members and connections only) though these buildings were designed per recent versions of building codes [FEMA 352].

Impulsive motion during near-field ground motions represents cumulative effects of seismic radiation from the fault. During a near-field earthquake event, propagation of fault rupture towards a site causes most of the seismic energy released from the rupture to arrive in a single large pulse of motion (“fling”) that occurs in the beginning of the record

[Hall et al (1995), Somerville et al (1997, 1998)]. The effects of rupture directivity are obvious and the fault-normal component of a "forward rupture directivity" record usually has longer period and larger amplitude than its fault-parallel counterpart. The impulsive characteristics are discernible not only in the recorded ground motion time histories, but also in the structural response histories. In time domain, dominating excitation characteristics can be extracted as pulse components. In frequency domain, these pulse components have the same dominating frequencies (periods) as the original records [Makris (1997), He (2003)].

Dominant pulses in near-field ground motions vary from earthquakes to earthquakes, which makes a consistent evaluation of near-fault effects difficult and cumbersome. For this reason, researchers have proposed various analytical models to characterize the property of near-field earthquakes. A detailed literature review on different pulse models has been presented in Chapter 2. In this research, the amplitude-modulated sinusoidal model proposed by He (2003) and He and Agrawal (2006) is used to investigate the effectiveness of various energy dissipation systems. This model has four characteristic parameters, e.g., period T_p or equivalently, frequency ω_p, magnitude scaling factor C, shape factor n and damping factor ζ_p. It consists of build-up and decay phases, and could be varied to represent various recorded near-field excitations (e.g., frequency, duration, shape, magnitude, etc) by adjusting corresponding parameters. Recent work has shown that this model can be used to study near-field effects on structural responses and seismic protective systems [He (2003), Wang et al (2002), Xu et al (2006), Agrawal et al (2006)].

It is known that earthquake motions are non-stationary stochastic processes. The statistical properties of an earthquake ensemble vary with time, and the next state of the

data can not be determined on the basis of the previous ones. Various numerical methods have been applied to analyze earthquake data. They include but not limited to Fourier transform, Laplace transform, Hilbert transform, Wavelet analysis, Wigner-Ville distribution [Cohen (1995)] and Evolutionary spectrum [Priestley (1965, 1988), Lin and Cai (1995)], etc. Recently Huang et al (1998, 1999) have developed a method based on Empirical Mode Decomposition (EMD) and Hilbert transform to analyze nonlinear and non-stationary time series ("Hilbert-Huang method"). In this approach, EMD approach is used to decompose target data into finite number of "Intrinsic Mode Functions (IMFs)" based on local characteristic time scale of the data at the first step. Then, using Hibert transformation, instantaneous frequencies of these IMFs are obtained as a function of time. These derived IMFs can then be used for further identification of the original data property, such as frequency contents, energy characteristics, etc. The Hilbert-Huang transformation (HHT) has been applied to analyze data from various engineering sources, such as winds, oceanic waves and earthquakes [e.g., Huang et al (2001), Huang (2003), Bazzurro and Luco (2003)].

In this chapter, the EMD method is used to analyze recorded near-field ground motion data. The capability and effectiveness of this model in capturing the pulse effects of near-field excitations are analyzed using an ensemble of eight earthquakes. The broadband frequency components of these near-field earthquakes and their effects on structural responses are also investigated. Contributions of pulse components and broadband frequency (high-frequency and long-period) components to the total acceleration records and their effects on structural responses are analyzed thoroughly.

The pulse model proposed by He (2003) and He and Agrawal (2006) is used to extract the dominating pulse components of near-field ground motions.

3.2 THE ANALYTICAL PULSE MODEL

The analytical velocity pulse model proposed by He (2003) is expressed as

$$\dot{u}_p = Ct^n e^{-at} \sin bt\,,\ a = \zeta_p \omega_p\,,\ b = \omega_p \sqrt{1-\zeta_p^2} \tag{3.1}$$

where $\dot{u}_p$ is the pulse velocity, n is a nonnegative shape parameter of the envelope, ζ_p is the pulse damping factor, $\omega_p = 2\pi/T_p$ is the pulse frequency (T_p being the pulse period), and C is the amplitude scaling factor with Ct^n having the unit of velocity. For the cases of small decay factors, say, ζ_p <20%, both b and ω_p will have the same interpretation.

Differentiating Eq. (3.1), the pulse acceleration is obtained as

$$\ddot{u}_p = Ct^n e^{-at} [(\frac{n}{t} - a)\sin bt + b\cos bt] \tag{3.2}$$

Displacement history can be obtained through numerical integration. Alternatively, it can be obtained through the following expression given that n is a positive integer, as

$$u_p(t) = C \cdot e^{-at} \sum_{r=0}^{n} \frac{(-1)^r n!\, t^{n-r}}{\rho^{r+1}(n-r)!} \sin[bt - (r+1)\alpha] + C \cdot \frac{(-1)^n n!}{\rho^{n+1}} \sin[(n+1)\alpha] \tag{3.3}$$

where

$$\rho = \sqrt{a^2 + b^2}\,;\ \rho\cos\alpha = -a;\ \ \rho\sin\alpha = b \tag{3.3'}$$

Special forms of Eq. (3.1) ~ (3.3) can be obtained for specified n values.

For illustrative purposes, displacement, velocity and acceleration histories of the pulse model are plotted in Fig. 3.1~3.3 by varying one of the parameters T_p, ζ_p and n at a

time. The amplitudes of velocity histories in these figures are normalized to unity by scaling the constant C. Then, the corresponding acceleration and displacement amplitudes are derived with the same parameters. Fig. 3.1 shows the influence of pulse period on the shape of pulse time histories. It is observed from Fig. 3.1 that pulse motion shifts towards right and the pulse duration becomes longer with an increase in T_p. As T_p increases from 1s to 3s, both the maximum displacement and the permanent ground displacement increase; however, the peak acceleration decreases with an increase in T_p.

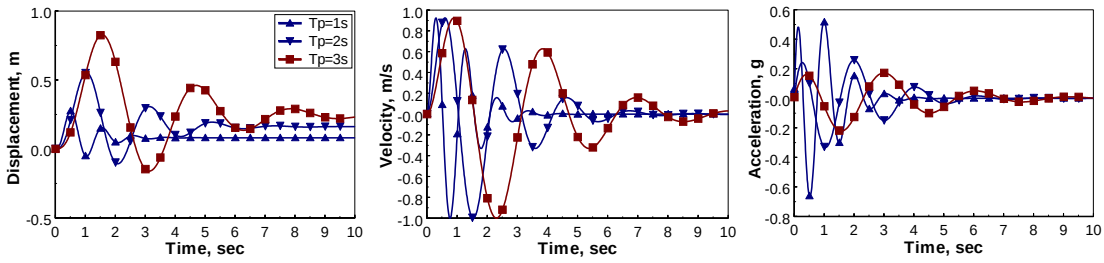

Figure 3.1: Pulse Shapes for Different Pulse Periods, T_p (ζ_p =0.3, n=1)

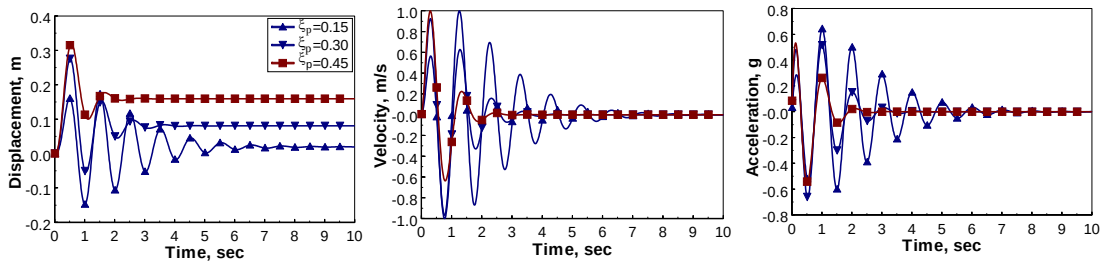

Figure 3.2: Pulse Shapes for Different Ground Damping Factor, ζ_p (T_p = 1 sec., n = 1)

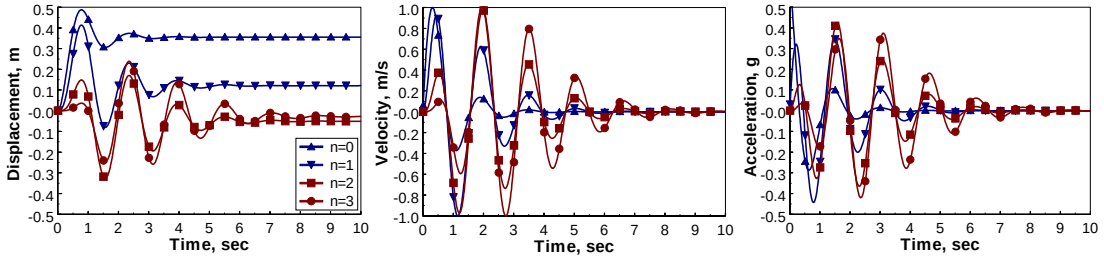

Figure 3.3: Pulse Shapes for Different Pulse Shape Factor, n (ζ_p =0.3, T_p = 1 sec.)

Fig. 3.2 shows the plots of the pulse time-history for different damping factors, ζ_p. It is observed that the duration of the pulse decreases with an increase in ζ_p. The peak acceleration decreases and the permanent ground displacement increases with increase in ζ_p for the same peak velocity. Fig. 3.3 shows the pulse time-history plots for n=0, 1, 2 and 3. It is observed that the velocity of the pulse increases at a faster rate and has larger magnitude in the beginning for smaller value of n. The permanent ground displacements are negative for n=0 and 1 and they are positive for n=2 and 3. The acceleration history is a decaying pulse with nonzero value at t = 0 for n = 0 and it starts from 0 at t = 0 for other values of n.

3.3 DOMINANT PULSE COMPONENT EXTRACTION USING THE PULSE MODEL

The dominant pulse components of near-field ground motions can be extracted by the pulse model through parametric optimization analysis. In this investigation, the characteristic parameters of the pulse components are obtained using the Least Square Quadratic analysis [MATLAB®], i.e.,

$$\Delta_v(C,n,a,b) = \sum_{t=t_0}^{t_1} [\dot{u}_g(t) - \dot{u}_p(t;C,n,a,b)]^2 \tag{3.4}$$

where t_0 and t_1 are start and end time instants of the target velocity pulse, $\dot{u}_g(t)$ and $\dot{u}_p(t)$ are the recorded ground and analytical pulse velocities, respectively. After determining the parameters C, n, a and b for the pulse velocity, the corresponding displacement and acceleration histories can be obtained through the inherent relationships or the expressions presented in the preceding section. It is noted that the optimization

process is dependent on initial values of these parameters and the results may only be based on the local minima. Details of the optimization procedure can be found in He (2003).

For illustration purpose, Fig. 3.4 shows 8 recorded near-field ground motions and their pulse components that are obtained by the regression analysis. Pulse parameters of these earthquakes are shown in the caption of the corresponding plots. Details of these earthquakes are listed in Table 3.1. Records presented in Fig. 3.4 correspond to fault-normal components during the 1994 Northridge earthquake (CA), 1995 Kobe earthquake (Japan), 1999 Chichi earthquake (Taiwan), 1992 Cape Mendocino earthquake (CA), 1979 Imperial Valley Earthquake (CA) and 1992 Turkey earthquake.

Table 3.1 Property of 8 near-field ground motion records

Records	Events	Magnitude (Mw)	PGA(g)	T_g(s)
KJM090	1995 Kobe earthquake	6.9	0.60	0.8
TAK090	1995 Kobe earthquake	6.9	0.62	1.3
RRS228	1994 Northridge earthquake	6.7	0.84	1.0
SYL090	1994 Northridge earthquake	6.7	0.61	2.4
ERZ-NS	1992 Turkey earthquake	7.1	0.52	1.8
TCU068N	1999 Chichi earthquake	7.6	0.46	8.0
E06230	1979 Imperial Valley earthquake	6.9	0.44	3.3
SCS052	1994 Northridge earthquake	6.7	0.61	2.9

It is observed from Fig. 3.4 that the pulse velocity histories match those of the recorded earthquakes very well. The major characteristics of the recorded velocities, e.g., magnitude, shape, and number of half-cycles, etc, are properly represented by the corresponding pulse models. In terms of the acceleration histories, it is noted that the high-frequency acceleration components of the recorded earthquakes are rejected by the pulse accelerations. As a result, the peak values of pulse acceleration time histories are

less than those of recorded accelerations. Both the displacement histories for the pulses and the recorded earthquakes are obtained by direction integration in Fig. 3.4. It is observed that the dominant cycles of the two displacement curves match each other with good accuracy for most cases.

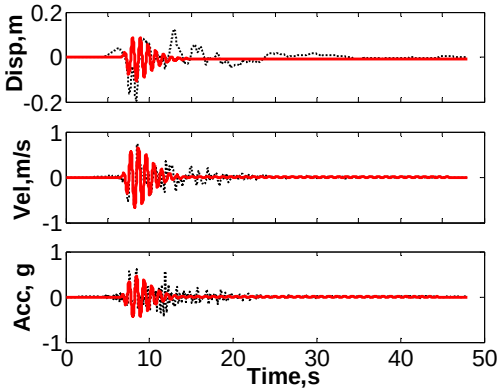

KJM090 during 1995 Kobe earthquake
[*C, n, a, b, t_0*]= [150, 2.0, 1.1, 6.8, 6.6]

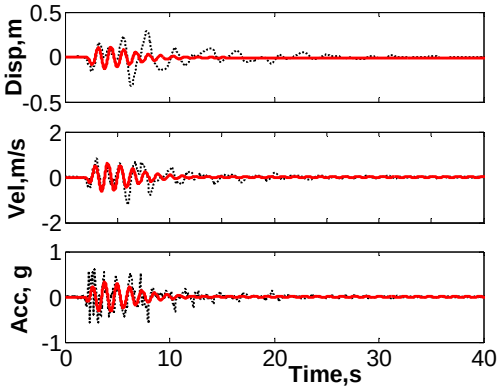

TAK090 during 1995 Kobe earthquake
[*C, n, a, b, t_0*]= [-90.7, 1.0, 0.54, 5.25, 2.0]

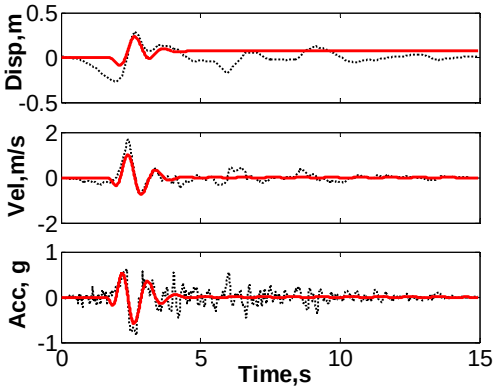

RRS228 during 1994 Northridge earthquake
[*C, n, a, b, t_0*]= [-3200, 3, 3.5, 6, 1.6]

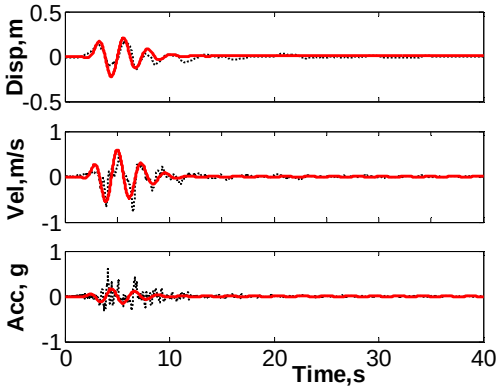

SYL090 during 1994 Northridge earthquake
[*C, n, a, b, t_0*]= [-18.29, 4, 1.09, 2.73, 1.0]

Figure 3.4 Displacement, velocity and acceleration of recorded near-field earthquakes (dashed lines) and the corresponding pulse approximations (solid lines).

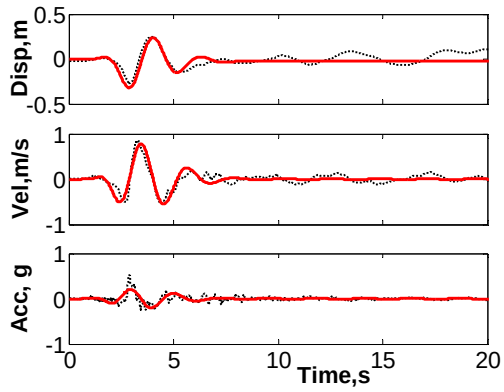

ERZ-NS during 1992 Turkey earthquake
[*C, n, a, b, t_0*]= [70.57, 5, 1.8, 2.75, 0.6]

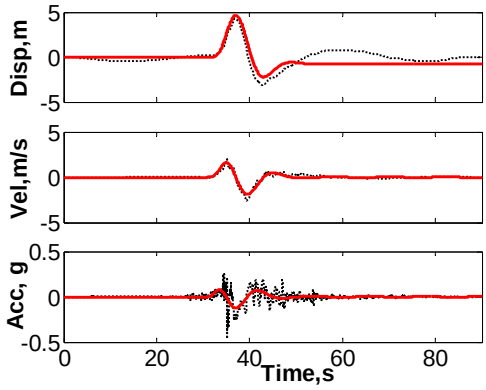

TCU068N during 1999 Chichi earthquake
[*C, n, a, b, t_0*]= [17.4, 3.2, 0.52 ,0.52, 31]

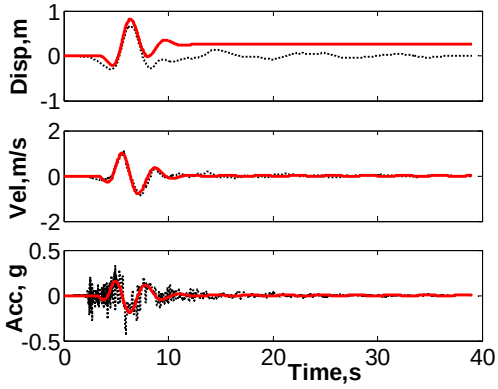

E06230 during 1979 Imperial Valley earthquake
[*C, n, a, b, t_0*]= [-80.4, 3.5, 1.2, 1.86, 3.0]

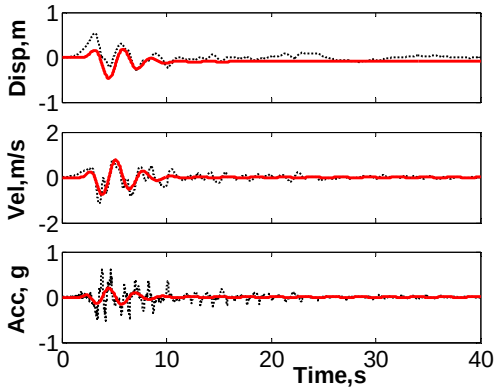

SCS052 during 1994 Northridge earthquake
[*C, n, a, b, t_0*]= [85, 2.5, 0.93, 2.33, 1.8]

Figure 3.4 (continued) Displacement, velocity and acceleration of recorded near-field earthquakes (dashed lines) and the corresponding pulse approximations (solid lines).

3.4 PULSE AND BROADBAND FREQUENCY CONTENTS OF NEAR-FIELD EARTHQUAKES

It is noted that although the pulse curves match the shapes of the recorded earthquakes with good accuracy, the pulse curves reject the inherent high-frequency contents of the recorded earthquakes at the same time. To clearly understand the properties of recorded near-field earthquakes, it is necessary to investigate the

characteristics of broadband frequency contents of the earthquakes. In this section, the Empirical Mode Decomposition (EMD) method is employed to analyze the broadband frequency characteristics of both the total acceleration data and the residual acceleration data (i.e., after extracting pulse components from the full acceleration records) of recorded earthquakes.

3.4.1 The Empirical Mode Decomposition (EMD) Method

The EMD method has been shown to be able to effectively decompose complicated data, either stationary or non-stationary, into a series of simple signals within time domain [Huang et al (1998, 1999)]. The mathematical form of the decomposition is

$$X(t) = \sum_{i=1}^{n} c_i(t) + r_n(t) \tag{3.5}$$

in which $X(t)$ is the original data to be decomposed; $c_i(t)$ is the *i*-th component signal (mode) denoted as Intrinsic Mode Function (IMF); $r_n(t)$ is the residual signal after *n* times decompositions. An IMF is a signal that satisfies two conditions: the number of extrema and the number of zero crossings must either be equal or different by one in the whole history; and the mean value of the envelope defined by the local maxima and the envelope defined by the local minima is zero at any point [Huang et al (1998, 1999)].

The decomposition is realized through "sifting" process to identify the intrinsic oscillatory modes by the characteristic time scales in the data, i.e., removing the mean of the upper and lower envelopes repeatedly from the original signal $X(t)$. The upper and lower envelopes in the decomposition are cubic spline curves connecting local maxima and minima of the signal. The decomposition is repeated until certain stopping criteria

are met. To start the sifting procedure, upper and lower envelopes of $X(t)$ are obtained and the mean of the envelopes, $m_1(t)$, is calculated at the beginning. After this,

1) subtract $m_1(t)$ from $X(t)$ to get the residual $h_1(t)$, i.e., $X(t) - m_1(t) = h_1(t)$;
2) repeat step 1) and 2) for the residual signal $h_1(t)$, i.e., $h_1(t) - m_{11}(t) = h_{11}(t)$;
3) repeat k times for the corresponding residual signal, $h_{1(k-1)}(t) - m_{1k}(t) = k_{1k}(t)$, until 3 ~ 5 consecutive siftings yield the same number of zero-crossings and extrema; then the first component $c_1(t)$ is obtained as $c_1(t) = k_{1k}(t)$; and the residual signal is obtained as $X(t) - c_1(t) = r_1(t)$;
4) repeat step 1) ~ 4) for n times, i.e,, $r_1(t) - c_2(t) = r_2(t)$, …, $r_{n-1}(t) - c_n(t) = r_n(t)$, until the residue $r_n(t)$ is either insignificantly small in magnitude or has become a monotonic function.

The purpose of the above sifting process is to eliminate riding waves and to make uneven amplitudes smooth. As a result, the frequency of $c_i(t)$ decreases with the increase of the subscript index *i*.

3.4.2 Empirical Mode Decomposition of Acceleration Records

As an example, the EMD method is used to analyze the 1994 Northridge Earthquake data recorded at Rinaldi Receiving Station (RRS228). Detailed information of this record is shown in Table 3.1. Displacement, velocity and acceleration time histories of this record are shown in Fig. 3.4.

In the following analysis, the EMD approach is used to decompose both the total acceleration record and the "residual" acceleration record (which is obtained by subtracting the dominant pulse component represented by the pulse model from the total

record). Components obtained through the EMD analysis are classified into three types considering the major frequency characteristics of these components with respect to the dominant frequency of the record. Hence, if the EMD analysis is executed for the total record, the resulting components that have dominant periods close to the predominant period of the record are classified as “intermediate” components; those having shorter dominant periods are classified as “high-frequency” components and those having longer dominant periods are classified as “long-period” components. If the EMD analysis is carried out for the residual acceleration, since the dominant pulse component has been extracted by the pulse model, the resulting components will either have period longer or shorter than the dominant pulse period. Accordingly, the components having shorter periods are classified as “high-frequency” components and those have longer periods are classified as “long-period” components. The pulse components (“intermediate component”) identified by the EMD analysis and by the pulse model are also compared.

3.4.2.1 Decomposition of Total Acceleration by EMD Analysis

The full record of the RRS228 acceleration is decomposed into IMFs through the EMD approach following the procedure presented in the preceding section. Fig. 3.5 shows the time-history plots of the resulting acceleration components in the units of cm/s^2. In Fig. 3.5, C1~C8 are the eight components and R is the residual signal. For comparison purpose, the total acceleration history is also shown in the first row (denoted as “Tot”). The Y-axis of each plot is appropriately scaled for the purpose of better presenting the magnitude of each component. It is observed that as the index increases from C1 to C8, the plots becomes more harmonic with respect to time, and the period of oscillation increases. Components C3 and C4 contain distinct impulsive behavior

similar to that of the total acceleration during the time intervals shown by two vertical dashed lines in the plots of these two components in Figure 3.5.

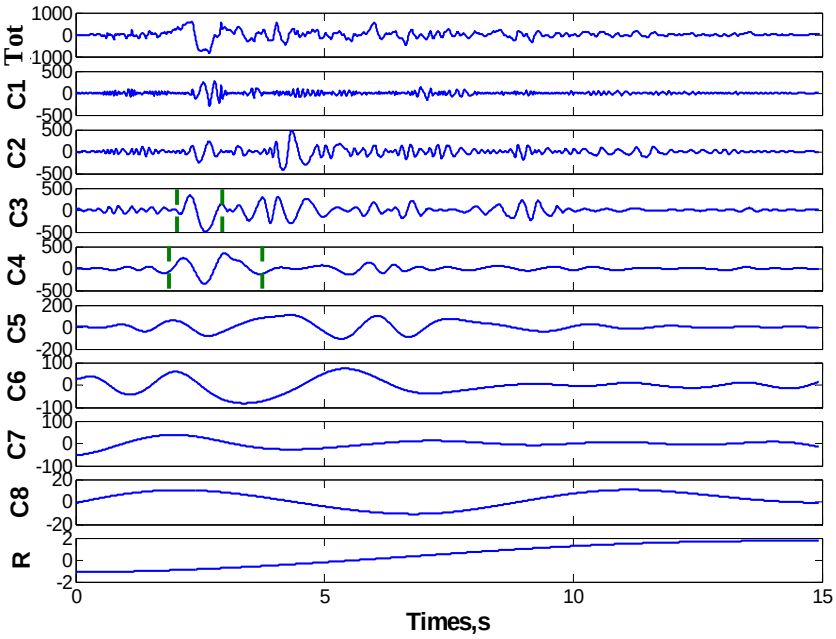

Figure 3.5 Time-history plots of the total acceleration and IMF components of the RRS228 record.

Peak Acceleration: Fig. 3.6 shows the magnitude of the total acceleration and its components (i.e., IMFs). It is observed that the peak values of the first 4 components, C1~C4, are much larger than others and they account for the major content of the total acceleration. Generally, the peak values of these components have a decreasing trend with an increase in the index of the component, except for C1. The peak accelerations of C8 and R are insignificant compared to others. It is noted that the peak accelerations of different components occur at different time instants. Hence, the magnitude of the total acceleration is not equal to the summation of those of the components.

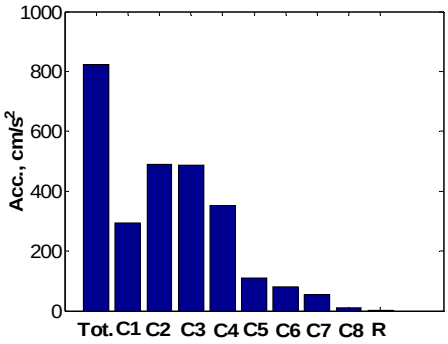

Figure 3.6 Peak values of the total acceleration and IMF components of the RRS228 record.

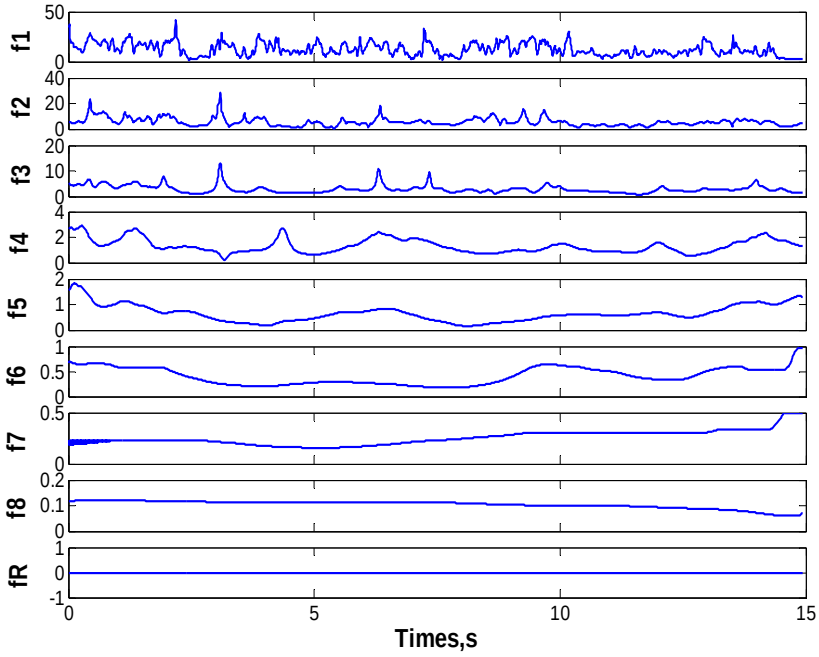

Figure 3.7 Instantaneous frequency contents of the IMF components, units in Hz

Instantaneous Frequency Contents: Fig. 3.7 plots the instantaneous frequency contents of each component as a function of time. The instantaneous frequency represents local data property in terms of time, which quantitatively demonstrates the variation of data. Details of instantaneous frequency for non-stationary data can be found in Huang et

al (2001). It is observed that both the peak values and the extent of fluctuation of these plots decrease with an increase in the component index, which means that the component become harmonic with an increase in index number.

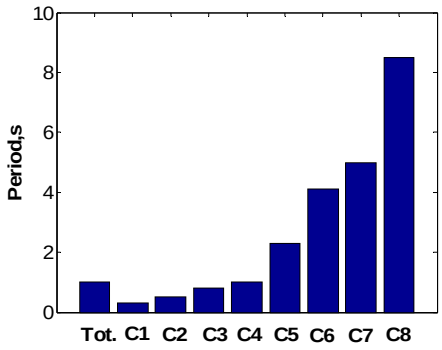

Figure 3.8 Dominant period of the RRS228 and its IMF components

Dominant Period: Fig. 3.8 presents the dominant period of these components. The dominant periods are obtained by carrying out relative velocity response spectrum analysis for these components. It is observed that the dominant periods increase with an increase in component index; which is the distinct characteristic of EMD analysis. The periods of component C3 and C4 are close to that of the recorded earthquake (1.0s, shown as "total" at first column). Therefore, these two are grouped into "intermediate" component. For components C1 and C2, the corresponding dominant periods are much smaller than that of the "total" acceleration. Hence, they are "high-frequency" in nature. The periods of components C5, C6, C7 and C8 are much larger and thus they are classified as "long period" components in the following analysis.

Peak Responses: To further investigate the characteristics of these components, the peak responses of relative displacement ("Disp"), relative velocity ("Vel") and absolute acceleration ("Acc") of a SDOF structure with T_n=1.0s and 5% inherent damping, subjected to the total acceleration and its components in Fig. 3.5, are calculated and

shown in Fig. 3.9. It is observed from Fig. 3.9 that these quantities increase with an increase in index number up to C4, and then decrease as the index number increases from C4 to C8. This happens not only because that C3 and C4 have larger magnitudes among these components, but mainly because the periods of C3 and C4 are closest to the structural period (1.0s). Overall, the contribution of C3 and C4 to the total response is dominant in all three plots. It is also observed that the peak total responses can not be obtained through the summation of the corresponding peak responses of components; which is due to the fact that the peak responses of these components occur at different time instants. However, the response histories obtained for the total acceleration is equal to the summation of response time histories for these components at every time instant for linear structural systems.

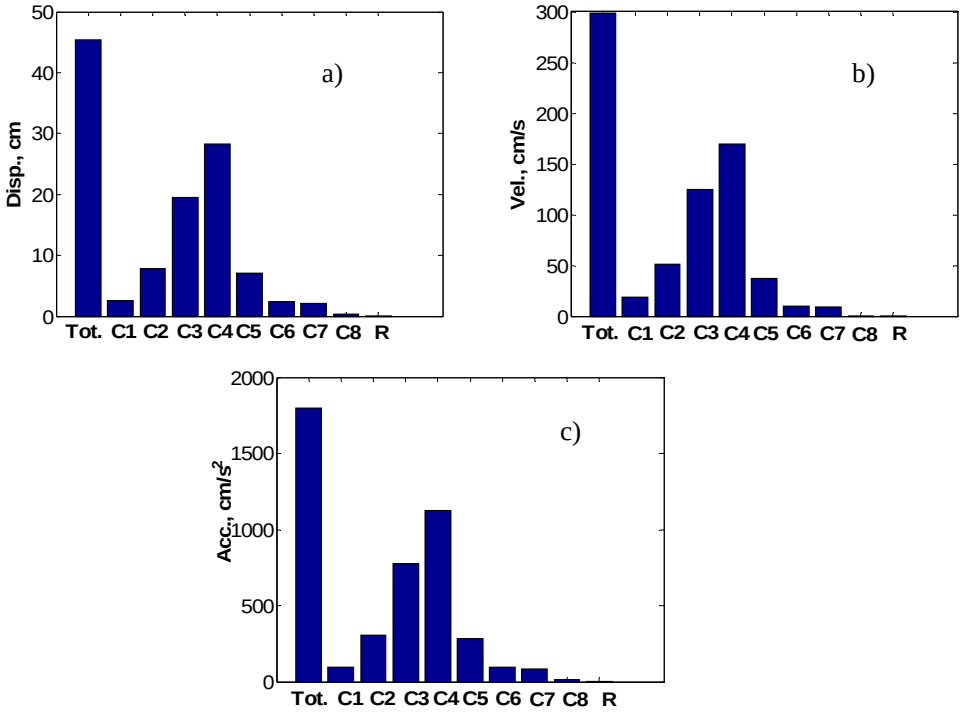

Figure 3.9 Peak response of a SDOF structure with T_n=1 second subjected to the RRS228 record and its IMF components: a) Displacement; b) Velocity and c) Absolute Acceleration.

3.4.2.2 Decomposition of Total Acceleration into Pulse and IMF Components

To investigate the response of structures subjected to the pulse excitation and broadband frequency excitations, it is necessary to separate the dominant pulse component and broadband frequency components of recorded near-field ground motions using a combination of the pulse model and the EMD analysis. The RRS228 record is used in this investigation for illustration purpose. The dominant pulse component of the RRS228 record is extracted using the pulse model as described in section 3.3 at first. Then, the rest of the acceleration, which contains broadband frequency contents, is further decomposed into IMFs using the EMD method.

The total acceleration, pulse component and the residual acceleration of the RRS228 are plotted in Fig. 3.10. It is observed that the peak value of the pulse component occurs at the same time instant and is almost equal to that of the total acceleration. It is noted that the period of the pulse component is also the same as that of the total acceleration (i.e., T_p=1.0s) in this case. The broadband frequency contents are contained in the residual acceleration.

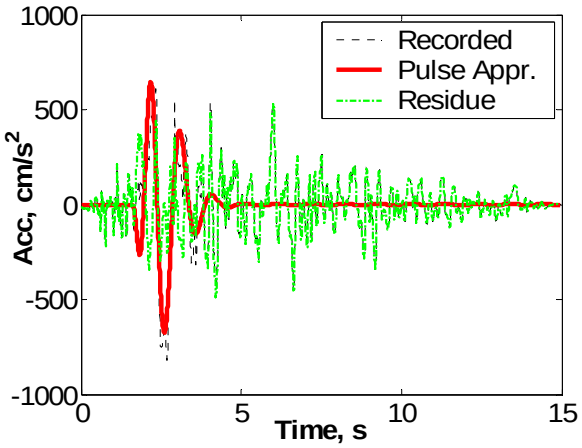

Figure 3.10 Total, pulse and the residual acceleration of the RRS228 record.

IMF of the Residual Acceleration: The EMD analysis is applied on the residual acceleration (R.A) of the RRS228 and the results are shown in Fig. 3.11. Seven IMF components, C1 ~ C7, are obtained for the residual acceleration compared with eight for the total acceleration shown in previous section. It is observed from Fig. 3.11 that the EMD components for the residual acceleration do not contain distinct pulse components as those of C3 and C4 as shown in Fig. 3.5. By observation, the high frequency (e.g., C1 and C2) and long period components (e.g., C5, C6 and C7, etc) of the residual acceleration in Fig. 3.11 are similar to those of the total acceleration in Fig. 3.5. This indicates that components C3 and C4 of the total acceleration are similar to the pulse component represented by the pulse model.

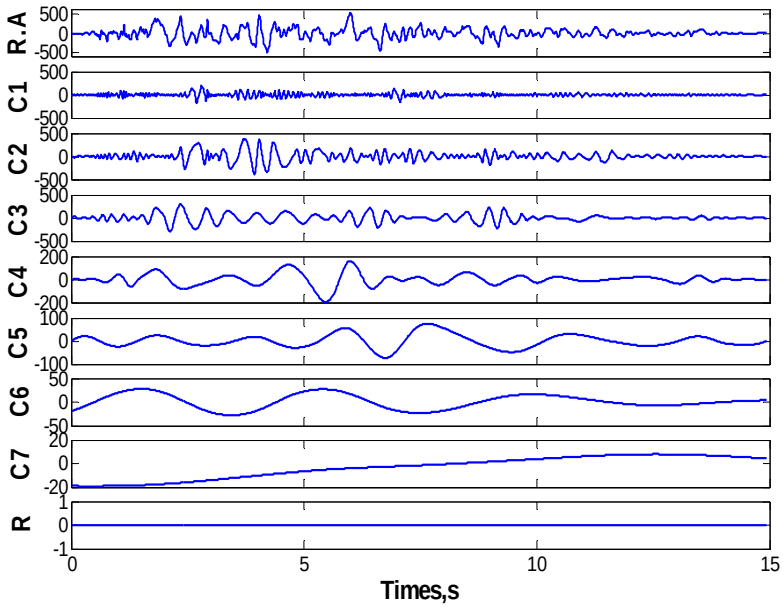

Figure 3.11 The residual acceleration and its EMD components of the RRS228 record after subtracted dominant pulse component

Peak Acceleration: The peak values of the pulse component and the IMFs of the residual acceleration are presented in Fig. 3.12 by histogram. It is observed that the

magnitude of the pulse component (denoted as “Pul” in abscissa) is much larger than that of the IMFs since that the pulse component is the major content. Among the IMFs, the peak values corresponding to C2 and C3 are larger than others. However, these components occur at different time instants and thus do not contribute to the magnitude of the total acceleration.

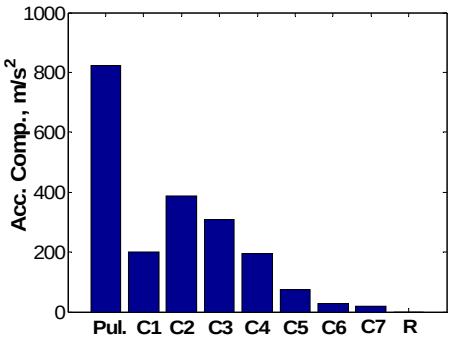

Figure 3.12 Peak values of the pulse component and the IMFs of the residual acceleration of the RRS 228 record

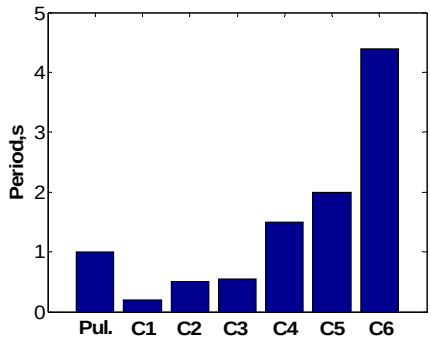

Figure 3.13 Dominant periods of the pulse component and the IMF components of the residual acceleration of the RRS228 record: C1~C6 are for the IMF components and “Pul” represents the pulse component.

Dominant Period: The dominant periods of the pulse component (denoted as “Pul” in abscissa) and the IMFs of the residual acceleration are shown in Fig. 3.13. It is clear that the dominant periods of these residual IMFs are out of the range of the pulse period (T_p=1s). Among these components, C1, C2 and C3 are “high-frequency” components and

their periods are less than the pulse period, other components are “long-period” components and have longer periods. Hence, subtracting the pulse component from the total record eliminates the component having frequency contents close to the predominant period of the record.

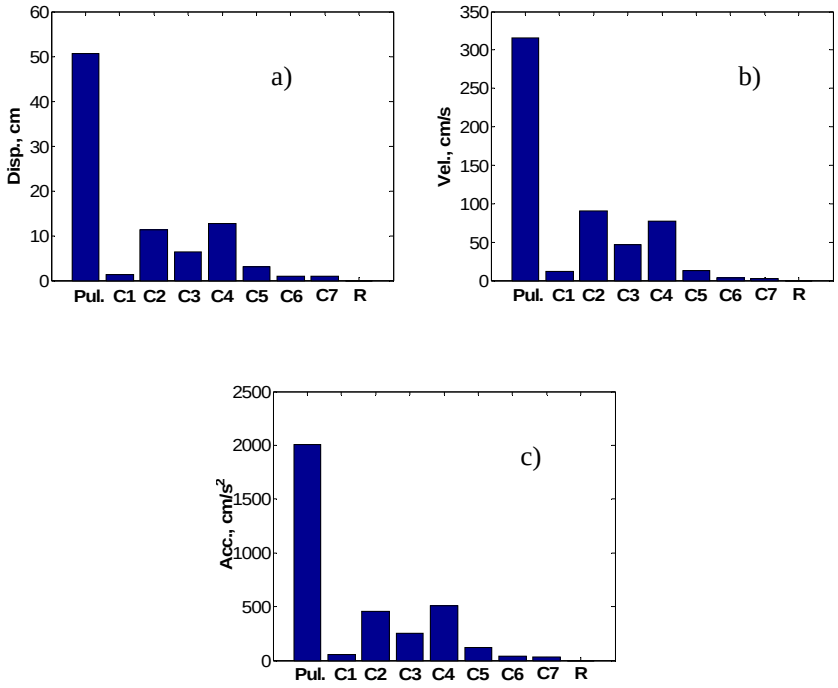

Figure 3.14 Maximum response of a SDOF structure (T_n=1.0s) subject to the pulse and the IMF components of the residual acceleration of the RRS228 record: a) Displacement; b) Velocity and c) Absolute Acceleration.

Peak Responses: Fig. 3.14 presents the maximum displacement, velocity and acceleration responses of a SDOF structure (T_n=1.0s, 5% inherent damping) subject to the pulse component and the IMF components of the residual acceleration of the RRS228 record. It is observed that the responses corresponding to the pulse component are the largest in each case. This demonstrates that the dominant frequency component of the record has been successfully extracted by the pulse model. On the other hand, the

responses to other components are much smaller since 1) the corresponding peak accelerations are small; 2) the periods are far from the predominant earthquake period and 3) the peak values of different components occur at different time instants.

3.4.3 Dominant Pulse Components

It is observed from Fig. 3.5 that the component C3 and C4 of the total acceleration obtained by EMD analysis show distinct impulsive characteristics. The dominant periods of these two components are close to that of the earthquake (Fig. 3.8) and the peak responses corresponding to these two components are also much larger than others (Fig. 3.9). On the other hand, the pulse component of the RRS228 can also be extracted using the pulse model described in Eq. (3.1), as shown in Fig. 3.10. Fig. 3.15 shows the comparison of the pulse components resulted from the pulse model and the EMD analysis (which is taken as the summation of C3 and C4 from Fig. 3.5). It is observed that the major pulses of the two plots match each other well, although the summation of C3 and C4 has more spikes during other time instants.

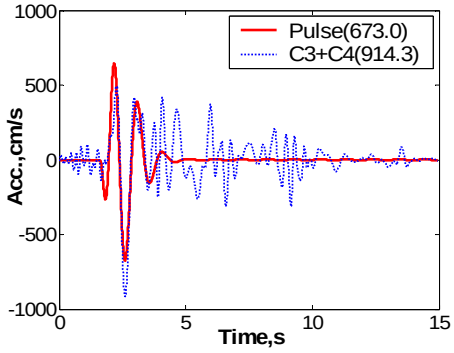

Figure 3.15 Comparison of the pulse component extracted using the pulse model and the EMD analysis

Fig. 3.16 shows the response histories of a SDOF structure (T_n=1.0s, 5% inherent damping) subjected to the pulse components obtained by the pulse model and the EMD analysis. It is observed that the responses corresponding to the two types of "pulse" excitations match very well in the entire history for all three quantities. Hence, the effects of the pulse components obtained by the EMD analysis and the pulse model on structural responses are equivalent. However, it is observed from Fig. 3.15 that the pulse component expressed by the pulse model is smooth and is a continuous function of time. Hence, the pulse model is preferable over the EMD approach in obtaining pulse components of near-field earthquakes for systematic studies.

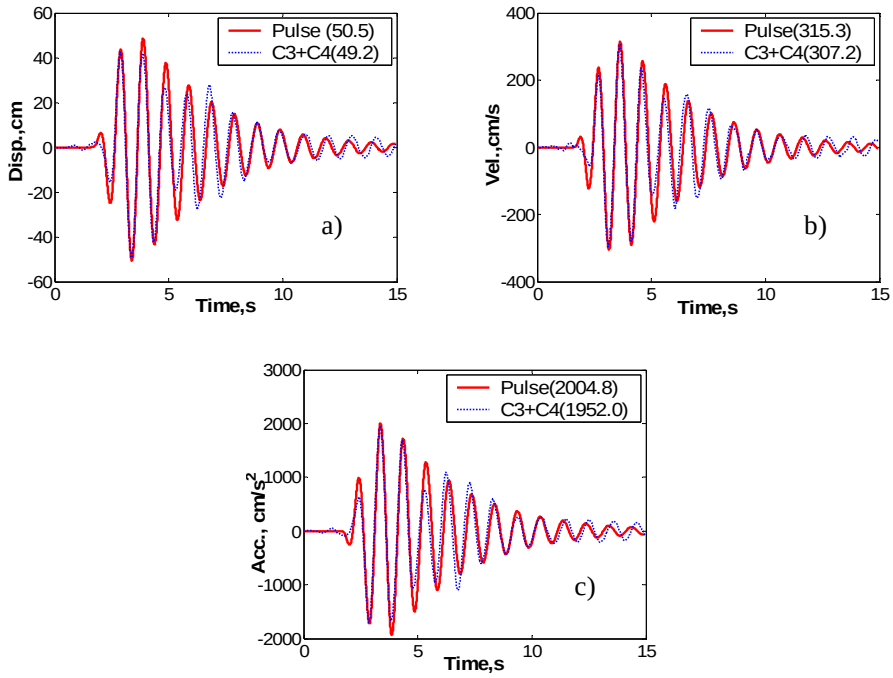

Figure 3.16 Comparison of the response time histories of the pulses component extracted using the pulse model and the EMD: a) Displacement; b) Velocity and c) Acceleration.

3.4.4 Responses of Short-, Intermediate- and Long-period Structures

Linear Structures: It is observed from Fig. 3.11 and 3.13 that the dominant periods of the IMFs of the residual acceleration are either greater or less than the dominant period of the full acceleration (1.0s). The components of the full acceleration are then divided into three categories based on their dominant periods: the pulse component (represented by the pulse model), high-frequency component (summation of C1, C2 and C3 in Fig. 3.11) and long-period component (summation of C4, C5, C6, C7 and R in Fig. 3.11). Fig.3.17 shows the time-history plot of the three distinct components. It is noted that the summation of high-frequency and long-period components accounts for the total broadband frequency effect.

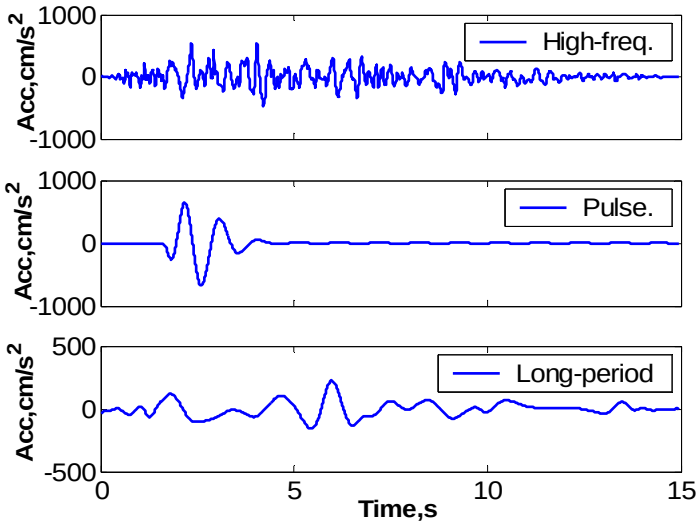

Fig 3.17 High-frequency, dominant pulse and long-period components of RRS228 record.

Fig.3.18 shows the displacement, velocity and acceleration response histories of three different SDOF structures (T_n=0.2, T_n=1.0s and T_n=5s) subjected to the full RRS228

excitation and it's components in Fig.3.17. These three structures are used to represent short (rigid), intermediate and long period (flexible) structural systems correspondingly. For simplicity, the SDOF structures are assumed to have unit mass (m=1). The peak response quantities of each case are shown in the parentheses of Fig. 3.18. It is noted that the responses to the total acceleration are equal to the summation of the responses to the components at every time instant for linear structural systems.

It is observed from Fig.3.18a that the responses to high-frequency component are prevailing in each plot during most of the time instant. The pulse component only has two response cycles (between 2 and 4s) and does not obviously affect the response at other time instants. However, it contributes a significant portion to the peak responses.

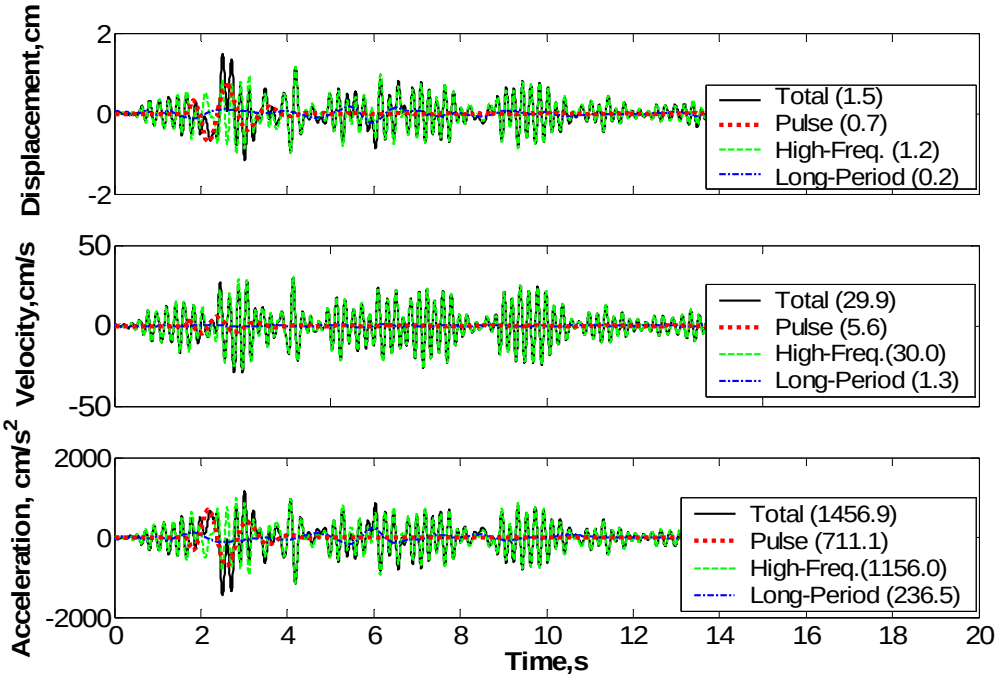

a) T_n=0.2s

Figure 3.18 Response histories of SDOF structures subjected to the total acceleration, pulse, high-frequency and long-period component: a) T_n=0.2s

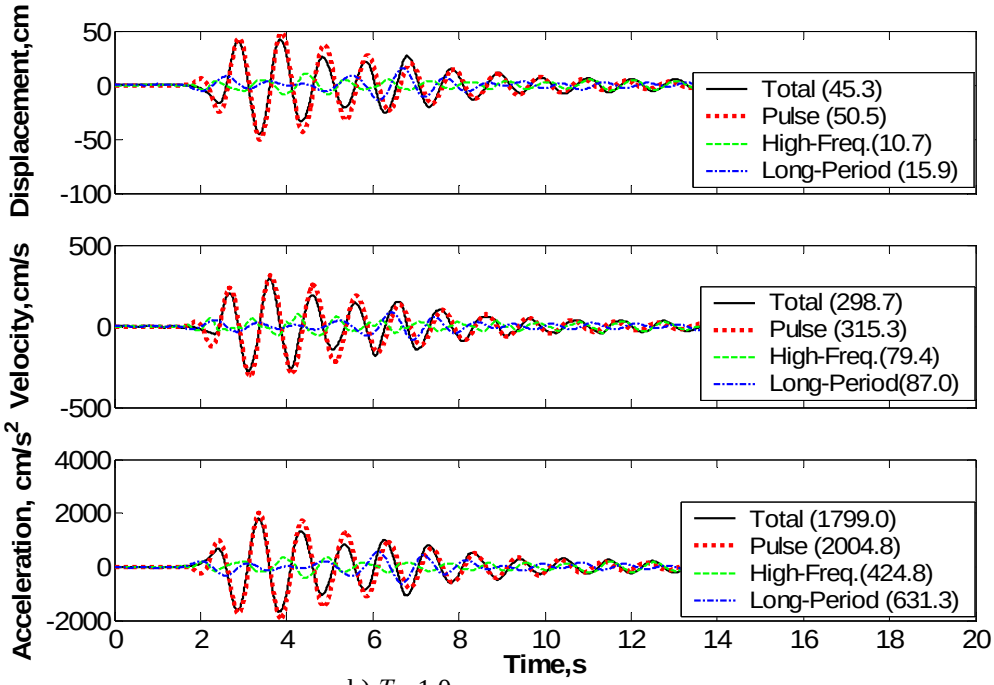

b) T_n=1.0s

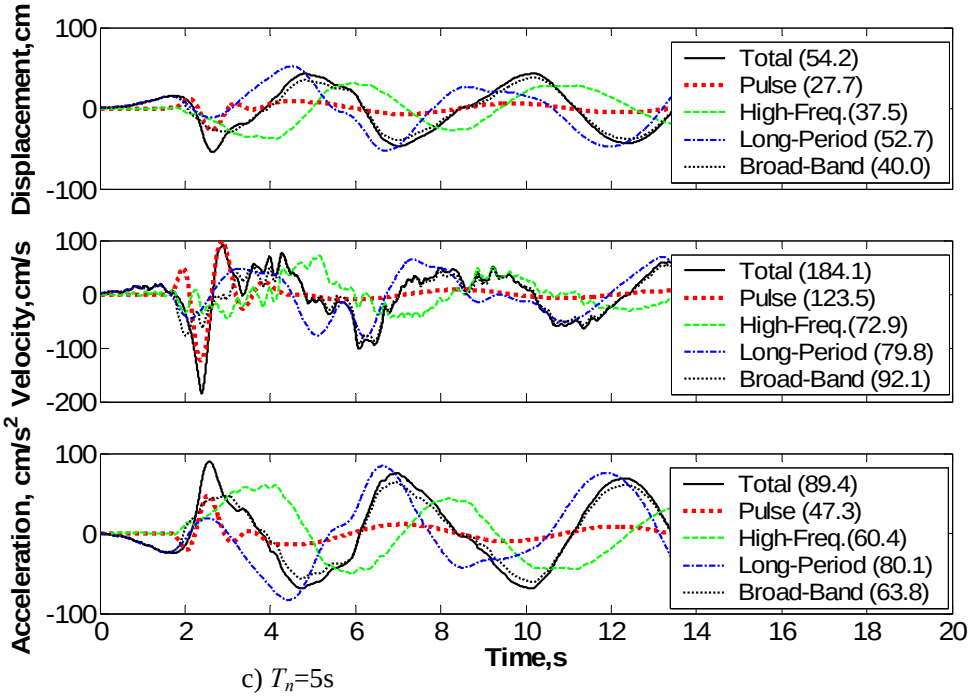

c) T_n=5s

Figure 3.18 (Cont.) Response histories of SDOF structures subjected to the total acceleration, pulse, high-frequency and long-period component: b) T_n =1.0s; c) T_n =5.0s

For the case of intermediate structure (T_n =1.0s) shown in Fig. 3.18b, responses to the pulse component are dominating and match the corresponding total responses very well. The contributions from both the high-frequency and long-period components are very small.

For the case of long-period structure (T_n =5s) shown in Fig. 3.18c, the responses to all three components are all significant. The pulse component again makes significant contribution to the overall peak responses during 2 ~ 4s. However, the high-frequency and long period components are dominating during other time instants. It is observed from Fig. 3.18c that the peak responses to the high-frequency and long-period components are comparable in all three response plots. However, the responses to these two components counteract with each other due to the phase difference; which results in a smaller broadband frequency component response (summation of high-frequency and long period components). Since the pulse characteristic only exists during a short time (approximately 2~4s for this case), the response to the total acceleration is almost coincident with that of the broadband frequency component when t is out of this range. Compared with Fig. 3.18a and 3.18b, it is observed that the acceleration response in Fig. 3.18c (long period structure) is much smaller and the displacement response is much larger, which are the distinct response characteristics of long period structures.

It is concluded from the above analysis that the pulse component controls the peak responses of a structure, which occur during a short time range. Broadband frequency components (i.e., high-frequency and long period) affect responses of other time instants over which the magnitude is relatively small.

Nonlinear structures: To further investigate the effects of pulse and broadband frequency components on structural responses, three elastic-perfectly-plastic SDOF structures with the corresponding elastic periods equal to 0.2s, 1.0s and 5.0s are employed in this investigation. To simplify the analysis, the nonlinear SDOF structures are assumed to have unit mass and have ductility factor μ = 4 when subjected to the full excitation. The other properties of these nonlinear SDOF structures are presented in Table 3.2. In Table 3.2, T_n is the elastic period, μ is the ductility factor resulted from the full RRS228 excitation, k is the elastic stiffness, U_y is the yielding displacement limit at μ = 4, U_0 is the maximum elastic structural displacement subjected to the full excitation, U_{max} is the maximum nonlinear structural displacement and F_y is the yielding force. It is noted that the U_0, $Umax$, U_y and F_y are corresponding to the full RRS228 excitation at μ=4.

Table 3.2 Property of SDOF nonlinear structures with unit mass

	T_n(s)	μ	k	U_y	F_y (N)	U_0	U_{max}
SDOF1	0.2	4	986.96	0.80	792.42	1.47	3.19
SDOF2	1.0	4	39.48	10.84	428.06	45.34	43.32
SDOF3	5.0	4	1.58	15.66	24.73	54.22	62.54

The nonlinear structural behavior is modeled by the Bouc-Wen model with parameters α = 0, β = 0.5, γ = 0.5, n = 3, and A = 1.0. Details of using the Bouc-Wen model in representing nonlinear structural behaviors will be covered in Chapter 4 and 5. Figs. 3.19~3.21 show the response information of the three SDOF structures subjected to the full excitation, pulse component and broadband frequency component of the RRS228 record, respectively.

It is observed from Fig. 3.19a that when the T_n=0.2s ("rigid") structure is subjected to the full excitation, it is displaced to a new position due to yielding after experiencing several elastic oscillation cycles with respect to its original position during first few seconds. The inelastic deformation causes the mass center shifted by 2.2 cm and this inelastic deformation cannot be recovered. It is noted that the inelastic deformation is formed by a single pulse motion ("displacement jump") rather than cumulative displacement. It is also observed that the response to the broadband frequency component alone has the same oscillation style as that of the total acceleration when t < 2.0s or t > 4.0s.

It is known from Table 3.2 that the yielding displacement limit for this case is 0.80cm, which is shown by the two dashed horizontal lines in Fig. 3.19a. The inelastic deformation is formed during 2~4 seconds for this case, which is primarily caused by the pulse effects. The response to the total acceleration during other time is determined by the broadband frequency component in that the two response curves are essentially similar if the influence of permanent displacement is disregarded.

Fig. 3.19b shows the structural force response history. The yielding strength for this case is 792.42 N as shown in Table 3.2. The circle in this plot denotes the time during which the structure reaches yielding. It is observed that the pulse force history has similar trend as that of the total acceleration during 2 ~ 4 seconds and the major plastic deformation is formed herein. During other time, the force corresponding to the broadband frequency component almost coincides with that of the total acceleration while the force corresponding to the pulse is almost zero. It is noted that the structure experiences elastic deformation with respect to its original position when t < 2.0s and it

vibrates at a new position with permanent deformation when t > 4.0s. Pulse component in near-field ground motion imposes much higher level of displacement demand than broadband components and is responsible for inelastic deformation. The pulse component pushes the structure close to yielding limit and a small additional contribution from broadband frequency component eventually drives the structure beyond elastic limit and results in large inelastic deformation. These phenomena can be further verified by the hysteresis plot in Fig. 3.19c.

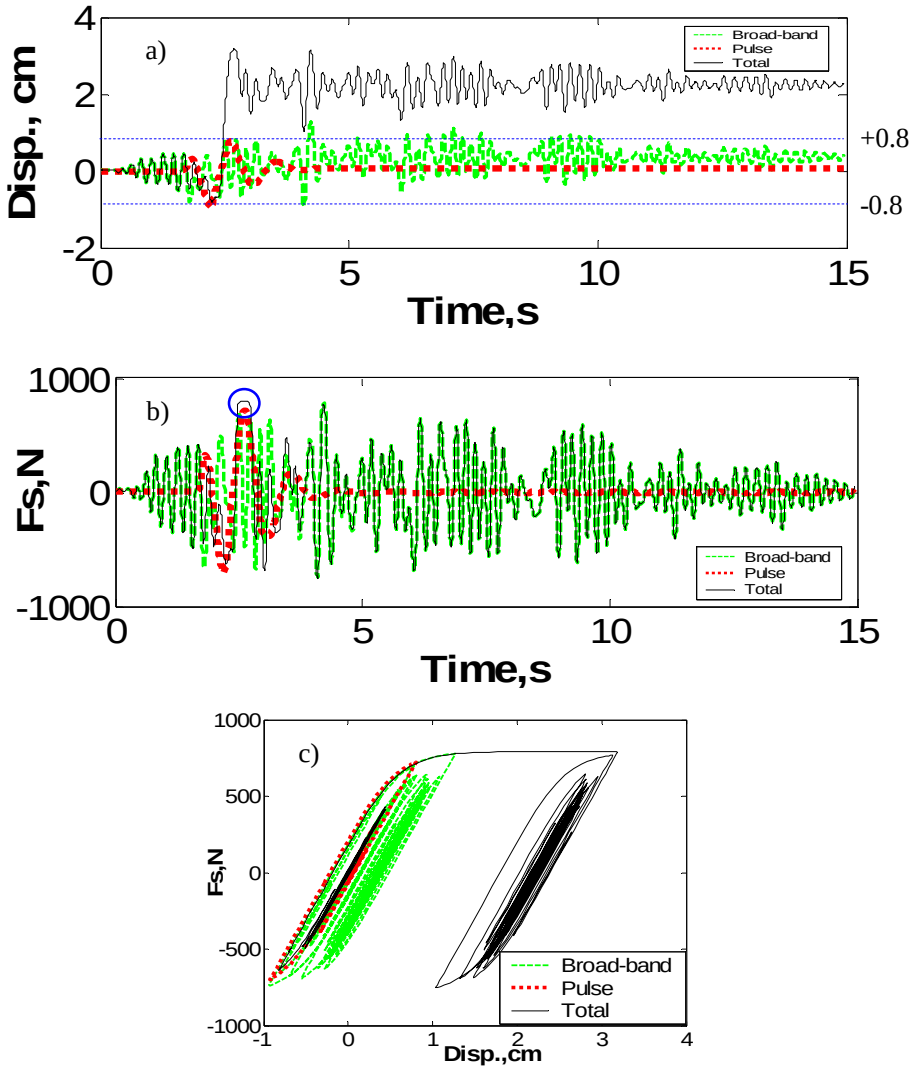

Figure 3.19 Response information of the rigid nonlinear SDOF structure (T_n =0.2s): a) Displacement history; b) Structural force history; c) Hysteretic loop

Fig.3.20 shows plots for intermediate nonlinear structure with T_n = 1.0s. It is noted that the effect of the pulse component is distinctive in this case since the elastic structural period is close to the predominant period of the record. The yielding displacement limit for this case is 10.84 cm, as shown by the two dashed lines in Fig. 3.20a. The pulse component is strong enough to cause inelastic deformation of the structure, although the structure develops permanent displacement because of combined effects of the pulse and broadband frequency components. The displacement jump observed from the hysteretic loop in Fig. 3.20c shows that the permanent displacement is developed during just one loading cycle. The area enclosed by the hysteretic loop because of the pulse component alone contributes most significantly to the area enclosed by the total ground acceleration, which confirms that the pulse component alone can cause significant inelastic deformation in this case.

Fig. 3.21 shows the result for a flexible structure with T_n=5.0s subjected to pulse, broadband and total ground accelerations. The yielding displacement limit for this case is 15.66 cm. The structure is excited strongly by the broadband frequency component in this case because this component has frequency contents in the range of the structural frequency. However, the pulse component alone is also capable of pushing the structural displacement to the yield displacement limit. As a result, the pulse component develops permanent displacement and the magnitude of this permanent displacement increases because of the contribution from the broadband frequency component.

Hence, it can be concluded for the above three cases that the pulse effect is dominating in causing the major inelastic deformation for all types of structures during

pulse-type ground motions and the broadband frequency components are more influential on the post-yielding behavior of structures.

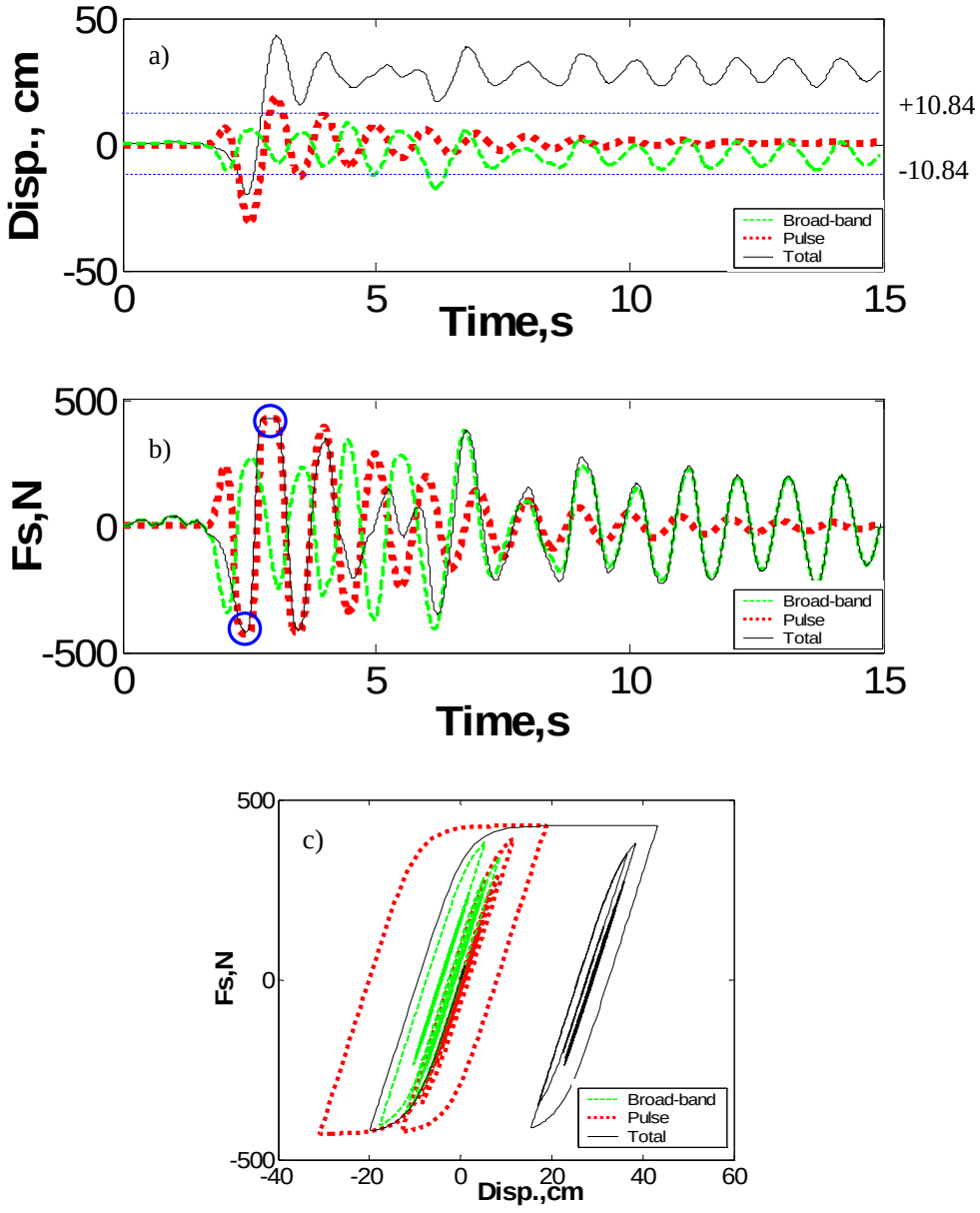

Figure 3.20 Response information of the intermediate nonlinear SDOF structure (T_n =1.0s): a) Displacement history; b) Structural force history; c) Hysteretic loop

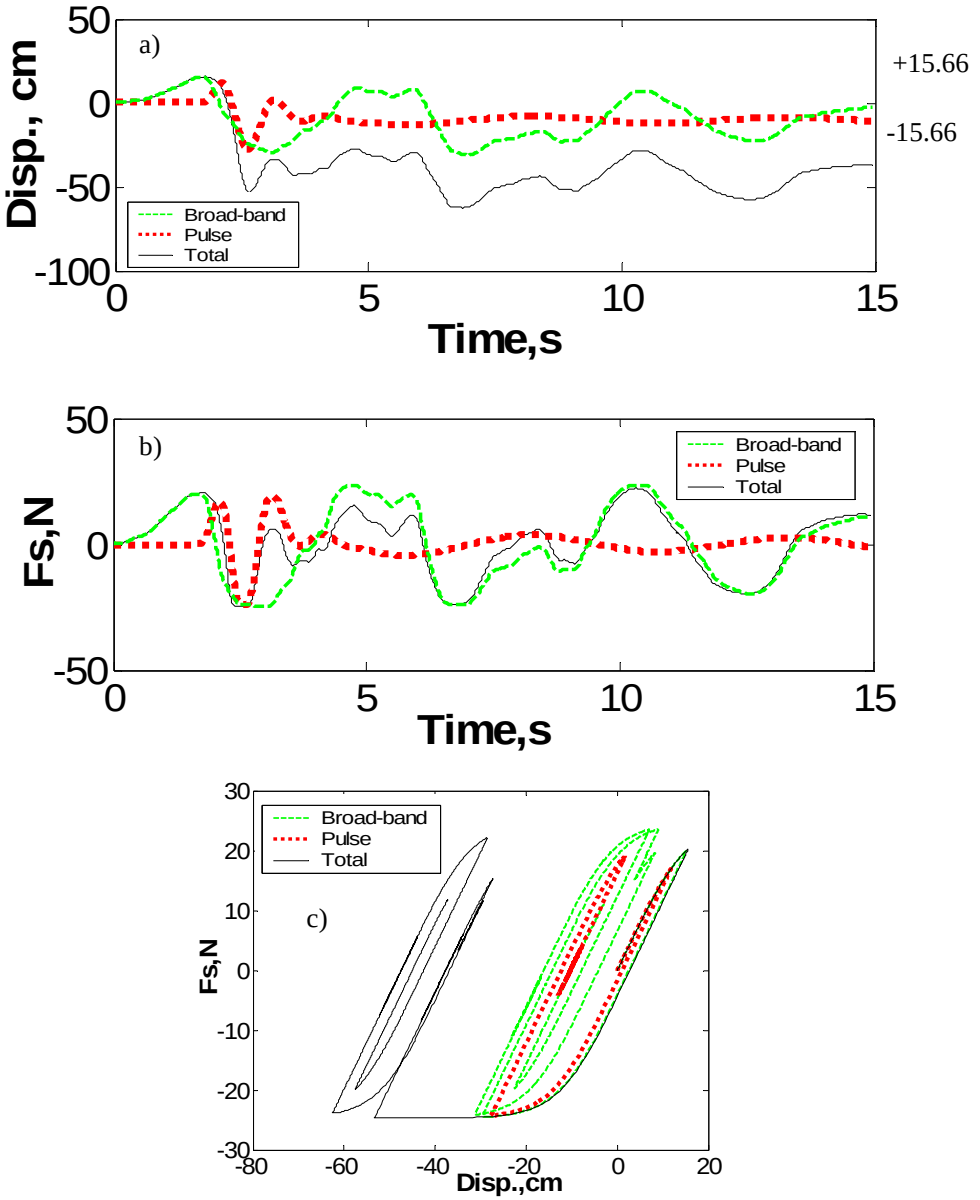

Figure 3.21 Response information of the flexible nonlinear SDOF structure (T_n =5.0s): a) Displacement history; b) Structural force history and c) Hysteretic loop.

Formation of Inelastic Displacement: It is observed from the force-displacement plots in Fig. 3.19 ~ 3.21 that permanent displacement caused by the total ground acceleration is formed within one loading cycle in these cases, which is displayed as "displacement jump" in the displacement time history plot of each case. This happens

because there is only one major pulse cycle in the RRS228 record. However, if an earthquake has several dominant impulsive cycles (such as the KJM090, TAK090 and the LGP090 records in Fig. 3.4), the permanent displacement is developed in a cumulative manner through cyclic accumulation.

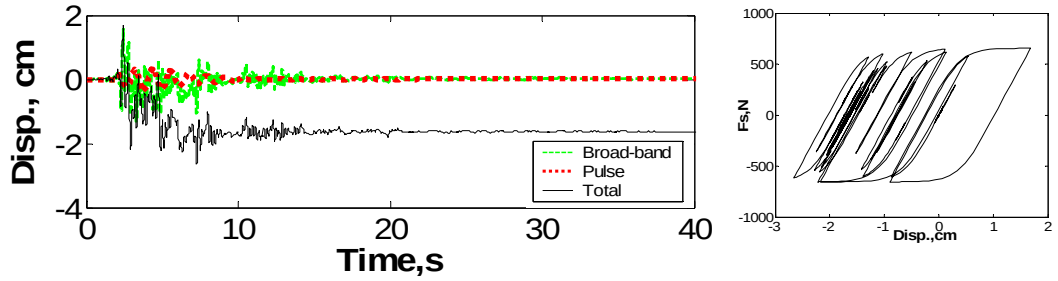

a) T_n=0.2 sec.

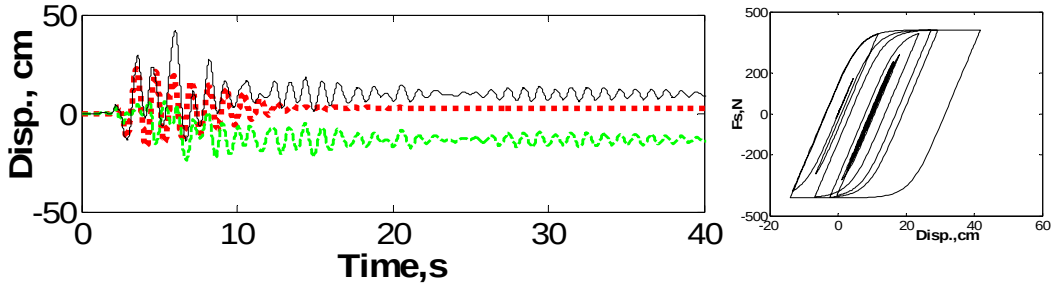

b) T_n=1.0 sec.

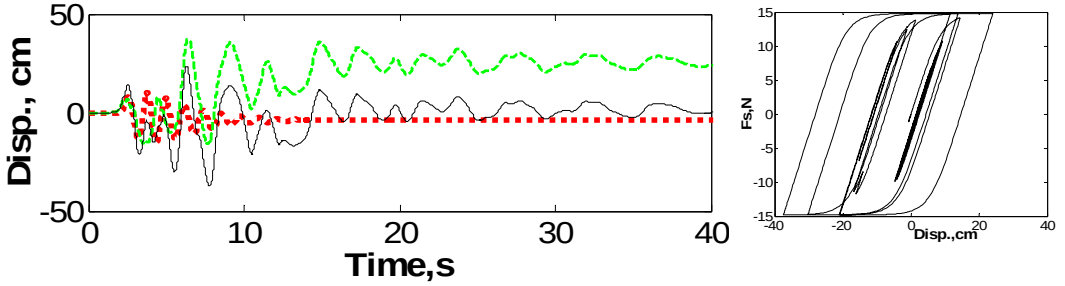

c) T_n=5.0 sec.

Figure 3.22 Displacement response history and corresponding hysteretic loop for nonlinear structures with an elastic period of: a) Tn=0.2s; b) Tn=1.0s and c) Tn=5.0s, subjected to the full excitation of TAK090 record and its component.

As a comparison, Fig. 3.22 shows the displacement response history of the three nonlinear structures subjected to 1995 Kobe earthquake recorded at Taktori station

(TAK090 component). The hysteretic loop corresponding to the total ground acceleration in each case is shown on the right of each plot. It is noted that the pulse behavior is the major factor causing the structure undergoing plastic deformation. Obviously, this record has more pulse cycles than the RRS228 record. As a result, the permanent displacement builds up gradually within 2 to 10 seconds and the corresponding hysteretic loop gradually expands with repetitive loading-unloading cycles in each case.

3.4.5 Peak Responses during the Recorded Earthquakes and Their Components

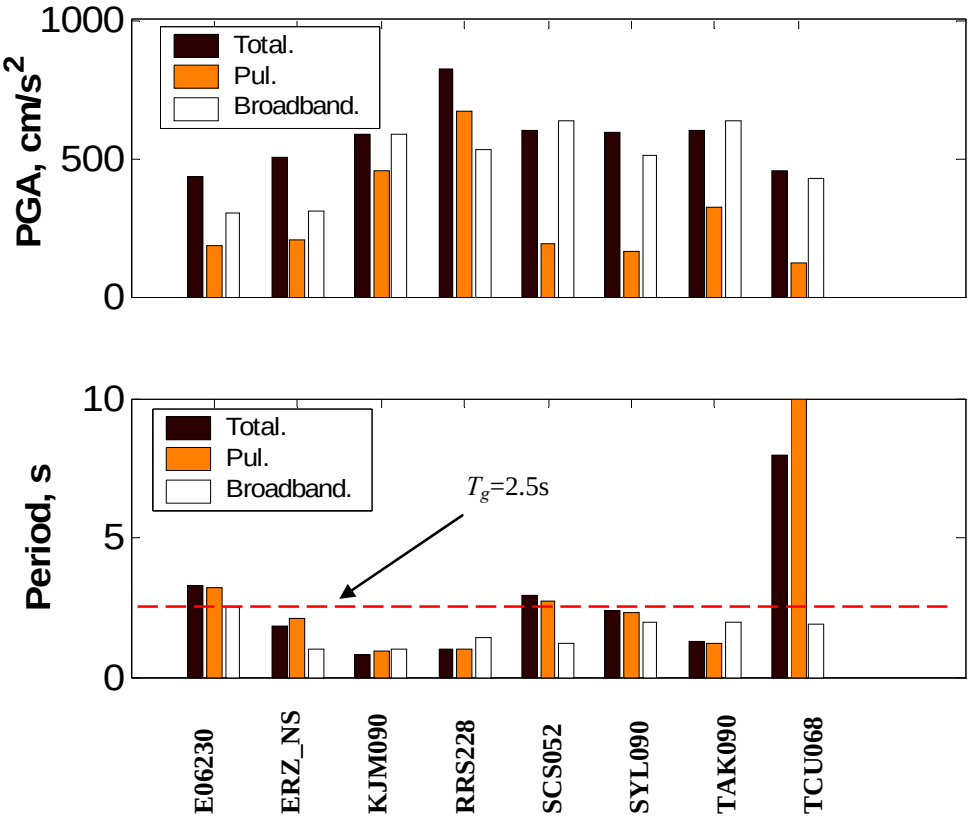

Figure 3.23 Peak accelerations and the dominant periods of the total acceleration, pulse component and broadband frequency component of the eight near-field ground motions, a) Peak accelerations and b) Dominant periods.

The pulse and broadband frequency characteristics of the eight near-field records listed in Table 3.1 are investigated in this section. Fig. 3.23 shows the peak accelerations

and dominant periods of the eight near-field ground motions and their pulse and broadband frequency components. Pulse components of these earthquakes are obtained using the pulse model as shown in Fig 3.4. Broadband frequency components are obtained by subtracting the pulse components from the total accelerations.

It is observed from Fig.3.23a that the PGAs of the pulse components are less than those of the broadband frequency components for these records, although the pulse components are dominant in nature. It is noted that the periods of these records vary from 0.8s to 8.0s and the corresponding pulse components also have the similar periods.

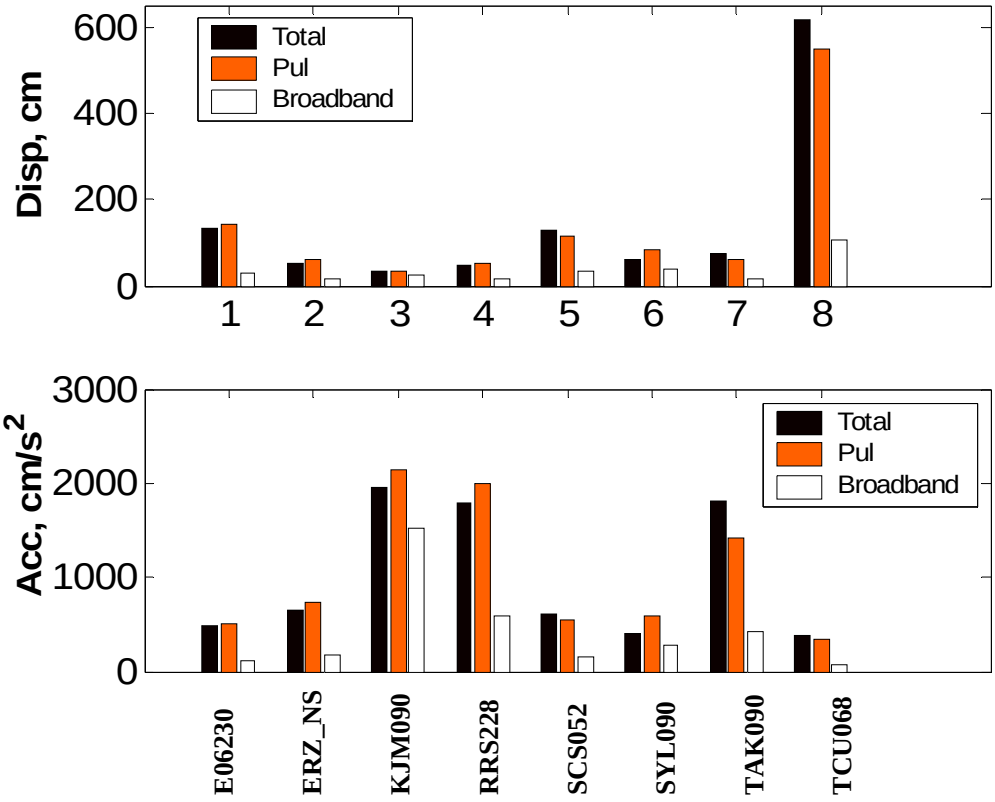

Figure 3.24 Peak displacement and acceleration responses of linear SDOF structures having T_n=T_g subjected to the total acceleration, pulse component and broad-band frequency component excitations of the eight near-field ground motions, a) Peak displacement response and b) Peak acceleration response

Fig.3.24 shows peak displacement and acceleration response quantities of linear SDOF structures subject to total ground accelerations, pulse and broadband frequency components. Response quantities in Fig. 3.24 are obtained for the case of T_n/T_g=1.0, i.e., periods of the SDOF structures are the same as those of total ground accelerations. It is observed that response quantities for the pulse component of each earthquake are very close to those for total ground acceleration in all cases. On the contrary, response quantities for the broadband frequency components are much smaller, although peak values of these components may be larger than those of the pulse components. It is noted that the peak displacement of TCU068 earthquake is much larger than others since the dominant period of this earthquake is much longer (8.0s).

Fig. 3.25 shows peak displacement and acceleration responses of a linear SDOF structure with T_n=2.5s, subjected to total excitation, pulse and broadband frequency components of the eight near-field records. It is observed from Fig. 3.25 that peak responses subjected to the broadband frequency components of TAK090 and TCU068 are larger than those of the pulse components for these two earthquakes. This happens because the dominant periods of the broadband frequency components of these two earthquakes are closer to 2.5 sec. Response quantities of pulse components are dominant for all other earthquakes. It is noted that peak response quantities for broadband frequency components and the pulse components cannot be added to obtain peak response quantities for total excitations, since peak values of broadband frequency components and pulse components occur at different time instants.

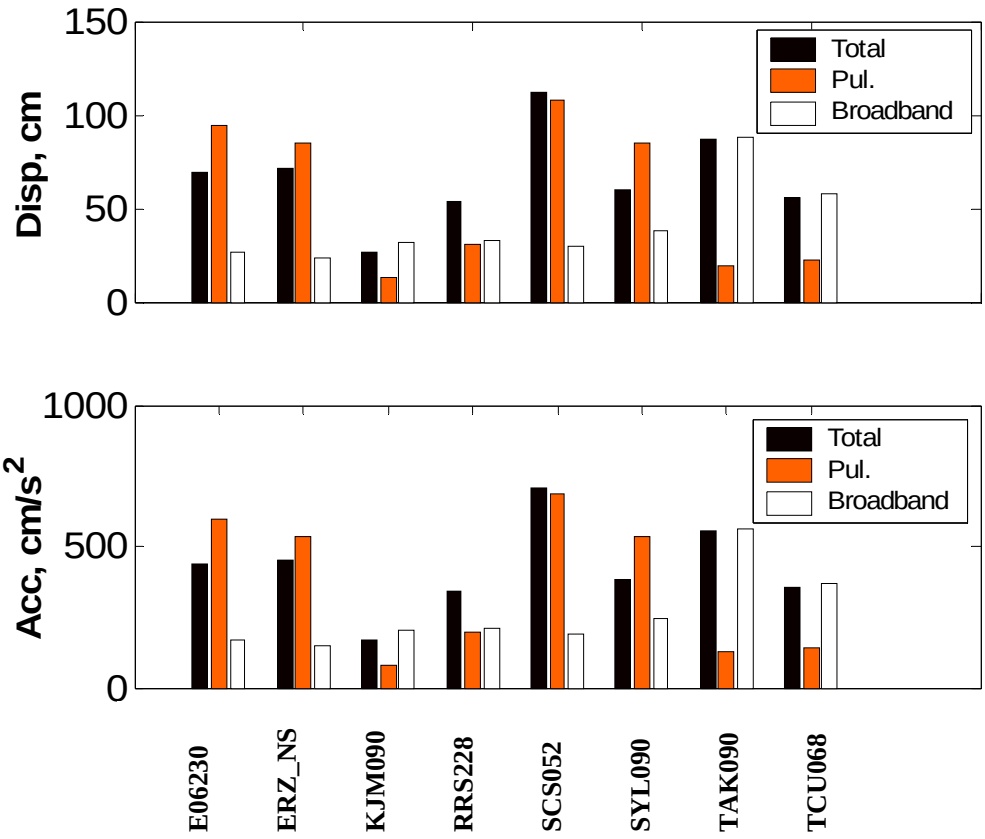

Figure 3.25 Peak displacement and acceleration responses of a linear SDOF structure having T_n=2.5s subjected to the total acceleration, pulse component and broad-band frequency component excitations of the eight near-field ground motions, a) Peak displacement response and b) Peak acceleration response

Hence, the accuracy of the pulse model in characterizing the dominant near-field ground motion effects depends on the ratio of structural period and the predominant period of ground motions. When the two periods are close to each other, the pulse excitation effect of a near-field record is more noteworthy. In practice, this will be the worst scenario since the structure will be subjected to largest deformation demands.

3.5 CONCLUSIONS

The characteristics of near-field ground motions are investigated in this Chapter. Utilizing the velocity pulse model proposed by He (2003), dominant pulse components of

near-field ground motions can be successfully extracted. An earthquake record can also be decomposed into a series of Intrinsic Mode Functions having different frequencies via the Empirical Mode Decomposition approach. Using these two methods, a near-field ground motion record can be separated into three components, i.e., high-frequency component, dominant pulse component and long-period component. The summation of high-frequency component and long-period component is also regarded as broadband frequency component.

Characteristics of different components and their effects on structural responses are investigated using 8 near-field ground motion records. It is demonstrated that the pulse effect is a distinct characteristic of near-field ground motions and the pulse component is responsible for imposing excessive deformation demand on both linear and nonlinear structure. In fact, the pulse component has the most significant contribution in pushing a nonlinear structure to the limit of elastic deformation or into inelastic stage. The broadband frequency components account for post-yielding deformation with respect to permanent displacement.

Responses of a linear SDOF systems with T_n=2.5s and T_n=T_g subjected to the eight recorded earthquakes and their pulse and broadband frequency components show that the pulse model can be very effective in representing recorded ground motions when the period of a structure and the predominant period of an earthquake are close to each other. Under this situation, the peak structural response behavior is mainly dominated by the pulse characteristic of a near-field record.

CHAPTER 4

PERFORMANCE OF PASSIVE ENERGY DISSIPATION SYSTEMS DURING NEAR-FIELD GROUND MOTION TYPE PULSES FOR LINEAR STRUCTURES

4.1 INTRODUCTION

Passive energy dissipation systems (PEDS) have been used widely for the retrofit of existing structures and performance based design of new structures to reduce structural responses during seismic and wind excitations [e.g., Soong and Dargush (1997), Soong and Spencer (2002), Spencer and Nagarajaiah (2003)]. Most widely used PEDS are linear and nonlinear viscous dampers [Terenzi (1999), Lin and Chopra (2002)], frictional dampers [Pall and Marsh (2002)] and yielding dampers [Aiken and Kelly (1992)]. It has been observed that the performance of PEDS in a linear structure varies during different near-field ground motions, even though PEDS are assumed to be linear [Agrawal and Yang (1999)]. In this Chapter, performance of PEDS during pulse type near-field ground motions is investigated extensively through pulse response spectra and energy balance analysis.

Systematic study of dynamic behavior of structures based on energy characteristics was first proposed by Housner (1959) for earthquake-resistant design. Iwan (1980) has investigated the input energy dissipated due to the inelastic deformation. Uang and Bertero (1988a, 1988b, and 1990) have proposed to use energy concepts as a basis for

structural design and investigated input energy and energy dissipated in structures in the forms of viscous and hysteretic energy. Goel (1997) and Fu and Kasai (1998) have discussed the idea of energy balance for designing supplementary energy dissipation devices. These studies have demonstrated that PEDS not only dissipate energy input to a structure, but also can increase or reduce the total energy input.

It has been observed from recent earthquake records that motions in fault-normal direction contain destructive long-period pulses with high peak ground velocities. Several analytical models have also been proposed by different researchers as mentioned in previous chapters. Among these models, the velocity pulse model proposed by He (2003) is a continuous and is quite simple in form. The validity of this model has been established through comparison with numerous recorded ground motions and corresponding response spectra in several recent studies [He (2003), Wang et al (2002)]. Applications of the pulse model have been demonstrated for pulse strength reduction factor spectra for inelastic structures [Agrawal and He (2004)], and response control of a cable-stayed bridge [He and Agrawal (2005)]. A pulse filter based on the pulse model has also been developed for an optimal design of active and semi-active controllers that can significantly reduce the base and super-structure responses of base-isolated buildings simultaneously [Agrawal et al (2006), Agrawal et al 2005), Xu et al (2005)]. In this Chapter, the pulse model is used to systematically investigate the performance of different PEDS during near-field ground motions.

4.2 BACKGROUND INFORMATION

4.2.1 Motion Equation with Passive Energy Dissipation Systems

The motion equation of a single-degree-of-freedom (SDOF) system can be expressed as

$$m\ddot{x}(t) + c\dot{x}(t) + f_r + u = -m\ddot{x}_g(t) \tag{4.1}$$

where m and c are the mass and damping coefficient, $\dot{x}(t)$ and $\ddot{x}(t)$ are the velocity and acceleration of structure, respectively, $\ddot{x}_g(t)$ is the earthquake excitation, u is the control force due to passive dampers. For linear structural systems, f_r is the elastic structural restoring force only, i.e.,

$$f_r = k_s x(t) \tag{4.2a}$$

where k_s is the structural elastic stiffness. For nonlinear structures, f_r consists of both elastic restoring force and hysteretic force, i.e.,

$$f_r = f_r(t, x, \dot{x}) \tag{4.2b}$$

which can be described as a combination of elastic and inelastic forces:

$$f_r = \alpha_s k_s x(t) + (1-\alpha_s) k_s U_{ys} z(t) \tag{4.2c}$$

where α_s is the parameter that controls the post-yielding stiffness of structure, U_{ys} is the structural yielding limit and $z(t)$ is a dimensionless hysteretic quantity given by the Bouc-Wen model [Wen (1988)]

$$U_{ys}\dot{z} + \gamma_s \mid \dot{x}(t) \mid z \mid z \mid^{n_s - 1} + \beta_s \dot{x}(t) \mid z \mid^{n_s} - A_s \dot{x}(t) = 0 \tag{4.3}$$

where β_s, γ_s, n_s and A_s are the dimensionless parameters that control the shape of the hysteretic loop of the structure.

The control force u by nonlinear viscous dampers with damping coefficient c_d is expressed as

$$u = c_d \left|\dot{x}\right|^{\alpha} \operatorname{sgn}(\dot{x}) \tag{4.4}$$

In Eq.(4.4), the exponent α controls the damper nonlinearity and has typical values in the range of 0.35 ~1 for seismic applications [Lin and Chopra (2002)]. For the special case of α=1, Eq.(4.4) represents the force applied by linear viscous dampers. For a simplified analysis, equivalent viscous damping ratio (ζ_d) of nonlinear viscous dampers during sinusoidal excitation is expressed as [Terenzi (1999), Lin and Chopra (2002), Pekcan et al (1999)],

$$\zeta_d = \frac{c_d \lambda}{2\pi m_s} D^{a-1} \left(\frac{2\pi}{T_e}\right)^{a-2}; \quad \lambda = 4 \cdot 2^a \frac{\Gamma^2(1+a/2)}{\Gamma(2+a)} \tag{4.5}$$

where $\Gamma(.)$ is the gamma function, D is the maximum displacement, T_e is the effective natural period and m_s is the structural mass.

The behavior of yielding damper is also represented by Bouc-Wen model in this investigation and the control force u is then given in terms of damper yielding displacement U_{yd}, damper post-yielding stiffness ratio α, and damper reference stiffness K_d as,

$$u = \alpha K_d x(t) + (1-\alpha) K_d U_{yd} z(t) \tag{4.6}$$

in which $z(t)$ is the dimensionless hysteretic quantity given by the Bouc-Wen model [Wen (1988)],

$$U_{yd}\dot{z} + \gamma_d \left|\dot{x}(t)\right| z \left| z \right|^{n_d - 1} + \beta_d \dot{x}(t) \left| z \right|^{n_d} - A_d \dot{x}(t) = 0 \tag{4.7}$$

In Eq. (4.7), shape of the damper hysteretic loop is controlled by dimensionless parameters β_d, γ_d, n_d and A_d.

4.2.2 **Relative and Absolute Energy Balance**

The energy input to an elastic structure during an earthquake is dissipated by damping mechanism, either inherent or supplemental, exclusively, by the end of the earthquake. However, for an inelastic structure, input energy is dissipated by the combination mechanism of damping and structural yielding. The energy balance information can be obtained by integrating Eq. (4.1) with respect to a small displacement *dx* as [Chopra (2001), Uang and Berto (1988a, 1988b, 1990)]

$$\int_0^x m\ddot{x}(t)dx + \int_0^x c\dot{x}(t)dx + \int_0^x f_r dx + \int_0^x u dx = -\int_0^x m\ddot{x}_g(t)dx \tag{4.8a}$$

i.e.,

$$E_k + E_{in} + E_s + E_u = E_I \tag{4.8b}$$

In which the kinetic energy can be expressed as

$$E_k(t) = \int_0^x m\ddot{x}(t)dx = \int_0^{\dot{x}} m\dot{x}(t)d\dot{x} = \frac{m\dot{x}^2}{2} \tag{4.9}$$

The energy dissipated by the inherent viscous damping is

$$E_{in} = \int_0^x c\dot{x}(t)dx = \int_0^t c\dot{x}^2 dt \tag{4.10}$$

For nonlinear structures, the energy of the third term consists of the recoverable strain energy as well as the yielding (hysteretic) energy, i.e.,

$$E_s = E_r + E_y = \int_0^x f dx = \int_0^t f\dot{x}dt \tag{4.11}$$

where the E_r is the recoverable energy and E_y is the structural hysteretic energy dissipated through the structural yielding, i.e.,

$$E_y = E_s - E_r = \int_0^x f dx - \int_0^x kx dx = \int_0^t f\dot{x} dt - \frac{1}{2}kx^2 \tag{4.12}$$

The energy dissipated by supplemental energy dissipation systems is obtained as

$$E_u = \int_0^x u dx = \int_0^t u\dot{x} dt \tag{4.13}$$

If only supplemental linear viscous damping is provided, it has a similar form as that of Eq. (4.10). For other types of dampers, E_u can be obtained by directly integrating Eq. (4.13).

The total input energy is obtained by integrating the right side of Eq. (4.8a), as follow,

$$E_I = -\int_0^x m\ddot{x}_g(t) dx = -\int_0^t m\ddot{x}_g(t)\dot{x} dt \tag{4.14}$$

The above definitions correspond to "relative" input energy; in conjunction with the "relative" energy equations defined above, the "absolute" energy equations can also be derived as follows [Uang and Berto (1988a, 1988b, 1990)]:

$$\int m\ddot{x}_t(t) dx + \int c\dot{x}(t) dx + \int f_r dx + \int u dx = 0 \tag{4.15}$$

Note that $x_t = x + x_g$, $\dot{x}_t = \dot{x} + \dot{x}_g$ and $\ddot{x}_t = \ddot{x} + \ddot{x}_g$, the first term of Eq. (4.15) can also be expressed as

$$\int m\ddot{x}_t(t) dx = \int m\ddot{x}_t(t)(dx_t - dx_g) = \frac{m\dot{x}_t^2}{2} - \int m\ddot{x}_t dx_g \tag{4.16}$$

Inserting Eq.(4.16) into Eq. (4.15), one obtains

$$\frac{m\dot{x}_t^2}{2} + \int c\dot{x}(t) dx + \int f_r dx + \int u dx = \int m\ddot{x}_t dx_g \tag{4.17}$$

i.e.,

$$E_k^a + E_{in} + E_s + E_u = E_I^a \tag{4.18}$$

where E_k^a and E_I^a are called "absolute" kinetic energy and "absolute" input energy, respectively. Other terms are as defined as before.

Rewriting the absolute input energy as

$$\begin{aligned} E_I^a &= \int m\ddot{x}_t dx_g = \int m\ddot{x}_t (dx_t - dx) \\ &= \int m\ddot{x}_t dx_t - \int m(\ddot{x} + \ddot{x}_g) dx = \frac{m}{2}\dot{x}_t^2 - \frac{m}{2}\dot{x}^2 - \int m\ddot{x}_g dx \end{aligned} \tag{4.19}$$

One obtains

$$E_I^a - E_I = \frac{m}{2}\dot{x}_t^2 - \frac{m}{2}\dot{x}^2 = \frac{m}{2}\dot{x}_g^2 + m\dot{x}\dot{x}_g = E_k^a - E_k \tag{4.20}$$

In this chapter, the "relative" energy balance information is investigated as a criterion in evaluating the structure and damper property. The "absolute" energy will be investigated for comparison purpose in section 7 of Chapter 5.

4.2.3 Pulse-type Excitations

The analytical velocity pulse model proposed by He (2003) and He and Agrawal (2006) is used in this chapter to generate impulsive excitations in the investigation of various passive energy dissipation systems. Details of the analytical model are described in Chapter 3.

Fig. 4.1 shows time-history plots of displacement, velocity and acceleration for a velocity pulse with parameters $T_p = 2\pi/\omega_p$ =1 sec, n=1, a = 2.51, and C=7.17 in Eq. (3.1). These parameters have been selected to obtain 1 m/sec peak pulse velocity and

0.6g peak pulse acceleration. It is observed that the velocity pulse consists of only one and half cycles, and causes 0.13m permanent ground displacement. This type of behavior has been frequently observed in near-field ground motions. It has been shown in Chapter 3 that the pulse model can represent the pulse components of near-field ground motion records reasonably well.

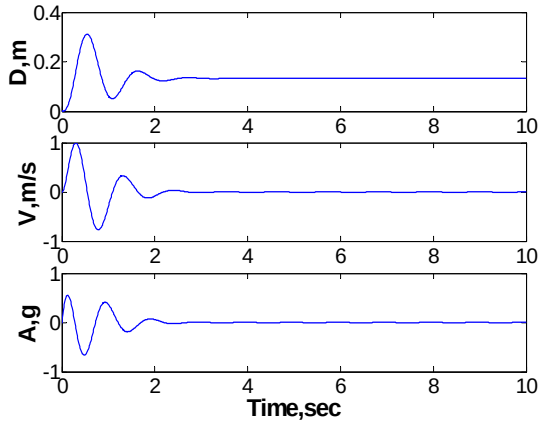

Fig. 4.1: Displacement, velocity and acceleration time histories of the pulse-type ground motion with T_p =1 sec, n=1, a = 2.51, peak velocity = 1m/s and peak acceleration of 0.6g.

4.2.4 Excitation and Damper Parameters

Performance of PEDS is investigated by subjecting SDOF structures with 5% inherent damping ratio to pulse, sinusoidal and recorded near-field ground motions. The pulse ground motion records (pulse excitation) are generated by assuming parameters n=1, $a = 2.51/T_p$ and peak ground acceleration of 0.6g for different pulse period, T_p in Eq.(3.1) of Chapter 3. Peak values and periods for sinusoidal ground accelerations are assumed to be the same as those of the pulse excitations.

Viscous dampers are designed by considering equivalent damping ratios of ζ_d = 15% and 25% using Eq. (4.4). Effects of damper nonlinearity are investigated by considering

α_d = 0.3, 0.5 and 1.0. Parameters of yielding dampers in Eqs. (4.6) and (4.7) are taken as α_d = 0, β_d = 0.5, γ_d = 0.5, n_d = 3, and A_d = 1.0. The yield stiffness (k_d) and yield displacement (U_{yd}) of yielding dampers are expressed in terms of stiffness and displacement capacity of the structure and are varied to investigate their effects on damper performance. Fig. 4.2 shows the behavior of a SDOF linear structure equipped with a yielding damper. It is observed from Fig. 4.2 that the yielding damper increases both stiffness and damping of the structure.

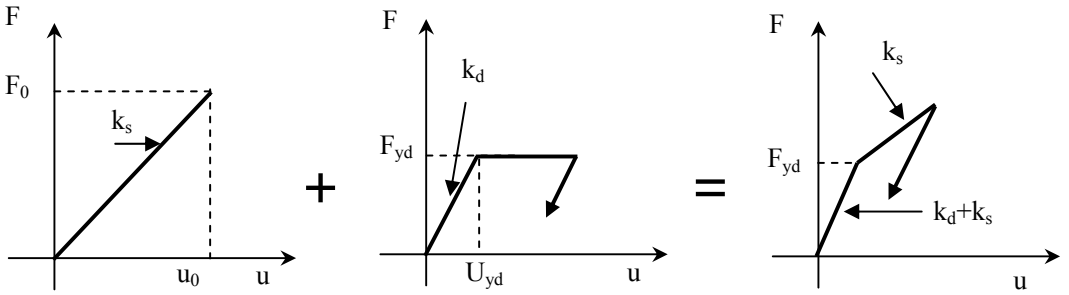

a) Elastic structure b) Yielding damper c) Structure + yielding damper

Figure 4.2: Force-deformation behavior of an elastic structure without and with yielding damper.

4.2.5 Performance Criterion

Performance criteria in terms of normalized spectral displacement, J_D, normalized spectral acceleration, J_A, and normalized maximum input energy, J_{EI}, are defined to evaluate performance of various PEDS as,

$$J_D = \frac{SD(5\%+\zeta)}{SD(5\%)};\ J_A = \frac{SA(5\%+\zeta)}{SA(5\%)};\ J_{EI} = \frac{EI(5\%+\zeta)}{EI(5\%)} \tag{4.21}$$

where, *SD(5%+ζ)*, *SA(5%+ζ)*), *EI(5%+ζ)* are the spectral displacement, spectral acceleration and input energy of the structure equipped with PEDS; and *SD(5%)*, *SA(5%)*,

EI(5%) are the corresponding response quantities without PEDS, respectively.

4.3 RESULTS AND DISCUSSIONS

4.3.1 Response Spectra for Pulse-type versus Sinusoidal Excitations

Extensive numerical simulations are carried out to compare the effects of damping during pulse-type and sinusoidal excitations. Plots in Figs. 4.3(a) and (b) show three-dimensional displacement spectra (SD) as functions of pulse period (T_p) and structural period (T_n) for the SDOF structure subject to pulse-type and sinusoidal excitations, respectively. Plots in Fig. 4.3 are obtained for the cases of the structure without dampers and with linear viscous dampers capable of adding 25% supplemental damping. Both structural and excitation periods are varied from 0.1 to 5 seconds in Fig. 4.3.

It is observed from Figs 4.3(a) and 4.3(b) that the displacement increases with increase in T_n and T_p for both pulse and sinusoidal excitations. For a given T_n or T_p, maximum displacement response occurs when $T_n \approx T_p$. The displacement response caused by sinusoidal excitation is much higher than that by pulse excitation in the vicinity of $T_n \approx T_p$ for the structure with and without dampers. A larger displacement response in the case of sinusoidal excitation is caused by the buildup of response at resonance. The resonance effect during pulse excitation is not as strong as that during sinusoidal excitation since the pulse excitation does not contain enough repeated excitation cycles for the displacement response to build up, as seen from Fig. 4.1. Displacements during both excitations are significantly reduced by the 25% supplemental damping, as demonstrated by the response surfaces corresponding to ζ_d =0 and ζ_d =25% in each plot.

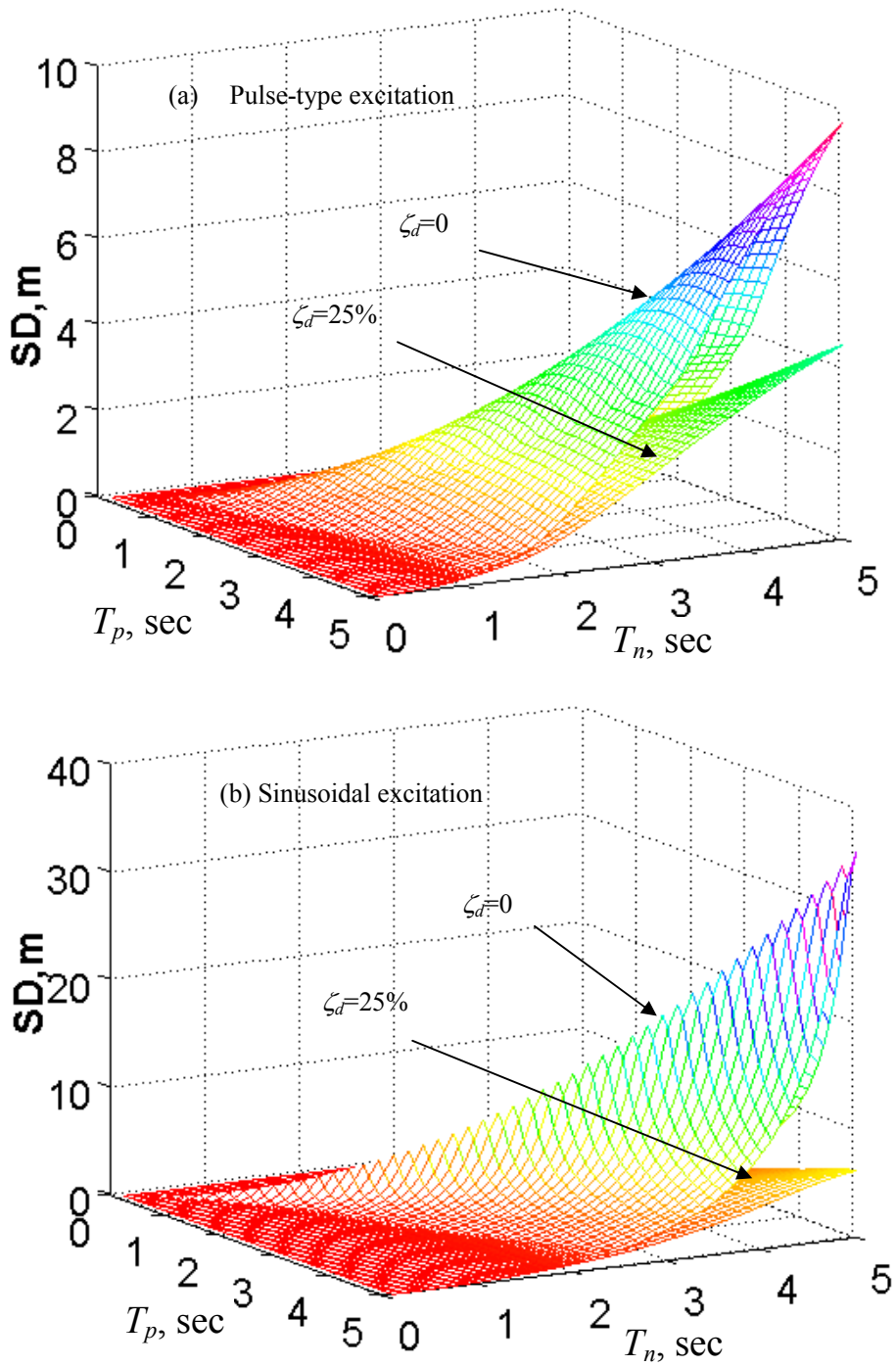

Figure 4.3. 3-Diemsional pulse period (T_p) – structural period (T_n) – peak displacement response spectrum using (a) Pulse-type excitation; (b) Sinusoidal excitation.

(a): Pulse-type excitation

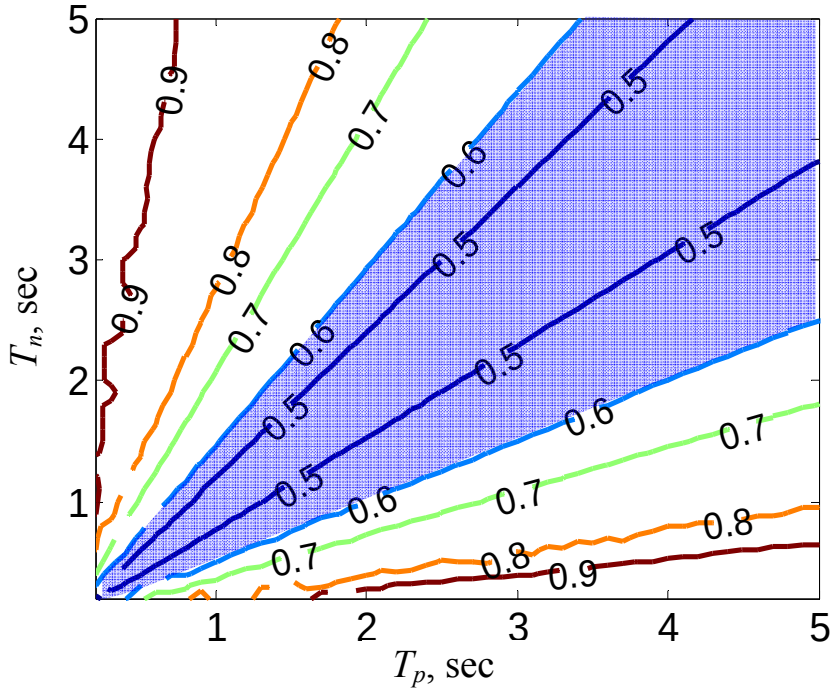

(b): Sinusoidal excitation

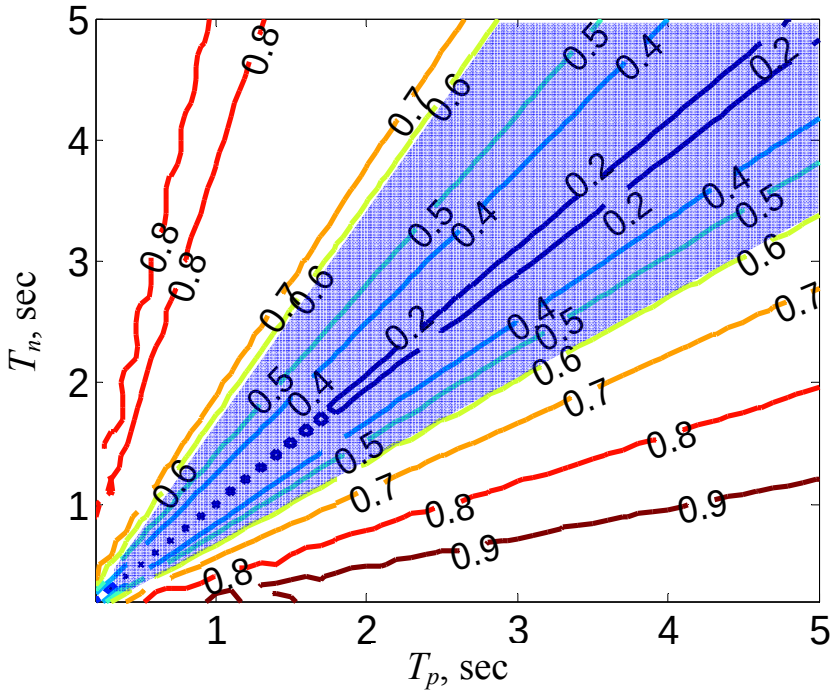

Figure 4.4: Pulse period (T_p) – structural period (T_n) – normalized spectral displacement (J_D) contour plot using (a) Pulse-type excitation; (b) Sinusoidal excitation.

Fig. 4.4 shows contour plots of normalized displacement (J_D) as functions of pulse period (T_p) and structural period (T_n). It is noted that a smaller value of J_D means a better effectiveness of supplemental damping. The hatched areas (mainly within the range of $3/5 < T_n/T_p < 5/3$) in Figs. 4.4(a) and (b) show the region in which more than 40% displacement reduction (i.e., J_D < 0.6) can be achieved during the pulse-type and sinusoidal excitations. The J_D in Figs. 4.4(a) and (b) for pulse-type and sinusoidal excitations equals to 0.48 and 0.18, respectively, along the $T_n = T_p$ line. This demonstrates that supplemental damping is significantly more effective during sinusoidal excitation than during pulse-type excitation near resonance. It can also be observed in the hatched area that the increase in J_D for sinusoidal excitation is much faster than that for pulse-type excitation when (T_p, T_n) pairs move away from the resonance line (i.e., $T_n = T_p$). Overall, the effectiveness of supplemental damping remains almost the same (J_D between 0.5 and 0.6) in the entire hatched area in Fig. 4.4(a) for the pulse-type excitation. Hence, the performance of supplemental damping is less sensitive to resonance during pulse-type excitations.

Plots of J_D versus T_p for the structure with viscous dampers are shown in Fig. 4.5(b). For $T_p \approx T_n$ (near resonance), it is observed that J_D of sinusoidal excitation is much smaller than that of pulse-type excitation, i.e., viscous dampers perform better during sinusoidal excitation near resonance. However, as the excitation period (T_p) increases beyond 4 sec, viscous dampers perform significantly better during pulse-type excitation.

a)

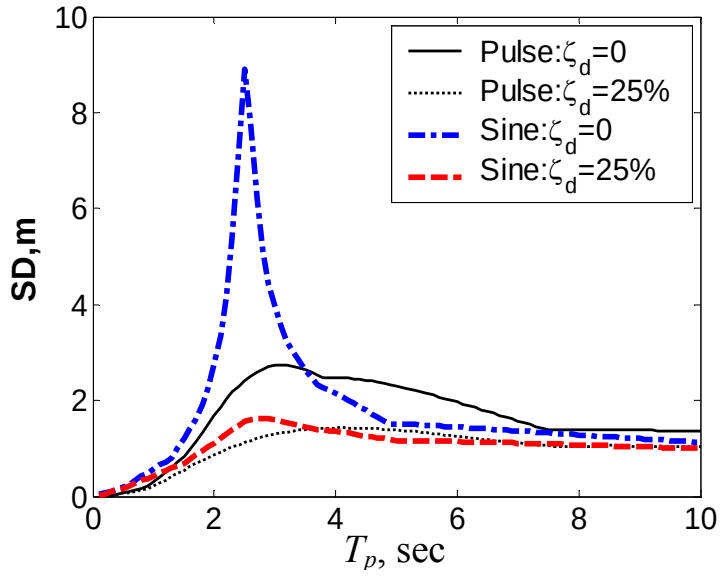

b)

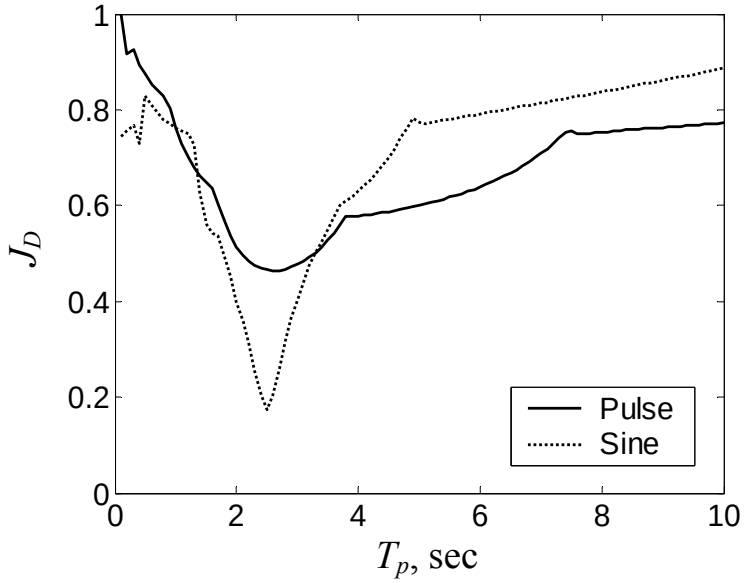

Figure 4.5 Response of a SDOF structure (T_n=2.5 sec) subject to sinusoidal and pulse excitations: a) Spectrum displacement; b) Normalized displacement

4.3.2 Pulse Response Spectra for Linear versus Nonlinear Viscous Dampers

Linear viscous dampers have been found to perform well during mild to moderate earthquakes. However, the force demand on linear dampers during pulse type excitations

may be excessive, leading to device capacity saturation and larger force demands on structural components. Nonlinear viscous dampers may be more suitable in such situations because of their inherent force saturation capability at high velocities. Lin and Chopra (2002) have investigated the response of elastic SDOF structure with nonlinear viscous dampers using selected ground motion records and have shown that the damper nonlinearity doesn't have significant effect in the velocity sensitive region and up to 14% difference in other regions. In this section, the effects of damper nonlinearity on the performance of nonlinear viscous dampers during pulse-type ground motions are investigated.

Left column of Fig. 4.6 shows contour plots of spectral displacement (SD), acceleration (SA) and input energy (EI) as functions of pulse period (T_p) and structural period (T_n) for linear viscous dampers capable of adding 25% supplemental damping. In Figs. 4.6(a) and 4.7(c), SD=0 and EI=0 contour line exists when either T_n or T_p=0, and the contour plots have the largest gradient along the line $T_n = T_p$. For a structure with T_n = 1s, displacement response in Fig. 4.6(a) remains around 0.22 m as the pulse period increases from 1s to 5s. However, for a structure with T_n = 5s, the displacement response increase from 0.22 m to a value larger than 3.85m as the pulse period increases from 1s to 5s. This shows that an increase in pulse period will increase the displacement response of long period structures more significantly than that of short period structures. Although the peak value of pulse acceleration is 0.6g (i.e., PGA=0.6g), it is observed from Fig. 4.6(b) that the peak absolute acceleration of the structure with linear viscous damper is larger than the PGA when $T_p > \frac{4}{5}T_n$, and it is reduced below 0.6g PGA when $T_p < \frac{4}{5}T_n$.

Plots in Fig. 4.6(c) for the input energy spectrum show a trend similar to that of displacement spectrum. It is observed that input energy contour plots are nearly symetric with respect to $T_n = T_p$. Hence, both T_n and T_p play a similar role in terms of input energy response.

Right column of Fig. 4.6 shows corresponding plots of $SD(\alpha = 0.5)/SD(\alpha = 1.0)$, $SA(\alpha = 0.5)/SA(\alpha = 1.0)$ and $EI(\alpha = 0.5)/EI(\alpha = 1.0)$, where $SD(\alpha = 0.5)$, $SA(\alpha = 0.5)$ and $EI(\alpha = 0.5)$ are spectral displacement, acceleration and input energy for a structure equipped with nonlinear viscous dampers having $\alpha = 0.5$ and equivalent damping of 25%. It is observed from Fig. 4.6(d) that the damper nonlinearity gives 5 to 10% additional reduction in peak displacement only when $T_p \geq \frac{4}{5} T_n$. The peak acceleration because of damper nonlinearity remains almost unaffected when $T_p \geq \frac{2}{5} T_n$ and it is reduced up to 40% when $T_p < \frac{2}{5} T_n$, as shown in Fig. 4.7(e). The damper nonlinearity causes the input energy in Fig. 4.6(f) decreases up to 10% when $\frac{4}{5} T_n < T_p < \frac{5}{2} T_n$ and increase up to 20% around $T_p = 0$ or $T_n = 0$; however, the increase in input energy does not have practical significance because these cases either represent zero pulse loading or rigid structural systems. Moreover, peak magnitudes of response quantities for these cases are very small. Hence, nonlinear viscous dampers are more advantageous than linear viscous dampers in reducing peak structural displacements and peak input energies when a structure is subject to pulse-type excitation with pulse period longer than the structural period.

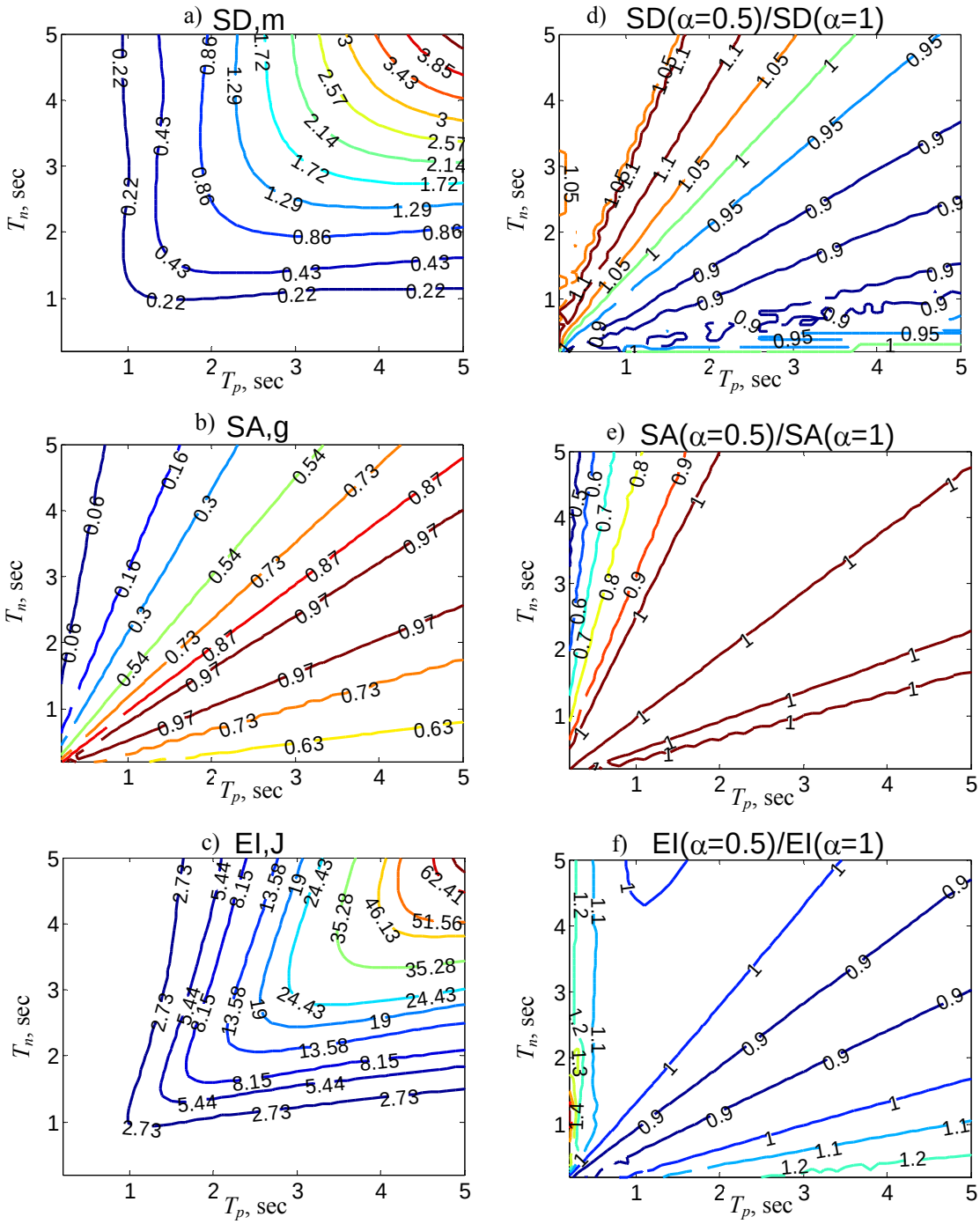

Figure 4.6: Influence of damper nonlinearity on structural response; (a)-(c): Displacement, acceleration and input energy spectrum for structures with 25% linear viscous damping (α=1, ζ_d=25%); (d)-(f): Ratios of response quantities with nonlinear (α=0.5, ζ_d=25%) and linear viscous dampers (α=1.0, ζ_d=25%) showing effects of damper nonlinearity.

4.3.3 Pulse Response Spectra for Yielding Dampers

As shown in Fig. 4.2, yielding dampers protect structures by undergoing inelastic deformation at preset displacement when the structure is subject to large displacement demand. Figs. 4.7(a) – (c) show contour plots of spectral displacement (SD), acceleration (SA) and input energy (EI) as functions of pulse period (T_p) and structural period (T_n) for the uncontrolled structures subject to pulse-type excitation. Figs. 4.7(d)-(f) and 4.7(g)-(i) show contour plots for J_D, J_A and J_{EI} using yielding dampers with $k_d = k_s$, $U_{yd} = 0.2u_0$ [i.e., $F_{yd} = 0.2F_0$] and $k_d = k_s$, $U_{yd} = 0.8u_0$ [i.e., $F_{yd} = 0.8F_0$], respectively. Here, k_s is the structural stiffness, and u_0 and F_0 are the maximum elastic displacement and force responses of the structure without dampers. The yielding damper with $F_{yd} = 0.2F_0$ is considered as "small capacity" damper, whereas that with $F_{yd} = 0.8F_0$ is considered as "large capacity". It is observed from Figs. 4.7(a)-(c) that SD, SA and EI increase with increase in T_p when $T_p < T_n$ and decrease with decrease in T_n when $T_p > T_n$. The performance indices J_D, J_A and J_{EI} are less than 1 mainly when $T_p \geq T_n$, as shown by hatched regions in Fig.s 4.7(d) – (i). In fact, up to 60% reduction in peak displacement and peak input energy and up to 30% reduction in peak absolute acceleration can be obtained in the $T_p > T_n$ region. It is noted that the effective period of a structure with yielding damper decreases compared with its uncontrolled counterpart due to the action of damper stiffness. Hence, the displacement spectrum is "pushed" toward larger structural period side after adding yielding dampers. As a result, structures with period $T_n \leq T_p$ will experience smaller displacement response and those with $T_n > T_p$ might experience larger displacement response.

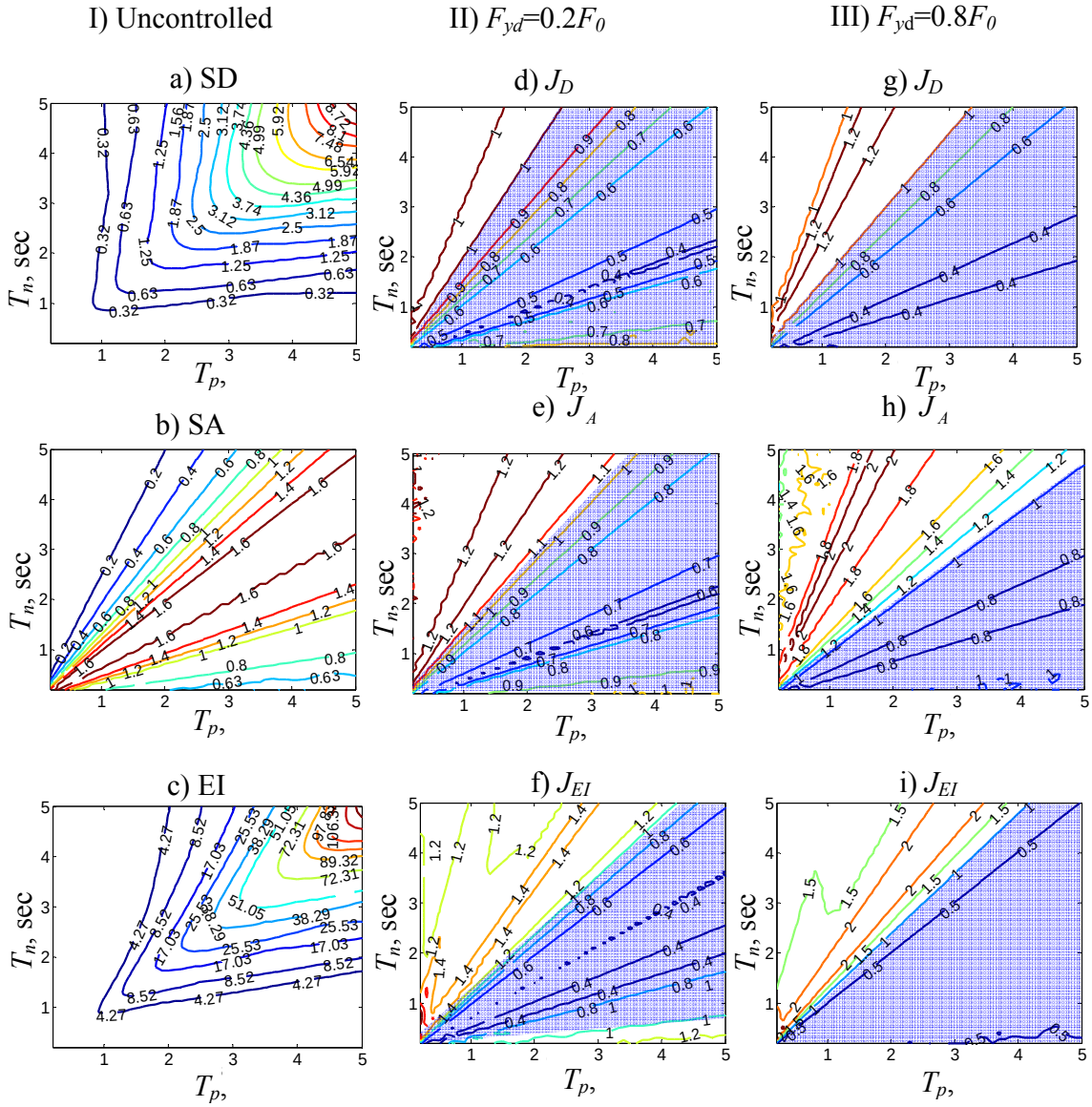

Figure 4.7: Displacement, acceleration and input energy spectra and corresponding normalized spectra for yielding dampers; Column I: Displacement, acceleration and input energy spectra without dampers; Column II: Normalized displacement, acceleration and input energy spectra with F_{yd}=0.2F_0 capacity yielding damper; Column III: Normalized displacement, acceleration and input energy spectra with F_{yd}=0.8F_0 capacity yielding damper.

It is also observed from pulse spectra for "small capacity" and "large capacity" yielding damper in Figs 4.7(d)-(f) and 4.7(g)-(i) that the yielding capacity F_{yd} significantly affects the level of response reduction. The larger the yielding capacity,

more reduction is obtained in the hatched region. On the other hand, response quantities are futher amplified with increase in yielding capacity in the $T_p < T_n$ region.

4.3.4 Comparisons of Pulse Spectra for PEDS

Fig. 4.8 shows plots of J_D and J_A as the function of period ratio T_n / T_p for structures with linear viscous and yielding dampers for structural periods in the range of 0.1 to 5 seconds subject to the pulse-type excitation in Fig. 4.1. Figs. 4.8(a) and 4.9(b) show J_D and J_A spectra for structure with linear viscous dampers capable of adding 15% and 25% supplemental damping. It is observed from Figs. 8(a) and 8(b) that higher reduction in displacement is obtained for larger supplemental damping, and the largest reduction is obtained for $T_n/T_p \approx 1$. However, acceleration response only decreases with increase in supplemental damping when $T_n/T_p < 2$ and it is amplified for both levels of supplemental damping when $T_n/T_p > 2$.

Figs. 4.8(c) and (d) show J_D and J_A spectra for structures equipped with yielding dampers having yielding capacities $F_{yd} = 0.1F_0$, $F_{yd} = 0.5F_0$ and $F_{yd} = 0.8F_0$. It is observed from Fig. 4.9(c) that the J_D can be divided into three regions of T_n/T_p. In region I ($0 < T_n/T_p < 1.5$), J_D is less than 1, and it decreases with an increase in F_{yd}/F_0 from 0.1 to 0.5; which is caused by the increase in the area enclosed by the damper hysteretic loop as the increase of F_{yd}/F_0. Increasing the yielding capacity F_{yd}/F_0 from 0.5 to 0.8 doesn't yield further reduction in J_D. Significant displacement reduction (more than 50%) is obtained only for $T_n/T_p < 1$, since the effective natural

period of the structure decreases caused by the addition of damper stiffness. In region II ($1.5 < T_n/T_p < 3.5$), J_D increases with an increase in F_{yd}/F_0 and yielding dampers are detrimental to the structural safety. In Region III ($T_n/T_p > 3.5$), yielding dampers don't offer any noticeable advantage since J_D is close to 1. It is observed from Fig. 4.8(d) that the peak absolute acceleration is decreased only for $T_n/T_p < 1$, and it is amplified significantly for $T_n/T_p > 1$. Figs. 4.8(e) and (f) show J_D and J_A spectra for structures with yielding dampers having stiffness coefficients $k_d = k_s$, $k_d = 5k_s$ and $k_d = 10k_s$, and the same yielding strength $F_{yd} = 0.1F_0$. It is observed from Figs. 4.8(e) and 4.8(f) that J_D and J_A don't change significantly with the increase in damper stiffness. This happens because an increase in damper stiffness does not significantly increase the enclosed area of the damper hysteretic loop, if the yielding strength is fixed.

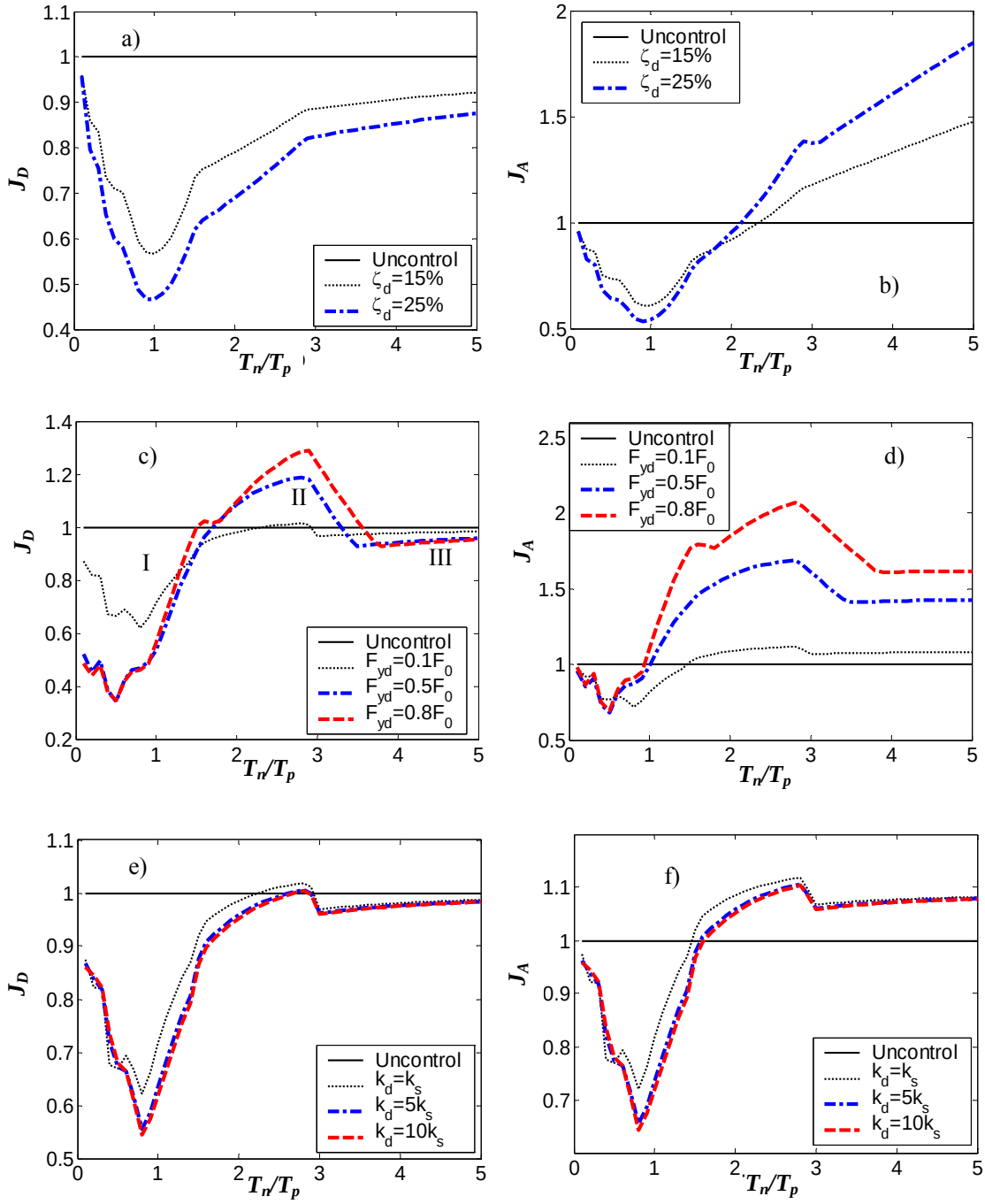

Figure 4.8: Influence of damper parameters on the spectra of normalized displacement and acceleration; (a) – (b) Linear viscous dampers; (c) – (d) Yielding dampers with different strength; (e) – (f): Yielding Dampers with different stiffness.

4.3.5 Correlations with Recorded Near-field Ground Motions

In order to show the correlations of pulse spectra J_D with those using recorded ground motions, Figs. 4.9 (a) and (b) show J_D spectra as a function of period ratio T_n/T_p for both viscous and yielding dampers. Linear (α = 1) and nonlinear (α = 0.5) viscous dampers are designed to add 25% supplemental damping. The parameters of yielding dampers are considered as $F_{yd} = 0.1F_0$ and $k_d = 10k_s$. In addition to the pulse-type excitation, 11 near recorded field ground motions in Table 4.1 have been used to obtain plots in Fig. 4.9.

Table 4.1. Recorded Near-field Ground Motions

Description of earthquakes	T_g (sec)	PGA (g)
FN Erzikan, 1992	2.1	0.43
FP Erzikan, 1992	1.9	0.46
FN Northridge Rinaldi 1994	1.0	0.89
FP Northridge Rinaldi 1994	2.7	0.39
FN Northridge Olive View 1994	2.6	0.73
FP Northridge Olive View 1994	0.5	0.60
FN Kobe Takatori 1995	1.3	0.79
FP Kobe Takatori 1995	1.2	0.42
TCU065 EW Chi-chi 1999	4.5	0.81
TCU065 NS Chi-chi 1999	6.4	0.60
Gebze Turkey 1999	4.2	0.27

Fig. 4.9(a) shows comparisons between J_D spectra for pulse and those obtained by average of 11 recorded ground motions for both the linear and nonlinear viscous dampers. It is observed from Fig. 4.9(a) that the J_D pulse spectra possess a trend similar to that of the average of recorded ground motions, and the plots match closely around $T_n/T_p \approx 1$. In both cases, viscous dampers perform best when $T_n/T_p \approx 1$. The reduction factor J_D

for the pulse excitation is larger than that for the recorded earthquakes when $T_n/T_p > 1.5$ or $T_n/T_p < 0.5$. This happens because the contribution of broadband frequency components in the recorded ground motions for structures with periods in these ranges is effectively damped out by PEDS. However, these broadband components are excluded in the analytical pulse model. It is also observed from Fig. 4.9(a) that nonlinear viscous damper perform better in acceleration-sensitive region ($T_n/T_p << 1$) than linear viscous dampers in terms of displacement mitigation, which is consistent with Fig. 4.6(d).

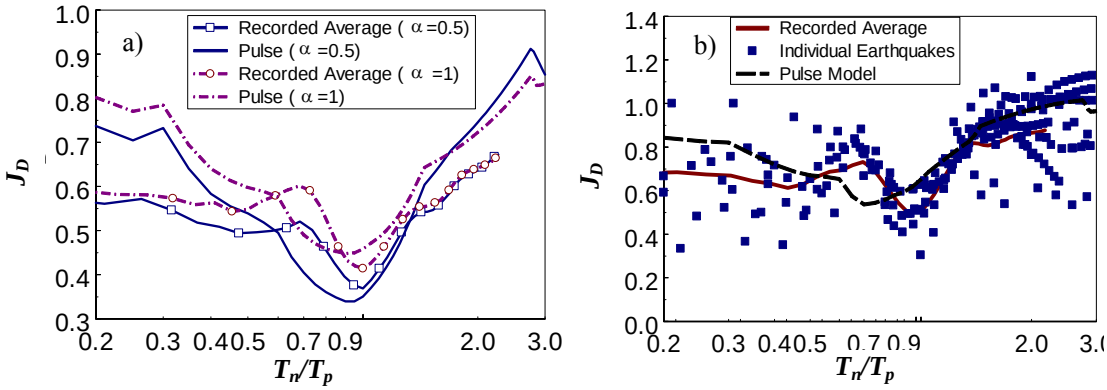

Fig. 4.9: Spectra of normalized displacement for pulse type and recorded ground motions with: (a) Linear viscous damper; (b) Yielding damper

Fig. 4.9(b) shows J_D spectra of the yielding damper for both pulse and recorded ground motions. For recorded ground motions, the minimum average J_D is approximately 0.5 around T_n/T_p = 0.85, although J_D for some individual ground motions could be much smaller. The minimum value of J_D equals to 0.6 during pulse excitation occurs around T_n/T_p = 0.7, instead of T_n/T_p = 0.85 for recoded ground motions. Significant scattering in J_D values for recorded ground motions are attributed

to the nonlinear behavior of yielding dampers and the presence of high frequency components in recorded ground motions. Nevertheless, pulse J_D spectra can be used as conservative estimate of performance of yielding dampers. Better correlations with recorded ground motions can be obtained by using simulated near-field ground motion records proposed by Tan et al (2005).

4.3.6 Damping Effects vs Earthquake Components

It is noted from Chapter 3 that a near-field earthquake record can be decomposed into dominant pulse, high-frequency and long-period components using the pulse model and the Empirical Mode Decomposition method. A combination of the high-frequency and the long-period component is also regarded as "broadband" frequency component as compared with the pulse component.

It is known that the effectiveness of PEDS is not only related to structural properties, but also related to the excitation properties. To study why the performance of PEDS with respect to excitation properties, it is necessary to investigate the performance of PEDS subjected to different excitation components.

Fig.4.10 shows the effectiveness of 25% linear viscous dampers in reducing displacement and acceleration responses subjected to the excitation of full accelerations and their components. The results plotted in Fig. 4.10 are the average of the eight near-field ground motion records described in Chapter 3. Details of the eight records can be found in Table 3.1 of Chapter 3.

It is observed from Fig. 4.10 that the linear viscous dampers perform the best in the range of $0.7 < T_n/T_p < 1.3$ for both total acceleration and pulse component results. In this range, response reductions obtained for the total accelerations and pulse components are

almost the same. Performance indices J_D and J_A using pulse components are larger than those using the total accelerations and other components when T_n/T_p is out of this range since the pulse components only have a narrow-band frequency content compared to others. The dependency of displacement and acceleration reduction on frequency contents is also obvious in other regions: for T_n/T_p <0.7, viscous dampers are much more effective in reducing responses caused by high-frequency components than those caused by the pulse and long-period components; When T_n/T_p >1.3, they are more effective in reducing responses caused by long-period excitations.

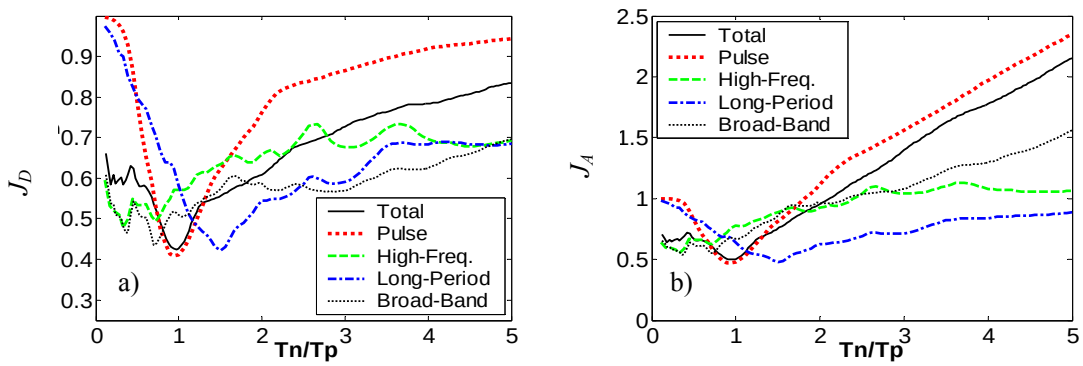

Figure 4.10 Average performance index spectra of 25% supplemental damping on different frequency components: a) Displacement performance index; b) Acceleration performance index.

It is also observed from Fig. 4.10 that although linear viscous dampers do not perform effectively for the pulse and long-period excitation components when T_n/T_p is less than 0.7, the performance in terms of the total acceleration is still significant due to the existence of high frequency contents. For relatively short period structures, periods of the pulse and long-period components are much longer than the structural periods and these two excitations can be regarded as "static force". Hence, the effectiveness of

damping is limited for these two types of excitations. For T_n/T_p >1.3, linear viscous dampers seem to perform best during long-period and broadband excitations and they perform the worst during pulse excitations. However, the performance degrades for all types of excitations as T_n/T_p continually increases, which indicates a degradation of damping efficiency for flexible structures.

Hence, linear viscous dampers perform effectively for short period structures during high frequency excitations, for long-period structures during long-period excitations and for intermediate structures during pulse type excitations. When the excitation contains distinct pulse component, the effectiveness of viscous dampers is only significant when T_n is in the vicinity of T_p.

4.3.7 Energy Response of Passive Damper Systems during Pulse-type Excitation

The dynamic behavior of a structure depends on relative balance of input, dissipated, kinetic and strain energies in the structure during an earthquake. To investigate this phenomenon, performance of PEDS is evaluated through energy balance approach in the following.

i) Instantaneous energy balance

Fig. 4.11 shows time-history plots of instantaneous input, dissipated, kinetic and strain energies for three SDOF structures (T_n=0.2 sec, T_n=1 sec and T_n=5 sec) with 25% supplemental damping subjected to the pulse excitation in Fig. 4.1. The nonlinearity exponent of viscous dampers are considered as α = 0.3, 0.5 and 1 herein. It is observed from Fig. 4.11 that the input energy (E_I) increases significantly with an increase of damper nonlinearity (i.e., decrease of α) for the T_n = 0.2 sec structure, and it decreases

for the T_n = 1.0 sec and the T_n = 5.0 sec structures. Hence, linear viscous dampers (i.e., α = 1) will increase the input energy for intermediate and long period structures. Instantaneous damper dissipated energy (E_d) follows the same trend as the input energy for three levels of damper nonlinearity. Strain (E_s) and kinetic (E_k) energies are not noticeably affected by the damper nonlinearity in all three cases.

For T_n = 1.0 sec structure, it is observed from Fig. 4.11(b) that the instantaneous damper dissipated energy builds up in phase with input energy at all time instants, whereas both instantaneous strain and kinetic energies are significantly smaller than the input energy. Hence, both nonlinear and linear viscous dampers are effective in dissipating the input energy at every time instant for structures with $T_n/T_p \approx 1$. On the other hand, while the instantaneous input energy fluctuates significantly for T_n = 0.2 sec and T_n = 5.0 sec structures, the instantaneous damper dissipated energy builds up monotonically for these structures. Hence, the dampers are not able to dissipate input energy instantaneously during first few seconds of the pulse motion when input energy fluctuates significantly. For T_n = 0.2 sec structure, the instantaneous input energy not dissipated by dampers is converted mostly into strain energy and for T_n = 5.0 sec structure, this part of energy is converted mostly into kinetic energy. In both cases, the effectiveness of viscous dampers degrades and the residual (not dissipated) instantaneous input energy may cause the structures undergo excessive deformation.

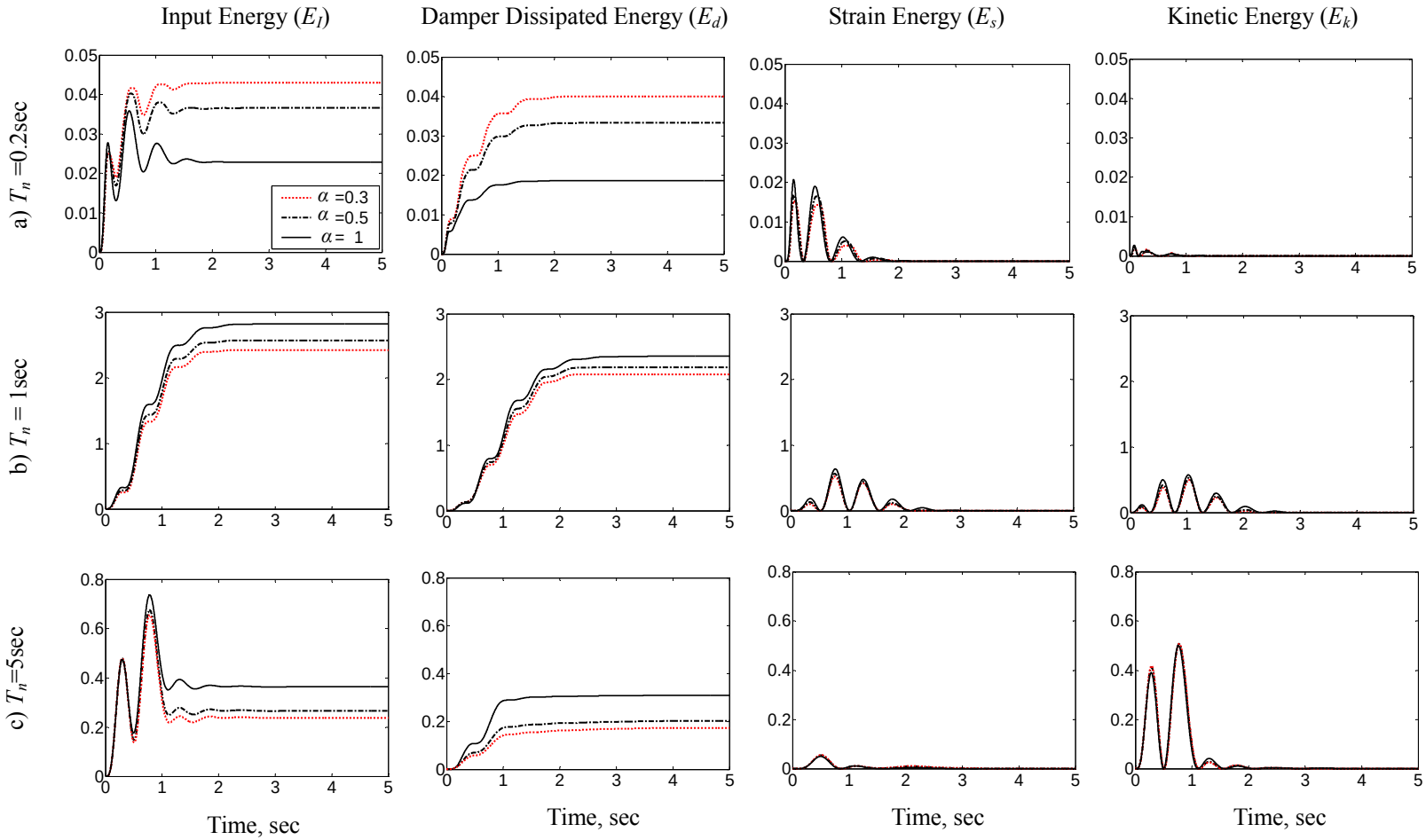

Figure 4.11: Time history plots of input energy, damper dissipated energy, strain energy and kinetic energy of three SDOF structures subject to the pulse excitation with T_p =1 sec: a) T_n = 0.2sec; b) T_n =1sec; c) T_n =5sec. Energy units in per unit mass.

ii) Maximum energy balance

Fig. 4.12 shows plots of maximum energies and ratios of maximum energies as a function of T_n/T_p for viscous (α =1 and ζ_d = 25%) and yielding (U_{yd}= 0.08U_0, k_d = 10k_s) dampers subjected to the pulse-type excitations. In Fig. 4.12, "*EImax*", "*Edmax*", "*Esmax*", and "*Ekmax*" represent maxima of input energy, damper disipated energy, strain energy, and kinetic energy, respectively.

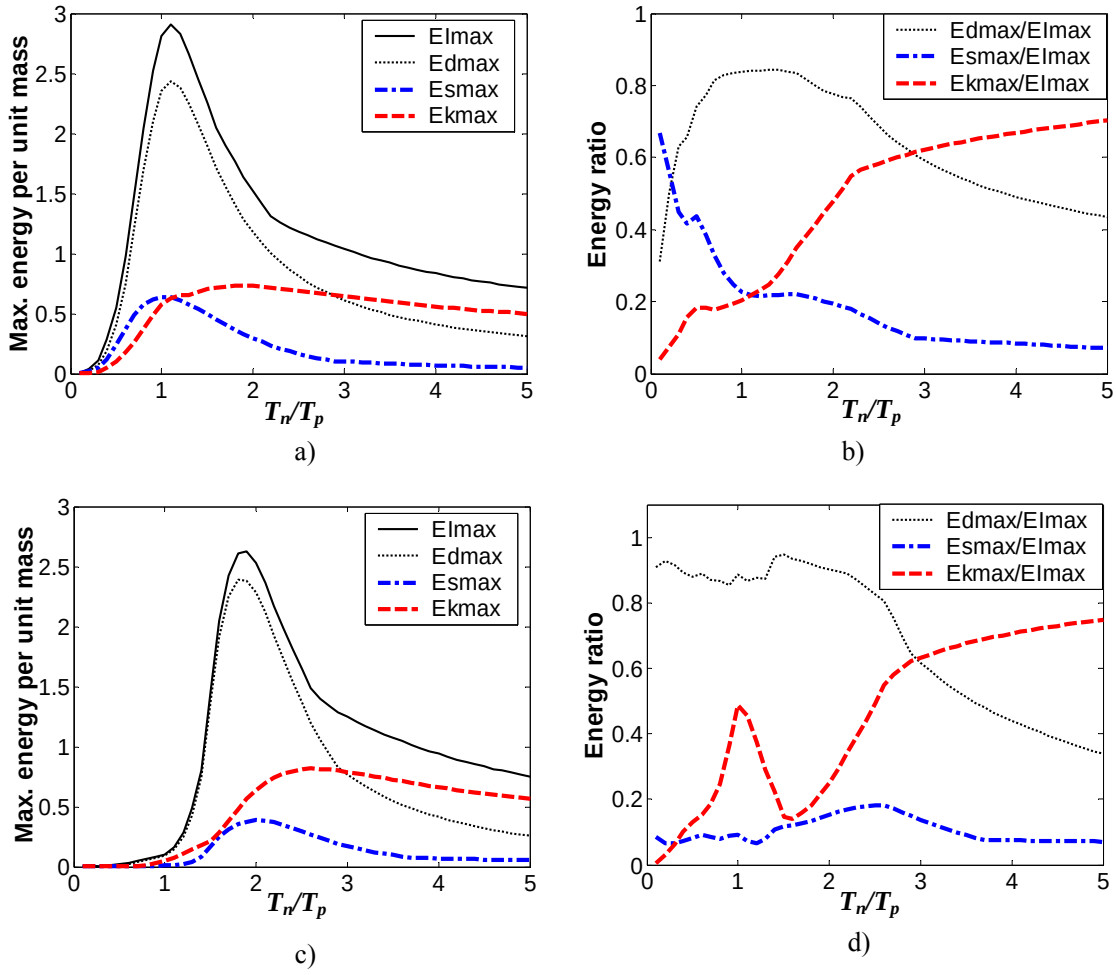

Fig. 4.12: Maximum energy information for structures with PEDS; (a) – (b): Linear viscous damper; (c) – (d): Yielding damper.

It is observed from Fig. 4.12(a) that *Edmax* and *EImax* evolve in a similar way with the increase of T_n/T_p . However, difference between *Edmax* and *EImax* increases as T_n/T_p increase beyond 2. This happens because of the fluctuation in instantaneous input energy and the monotonic buildup style of instantaneous damper dissipated energy, as illustrated in Fig. 4.12(c) for T_n = 5 sec structure. Maximum strain energy, *Esmax,* increases for 0< T_n/T_p < 1, and it decreases gradually to zero for T_n/T_p >1. On the other hand, maximum kinetic energy, *Ekmax*, increases for T_n/T_p < 1 and stays almost constant for T_n/T_p > 1. In fact, *Ekmax* is greater than *Edmax* when T_n/T_p > 2.9; which implies that a significant part of input energy is converted into kinetic energy and the damper is not able to dissipate the input energy synchronously herein. Fig. 4.12(b) shows plots of ratios *Edmax/EImax*, *Ekmax/EImax* and *Ekmax/EImax* as the function of T_n/T_p . It is obsertved that *Edmax* is more than 60% of the *EImax* in the range of 0.3 < T_n/T_p < 2.9. Hence, dampers are most effective in this range. For T_n/T_p > 2.9, more energy is converted into kinetic energy than instantaneously dissipated by dampers. Hence, plots in Figs. 4.12 (a) and 4.12(b) show that linear viscous dampers are less effective for short and long period structures due to transfer of a significant portion of input energy into strain and kinetic energy, respectively, in these structures. Although total input energy will ultimately be dissipated by supplemental damping and the inherent damping in each case, conversion of the input energy that is not dissipated by dampers to strain energy (for short period structures) and kinetic energy (for long-period structures) may still cause damages in these structures, if displacement demand exceeds the design limit.

Figs. 4.12(c) and 4.12(d) show maximum energy and energy ratio plots for yielding dampers. Plots in Fig. 4.12(c) are similar to those for viscous dampers in Fig. 12(a), except that the peak value of *EImax* occurs around $T_n/T_p \approx 1.8$; which is caused by the addition of stiffness by yielding dampers. It is further observed from Fig. 4.12(d) that yielding dampers are effective in dissipating 90% of input energy for structures in the range of T_n/T_p < 2.2 and between 60% to 90% of input energy for structures in the range of 2.2 < T_n/T_p < 2.9. Effects of yielding dampers are similar to those of viscous dampers for structures in the range of T_n/T_p > 2.9.

iii) Influence of damper parameters on energy balance

In order to further investigate the performance of viscous and yielding dampers, changes in maximum input energy and damper dissipated energies are compared for different levels of supplemental damping and yielding force. Figs. 4.13(a) and 4.13(b) show plots of maximum input energy and maximum energy dissipated by dampers as a function of T_n/T_p for linear viscous dampers adding 15% and 25% supplemental damping ratios. It is observed from Figs. 4.13(a) and 4.13(b) that the maximum input energy decreases significantly and the peak damper dissipated energy increases slightly around $T_n/T_p \approx 1$, as the increase of supplemental damping ratio. For T_n/T_p < 1, while the maximum input energy decreases with increase in supplemental damping, maximum damper dissipated energy does not change noticeably. For structures with T_n/T_p >1.7, the input energy is actually increased due to an increase in supplemental damping. In fact, increase in input energy is followed by a slightly larger increase in damper dissipated energy. Hence, displacement is still reduced herein. However, the amount of reduction

caused by the increase in damping ratio is not as significant as that in the vicinity of T_n/T_p =1, as shown by the J_D spectra in Fig. 4.8(a).

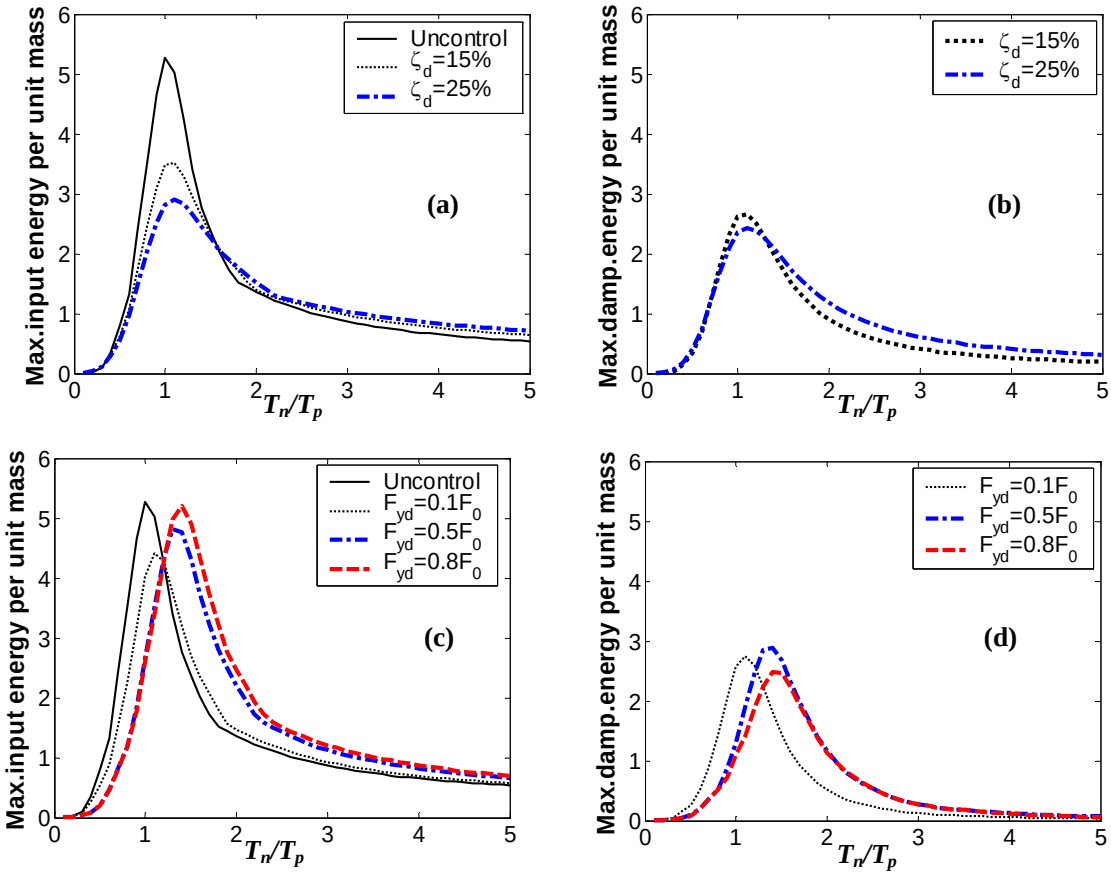

Fig. 4.13: Influence of damper parameters on the spectra of maximum input energy and maximum damper dissipated energy; (a) – (b): Linear viscous dampers; (c) – (d): Yielding dampers.

Figs. 4.13(c) and 4.13(d) show plots of maximum input energy and maximum damper dissipated energy for yielding dampers with stiffness $k_d = k_s$ and yielding strengths F_{yd}=0.1F_0, F_{yd}=0.5F_0 and F_{yd}=0.8F_0. It is observed from Fig. 4.13(c) that the peak value of the maximum input energy shifts towards $T_n/T_p > 1.0$ with an increase in F_{yd}/F_0, due to the increase in effective supplemental damper stiffness. Both maximum

input energy and maximum damper dissipated energy decrease for T_n/T_p < 1.2 with the increase in F_{yd}/F_0; and the decrease in the maximum input energy is more than the decrease in the damper dissipated energy. Hence, yielding dampers effectively reduce the displacement and acceleration responses for structures in this range as observed from Figs. 4.8(c) and 4.8(d). On the other hand, both the maximum input energy and the maximum damper dissipated energy increase when T_n/T_p > 1.2. Moreover, the increase in the input energy becomes larger than the increase in the damper dissipated energy as T_n/T_p increases beyond > 1.2. Hence, displacement reductions by yielding dampers gradually decrease for structures with T_n/T_p > 1.2 and the displacement of the structure with yielding dampers will eventually be amplified when T_n/T_p increases beyond 1.5, as observed in Fig. 4.8(c).

4.4 CONCLUSIONS

In this chapter, the performance of passive energy dissipation systems during pulse-type near-field ground motions is investigated through response spectrum and energy balance analysis. An analytical ground velocity pulse model is used to represent dominant characteristics of near-field ground motion pulses. In addition, 11 near-field ground motion records are used to verify the conclusions based on the pulse model.

For viscous fluid and yielding dampers, systematic investigations are performed to develop displacement and acceleration response spectra as functions of pulse period (T_p), structural natural period (T_n) or the ratio of T_n/T_p. The response spectra can be used to design most effective PEDS for a particular structure considering site conditions.

It is concluded that the performance of viscous dampers during pulse-type and sinusoidal excitations is significantly different. Near resonance, response quantities as well as response reductions during sinusoidal excitations are much larger than those during pulse-type excitations. For a SDOF structure with 2.5s period and 5% inherent damping, displacement reductions by linear viscous dampers with 25% supplemental damping are 82% and 52% during sinusoidal and pulse-type ground motions, respectively, when $T_n > T_p$. However, linear viscous damper achieve more displacement reduction during pulse-type ground motion when $T_p > T_n$.

The damper nonlinearity does not significantly influence the displacement response. Nonlinear viscous dampers with nonlinearity factor α=0.5 can give 5 to 10% additional reduction in peak displacements over those by linear viscous dampers when $T_p \geq \frac{4}{5} T_n$, and additional 40% reduction in peak absolute acceleration when $T_n > 2.5T_p$. Yielding dampers are more effective than viscous dampers in reducing response of short period structures. They are effective in reducing displacement, acceleration and input energy only when $T_p \geq T_n$, and may amplify these quantities when $T_p < T_n$. Hence, yielding dampers may actually be detrimental to structural safety when $T_p < T_n$ due to the decrease of equivalent system period

Performance of PEDS depends on their absorbability of instantaneous input energy. If a PEDS cannot dissipate the input energy instantaneously, even though it may have an excellent ability to dissipate the total input energy, the structure may still undergo damage due to the instantaneous accumulation of input energy during the course of an earthquake. In other word, PEDS are most effective when the variation of instantaneous

damper dissipated energy is in phase with instantaneous input energy at all time instants. When the instantaneous damper dissipated energy doesn't follow the variation in instantaneous input energy, PEDS become less effective.

For a given structure, performance of different PEDS depends significantly on the period of excitation. For example, a yielding damper can actually amplify response quantities of a structure when $T_p < T_n$. Dominant excitation periods based on site conditions must be carefully considered in designing PEDS to achieve best performance. It is also found that the performance of viscous damping during a recorded earthquake depends on the frequency content of this earthquake. When the excitation contains distinct pulse component, the effectiveness of damping is only appreciable when T_n is in the vicinity of T_p and significantly degrades when T_n is out of T_p. Due to the distinct impulse characteristics of near-field earthquakes compared with the broadband frequency characteristics of far-field earthquakes, the same amount of damping would perform better in controlling structures subject to far-field earthquakes than near-field earthquakes especially when the dominant period is much different from the structural period.

CHAPTER 5

BEHAVIOR OF NONLINEAR STRUCTURES SUBJECTED TO NEAR-FIELD AND PULSE-TYPE EXCITATIONS

5.1. INTRODUCTION

Parameters required for characterizing the severity and the damage potential of earthquake excitations include both the ground motion properties and structural properties [Veletsos and Newmark (1960), Anderson and Bertero (1987), Bertero et al (1991), Chopra and Chintanapakdee (2001) and Singh (1995)]. Ground motion properties can be characterized by peak ground motion parameters (e.g., PGA, PGV and PGD), frequency contents, duration, velocity, displacement, incremental velocity, incremental displacement, and the ratio of PGD/PGV and PGV/PGA. The structure and response parameters include the structural frequency and damping characteristics, which determine both strength-related (e.g., relative and pseudo response spectra) and energy-related response spectra (e.g., input and hysteretic energy spectra).

To quantitatively define the damage potential of a structure, a damage index can be established to account for the maximum and cumulative responses of the structure, as a function of desired behaviors for different design ground motions. For ductile RC structure without supplemental devices, Park et al (1987) has developed a damage index to investigate the level of nonlinear structural deformation. According to this model, the damage consists of linear combination of the normalized values of maximum

displacement and hysteretic energy via the use of combination parameters. The model has the form of

$$DI = \frac{\delta}{\delta_u} + \beta \frac{E_{H\mu}}{F_y \delta_u}$$

where δ is the maximum lateral displacement demand during the design ground motion, δ_u is the ultimate displacement capacity under monotonically increasing lateral deformation, $E_{H\mu}$ is the hysteretic energy dissipation demand during the design ground motion, F_y is the yield strength and β is a parameter determined experimentally. According to this definition, a value of *DI* less or equal than 0.4 can be interpreted as repairable damage; from 0.4 to less than 1.0, as nonrepairable damage; and larger than 1.0 as failure; while 0.15 corresponds to the median of the values of β obtained experimentally (Gilmore 1997).

Spectrum analysis has been used widely for investigating the seismic response characteristics of various structures. The earliest work on nonlinear structural response spectra can be dated back to 1960. Veletsos and Newmark (1960, 1965) have developed μ-related strength reduction factors for elasto-plastic structures. This relationship was later on modified by Newmark and Hall (1982) to better fit the results of far-field earthquakes and is widely employed in current design practice. Recently, many researches have proposed other types of R-μ relationships, e.g., site-dependent R-μ relationship with the consideration of long period pulses [Miranda (1993)], R-μ relationship for bilinear and stiffness degrading structures [Vidic et al (1994)], R-μ relationship for RC structures [Priestley (1995)], etc. Cuesta and Aschheim (2001b) have investigated isoductile strengths and strength reduction factors of elasto-plactic SDOF systems subjected to simple waveforms. They have also investigated inelastic response

spectra by comparing conventional and pulse *R*-factors [Cuesta and Aschheim (2001a, 2004)]. More recently, Chopra and Chintanapakdee (2001) have compared the response of structures subject to near- and far-field earthquakes and concluded that the Newmark-Hall (1982) relationship is valid for near-field earthquakes, provided that the characteristic period values, T_a, T_b, and T_c are modified for these ground motions. Mavroeidis et al (2004) have concluded that the Newmark-Hall relationship is valid for near-field earthquakes, provided that the expression is presented with normalized time scale, T_n/T_p, which is determined by investigating the acceleration, velocity and displacement-sensitive regions in response spectra. MacRae et al (2001) have investigated the rupture directivity effects on inelastic responses of SDOF structures using an ensemble of 154 records.

In addition to conventional earthquake-resistant design, recent studies have focused on the use of energy concepts as an alternative way for identification of both the seismic demands imposed by earthquakes and the structural capacities to meet such demands [Uang and Bertero (1988a, 1988b, 1990), Naeim and Anderson (1993), H. Akiyama 1998]. Naeim and Anderson (1993) have developed input energy spectra and hysteretic energy spectra for a large database of recorded ground motions. Fajfar and Vidic (1994) have investigated the relationship of the hysteretic to input energy ratio with ductility factor, structural period and hysteretic model. Climent et al (2002) have proposed input energy spectra for seismic design of structures located in low-to-moderate seismicity regions. Wong and Yang (2001, 2002) have used state-space method to evaluate the energy transformation and distribution of multi-degree-of-freedom systems. They found that the damping energy of the upper floors is larger than that of the lower floors, and the

plastic energy of lower floors is larger than those of the upper floors. Decanini and Mollaioli (2004) have proposed a methodology for the assessment of the seismic energy demands imposed on structures by investigating nonlinear design input energy spectra and by comparing elastic to nonlinear input energy spectral ratio, and the spectra of the hysteretic to input energy ratio. Yamaguchi and El-Abd (2003) have defined the performance of hysteretic dampers as the ratio of hysteretic energy to the input energy and have demonstrated through an example of 10-story shear-type building that the efficiency of hysteretic dampers is affected by equivalent velocity ($Ve = \sqrt{\frac{2E_{Im\,ax}}{m}}$), energy-based effective excitation duration and dominant response period (obtained by normalized PSD spectrum). Pavlou and Constantinou (2004) have investigated the effect of near-field and soft-soil ground motions on elastic and inelastic structures with viscous damping systems and compared the results with those in specifications recommended by NEHRP (2000).

It is noted that both the elastic and nonlinear strength-related response spectra are mainly concerned with peak responses and they do not account for the duration of input ground motions [Singh (1995)]. However, energy-related spectra can better address this issue by considering the relationship between the energy dissipation demands and the duration of an excitation. For example, pulse-type near-field ground motions show distinct energy response characteristics compared with far-field earthquakes. Near-field impulsive ground motions usually result in a sudden burst (impulsive release) of energy into the structures, which must be dissipated immediately. Otherwise, the rapid energy accumulation will result in a single or finite number of unidirectional large yield excursions [Xu et al (2006)]. On the other hand, the far-field earthquakes have longer

duration and they require steadier energy dissipation over a longer period of time with numerous yield reversals.

Hence, it is necessary to investigate energy response characteristics of nonlinear structures subjected to pulse-type and near-field excitations for a better understanding of the nonlinear structural and damping behavior and to facilitate the performance-based design of structures. In this chapter, the nonlinear structural behavior and the performance of passive energy dissipation systems subjected to pulse-type and recorded near-field ground motions are investigated. The strength-related property, i.e., the R-μ relationship and the influence of structural parameters are analyzed in the beginning. Then, the energy-related property of nonlinear structures, e.g., the input energy spectrum (E_I), yielding (hysteretic) energy spectrum (E_h), damper-dissipated energy spectrum (E_d) and the spectra of the ratio of hysteretic to input energy ($E_{h/I}$) for pulse-type and near-field excitations are investigated. For structures equipped with supplemental energy dissipation devices, the ratio of damper dissipated energy to input energy ($E_{d/I}$) are also investigated. The E_I and $E_{h/I}$ spectra facilitate the evaluation of seismic demands in terms of maximum input energy. The E_d and $E_{d/I}$ spectra provides effective criteria for evaluating the performance of passive energy dissipation systems. The significance of the spectra lies in the fact that once the nonlinear design input energy spectra are decided for a particular structure, energy dissipated by means of nonlinear structural deformations and supplemental dampers follows directly from the knowledge of $E_{h/I}$ and $E_{d/I}$ spectra.

5.2 BACKGROUND INFORMATION

In this investigation, performance of PEDS in protecting nonlinear structures is investigated by subjecting SDOF structures with 5% damping ratio to pulse-type excitations and 50 recorded near-field ground motions. The pulse-type excitations are generated by the pulse model described in Chapter 3 with the parameters n = 1, a = 2.51/T_p and peak ground acceleration of 0.6g for different pulse period, T_p, as described in Chapter 3.

Fifty near-field earthquake records downloaded from PEER Website (http://peer.berkeley.edu/) are used in this investigation. They are either fault-normal or fault-parallel records and have magnitude (ML) > 5.5, distance to fault < 10kM, PGA > 0.25g and PGV > 25cm/s. Soil type of these records varies from types A, B and C per USGC soil classification standards. Detailed information of these 50 recorded ground motions is presented in the appendix.

Viscous dampers are designed by considering equivalent damping ratios ζ_d = 15%, 25% and 45%, corresponding to different damping levels. Influence of damper nonlinearity on nonlinear structural responses is also investigated by considering α = 0.5 and 1.0, using both pulse-type excitations and recorded ground motions. Parameters of yielding dampers are taken as α_d = 0, β_d = 0.5, γ_d = 0.5, n_d = 3, and A_d = 1.0 in Eq (4.7) of Chapter 4. The yielding stiffness (k_d) and yielding strength (F_{yd}, or equivalently, yielding displacement, U_{yd}) of yielding dampers are expressed in terms of the corresponding structural parameters and are varied to investigate their effects on damper performance.

The nonlinear SDOF structures investigated in this study are represented by Bouc-Wen model with β_s = 0.5, γ_s = 0.5, n_s = 3 and A_s = 1.0. The parameter α_s, which controls

the post-yielding capacity of nonlinear structures, is taken as 0~0.5 times of the elastic structural stiffness (k_s). Both the yielding dampers and the structures are assumed to be inelastic without pinching and degradation behaviors. Inelastic behavior of the structures is investigated by considering ductility ratios μ=2, 4, 6 and 8. Fig. 5.1 shows the definition and relationship of strength reduction factor (R), ductility factor (μ) and other quantities, using bilinear structural behavior.

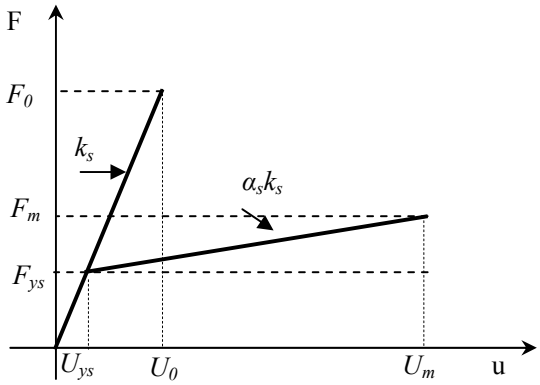

Figure 5.1 Nonlinear and linear structural behavior

In Fig. 5.1, F_{ys}, F_m and F_0 are yielding strength, maximum nonlinear strength and maximum elastic strength of the structure, respectively. Parameters U_{ys}, U_m and U_0 are yielding displacement, maximum nonlinear displacement and maximum elastic displacement of the structure, respectively. The elastic stiffness is k_s and the post-yielding stiffness is $\alpha_s k_s$, in which α_s is the ratio of post-yielding stiffness over the elastic stiffness. By definition, the ductility factor (μ) and strength reduction factor (R) are expressed as

$$\mu = \frac{U_m}{U_{ys}} \tag{5.1}$$

$$R = \frac{F_0}{F_{ys}} \tag{5.2}$$

Hence, μ and R is related as,

$$R = \frac{F_0}{F_{ys}} = \frac{U_0}{U_{ys}} = \mu \frac{U_0}{U_m} \tag{5.3}$$

Fig. 5.2 shows the behavior of a SDOF nonlinear structure equipped with a yielding damper. For the controlled system, the total dissipated energy in Fig. 5.2c consists of both the energy dissipated by the yielding damper (E_d) and the hysteretic energy of the structure (E_h). Hence, both the effective stiffness and the energy-dissipation capacity of the controlled structure-damper system are increased. As a result, both the damage and the energy input to the structure are expected to be decreased.

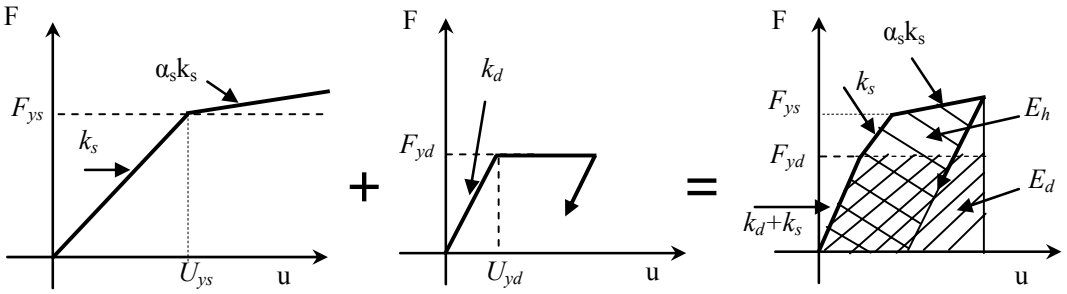

a) Nonlinear structure b) Yielding damper c) Structure + damper

Figure 5.2: Force-deformation behavior of nonlinear structure with and without yielding damper.

In addition to strength reduction factor (R) and ductility factor (μ), the performance indices used to evaluate the nonlinear structural behavior also include the spectrum displacement (SD), spectrum acceleration (SA), maximum input energy (E_I), maximum hysteretic energy (E_h) and normalized response quantities, e.g., the linear displacement, acceleration and input energy spectra normalized by the corresponding nonlinear spectra: SD(μ>1)/SD(μ=1), SA(μ>1)/SA(μ=1) and EI(μ>1)/EI(μ=1). The performance indices

used to evaluate the performance of passive energy dissipation systems are the damper dissipated energy (E_d) and the corresponding controlled structural responses. In addition, the following two performance indices are also defined to evaluate energy-related characteristics of the structures,

$$E_{h/I} = \frac{E_h}{E_I} \tag{5.4}$$

$$E_{d/I} = \frac{E_d}{E_I} \tag{5.5}$$

It is noted that in order to limit structural damage, the normalized structural yielding energy ($E_{h/I}$) should be as small as possible and the normalized damper-dissipated energy ($E_{d/I}$) should be as large as possible.

5.3 BEHAVIOR OF NONLINEAR STRUCTURES SUBJECTED TO PULSE-TYPE EXCITATIONS

5.3.1 Displacement and Acceleration Responses

The behavior of nonlinear structures without supplemental passive energy dissipation systems subjected to the pulse-type excitations is investigated in this section. Fig. 5.3 shows the contour spectra of displacement and acceleration as a function of T_n and T_p, where T_n being the elastic structural period and T_p being the excitation (pulse) period, respectively. Both T_n and T_p vary from 0.1 to 5 sec. The constant ductility ratio is kept as 4 and the post-yielding stiffness ratio α_s is chosen to be 0, i.e., the structure is elastic-perfectly-plastic. As a comparison, contour spectra of displacement and acceleration for linear structures and the normalized nonlinear responses are also presented in Fig. 5.4 and 5.5, respectively.

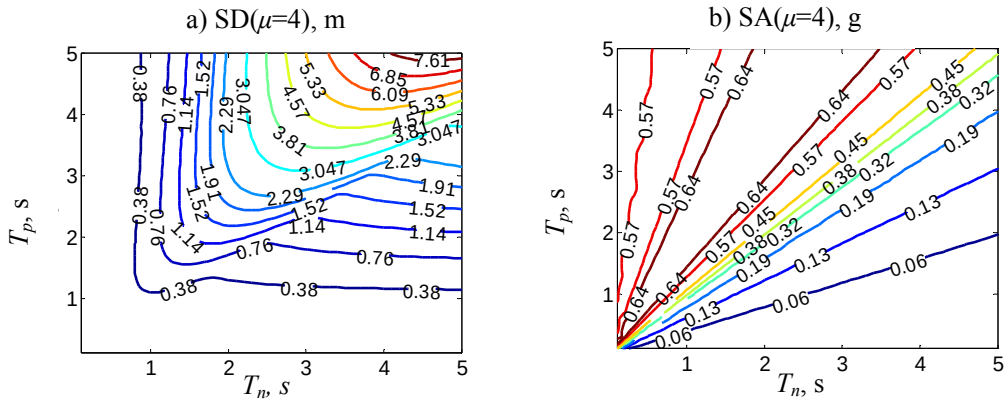

Figure 5.3: Contour response spectra of (a) Displacement and (b) Acceleration as a function of T_n and T_p for nonlinear structures with μ=4 subject to the pulse type excitations

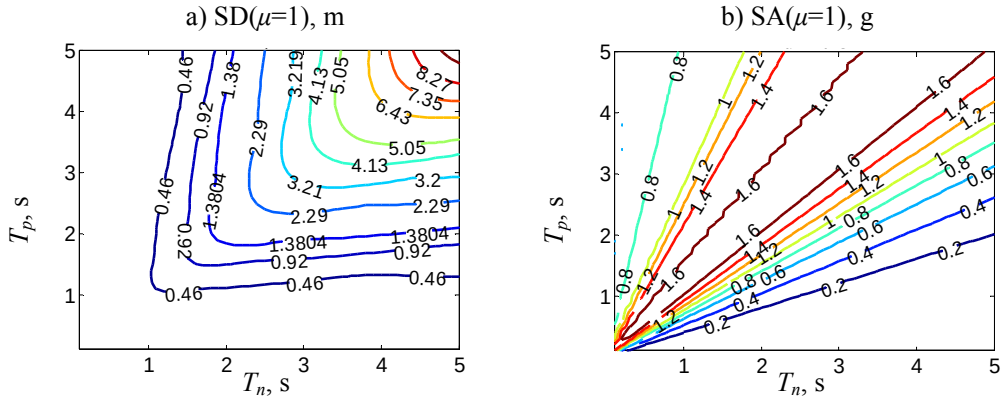

Figure 5.4 Contour response spectra of (a): Displacement and (b): Acceleration as a function of T_n and T_p for linear structures subject to the pulse type excitations

It is observed from Fig. 5.3a that nonlinear spectral displacements increase with an increase in T_n and T_p. Hence, the isolines become denser with increase in T_n and T_p as a result of increasing displacement gradient. The vertices of isolines also shift into the region of $T_p > T_n$ because of increase in effective structural period for nonlinear structures. However, the linear displacement spectrum is almost symmetric with respect to the axis of $T_n = T_p$ and the vertices of isolines also occur herein, as shown in Fig. 5.4a. Hence, T_n

and T_p play a similar role in terms of linear displacement response. However, this is not the case for nonlinear structures.

The nonlinear acceleration contour spectra plotted in Fig.5.3b show that acceleration response decreases with an increase in T_n/T_p. The spectral acceleration is in the range of 0.57~0.64 when T_n/T_p < 4/5 and it gradually decreases to 0 with increase in T_n/T_p. Compared with the linear acceleration spectra in Fig. 5.4b, it is observed that the nonlinear spectral accelerations are much smaller in the entire region. It is also observed that acceleration contour spectra for both linear and nonlinear structures are the function of the ratio T_n/T_p.

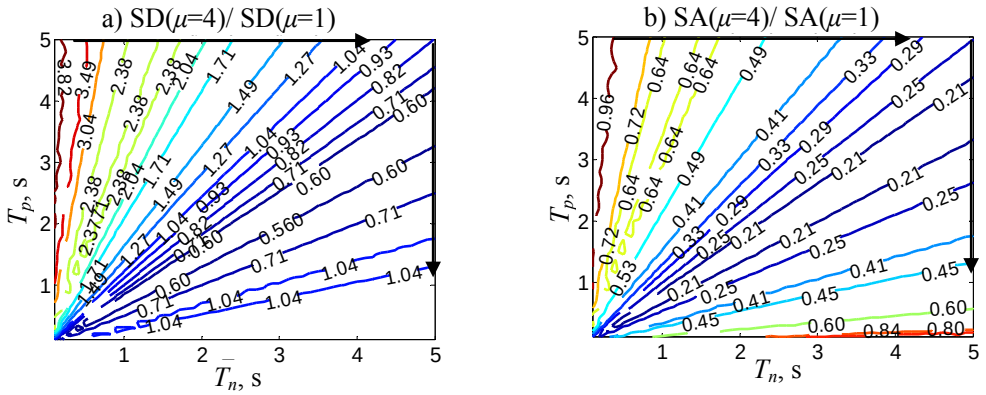

Figure 5.5 Normalized nonlinear responses: a) Displacement spectrum and b) Acceleration spectrum.

It is observed from Figs. 5.5a and 5.5b that the normalized nonlinear displacement and acceleration spectra are constant along T_n/T_p lines. The normalized displacement spectrum in Fig. 5.5a can be divided into three regions in terms of T_n/T_p: When T_n/T_p <4/5, the value is greater than 1 and it decreases with an increase in T_n/T_p (as shown by the horizontal arrow on the top border of the plot); when T_n/T_p >5/2, the value is approximately equal to 1; and when 4/5< T_n/T_p <5/2, it is less than 1 which indicates a

displacement decrease in nonlinear structures compared with that of the linear structures herein. It is noted from Eq. (5.4) that the displacement ratio plotted in Fig. 5.5a is essentially the ratio of ductility factor over strength reduction factor, i.e, μ/R. Hence, the contour value is close to μ (equals to 4 for this case) for the extreme case of $T_n/T_p \rightarrow 0$ since R approaches 1 in this range. For the case of $T_n/T_p > 5/2$, the contour value is close to 1 since μ is approximately equals to R for flexible structures. It is observed from Fig. 5.5b that the nonlinear acceleration is reduced by as much as 79%, depending on the value of T_n/T_p as compared to that of the linear structures. Generally, the reduction around the region of T_n or $T_p \approx 0$ is less compared with the region of $T_n \approx T_p$.

Fig. 5.6 shows the displacement and acceleration spectra subject to a pulse-type excitation with T_p =1s. The ductility factor of nonlinear structures in Fig. 5.6 varies from 2 to 8 corresponding to different yielding levels. The other structural and pulse parameters are the same as before.

It is observed from Fig. 5.6a that the displacement spectra can be divided into three regions with respect to T_n: when T_n <0.8 sec, displacement increases with an increase in ductility. For a T_n within 1.0~3.0 sec, displacement decreases significantly with the increase of ductility. The peak displacement also shifts towards left due to the increase of effective period in this region. For T_n > 3 sec, all curves start converging to peak pulse displacement. Spectrum acceleration in Fig. 5.6b decreases significantly with increase in ductility, especially when T_n <2.0 sec. This is the effect of significant strength reduction for structures undergoing nonlinear deformation. It is also observed that the sensitivity of acceleration response to structural nonlinearity decreases with increase in ductility since

the acceleration decrement for the case of linear and μ=2 is much larger than that for μ=2 and μ=4.

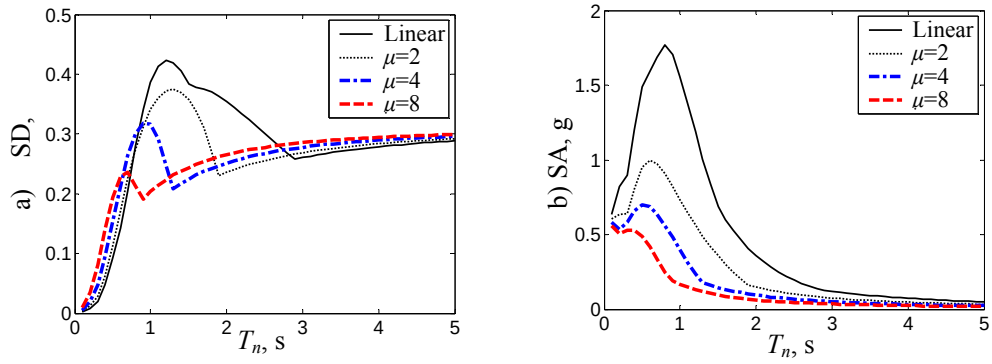

Figure 5.6 Displacement and acceleration spectra of nonlinear structures subject to the pulse-type excitation with T_p =1s: a) Displacement spectrum; b) Acceleration spectrum.

5.3.2 *R*-μ Relationship for Pulse-type Excitations

It is observed from Fig. 5.5 that the normalized nonlinear displacement SD(μ=4)/SD(μ=1) is a function of T_n/T_p and is not solely dependent on T_n or T_p. Hence, strength reduction factor R is also the function of T_n/T_p, since SD(μ=4)/SD(μ=1) equals to μ/R. Fig. 5.7 shows the plots of R versus T_n/T_p for elastic-perfectly-plastic structures with ductility factors μ=2, 4, 6 and 8. It is observed from Fig. 5.7 that (i) R = 1 when T_n/T_p < 0.1, regardless of μ; (ii) $R = \mu$ when T_n/T_p >3.0, and (iii) R increases from 1 to its peak value and then decreases towards μ with increase in T_n/T_p for 0.1<T_n/T_p <3.0. The peak value of R in Fig. 5.7 for each case is about 1.5 to 2 times μ, occurring at a T_n/T_p between 1 and 2.

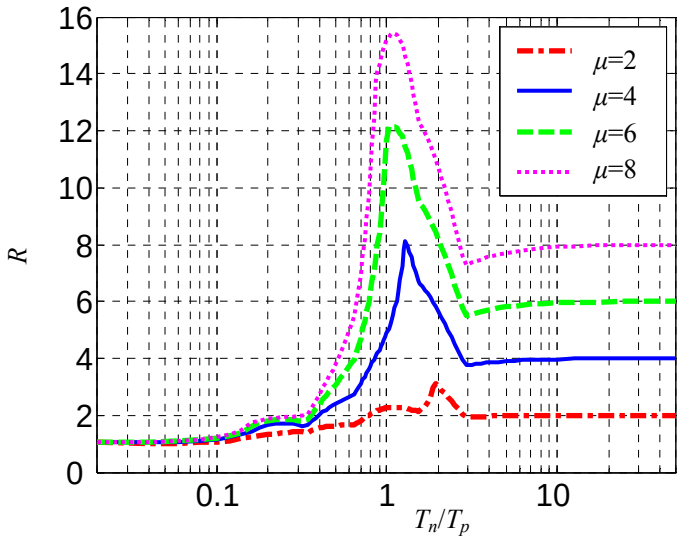

Figure 5.7 Strength reduction factor R for elastic-perfectly-plastic structures (α_s=0) as the function of T_n/T_p

The R-μ relationship in Fig. 5.7 as a function of T_n/T_p can be approximated by

$$R=\begin{cases}1 & \frac{T_n}{T_p}\le 0.1\\ C\cdot\mu^{(\frac{T_n}{T_p}-0.1)} & 0.1<\frac{T_n}{T_p}\le(\frac{T_n}{T_p})^*\\ \mu & \frac{T_n}{T_p}\ge 3\end{cases} \tag{5.6}$$

where C is the peak value factor having the form of

$$C=\frac{(\frac{T_n}{T_p}-0.1)R_0+((\frac{T_n}{T_p})^*-\frac{T_n}{T_p})}{(\frac{T_n}{T_p}-0.1)\mu^{(\frac{T_n}{T_p}-0.1)}+((\frac{T_n}{T_p})^*-\frac{T_n}{T_p})} \tag{5.7}$$

in which R_0 is the peak value of R corresponding to $(\frac{T_n}{T_p})^*$. In Eq.(5.7), values of $(\frac{T_n}{T_p})^*$ and R_0 are 1.9 and 3.1, 1.3 and 8.1, 1.1 and 12.0, 1.1 and 15.5 for μ=2, 4, 6 and 8,

respectively. Values of R corresponding to $\frac{T_n}{T_p} \in ((\frac{T_n}{T_p})^*, 3)$ are obtained by linear interpolation.

A more conservative R-μ relationship can be obtained by setting $R_0 = \mu$ when $R > \mu$,

$$R = \begin{cases} 1 & \frac{T_n}{T_p} \le (\frac{T_n}{T_p})_1 \\ C * \mu^{(\frac{T_n}{T_p} - (\frac{T_n}{T_p})_1)} & (\frac{T_n}{T_p})_1 < \frac{T_n}{T_p} \le (\frac{T_n}{T_p})_2 \\ \mu & \frac{T_n}{T_p} > (\frac{T_n}{T_p})_2 \end{cases} \tag{5.8}$$

in which

$$C = \frac{(\frac{T_n}{T_p} - (\frac{T_n}{T_p})_1)\mu + ((\frac{T_n}{T_p})_2 - \frac{T_n}{T_p})}{(\frac{T_n}{T_p} - (\frac{T_n}{T_p})_1)\mu^{(\frac{T_n}{T_p} - (\frac{T_n}{T_p})_1)} + ((\frac{T_n}{T_p})_2 - \frac{T_n}{T_p})} \tag{5.9}$$

where $(\frac{T_n}{T_p})_1 = 0.1$, $(\frac{T_n}{T_p})_2 = 0.8$ for all cases of ductility.

Fig. 5.8 shows the plots of R for the pulse model results and the proposed R-μ relationships in Eqs. (5.6) and (5.8). It is observed from Fig. 5.8 that that the proposed relationship in Eq. (5.6) matches with plots obtained for pulse-type excitation accurately. The R-μ relationship in Eq. (5.8) ignores the portion of $R > \mu$, which is conservative for inelastic design of structures.

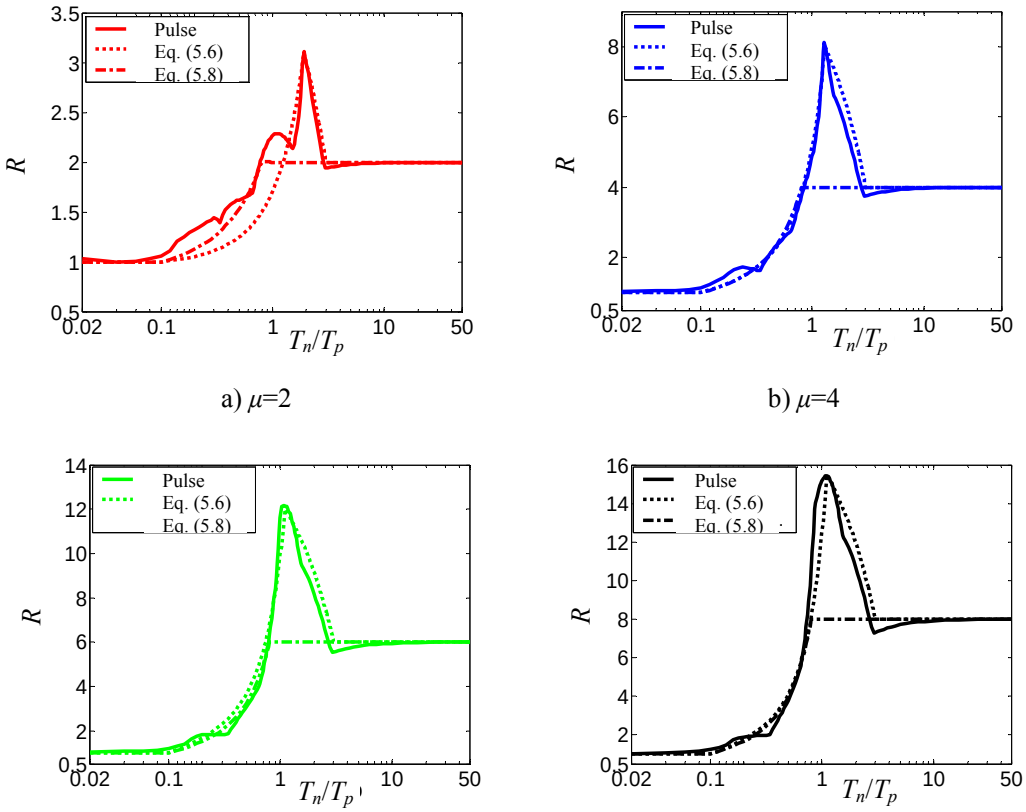

Figure 5.8 Pulse R-μ relationships as the function of T_n/T_p.

Influence of Post-yielding Stiffness on the Pulse R-μ Relationship

Fig. 5.9 shows the plots of μ/R as a function of T_n/T_p for nonlinear structures having post-yielding stiffness coefficient α_s varying from 0 to 0.5 and subjected to pulse-type excitations. The ductility factor μ equals to 4 in this analysis. It is observed from Fig. 5.9 that the influence of the post-yielding stiffness on R-μ relationship depends on the region of T_n/T_p. It has been seen earlier that R = 1 is valid when T_n/T_p <0.1 for the case of elastic-perfectly-plastic structures. However, it is observed from Fig. 5.9 that μ/R decreases from 3.9 to 1.6 as α_s increases from 0 to 0.5 for T_n/T_p =0.02, i.e., R increases and is larger than 1 with increase in α_s herein and as a result, μ/R decreases with increase

in α_s when T_n/T_p < 1.0. The minimum value of μ/R occurs in the range of 1.0 < T_n/T_p < 2.0, and it increases from 0.5 to 0.75 with increase in α_s from 0 to 0.5. As a result, the peak value of R decreases from 8 to 5.3 in this region. When T_n/T_p >3.0, μ/R equals to 1 and is independent of α_s.

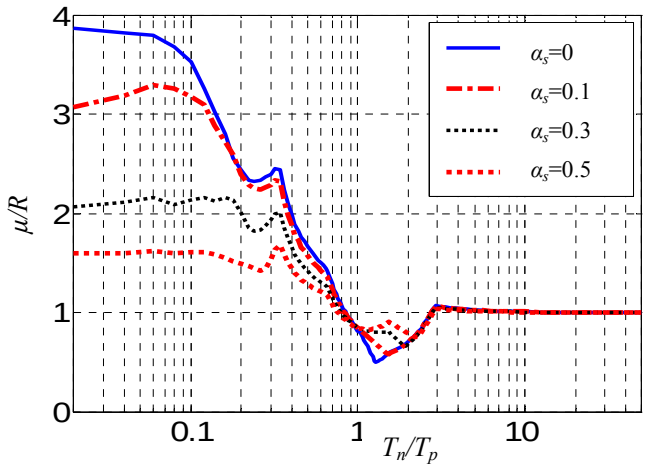

Figure 5.9 Influence of post-yielding stiffness (α_s) on the relationship of μ and R for constant ductility μ=4.

Influence of μ on Spectral Acceleration (SA) and R

Fig. 5.10 shows the normalized nonlinear acceleration spectrum SA(μ>1)/SA(μ=1) as a function of T_n/T_p for elastic-perfectly-plastic structures with ductility factors μ =2, 4, 6 and 8, subjected to pulse-type excitations. Also presented is the inverse of strength reduction factor (1/R) shown as bold curves.

It is observed from Fig. 5.10 that SA(μ>1)/SA(μ=1) is less than 1 for all cases during the entire T_n/T_p range. This demonstrates that the spectral acceleration of inelastic structure is always reduced because of yielding. When T_n/T_p <0.1, the ratio of SA(μ>1)/SA(μ=1) is between 0.8~1 for all four cases and the influence of μ is not significant. The ratio decreases as the increase of T_n/T_p when T_n/T_p is less than 1~2, depending on μ. When T_n/T_p >1~2, the ratio increases and converges to 1 as the further

increase of T_n/T_p. Hence, nonlinearity reduces acceleration response and thus lowers the base shear demand of structures all the time.

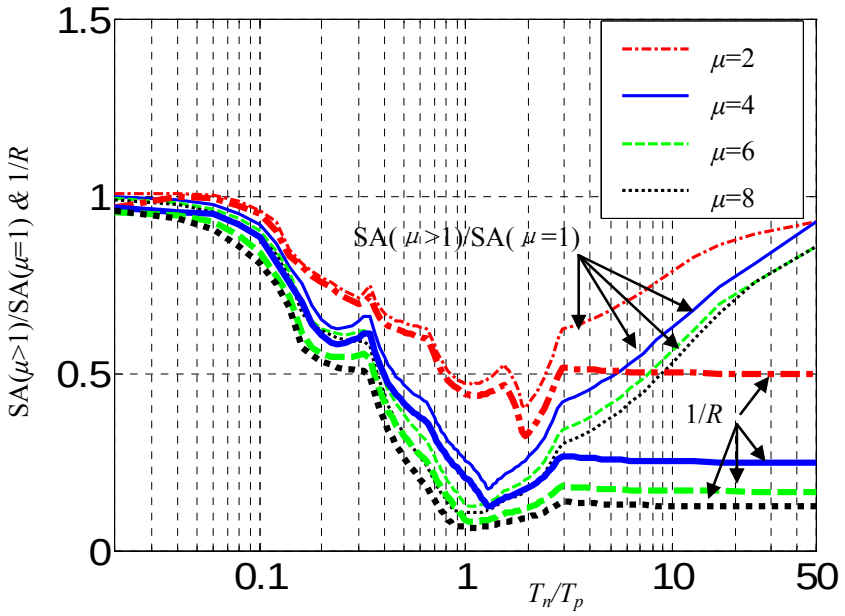

Figure 5.10 Influence of ductility factor on acceleration ratio and $1/R$ as the function of T_n/T_p.

It is observed from Fig. 5.10 that plots for both the $1/R$ and the ratio of SA follow each other closely when $T_n/T_p < 1\sim2$. However, when $T_n/T_p > 3$, the plots of $1/R$ become constant while the plots of the SA ratios continue increasing towards unity. This is due to the fact that R is equal to μ herein and the sensitivity of acceleration response to structural nonlinearity decreases for long period structures either. It is also observed that $1/R$ in Fig. 5.10 is less than the corresponding SA(μ>1)/SA(μ=1) during the entire range of T_n/T_p. This happens because the strength reduction factor, R, is related to Pseudo Spectrum Acceleration (PSA) while pseudo acceleration is less than absolute acceleration due to the existence of damping. And the difference increases as the increase of structural

period [Chopra (2001)]. Both the SA and 1/R are reduced by more than 50% when T_n/T_p is within the intermediate range and this value increases with increase in ductility.

5.3.3 R-μ Relationship for Recorded Near-field Ground Motions

The R-μ relationship for nonlinear structures subjected to recorded earthquakes has been an essential research topic since 1960. Although many researchers have developed different R-μ relationships based on various structural and ground motion properties recently [e.g., Miranda (1993), Vidic et al (1994)], the R-μ relationship proposed by Newmark and Hall (1982) for far-field earthquakes is still widely accepted in current design practices. In this section, the validity of Newmark-Hall principle for elasto-plastic structures subjected to the 50 recorded near-field earthquakes as well as pulse-type ground motions is investigated in detail.

Considering distinct impulsive characteristics of near-field earthquakes, the Newmark-Hall relationship is expressed in terms of T_n/T_p as,

$$R=\begin{cases} 1 & \dfrac{T_n}{T_p}\le\left(\dfrac{T_n}{T_p}\right)_a \\ \sqrt{2\mu-1} & \left(\dfrac{T_n}{T_p}\right)_b\le\dfrac{T_n}{T_p}<\left(\dfrac{T_n}{T_p}\right)_{c'} \\ \mu & \dfrac{T_n}{T_p}\le\left(\dfrac{T_n}{T_p}\right)_c \end{cases} \tag{5.10}$$

where

$$\left(\frac{T_n}{T_p}\right)_{c'}=\frac{\sqrt{2\mu-1}}{\mu}\times\left(\frac{T_n}{T_p}\right)_c \tag{5.11}$$

Fig. 5.11a, b, c and d show the plots of R for the recorded earthquakes and the pulse excitation as the function of T_n/T_p for ductility factors μ =2, 4, 6 and 8, respectively.

Scattered thin curves in Fig. 5.11a, b, c and d are the results for each of the 50 individual earthquakes and the hatched region is bounded by the mean plus one σ and mean minus one σ results of the recorded earthquakes. The width of the hatched region in vertical direction reflects the variation of individual results as the increase of T_n/T_p. For some earthquakes, the maximum value of R could be 2~3 times of the corresponding μ value. In Fig. 5.11, $(\frac{T_n}{T_p})_a$, $(\frac{T_n}{T_p})_b$ and $(\frac{T_n}{T_p})_c$ are obtained by matching the Newmark-Hall relationship in Eq.(5.10) with that of mean plot for recorded earthquakes corresponding to the ductility factor μ=4 shown in Fig. 5.11b. Hence, $(\frac{T_n}{T_p})_a$ is obtained by linearly extending the mean curve and intersecting it with R=1, which results in $(\frac{T_n}{T_p})_a$=0.008. Parameters $(\frac{T_n}{T_p})_b$ and $(\frac{T_n}{T_p})_c$ are determined by intersecting $R = \sqrt{2\mu - 1}$ and R=μ with the mean R curve, which results in $(\frac{T_n}{T_p})_a$=0.19 and $(\frac{T_n}{T_p})_c$=0.75, respectively. It is noted that these parameters can also be identified by curving fitting or by investigating the boundaries for acceleration, velocity and displacement-sensitive regions [e.g., Chopra and Chintanapakdee (2001), Mavroeidis et al (2004)].

These parameters are applied to other cases shown in Figs. 5.11a, 5.11c and 5.11d. It is observed from Fig. 5.11 that the modified Newmark-Hall relationship in Eq. 5.10 fits all 4 cases very well and is bounded by mean and mean minus-1σ curves. The R curve of each case starts from 1 for very small T_n/T_p and increases towards the peak value occurring around $T_n/T_p \approx 1.0$ and then gradually converges to μ as the further increase of

T_n/T_p. The peak mean values of R are approximately 1.4 to 1.5 times of the corresponding ductility factors.

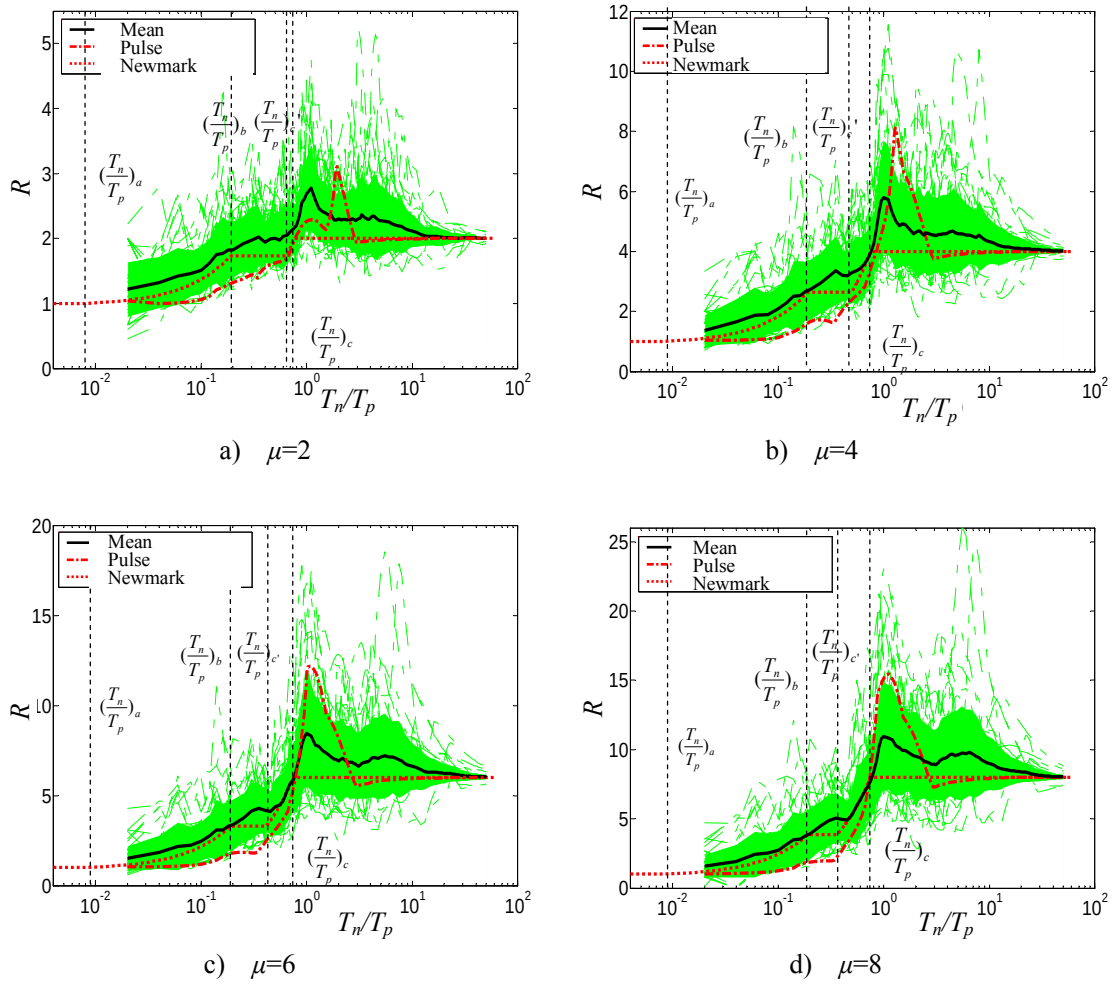

a) μ=2 b) μ=4

c) μ=6 d) μ=8

Figure 5.11 Strength reduction factors as the function of T_n/T_p: a) μ=2; b) μ=4; c) μ=6; d) μ=8.

Dot-dashed curves in Fig. 5.11 represent the results for pulse-type excitations. It is observed that the pulse R curves are close to the lower boundaries of the hatched regions in Fig. 5.11 when $(T_n/T_p)<(T_n/T_p)_c$. Hence, the pulse results yield more conservative estimation for recorded ground motions than the Newmark-Hall relationship when $(T_n/T_p)<(T_n/T_p)_c$. When T_n/T_p is greater than 3.0, the pulse and Newmark results are

coincident and converge to μ in a faster manner than the mean result. For a T_n/T_p between 1.0 and 2.0, the pulse *R*-factor is larger than that of the mean result, and is close to the mean plus one σ boundaries. However, the peak value of mean *R* could also be 1.4~1.5 larger than the corresponding ductility factor around T_n/T_p =1.0 and the mean *R* is still larger than the μ by 10~15% when T_n/T_p is not great than 10. The peak values of the mean results occur around T_n/T_p =1.0 for all μ cases as observed in Fig 5.11. On the other hand, the peak values for the pulse *R*-factors occur around T_n/T_p =2.0 for μ=2 (Fig. 5.11a) and shift to T_n/T_p ~= 1.0 for μ=8 (Fig. 5.11d).

Differences and similarities between pulse and mean results are due to the distinct properties of the analytical pulse model and recorded near-field earthquakes. The analytical pulse-model extracts the dominant pulse components of near-field earthquakes and excludes broadband frequency components [Agrawal et al (2005, 2006)]. Although pulse behavior is the distinct character of near-field earthquakes, broadband frequency contents influence the post-yielding behavior of nonlinear structures obviously as investigated in Chapter 3 and 4. Depending on the structure and excitation periods, high-frequency components play a considerable role for relative rigid structures. For intermediate structures, pulse component is dominant and for flexible structures, long-period component is important. Reflected in Fig. 5.11, pulse R is smaller than the mean result when T_n/T_p < 0.75 and T_n/T_p >2~3 and is greater otherwise.

A more detailed investigation on varies results is shown in Fig. 5.12, in which the *R* factors for the pulse, recorded earthquakes, Newmark-Hall relationship in Eq.(5.10) and the proposed relationship in Eq.(5.8) are plotted as a function of T_n/T_p for ductility factor μ=4. Characteristic values of $(T_n/T_p)_1$ and $(T_n/T_p)_2$ are taken as 0.1 and 0.75,

respectively, for the pulse R relationship in Eq. (5.8). It is observed that the proposed R expression in Eq.(5.8) is close to the pulse result and thus also fits the lower bound of the mean earthquake result when $T_n/T_p < 0.75$. Compared with the Newmark-Hall relationship, it is noted that the proposed R expression in Eq.(5.8) results in more conservative strength requirement when $T_n/T_p < 0.5$ they have same result when $T_n/T_p > 0.5$.

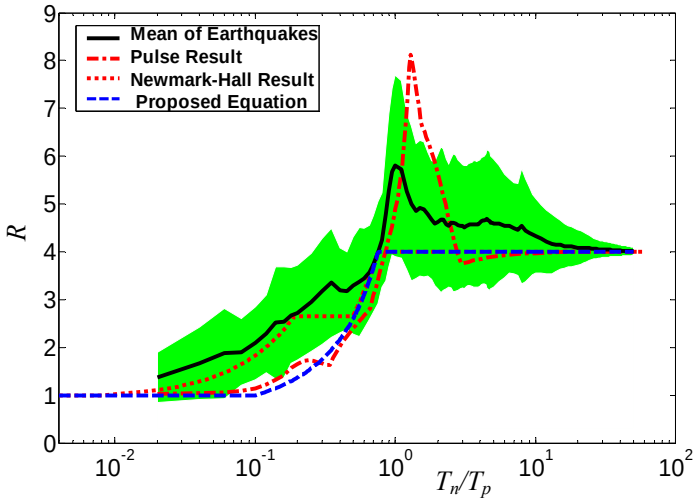

Figure 5.12 Strength reduction factors as the function of T_n/T_p for μ=4

Influence of Post-yield Stiffness on Mean Spectrum Using Recorded Earthquakes

Fig. 5.13 shows the influence of post-yielding stiffness on some mean spectra obtained using the 50 earthquake records. The ductility factor μ=4 and post-yielding stiffness coefficient α_s varies from 0 to 0.5. It is observed from Fig. 5.13a the mean displacement is only slightly influenced by variations in α_s in the range of $1 < T_n/T_p < 2$. On the contrary, mean spectral acceleration (SA) increases significantly with increase in α_s for T_n/T_p <3.

It is observed from Fig. 5.13c that μ/R decreases significantly with increase in α_s for T_n/T_p <0.8. Hence, the assumption of R =1 in Newmark-Hall relationship is only true for α_s=0 and only when T_n/T_p is very small. When T_n/T_p is greater than 1, μ/R gradually

increases and converges to 1. The R plot in Fig 5.13d is consistent with μ/R in Fig.5.13c. The influence of α_s when T_n/T_p is greater than 0.8 may be neglected since R is assumed to be equal to μ in this region for both the Newmark-Hall relationship and the proposed pulse R-factor relationship in Eq.(5.8).

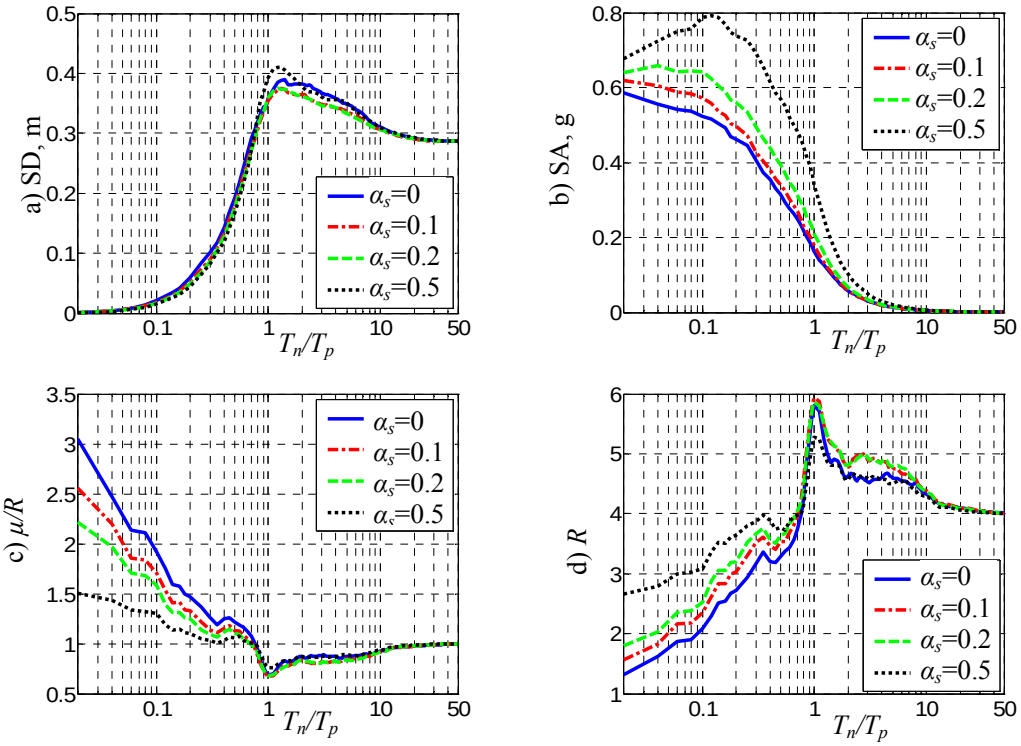

Figure 5.13 Influence of post-yielding stiffness on the average spectra using 50 near-field earthquake records: a) Displacement spectrum; b) Acceleration spectrum; c) Ratio of ductility and strength reduction factor; d) Strength reduction factor.

5.4 EFFECTS OF PASSIVE ENERGY DISSIPATION SYSTEMS ON NONLINEAR RESPONSES

5.4.1 Effects of Viscous Damping and Damper Nonlinearity

Fig. 5.14 shows the contour spectra of SD, μ and SA for nonlinear structures equipped with linear viscous dampers (α=1) capable of providing 25% supplemental

damping and subjected to pulse type excitations. The uncontrolled nonlinear structures are elastic-perfectly-plastic with constant ductility equal to 4 when subjected to the pulse excitations.

It is observed from Fig. 5.14a that the displacement response with supplemental viscous damping is significantly reduced compared with that in Fig. 5.3a. Consequently, ductility factor in Fig. 5.14b is decreased from 4 to 2 when T_n/T_p <4/5 and is in the range of 2~3.5 for other values of T_n/T_p. However, the acceleration response in Fig. 5.14c is amplified to some degree compared with the uncontrolled result in Fig. 5.2b as a result of decreased structural nonlinearity.

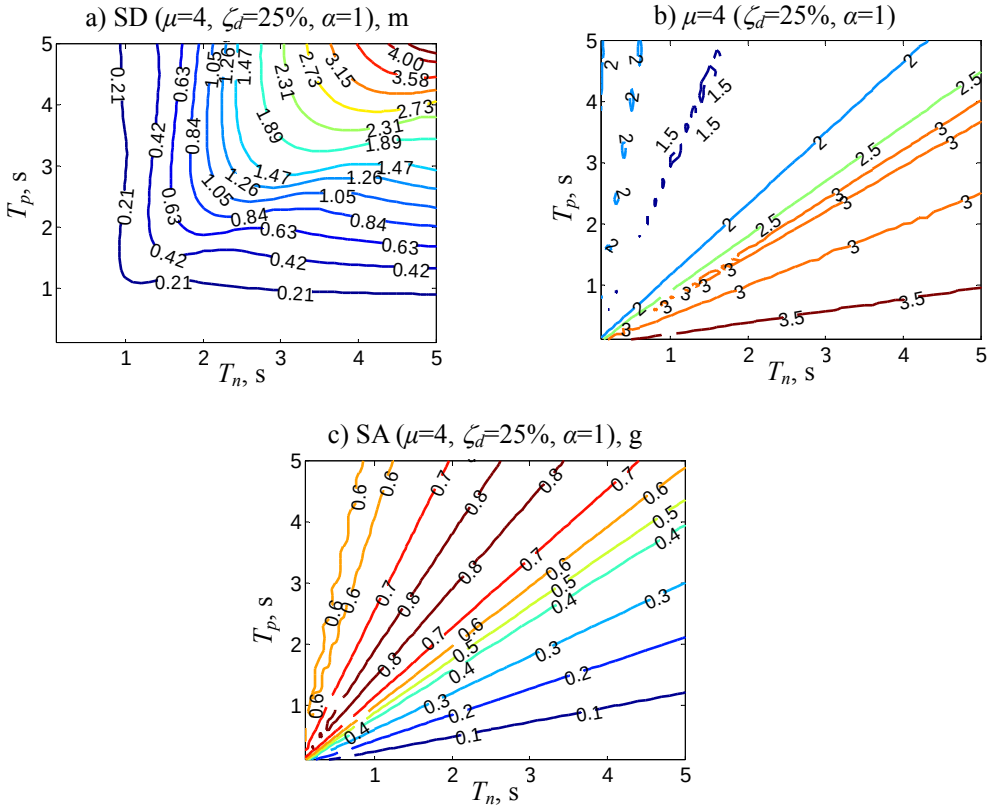

Figure 5.14 Response spectra of nonlinear structures with 25% linear viscous damping (α=1, ζ_d=25%) subjected to the pulse-type excitations: a) Displacement spectrum, b) Ductility spectrum and c) Acceleration spectrum.

The influence of damper nonlinearity on nonlinear structural responses is similar to that on linear structures, as investigated in Chapter 4. Fig. 5.15 shows the ratios of average displacement and acceleration spectra of the 50 recorded earthquakes as a function of T_n/T_p. The hatched area represents the region bounded by the mean ± 1σ for the average results in each plot. The supplemental damping ratio is 25% for both linear (α=1) and nonlinear (α=0.5) dampers. It is observed from Fig. 5.15a that nonlinear viscous dampers can more significantly reduce the average displacement response when T_n/T_p <1 but are less effective than their linear counterparts when T_n/T_p >1. For T_n/T_p in the vicinity of 1, they have similar efficiency. The acceleration spectrum ratio in Fig. 5.15b shows that damper nonlinearity does not affect acceleration response when T_n/T_p<1. However, structures with nonlinear dampers have smaller acceleration responses compared to those with linear dampers when T_n/T_p > 1 as seen from Fig 5.15b. It is also observed from Figs. 5.15a and 5.15b that the variation of displacement ratio due to damper nonlinearity is much larger than that of the acceleration ratio.

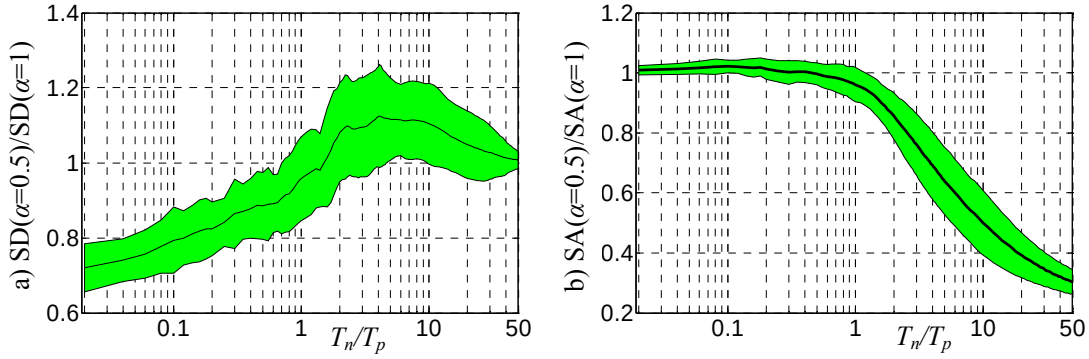

Figure 5.15. Influence of damper nonlinearity on nonlinear displacement and acceleration responses: a) Displacement spectrum ratio; b) Acceleration spectrum ratio.

5.4. 2 Effects of Yielding Dampers

Fig. 5.16 shows contour spectra of displacement, absolute acceleration and ductility for nonlinear structures equipped with yielding dampers subjected to pulse-type excitations. Displacement and accelerations in Figs. 5.16a and 5.16b are normalized by the corresponding uncontrolled response quantities. The behavior of yielding dampers is modeled by Bouc-Wen model with zero post-yielding stiffness (α_d=0). Tha damper yielding strength, F_{yd}, equals to $0.5F_{ys}$ and initial stiffness k_d is taken as the same as k_s, where F_{ys} and k_s are the yielding strength and elastic stiffness of the corresponding nonlinear structures.

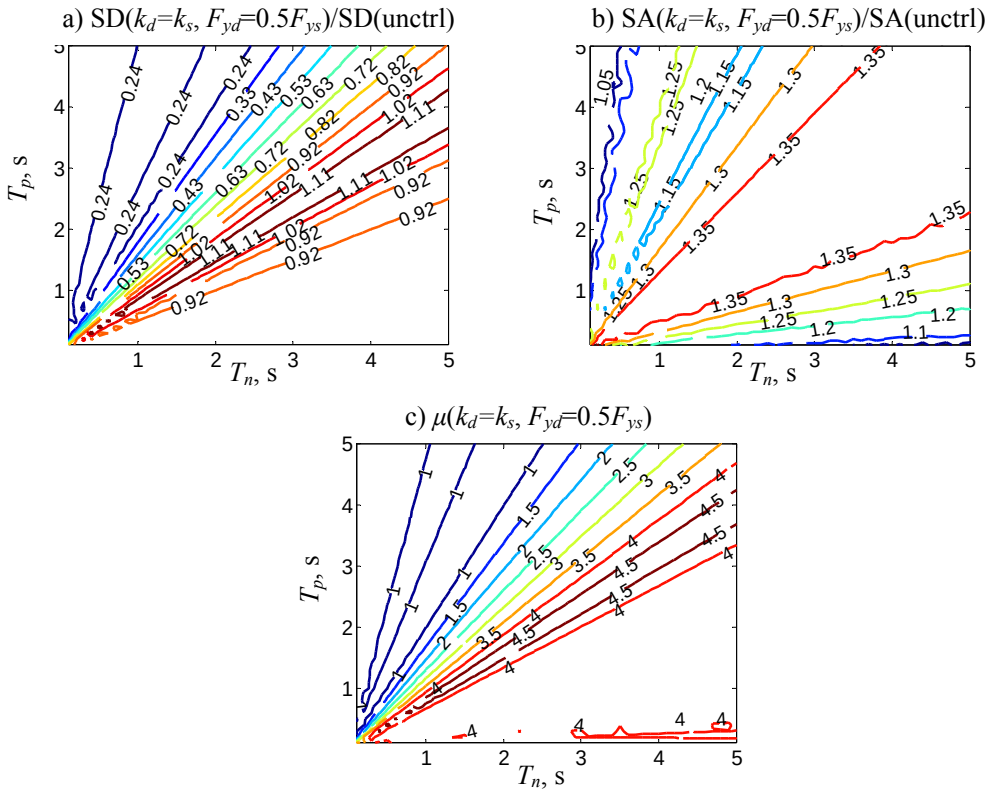

Figure 5.16 Response spectra of nonlinear structures with yielding dampers (F_{yd}=0.5F_y, k_d=k_s): a) Ratio of controlled displacement and uncontrolled displacement; b) Ratio of controlled acceleration and uncontrolled acceleration; c) Ductility.

It is observed from Fig. 5.16a that yielding dampers are effective in reducing displacement response of nonlinear structures when T_n/T_p<1. For T_n/T_p>1, displacement of structures with and without the dampers are almost the same, except in the vicinity of T_n/T_p=5/4, where the displacement is even amplified up to 10%. This is also reflected by the ductility spectrum in Fig. 5.16c, in which the μ is reduced down to 1 when T_n/T_p <1 and increased up to 4.5 otherwise. The acceleration response is always increased for nonlinear structures as shown in Fig. 5.16b. The maximum amplification could be 20%~35% when 3/5<T_n/T_p <5/2.

Fig. 5.17 shows mean displacement, ductility and acceleration spectra for nonlinear structures (μ=4, α_s=0) with yielding dampers subject to 50 recorded earthquakes. Initial damper stiffness is taken as the same as the elastic structural stiffness (k_d=k_s) and the damper post-yielding stiffness coefficient α_d = 0. Two levels of damper yielding capacity, i.e., F_{yd}=0.1F_{ys} (low yielding capacity) and F_{yd}=0.5F_{ys} (high yielding capacity), are considered.

It is observed from Fig. 5.17a that the yielding dampers reduce displacement only when T_n/T_p <1~2.0. When T_n/T_p is greater than 2.0, displacement is slightly amplified in fact. Correspondingly, the ductility in Fig. 5.17b is reduced when T_n/T_p <1~2.0 and is increased thereafter. The dampers with larger yielding capacity could achieve more displacement and ductility reduction when T_n/T_p <2.0; however, amplification in these response quantities is also larger otherwise. Similar to the pulse response result, the controlled acceleration is amplified in the entire T_n/T_p range, as shown in Fig. 5.17c.

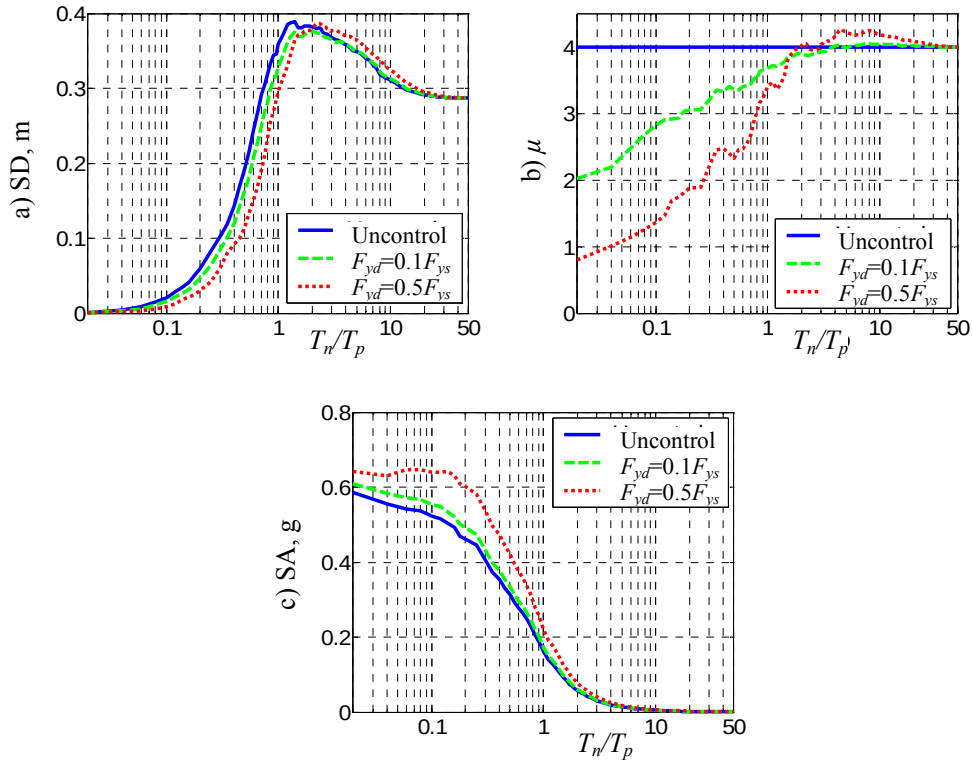

Figure 5.17 Performance of yielding damper on the average spectra of recorded earthquakes: a) Displacement spectrum; b) Ductility spectrum; c) Acceleration spectrum

It has been observed for linear structures in Chapter 4 that the performance of yielding dampers depends both on their stiffness and damping characteristics. The amplification of displacement and ductility for T_n/T_p> 1~2.0 is resulted from the stiffness effect of the yielding dampers. For yielding dampers with small yielding strength, their energy dissipation capacity is more significant than their stiffness effect and they dissipate energy through cyclic hysteretic deformation at small amplitudes. As a result, the effective structural period is not significantly affected and the amplification in displacement and ductility is negligible. For yielding dampers with large yielding capacity, both energy dissipation and stiffness effects are obvious and the effective structural period could be apparently decreased by the dampers. For nonlinear structures,

the effective period is not only influenced by the supplemental stiffness but also is a function of the structural deformation. Hence, the stiffness and yielding strength of yielding dampers should be carefully chosen in order to effectively control structural responses.

5.5. ENERGY-RELATED PROPERTIES OF NONLINEAR STRUCTURES SUBJECTED TO PULSE-TYPE AND NEAR-FIELD EXCITATIONS

5.5.1 Nonlinear Input Energy Spectra of Pulse-type Excitations

Fig. 5.18 shows the input energy spectra for nonlinear structures with $\mu = 4$, zero post-yielding stiffness and subjected to the pulse excitations. It is observed from Fig. 5.18a that nonlinear input energy increases with an increase in T_n and T_p, and vertices of contour lines gradually shift into the region of $T_p > T_n$. Compared to its linear counterpart, the nonlinear input energy could be significantly amplified when T_n/T_p <3/5, as shown in Fig. 5.18. On the other hand, it could also be reduced up to 35% compared to linear input energy when T_n/T_p >4/5. For structures with T_n/T_p >5, the input energy is not affected by structural nonlinearity.

Fig. 5.19 shows nonlinear input and hysteretic energy spectra subjected to the pulse-type excitation with T_p =1s. It is observed from Fig. 5.19a that the peak value of the input energy occurs around T_n = 1s for μ = 1 (linear structure) and decreases with increase in ductility. The variation of hysteretic energy in Fig. 5.19b follows the same trend as the input energy. Moreover, the input and hysteretic energy could be increased or decreased as the increase of ductility depending on the structural period. For long period

structures with T_n > 3s, hysteretic energy is negligible since input energy is mainly transformed into strain energy at all ductility levels.

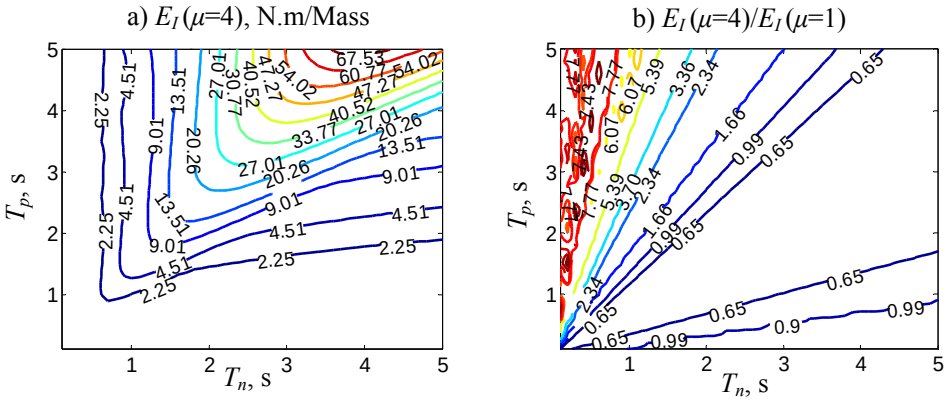

Figure 5.18 Absolute nonlinear input-energy spectra and the corresponding normalized spectrum subject to pulse excitation with μ=4, α_s=0.

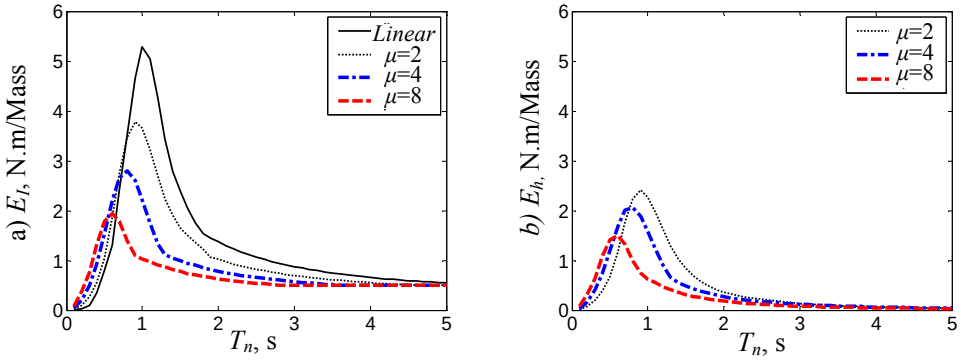

Figure 5.19 Nonlinear input and hysteretic energy spectra subject to the pulse-type excitation with T_p =1s. a) Input energy spectrum; b) Structural hysteretic energy spectrum

5.5.2 Influence of Post-yielding Stiffness on Input and Hysteretic Energy during Recorded Near-field Earthquakes

Fig. 5.20 shows the influence of structural post-yielding stiffness on nonlinear input and hysteretic energy spectrum as a function of T_n/T_p for the 50 recorded near-field earthquakes. The ductility factor is taken as 4 in this investigation. It is observed from Fig.

5.20a that the input energy E_I increases with increase in α_s only in the region 0.5< T_n/T_p<2 and is only significant as α_s increased from 0 to 0.1. Otherwise, α_s does not obviously affect the input and hysteretic energy.

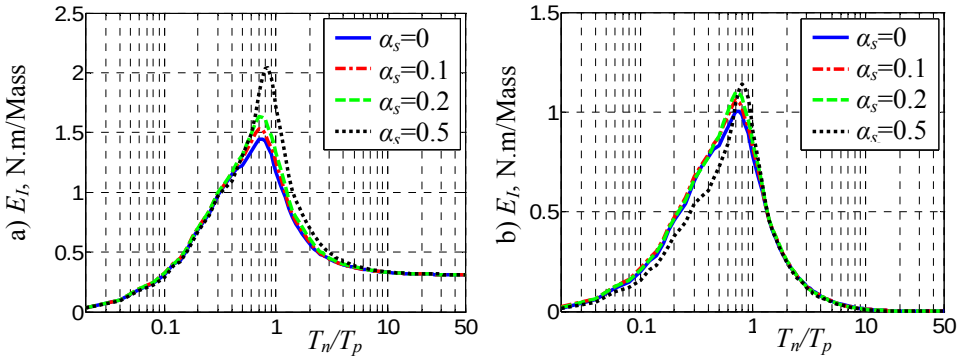

Figure 5.20 Influence of post-yielding stiffness to the input and hysteretic energy spectra: a) Input energy spectrum; b) Hysteretic energy spectrum.

5.5.3 Influence of Ductility Factor on the Input and Hysteretic Energy during Recorded Near-field Earthquakes

Fig. 5.21 shows the influence of structural ductility on the input and hysteretic energy of elastic-perfectly-plastic structures using the 50 recorded earthquakes. It is observed from Fig. 5.21a that the absolute value of the input energy spectrum is significantly reduced as the increase of ductility when 0.5< T_n/T_p <3. However, the input energy ratio in Fig. 5.21b decreases from a value close to the corresponding ductility factor and gradually converges to 1 as the increase of T_n/T_p for all cases. Hence, the input energy for structures have small T_n/T_p ratio is more significantly affected by structural nonlinearity. It is also observed that the normalized hysteretic energy in Fig. 5.21c increases with an increase in μ when T_n/T_p <1. For T_n/T_p >1.0, this influence is

insignificant. Moreover, the sensitivity of the normalized hysteretic energy to the variation of ductility factor decreases as the increase of ductility factor.

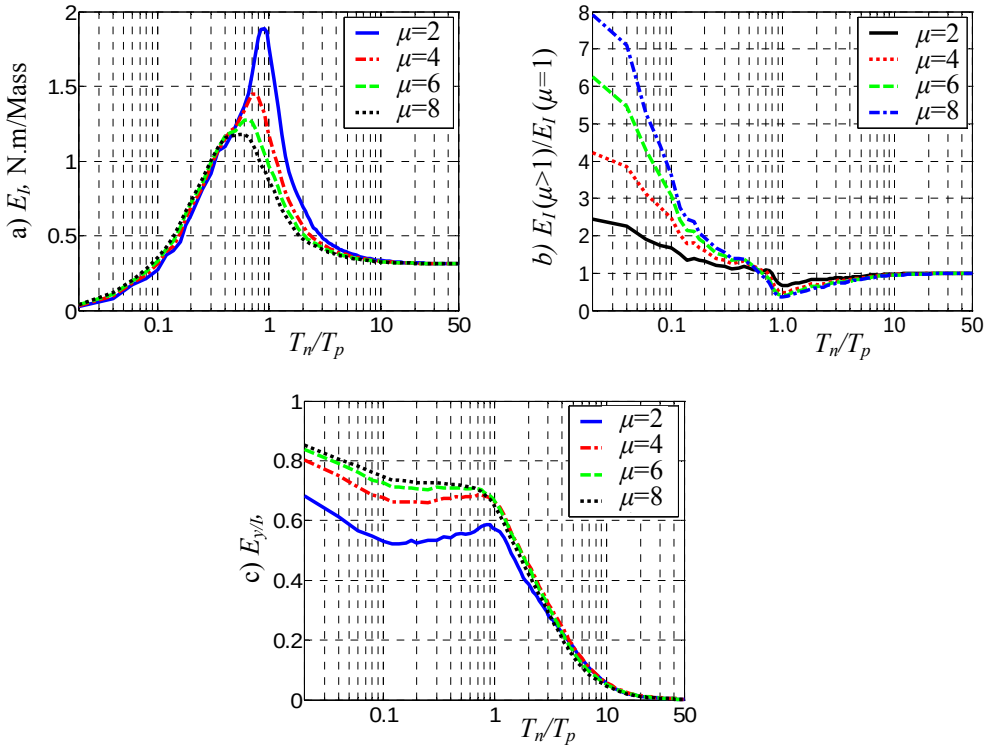

Figure 5.21 Influence of ductility factor on energy characteristics of nonlinear structures: a) Input energy spectrum; b) Normalized input energy spectrum and c) Normalized hysteretic energy spectrum.

5.6. EFFECTS OF PASSIVE ENERGY DISSIPATION SYSTEMS ON ENERGY-RELATED PROPERTIES OF NONLINEAR STRUCTURES

5.6.1 Energy Dissipation of Viscous Dampers

Fig. 5.22 shows the contour plots for nonlinear input energy, hysteretic energy and damper-dissipated energy spectra using pulse-type excitations. The nonlinear structures are supplemented with 25% linear viscous damping.

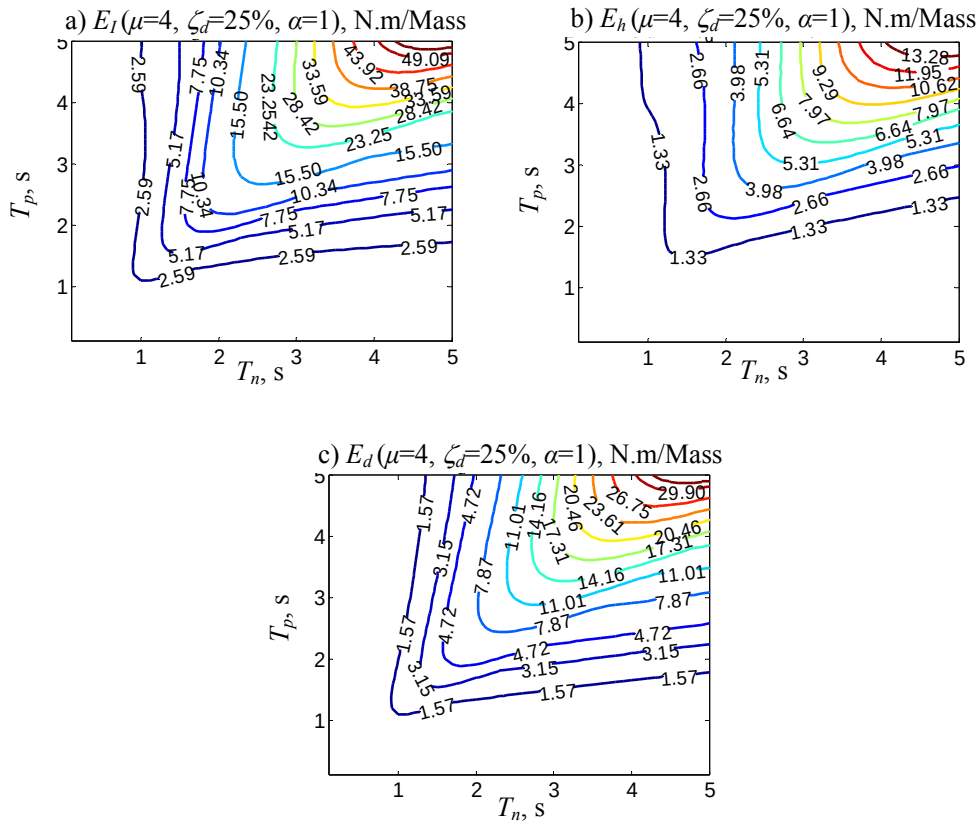

Figure 5.22 Energy response spectra of nonlinear structures with 25% linear viscous damping (μ=4, ζ_d=25%): a) Input energy spectrum; b) Structural hysteric energy spectrum and c) Damper-dissipated energy spectrum

It is observed from Fig. 5.22a that the controlled input energy spectrum is similar to that of the uncontrolled one in Fig. 5.18a, except that the energy magnitude in Fig. 5.22a is smaller in the majority of the region. The hysteretic energy in Fig. 5.22b is much smaller than the energy dissipated by the 25% damping in Fig. 5.22c since significant amount of input energy is dissipated by the supplemental damping and thus plastic deformation decreases accordingly. It is noted that the underlying basis of an energy demand-supply relationship for a structure to withstand strong ground motions is that the total energy input should be less than or equal to total energy dissipation capacity. For this case, the combined energy dissipation capacity of the inherent and supplemental

damping mechanism is still not enough to dissipate the total input energy since part of the input energy is also dissipated by structural hysteresis.

Fig. 5.23 shows the effect of supplemental damping on various types of energy using the 50 recorded earthquakes. Results in Fig. 5.23 are obtained for nonlinear structures with constant ductility 4 and zero post-yielding stiffness. The linear viscous damping ratio varies from 0 to 45%. It is observed from Fig. 5.23a that the influence of supplemental damping on input energy depends on the ratio of T_n/T_p: the input energy increases with an increase in supplemental damping for $T_n/T_p > 1.0$ and decreases for $T_n/T_p < 1.0$. On the other hand, hysteretic energy E_h in Fig. 5.23b always decreases with increase in supplemental damping, since more energy is dissipated by a larger capacity damper. As a result, the ratio of hysteretic to input energy ($E_{h/I}$) decreases with increase in supplemental damping as observed in Fig. 5.23c. $E_{h/I}$ is highest when $T_n/T_p <0.1$ and almost keeps constant in the range of $0.1< T_n/T_p <1.0$ for all cases. When $T_n/T_p >1.0$, the ratio decrease towards zero as the further increase of T_n/T_p due to the increase of kinetic energy for flexible structures. Fig. 5.23d shows the spectra for damper dissipated energy (E_d). It is observed that E_d increases with increase in supplemental damping ratio as a result of increasing energy-dissipation capacity. It is also noted that the increase in E_d for $T_n/T_p > 1$ is larger than that for $T_n/T_p < 1$ for the same amount of damping increment. However, the input energy also increases when $T_n/T_p > 1$ due to the increase of damping ratio, as shown in Fig. 5.23a. Hence, it is important to investigate the ratio of damper-dissipated energy, $E_{d/I}$, in Fig. 5.23e. It is observed from Fig. 5.23e that the dampers dissipate most of the input energy in the range of $0.1 < T_n/T_p<3$ for all supplemental damping levels. For example, more than 60% of the input energy is dissipated by the

25% supplemental damping in this region. For T_n/T_p > 3, energy dissipated by supplemental dampers decreases gradually with increase in T_n/T_p. It is noted that the $E_{h/I}$ and $E_{d/I}$ provide an efficient and direct way of evaluating the effectiveness of damping with respect to structural and excitation characteristics.

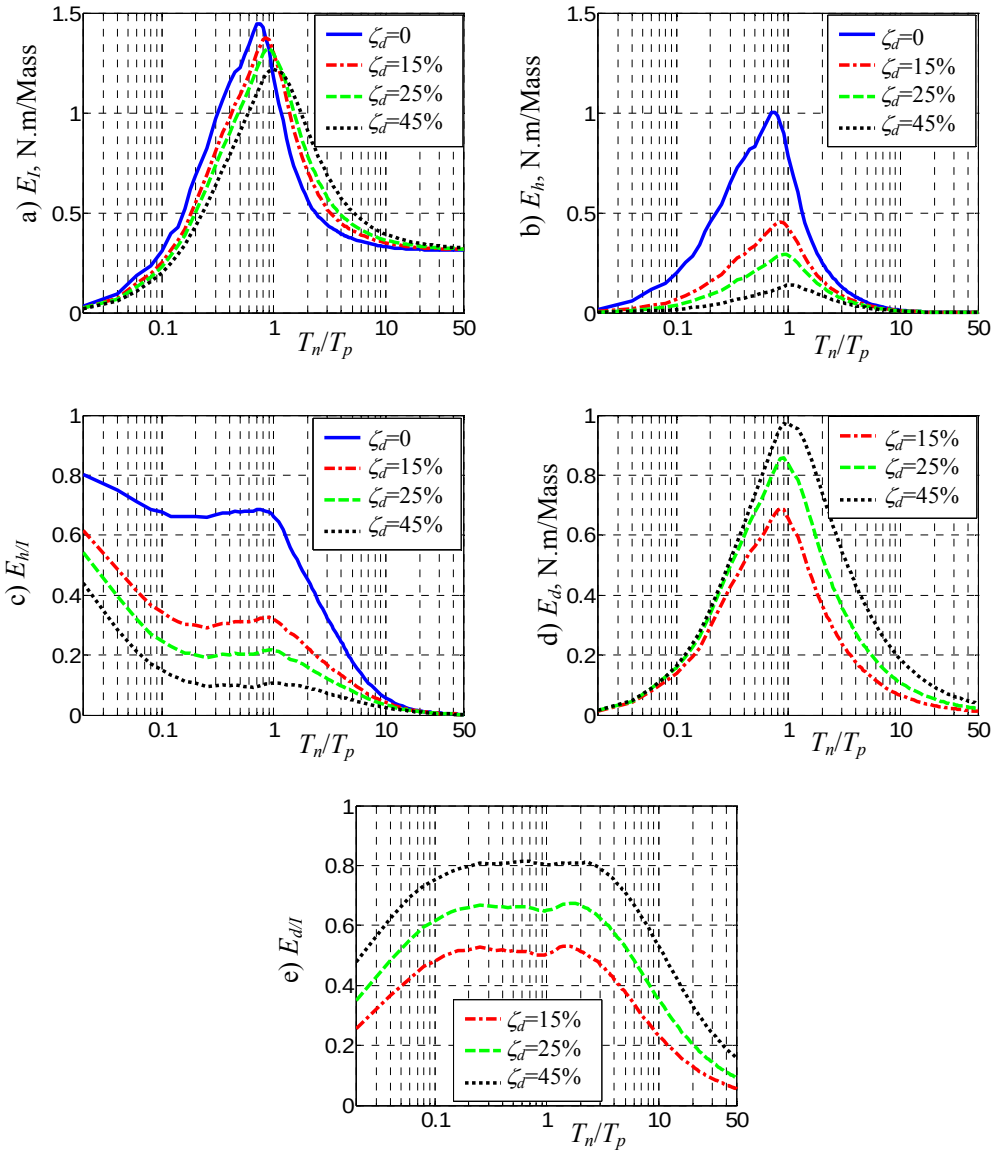

Figure 5.23 Effects of damping on the energy characteristics of structural and damper: a) Input energy spectrum; b) Yielding energy spectrum; c) Normalized hysteretic energy spectrum; d) Damper-dissipated energy spectrum; e) Normalized damper dissipated energy spectrum.

Fig. 5.24 shows the influence of ductility factor on $E_{h/I}$ and $E_{d/I}$ using the 50 recorded earthquakes. The supplemental damping ratio is 25% for each case. It is observed from Fig. 5.24a that the energy dissipated by the supplemental damping decreases as the increase of ductility factor since more energy is dissipated by structural hysteresis as μ increases from 2 to 8 as shown in Fig. 5.24b. Nevertheless, dampers with 25% supplemental damping can reduce the input energy by 60%, irrespective of ductility level, for nonlinear structures with $0.2< T_n/T_p < 3$, as observed from Fig. 5.24a.

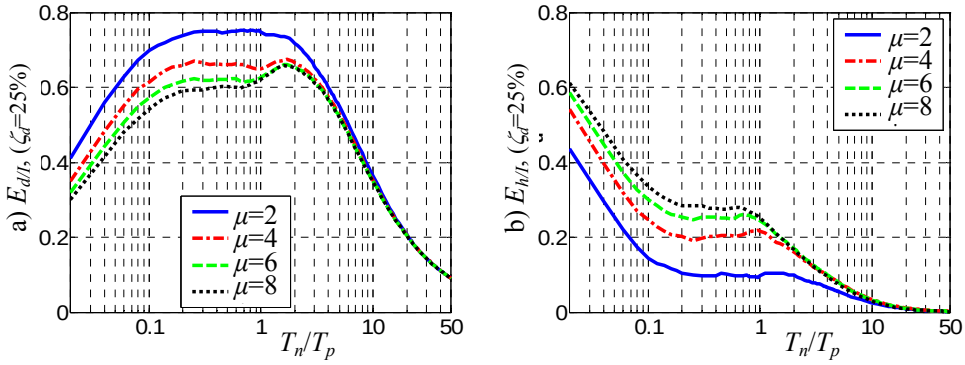

Figure 5.24 Influence of ductility factor on damper efficiency: a) Normalized damper-dissipated energy spectrum; b) Normalized hysteretic energy spectrum.

5.6.2 Energy Dissipation of Yielding Dampers

Fig. 5.25 shows contour energy spectra as a function of T_n and T_p for nonlinear structures controlled by yielding dampers. The yielding dampers are modeled by Bouc-Wen model with yielding strength F_{yd}=0.5F_{ys}, initial stiffness k_d=k_s and post-yielding stiffness α_d=0. The uncontrolled structural ductility μ= 4 and post-yielding stiffness α_s=0.

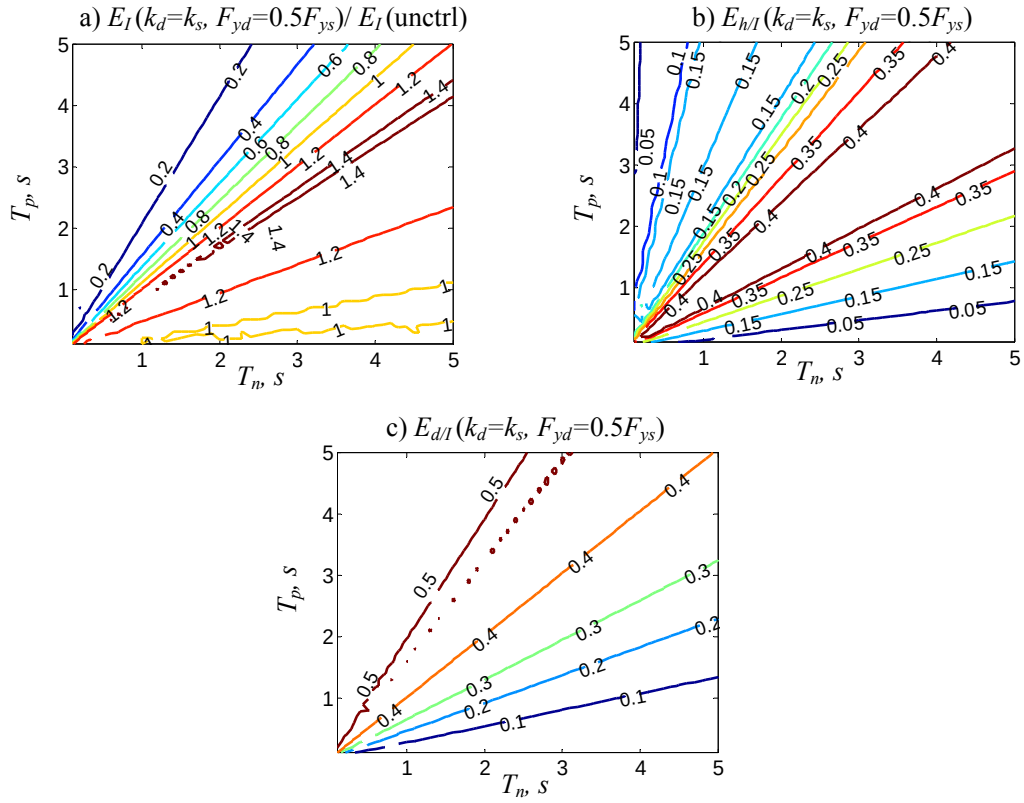

Figure 5.25 Normalized energy response spectra of nonlinear structures with yielding dampers (F_{yd}=0.5F_{ys}, k_d=k_s): a) Ratio of controlled and uncontrolled input energy; b) Ratio of structural hysteretic energy and input energy of controlled structures; c) Ratio of energy dissipated by yielding damper and the input energy of controlled structures.

Fig. 5.25a shows the ratio of controlled and uncontrolled input energy. It is observed that the input energy is reduced only when T_n/T_p<1 although this reduction could be as much as 80% if T_n/T_p< 2/5. As a result, structures with the yielding dampers almost do not undergo nonlinear deformation in this region, as shown in Fig. 5.16c. It is observed from Fig. 5.25b that the maximum energy dissipated by structural yielding is less than 40% in the entire plot region. From Fig. 5.25c, it is noted that the yielding dampers can dissipate more than 40% of total input energy when T_n/T_p <1.0. Although yielding dampers still dissipate input energy when T_n/T_p >1.0, the structures may undergo

larger plastic deformation due to the increase of input energy caused by the dampers herein.

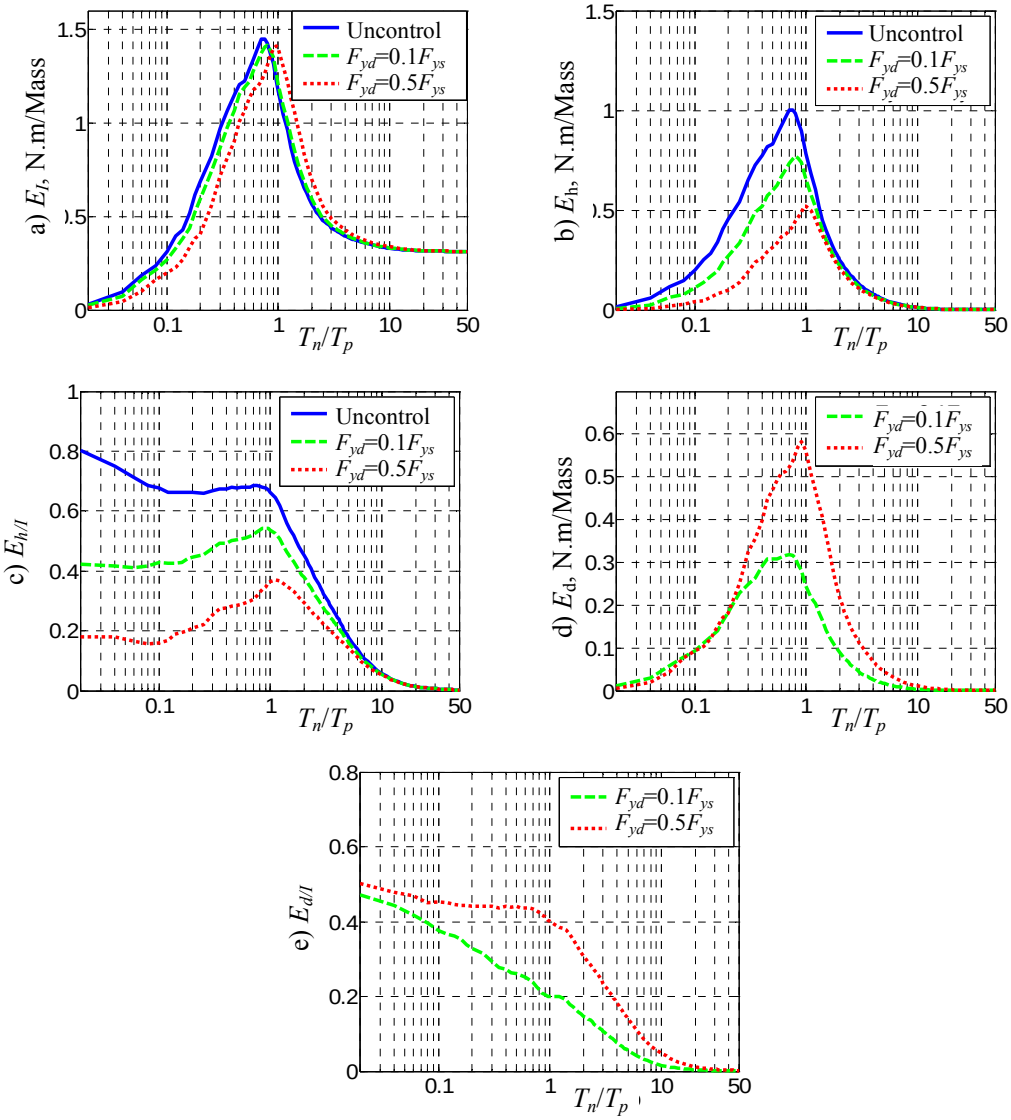

Figure 5.26 Energy response characteristics of controlled structure with yielding damper: a) Input energy spectrum; b) Hysteretic energy spectrum; c) Normalized hysteretic energy; d) Damper-dissipated energy and e) Normalized damper dissipated energy.

Fig. 5.26 shows the average spectra of E_I, E_h, $E_{h/I}$, E_d and $E_{d/I}$ for nonlinear structures (μ=4, α_s=0) with or without yielding dampers subjected to the 50 recorded

earthquakes. Initial damper stiffness k_d equals to k_s and post-yielding stiffness α_d=0 in this figure. Two levels of yielding strength, $F_{yd} = 0.1F_{ys}$ and $F_{yd} = 0.5F_{ys}$, are considered.

It is observed from Fig. 5.26a that the input energy shifts towards right after addition of yielding dampers. This results in the decrease of input energy when T_n/T_p <0.8 and the increase when T_n/T_p >1.0, which is consistent with the displacement and ductility spectra presented in Fig.5.16. Addition of yielding dampers reduces hysteretic energy dissipated by structural deformation. And this reduction is more significant for T_n/T_p <1.0, as shown in Fig. 5.26b and Fig. 5.26c. Plots in Fig. 5.26d domenstrates that the absolute energy dissipated by yielding dampers is largest in the vicinity of T_n/T_p=1 since the input energy is largest herein. However, it is noted from Fig. 5.26e that the performance of yielding dampers degrades as the increase of T_n/T_p since the ratio of damper dissipated energy and input energy decreases monotonically. Hence, the $E_{d/I}$ and $E_{h/I}$ greatly facilitate the assessment of the efficiency of yielding dampers.

5.7. DISCUSSION

The input energy used in this paper is "relative" input energy, which is obtained by integrating the "relative" energy equation as discussed in Chapter 4. In conjunction with the "relative" input energy, "absolute" input energy is obtained by integrating the "absolute" energy equation [Uang and Berto (1988a, 1988b, 1990)]. Recalling Eq. (4.14) and (4.19) in Chapter 4, it is noted that, for very short period structures, $\dot{x} \approx 0$, $x \approx dx \approx 0, \ddot{x}_t \approx \ddot{x}_g$; hence, $E_I^a \approx \frac{m}{2}\dot{x}_g^2$ and $E_I \approx 0$, i.e., absolute input energy is larger than relative input energy. For very long period structures, $x \approx -x_g$, $\ddot{x} \approx -\ddot{x}_g$, hence,

$x_t \approx 0$, $\ddot{x}_t = 0$, $E_I^a = \int m\ddot{x}_t dx_g \approx 0$ and $E_I = \int m\ddot{x}_g dx = \frac{m}{2}\dot{x}_g^2$, i.e., absolute input energy is smaller than the relative input energy. For intermediate structures, these two quantities are essentially the same.

To illustrate the above properties, Fig. 5.27 presents the energy response history of nonlinear structure with μ=4, T_n=2.5s, post-yielding stiffness α_s=0, 5% inherent damping and subjected to the SYL090 record of the 1994 Northridge earthquake. Fig. 5.27a shows the energy balance information in terms of relative input energy and Fig. 5.27b shows the same information but in terms of absolute input energy. The lowest un-filled area in these figures represents the energy dissipated by the inherent damping, and the upper areas show the strain energy, kinetic energy and hysteretic energy, respectively. It is observed that a majority of the input energy, both relative and absolute, is dissipated by structural yielding although the inherent damping also accounts for a significant portion of it. The kinetic and strain energy only have minor contribution to the total input energy during the entire response history for this case. However, they cause fluctuations in input energy, as seen from Fig. 5.27a.

Figs. 5.28 and 5.29 show spectra of relative and absolute input energy and normalized hysteretic energy for SPV270 and SYL090 records, respectively. The relationship of "relative" and "absolute" input energy is obvious for short, intermediate and long period structures in the plots. It is also observed that normalized hysteretic energy spectra ($E_{h/I}$) have contrary trends for short and long-period structures due to inherent relationships between "relative" and "absolute" energy.

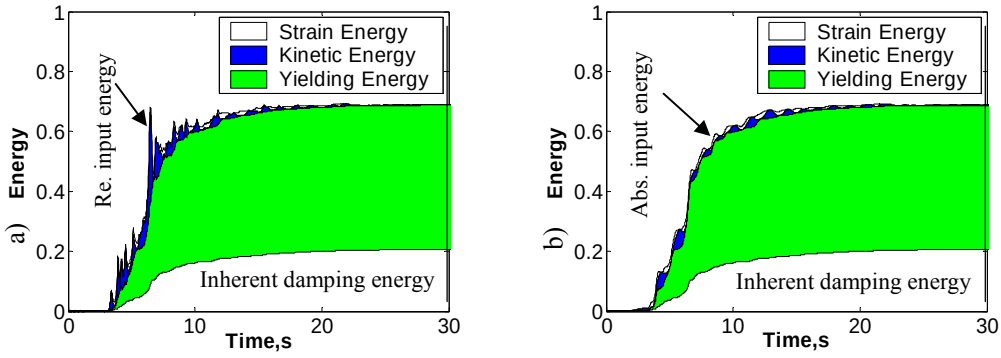

Figure 5.27 Energy response history of a nonlinear SDOF structure (T_n=2.5s, μ=4, α_s=0 and ζ_{in}=5%) subjected to SYL090 record of 1994 Northridge earthquake: a) Relative energy balance history; b) Absolute energy balance history

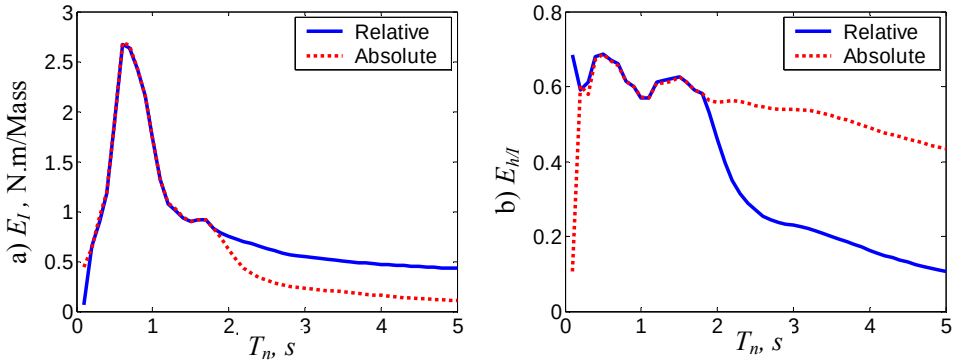

Figure 5.28 Comparison of absolute and relative spectra for nonlinear structures subjected to SPV270 record: a) Input energy spectra; b) Normalized hysteretic energy

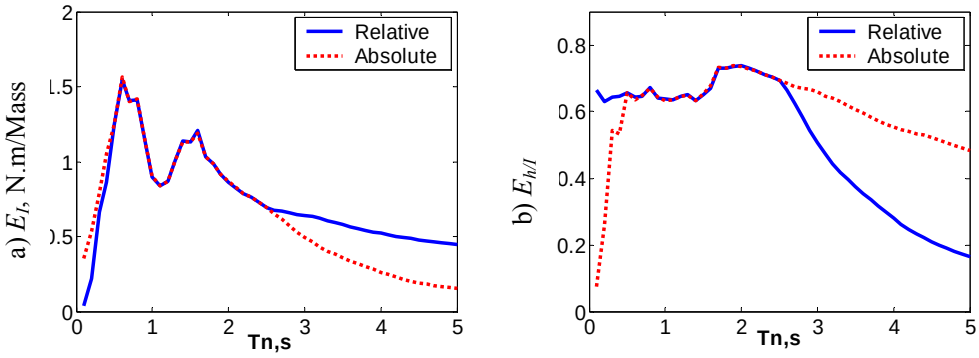

Figure 5.29 Comparison of absolute and relative spectra for nonlinear structures subjected to SYL090 record: a) Input energy spectrum; b) Normalized hysteretic energy spectrum

5.8 CONCLUSIONS

The behavior of inelastic structures with and without passive energy dissipation systems (e.g., viscous dampers and yielding dampers) during near-field and pulse-type excitations are investigated in this chapter.

It is noted that the level of structural damage due to earthquakes not only depends on the maximum response quantities, but also on cumulative effects of inelastic hysteretic cycles. In this chapter, both strength-based and energy-based inelastic structural characteristics are investigated. R-μ relationships for inelastic structures at different yielding levels subjected to both pulse-type and near-field earthquakes are investigated in terms of maximum response quantities. A R-μ relationship for pulse-type ground motions is proposed. This relationship matches well with the lower boundary (i.e., the mean-1σ curve) of the recorded ground motion result for $T_n/T_p<(T_n/T_p)_c$; when $T_n/T_p>(T_n/T_p)_c$, the proposed relationship yields same result as the Newmark-Hall relationship.

The cumulative excitation effects are evaluated by investigating the energy-related properties of inelastic structures. It is noted that the energy-related properties provide effective tools in characterizing cumulative damage process of structures and thus are widely applied for performance-based design. This property is investigated by studying the input energy spectra, hysteretic energy spectra, ratio of hysteretic to input energy as well as spectra of damper dissipated energy for both pulse-type and near-field ground motions.

Performance of passive energy dissipation systems for nonlinear structures is another topic of this chapter. Because of significant nonlinearity inherent in inelastic structures, performance of energy dissipation devices in nonlinear structures is inferior to

that in linear structures, since a significant portion of input energy may be dissipated through hysteretic structural behavior. As a result, it is found that energy dissipated by supplemental dampers decreases with increase in structural nonlinearity (ductility). However, for a given structure, supplemental energy dissipation devices still significantly reduce the energy input to the structure and thus prevent the structure from excessive damage during strong earthquakes.

It is noted that the performance of PEDS is significantly affected by the ratio of T_n/T_p, i.e, viscous dampers are most effective when T_n/T_p is in the vicinity of 1 and yielding dampers are most effective when $T_n/T_p<1$. Efficiency of these dampers can be evaluated from the energy spectrum plots, such as E_I , $E_{h/I}$, E_d and $E_{d/I}$.

CHAPTER 6

GROUND MOTION PULSE-BASED SEMI-ACTIVE AND ACTIVE CONTROLLER DESIGN FOR BASE-ISOLATED STRUCTURES

6.1 INTRODUCTION

Significant progress has been made in the area of active and semi-active control of civil infrastructures. A detailed literature review on the subject area can be found in Soong (1991), Spencer and Sain (1997), Housner et al (1997), Soong and Spencer (2002), and Spencer and Nagarajaiah (2003), Symans and Constantinou (1999). In active structural control, control force based on certain algorithm using response measurements or estimations is applied directly to the structure using direct actuation devices (e.g., hydraulic actuators) to achieve response control objectives. Other advantages of active control systems include relative insensitivity to site conditions and ground motions, applicability to multi-hazard situations (e.g., earthquakes and winds) and selectivity of control objectives, e.g., human comfort during non-critical time and safety during severe dynamic loading. To date, more than 40 buildings and towers, and more than 10 bridges, have been installed with active/hybrid control systems, mostly in Japan [Spencer and Nagarajaiah (2003)].

Although fully active structural control systems have been considered unsuitable for seismic protection of large scale infrastructure systems because of large power

demand requirement during earthquakes, hybrid control systems, e.g., active tuned mass damper (ATMD), base-isolation bearings in parallel with actuators, etc., however, are prospective due to the combined advantages of different control systems. Besides the applications of hybrid control systems on top of tall buildings [Soong and Spencer (2002)], their applications and performance have also been investigated for different types of base-isolated structures and cable-stayed bridges [e.g., Luo et al (1998), Yang et al (1995c, 1996c), Jung et al (2004), Nagarajaiah et al (1993, 2003)]. Since the performance of the control systems depends on the control algorithms, various modern control theories have been investigated, e.g., LQG/H2/H_∞ [Suhardjo et al (1990), Spencer et al (1993), Yang et al (1996b), Zhou et al (1996)], Sliding Mode Control [Utkin (1992), Yang et al (1994a-c, 1995a-b, 1996b), Moon et al (2003), Wu (2003), Wu and Yang 2004], optimal polynomial control [Agrawal and Yang (1995, 1996)], fuzzy logic and artificial neural network [Wang (1994), Nagarajaiah (1994), Battaini et al (1999), Symans and Kelly (1999)], etc.

Semi-active control devices inherit the advantages of both active and passive control systems and thus are expected to provide stable, adjustable control with low power demand. Various theoretical and experimental research results have shown that appropriately implemented semi-active devices could perform significantly better than passive devices and have the potential to achieve the majority of the performance of fully active systems; which allows for the possibility of reliable response reduction during a wide array of dynamic loading conditions. A detailed literature review of these devices is presented in Spencer and Nagarajaiah (2003) and Symans and Constantinou (1999).

Extensive investigations are being directed towards semi-active control of base-isolated buildings, also known as “smart” base-isolation systems. The basic objectives in the seismic isolation of building structures are to protect structural integrity and to prevent injury to the occupants and damage to the contents [Skinner et al (1993), Kelly (1997), Naeim and Kelly (1999)]. Base isolation systems, such as sliding and elastomeric bearing systems, reduce the super-structure responses, but with increased base displacements during near-fault ground motions. Current practice is to provide non-linear passive dampers to limit the bearing displacements. However, protection of base isolated buildings from strong and long-period pulses during near-field ground motions is challenging. To address the need for high damping to limit the isolation drift and low damping to improve the isolation effectiveness at high frequencies, various types of semi-active systems have been proposed. Examples of some of these systems are Magneto-rheological dampers [Spencer et al (1996, 1997a)], Electro-Rheological dampers [Ehrgott and Masri (1993), Gavin et al (1996a-b)], controllable friction dampers [He et al (2003), Hirai et al (1996)], variable fluid dampers [Symans and Constantinou (1995, 1997a-b)], and variable stiffness dampers [Nagarajaiah and Mate (1998), Narasimhan and Nagarajaiah (2005)].

Applications of semi-active control systems to base-isolated structures have received widespread attention because of the vulnerability of these structures to long period, high velocity near-field ground motion pulses. Ramallo et al (2002) and Yoshioka et al (2002) have investigated the smart base-isolation structure using Magneto-Rheological dampers. Their results show that it is possible to design a smart base-isolation system that can reduce the base-drift, superstructure drift and absolute

accelerations of the base and the super-structures simultaneously. Zhang and Iwan (2002) have investigated the control of base-isolated building using tuned interaction damper. With this system, it is possible to reduce the displacement of base isolators. However, other response quantities always increase. Madden et al (2003) present experimental verification for an adaptive sliding base-isolation system using shaking table tests and demonstrated that it is possible to reduce the interstory drift and base displacement simultaneously. Gavin et al (2003) have investigated the fault-tolerant semi-active control of a base-isolated building for the presence of time-lag in the control device during the application of control force and eccentricity in the structure. Their research showed that the differential time-lag in the device has minimal effect on the performance of the semi-active controller. On the other hand, mass eccentricity causes increase in torsional moment and isolator drift.

Traditionally, seismic excitations are neglected or assumed to be white noises in the design of optimal active and semi-active control systems. Hence, optimality of these "optimal" controllers cannot be guaranteed in the presence of seismic excitations with dominant pulse behavior. Yang (1975) has suggested designing controllers based on the augmented system consisting of structure and filter in which the earthquake excitation is modeled as a filtered white noise process and applied this approach for the control of nonlinear hysteretic structures [Yang et al (1994a)]. Panariello et al (1997) have proposed "optimal" structural control via training of an ensemble of earthquake ground motions using neural network. Yoshioka et al (2002) have modeled the earthquake excitation as second-order filtered white-noise shaping filter. In this model, ground motion is the acceleration response of white noise passing through a second order

dynamic system. The transfer function for the input shaping filter is obtained by fitting the PSD of the recorded earthquake with that of a second order transfer function. Ramallo et al (2002) have used the Kanai-Tajimi shaping filter [Soong and Grigoriu (1993)] in modeling the ground excitation to obtain the structural-excitation augmented system for the controller design. Although the use of Kanai-Tajimi based filters in modeling input excitations may result in better controller performance compared to regular LQG controllers, these filters overestimate the energy in the low frequency range, which affects the response of long period structures. Thus, Kanai-Tajimi filter cannot accurately characterize the near-field ground motion pulses for an effective controller design.

In this chapter, design of active and semi-active controllers incorporating dynamic models of pulse-type ground motions is presented. The Laplace domain transfer function based on the pulse model, i.e., the pulse filter, was first proposed by He (2003). In the design of active and semi-active controllers, the transfer function is converted into state-space form and augmented with the structural system

6.2 ANALYTICAL MODEL OF THE PULSE FILTER

The analytical velocity pulse model proposed by He (2003) and He and Agrawal (2006) has been described in Chapter 3. For convenience, it is repeated in the following:

$$\dot{u}_p = Ct^n e^{-at} \sin bt \text{ , and } a = \zeta_p \omega_p,\ b = \omega_p \sqrt{1-\zeta_p^2} \tag{6.1}$$

where $\dot{\boldsymbol{u}}_{\boldsymbol{p}}$ is the pulse velocity, n is the shape parameter of the envelope, ζ_p is the pulse damping factor, ω_p is the pulse frequency and C is the scaling factor for adjusting the amplitude of the pulse. Differentiating Eq. (6.1), the pulse acceleration can be obtained as

$$\ddot{u}_p = Ct^n e^{-at}[(\frac{n}{t} - a)\sin bt + b\cos bt] \tag{6.2}$$

Through mathematical operations, the Laplace transform of the pulse model is obtained as [He (2003)]:

$$F(s) = \mathcal{L}[\ddot{u}_p(t)] = (-1)^n \cdot Cb \cdot s \cdot \left[\frac{1}{(s+a)^2 + b^2}\right]^{(n)} \tag{6.3}$$

For n = 0, 1, 2, 3, the explicit form of Eq. (6.3) can be expressed as:

$$\mathcal{L}[\ddot{u}_p(t)] = \frac{Cb \cdot s}{[(s+a)^2 + b^2]} \text{ for } n=0 \tag{6.4}$$

$$\mathcal{L}[\ddot{u}_p(t)] = \frac{2Cb \cdot (s+a)s}{[(s+a)^2 + b^2]^2} \text{ for } n=1 \tag{6.5}$$

$$\mathcal{L}[\ddot{u}_p(t)] = \frac{2Cb \cdot [3(s+a)^2 - b^2]s}{[(s+a)^2 + b^2]^3} \text{ for } n=2 \tag{6.6}$$

$$\mathcal{L}[\ddot{u}_p(t)] = \frac{24Cb \cdot (a+s) \cdot (a^2 - b^2 + 2as + s^2]s}{[(s+a)^2 + b^2]^4} \text{ for } n=3 \tag{6.7}$$

The model parameters, T_p, ζ_p, and n in Eq. (6.1), are determined for a particular ground motion by nonlinear regression [He (2003)]. Difference and similarity between recorded near-field ground motions and their pulse-type components have been investigated in Chapter 3.

As mentioned earlier, several researchers have used the Kanai-Tajimi filter to model external excitations. The commonly used form of the Kanai-Tajimi filter is given as,

$$F(s) = \frac{2\omega_g \zeta_g s + \omega_g^2}{\omega_g^2 + 2\zeta_g \omega_g s + s^2} \tag{6.8}$$

where ω_g and ζ_g are ground motion frequency and ground damping factor, respectively.

Fig. 6.1 shows Power Spectral Density (PSD) plots of the pulse filter in Eqs. (6.5) and (6.7) for n = 1 and 3 respectively, Kanai-Tajimi filter in Eq. (6.8), and recorded ground motions RRS228 (Northridge 1999) and ERZ-NS (Turkey, 1992). Parameters of various filters described above are obtained for the two ground motions. It is observed that the Kanai-Tajimi filter has much higher Power Spectral Density (PSD) than those of recorded ground motions in lower frequency range where pulse behavior is dominant. On the other hand, the pulse filter can better represent the recorded ground motion character in this region. In higher frequency region, the PSD of the pulse filter having n=1 is much closer to that of the recorded excitation in both cases.

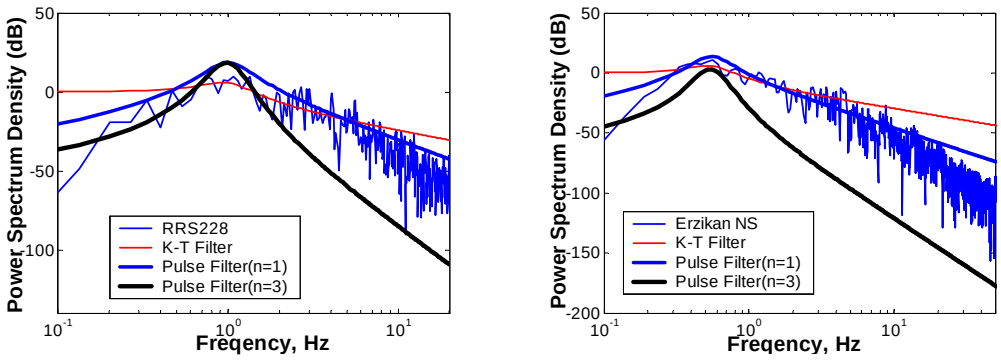

Figure 6.1: Power Spectral Density (PSD) plots of Kanai-Tajimi filter and the proposed pulse filter with n = 1 and n = 3 for 1994 Northridge (RRS228) and 1992 Turkey (NS component of Erzikan) earthquake.

6.3 DESIGN OF ACTIVE CONTROLLERS

The equation of motion for an N degree-of-freedom system equipped with active controllers and subjected to unidirectional ground motion can be written as

$$\boldsymbol{M}\ddot{\boldsymbol{x}} + \boldsymbol{C}\dot{\boldsymbol{x}} + \boldsymbol{K}\boldsymbol{x} = \boldsymbol{H}\boldsymbol{u} - \boldsymbol{M}\boldsymbol{\eta}\ddot{x}_g \tag{6.9}$$

where $\boldsymbol{M}$, $\boldsymbol{C}$ and $\boldsymbol{K}$ are ($\boldsymbol{N} \times \boldsymbol{N}$) mass, damping and stiffness matrices of the structure, respectively; $\boldsymbol{u}$ is ($\boldsymbol{r} \times 1$) control force vector, $\boldsymbol{r}$ being the number of controllers, $\boldsymbol{x}$, $\dot{\boldsymbol{x}}$ and $\ddot{\boldsymbol{x}}$ are the displacement, velocity and acceleration vectors, respectively, $\ddot{x}_g$ is the earthquake acceleration, $\boldsymbol{H}$ is ($\boldsymbol{N} \times \boldsymbol{r}$) controller location matrix and $\boldsymbol{\eta}$ is the earthquake influence vector. Eq. (6.9) can be rewritten in state-space form as

$$\dot{\boldsymbol{X}} = \boldsymbol{A}\boldsymbol{X} + \boldsymbol{B}\boldsymbol{u} + \boldsymbol{E}\ddot{x}_g \tag{6.10}$$

where $\boldsymbol{X}=[\,\boldsymbol{x}^{T}\ \dot{\boldsymbol{x}}^{T}]^{T}$ is the state vector, and $\boldsymbol{A}$, $\boldsymbol{B}$ and $\boldsymbol{E}$ are the coefficient matrices obtained as

$$\boldsymbol{A} = \begin{bmatrix} \boldsymbol{0} & \boldsymbol{I} \\ -\boldsymbol{M}^{-1}\boldsymbol{K} & -\boldsymbol{M}^{-1}\boldsymbol{C} \end{bmatrix}; \boldsymbol{B} = \begin{bmatrix} \boldsymbol{0} \\ \boldsymbol{M}^{-1}\boldsymbol{H} \end{bmatrix}; \ \mathbf{E} = \begin{bmatrix} \boldsymbol{0} \\ -\boldsymbol{\eta} \end{bmatrix} \tag{6.11}$$

For the purpose of controller design, input excitation is modeled as filtered white noise. Assuming that the ground motion $\ddot{x}_g$ in Eq. (6.10) is modeled by the pulse acceleration in Eq. (6.2), transfer function in Eq. (6.4) – (6.7) for a particular value of *n* can be converted to the state-space as

$$\begin{cases} \dot{\boldsymbol{\xi}} = \boldsymbol{A}_w\boldsymbol{\xi} + \boldsymbol{B}_w\boldsymbol{w} \\ \ddot{x}_g = \boldsymbol{C}_w\boldsymbol{\xi} \end{cases} \tag{6.12}$$

where $\boldsymbol{w}$ is scalar white noise excitation. Coefficient matrices, $\boldsymbol{A}_w$, $\boldsymbol{B}_w$ and $\boldsymbol{C}_w$ depend on the order and form of the transfer function used, e.g., Eq. (6.4) - (6.7).

Combining Eq. (6.10) and (6.12), the augmented system is expressed as

$$\begin{bmatrix} \dot{\boldsymbol{X}} \\ \dot{\boldsymbol{\xi}} \end{bmatrix} = \begin{bmatrix} \boldsymbol{A} & \boldsymbol{E}\boldsymbol{C}_w \\ \boldsymbol{0} & \boldsymbol{A}_w \end{bmatrix} \begin{bmatrix} \boldsymbol{X} \\ \boldsymbol{\xi} \end{bmatrix} + \begin{bmatrix} \boldsymbol{B} \\ \boldsymbol{0} \end{bmatrix} \boldsymbol{u} + \begin{bmatrix} \boldsymbol{0} \\ \boldsymbol{B}_w \end{bmatrix} \boldsymbol{w} \tag{6.13}$$

Denoting $\boldsymbol{X}_a=[\boldsymbol{X}^{T}\ \boldsymbol{\xi}^{T}]^{T}$ as the augmented state vector, Eq. (6.13) can be rewritten as

$$\dot{\boldsymbol{X}}_a = \boldsymbol{A}_a\boldsymbol{X}_a + \boldsymbol{B}_a\boldsymbol{u} + \boldsymbol{E}_a\boldsymbol{w} \tag{6.14}$$

The measured outputs of the control system are expressed as

$$\boldsymbol{Y}_a = \boldsymbol{C}_y \boldsymbol{X}_a + \boldsymbol{D}_y \boldsymbol{u} + \boldsymbol{F}_y \ddot{\boldsymbol{x}}_g + \boldsymbol{v} \tag{6.15}$$

where $\boldsymbol{C}_y$, $\boldsymbol{D}_y$ and $\boldsymbol{F}_y$ are appropriate matrices, and $\boldsymbol{v}$ is the measurement noise. For the base-isolated SDOF structural model employed in this investigation, the measured outputs are the displacement of base isolator, absolute accelerations of base isolator and superstructure, and ground acceleration. For the system in Eq. (6.14), the outputs to be regulated can be expressed as

$$\boldsymbol{Z}_a = \boldsymbol{C}_z \boldsymbol{X}_a + \boldsymbol{D}_z \boldsymbol{u} + \boldsymbol{F}_z \ddot{x}_g \tag{6.16}$$

where $\boldsymbol{C}_z$, $\boldsymbol{D}_z$ and $\boldsymbol{F}_z$ are appropriate matrices. In this paper, regulated outputs are the displacement of base isolator, relative displacement of super-structure with respect to base isolator, and absolute accelerations of base isolator and super-structure.

The augmented system in Eq. (6.14)-(6.16) can be used to design active controllers using any of the modern control approaches, e.g., Linear Quadratic Gaussian (LQG), Sliding Mode Control (SMC), etc. In this investigation, an optimal controller for the augmented system in Eq. (6.14) – (6.16) is designed by minimizing the following performance index using the H_2/LQG strategy

$$\boldsymbol{J} = \lim_{\tau \to \infty} \frac{1}{\tau} \boldsymbol{E}\left[\int_0^{\tau} \left\{ \boldsymbol{Z}^T \boldsymbol{Q} \boldsymbol{Z} + \boldsymbol{u}^T \boldsymbol{R} \boldsymbol{u} \right\} dt \right] \tag{6.17}$$

where $\boldsymbol{Q}$ and $\boldsymbol{R}$ are weighting matrices for regulated outputs and control forces, respectively. Minimization of the performance index $\boldsymbol{J}$ in Eq.(6.17) results in the optimal control force as

$$\boldsymbol{u} = -\boldsymbol{K} \boldsymbol{X}_a \tag{6.18}$$

where $\boldsymbol{K}$ is the control gain matrix. The augmented state vector $\boldsymbol{X_a}$ is estimated as $\hat{\boldsymbol{X}}_a$ through the Kalman-Bucy filter, given as

$$\dot{\hat{\boldsymbol{X}}}_a = (\boldsymbol{A}_a - \boldsymbol{L}\boldsymbol{C}_y)\hat{\boldsymbol{X}}_a + (\boldsymbol{B}_a - \boldsymbol{L}\boldsymbol{D}_y)\boldsymbol{u} + \boldsymbol{L}\boldsymbol{Y} \tag{6.19}$$

where $\boldsymbol{L}$ is the observer gain matrix. Schematic of the active controller design is presented in Fig. 6.2.

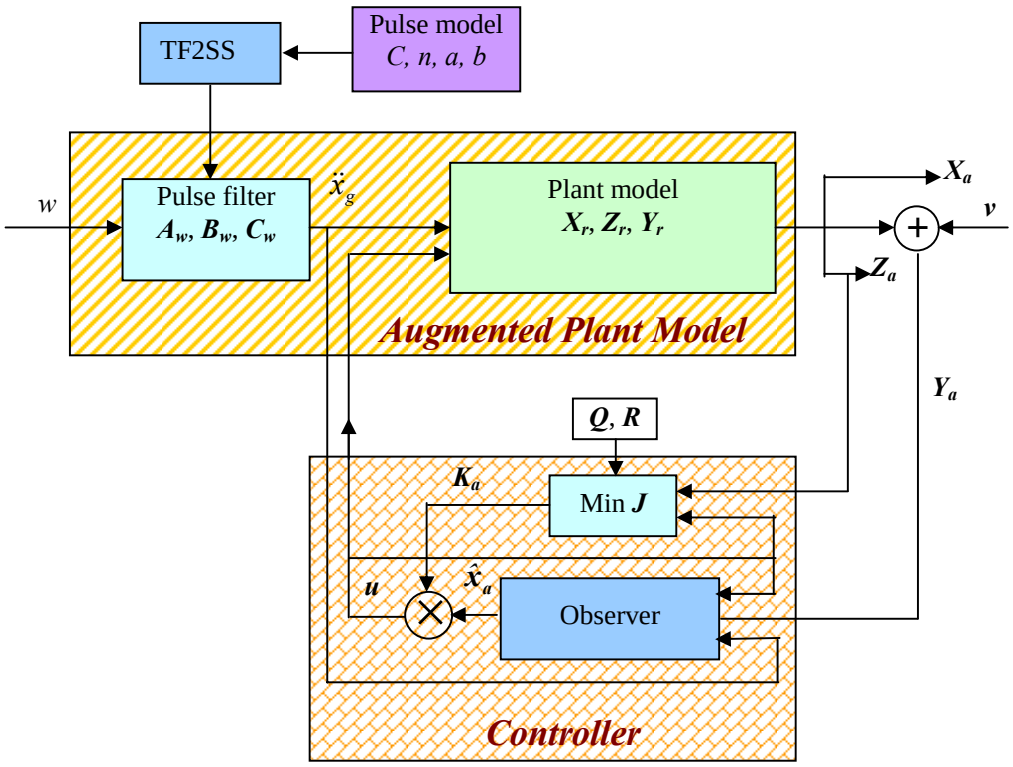

Figure 6.2 Schematic of the active pulse controller design using H2/LQG algorithm

6.4 DESIGN OF SEMI-ACTIVE CONTROLLERS

Both passive and semi-active friction dampers have been demonstrated to be effective in reducing peak response quantities during near-fault earthquakes. Inaudi (1997)

proposed Modulated Homogeneous Friction (MHF) controller for semi-active friction dampers. In this controller, the control force is directly proportional to the absolute value of the previous peak of the drift across the damper. However, the potential problem with this controller is that it doesn't guarantee continuous slip in the damper due to sticking and slipping phases, depending on the state and force across the damper. The performance of MHF can be improved by maintaining the damper in slipping phase continuously, since energy is dissipated in the slipping phase rather than in the sticking phase. He et al (2003) proposed modified form of MHF by introducing smooth boundary layer around zero velocity across the damper, i.e., $\dot{x}_i(t) = 0$, to eliminate high acceleration spikes caused by rapid switching during the operation of the friction damper. In this investigation, a semi-active controller is proposed by introducing the smooth boundary layer around the optimal feedback controller in Eq. (6.18). The semi-active controller obtained is then denoted as Semi-Active Continuous Friction Pulse (SACPF) Controller, expressed as,

$$f_{semi\_active} = -\mu g \left| \boldsymbol{K}\hat{\boldsymbol{X}}_{\boldsymbol{a}} \right| tanh(\alpha \dot{x}) \tag{6.20}$$

where μ is the friction coefficient and g is the control gain, α is a constant that determines the "thickness" of the boundary layer and $tanh(\alpha \dot{x})$ is a hyperbolic function. In this investigation, the magnitude of the control force is kept the same as that for the active controller, i.e., $\mu g = 1$. The parameter α is taken as 1 based on a parametric study.

6.5 GROUND EXCITATIONS AND STRUCTURAL MODEL

Active and semi-active controllers in Eqs. (6.18) - (6.20) are investigated through numerical simulation using 24 recorded near-field ground motions. Details of these

earthquakes are listed in Table 1 of the appendix. In addition, four earthquakes with full intensity are considered to investigate the sensitivity of response quantities to variations in filter parameters. These 4 earthquakes are: the 1940 El Centro earthquake recorded at Array #9 (PGA = 0.348g, T_g =1s); the North-South component of the 1992 Turkey earthquake recorded at Erzikan (PGA = 0.515g, T_g =1.8s); the 1995 Kobe earthquake recorded at Takatori000 (PGA = 0.611g, T_g =1.2s) and the fault-normal component of the 1994 Northridge earthquake recorded at Rinaldi 228 station (PGA = 0.838g, T_g =1.0s). The far-field El Centro earthquake record is included with other three near-field earthquakes for the sake of comparison. The parameter T_g is the pulse period in recorded ground motions.

The building model used in this study is a single degree of freedom (SDOF) system with a base isolation layer investigated by Ramallo et al (2002). The SDOF system represents the fundamental mode of the 5-story building model used by Kelly et al (1987). Schematic of the base-isolated model is presented in Fig. 6.3

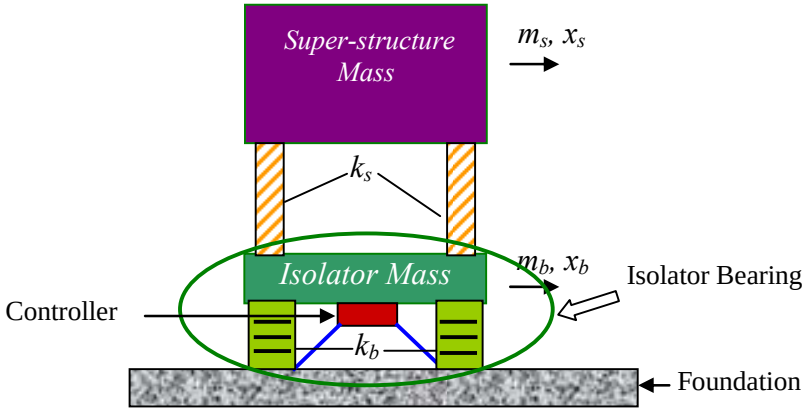

Figure 6.3 Schematic of the base-isolated model with controller

.The combined SDOF super-structure and base-isolation system is modeled as a 2-DOF system. The mass, stiffness and damping coefficient of the base isolator and the super-structure are: m_b = 6800 kg, m_s = 29485 kg; k_b=232kN/m, k_s = 11912kN/m; c_b = 3.7 kN.s/m, c_s = 23.71 kN.s/m, respectively. The fundamental period and damping ratio of the fixed-base building are 0.3 sec and 2%, respectively. With base-isolation, the fundamental periods and damping ratio are calculated to be 2.5s and 4%, respectively [Ramallo et al (2002)].

6.6 PERFORMANCE OF VARIOUS CONTROLLERS USING 4 RECORDED EARTHQUAKES

Fig. 6.4 shows plots of peak response quantities of the base-isolated building with different types of controllers as a function of control force for the four earthquakes mentioned above. The peak response quantities are base displacement, superstructure drift, and absolute base and superstructure accelerations. In Fig. 6.4, plots in rows (a)-(d) are for the El Centro (1940), Turkey (1992), Kobe (1995) and Northridge Rinaldi (1994), respectively. Six controllers representing passive, active and semi-active mechanisms are considered for comparison purpose in this investigation. They are: (i) Linear Viscous Damper (LVD, control force $u(t) = c_d \dot{x}_b(t)$, where c_d is the damper coefficient and $\dot{x}_b(t)$ is the base velocity), in which the control force is varied by varying c_d; (ii) Linear Quadratic Regulator (LQR) designed by using 2x2 Q matrix with non-zero elements as $Q(1,1) = 2\times10^6$ and $Q(2,2) = 2\times10^7$ and full-state measurement; (iii) Linear Quadratic Gaussian (LQG): LQG controller implemented by the observer in Eq. (6.19); (iv) Active Kanai-Tajimi Filter (AKTF) controller: active controller in Eq. (6.18) incorporating state-

space form of Kanai-Tajimi filter; (v) Active Pulse Filter (APF) controller: controller in Eq. (6.18) by assuming n = 1 for pulse model in Eq. (6.3). The non-zero elements of the 4×4 Q matrix are: $Q(1,1) = 2\times10^{6}$ and $Q(2,2)= 2\times10^{7}$. The weighting R is varied to obtain desired control force level; (vi) Semi-Active Continuous Pulse Friction (SACPF) controller as described by Eq. (6.20). It is observed from Fig. 6.4 that although all six controllers are capable of reducing peak base displacement (or drift of isolators), other response quantities such as peak drift of the superstructure, peak base absolute acceleration and peak super-structure absolute acceleration decrease slightly in the beginning and then starts increasing beyond certain control force level for all controllers. However, for APF and SACPF controllers, the reductions in above three quantities are substantially larger than other controllers. Response quantities corresponding to the APF controller are even much smaller than those of the SACPF controller.

The plots in Fig. 6.4 demonstrate that the APF and SACPF controllers are capable of reducing both the peak displacement and acceleration response quantities of the base isolator and the superstructure simultaneously and significantly. This is a distinct advantage of the proposed active and semi-active controllers designed for the augmented system using the pulse filter. It is also observed from Fig. 6.4 that, by incorporating the pulse filter, the active controller based on the augmented system is also effective in reducing the response quantities for far-field earthquakes (e.g., El Centro earthquake), although such ground motions do not have distinct velocity pulses.

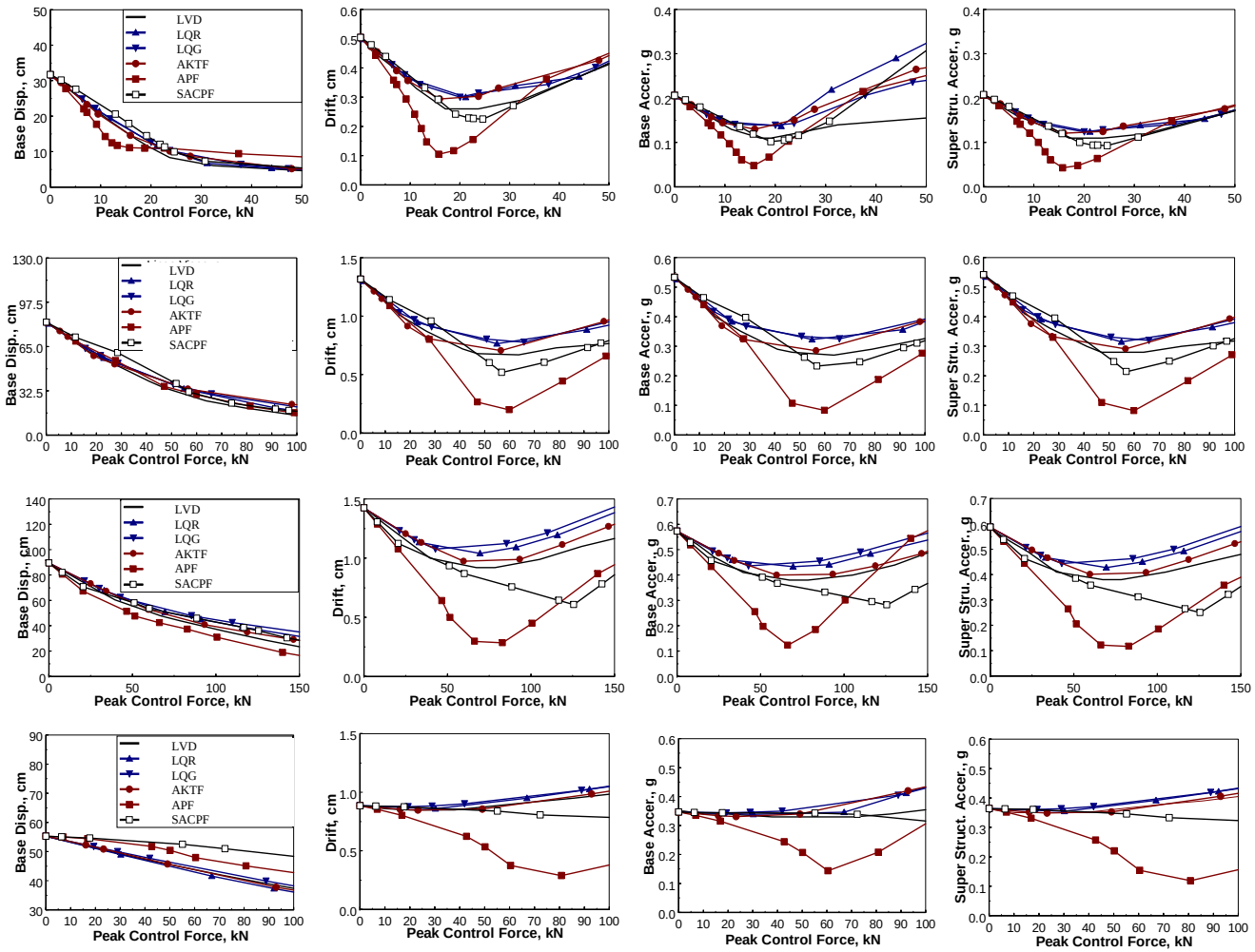

Figure 6.4: Peak response quantities using active and semi-active controllers subjected to (from Top): El Centro (1940); Turkey (1992); Kobe (1995) and Northridge (1994) earthquake.

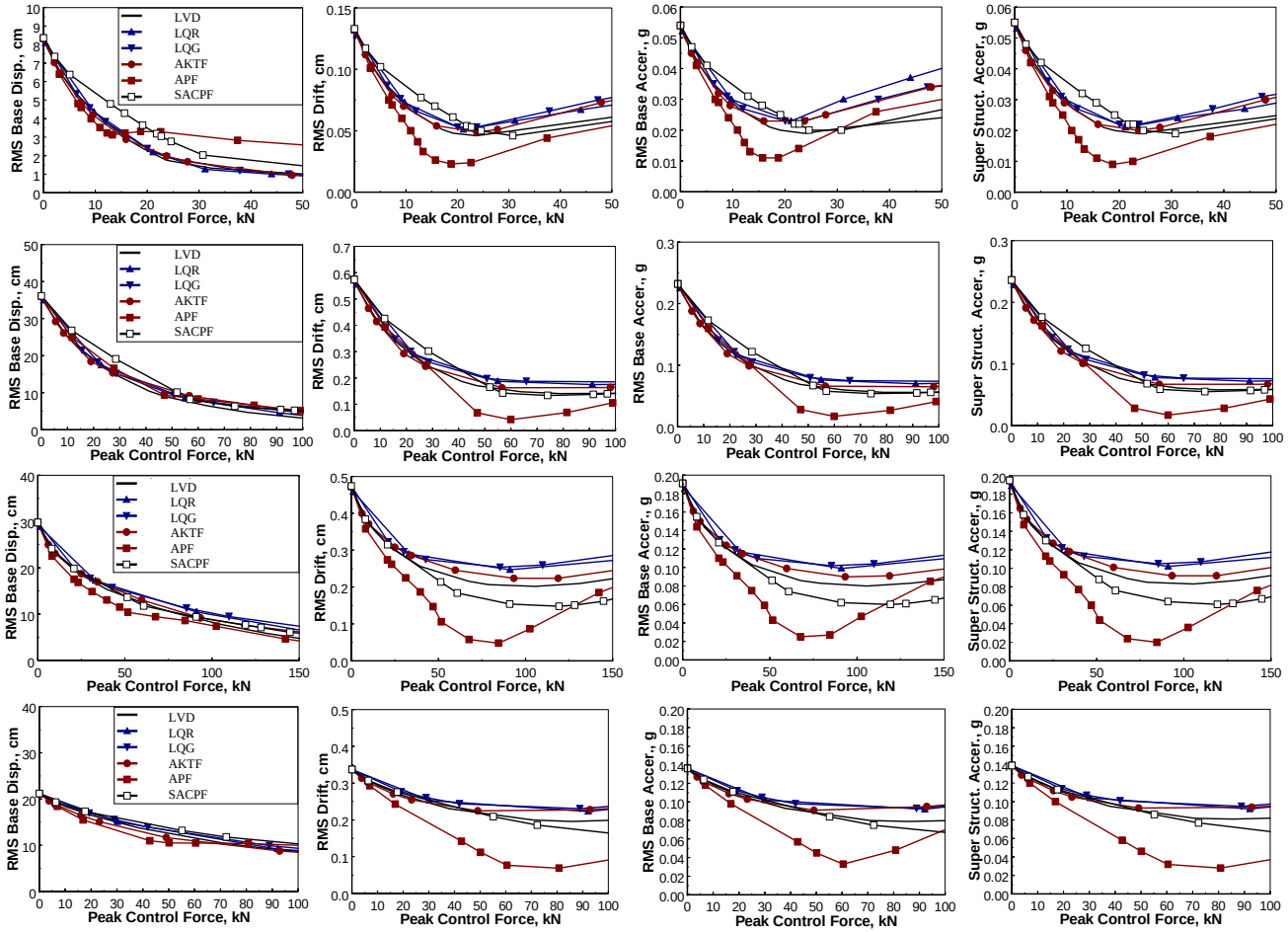

Figure 6.5: RMS response quantities using active and semi-active controllers subjected to (from top): El Centro (1940); Turkey (1992); Kobe (1995) and Northridge (1994) earthquake.

Fig. 6.5 shows the plots of RMS response quantities for the four earthquakes. The relative effectiveness of all controllers in reducing RMS response quantities is similar to those of peak response quantities in Fig. 6.4. It is noted again that the overall performance of APF is significantly better than other controllers. The overall performance of the SACPF controller is inferior to APF and is slightly better than other controllers.

6.7 ROBUSTNESS OF THE APF CONTROLLER

The objective of incorporating the pulse filter in the design of controller is to include the influence of ground excitation characteristics, such as the frequency content, ground damping factor, and the magnitude. Due to the uncertainty and stochastic nature of ground motions, parameters of the pulse model are not known as *a priori*. However, it is possible to estimate these parameters based on available ground motion records, soil and rock conditions [Sommerville (1998)]. Since the design of active controllers in Eq. (6.18) depends on preset model parameters, the performance sensitivity of the APF controller with respect to the pulse filter parameters T_p (pulse period), ξ_p (damping factor) and n (filter order) is investigated in this section.

6.7.1 Influence of Pulse Period, T_p

Several recent studies have shown that the pulse period is the most important parameter affecting the response of structures [He and Agrawal (2004a, b), Mavroeidis et al (2004)]. Using near-fault records that exhibit forward directivity effect and assuming that the duration of the pulse is independent of the source-station distance for stations

located within 10 km from the causative fault, Mavroeidis et al (2004) have shown that the pulse period, T_p, varies as a function of moment magnitude M_w as

$$\log T_p = -2.9 + 0.5M_w \tag{6.21}$$

Although T_p can be estimated from Eq. (6.21) for a design earthquake magnitude, the estimated value is likely to be significantly different than the actual value during an earthquake. Hence, error analysis needs to be carried out to obtain reasonable limits on the variation of the estimated T_p .

The sensitivity of APF controller to the variation of period, T_p, of the pulse filter is investigated by decreasing and increasing T_p with respect to the actual pulse period, T_g, of the recorded ground motion. The influence of T_p on the shape of the pulse history can be found in Fig. 3.1 of Chapter 3.

In the investigation of the controller sensitivity to the pulse period, T_p, the magnitude of the filter is first chosen by trial-and-error for $T_p = T_g$ to obtain a reasonable control gain matrix. Then, the filter magnitude is adjusted at different pulse periods by keeping the maximum instantaneous kinetic energy of the pulse excitation at any pulse period, T_{pi}, the same as that at T_g , i.e.,

$$Coe(T_{pi}) = \frac{max[E_k(T_{pi},t)]}{max[E_k(T_g,t)]} Coe(T_g) \tag{6.22}$$

In Eq.(6.22), T_{pi} is the pulse period used in filter design, T_g is period of the pulse in the recorded earthquake ground motion, t is the duration of the pulse model, $E_k(...,t)$ is the instantaneous kinetic energy, and $Coe(T_g)$ is the magnitude of the filter at T_g, which equals to a constant C divided by the corresponding design frequency, i.e.,

$$Coe(T_g) = C/\omega_g \tag{6.23}$$

In Eq. (6.23), the constant C is appropriately chosen to obtain reasonable control performance for $T_p = T_g$, which may be different for different earthquakes. Based on simulation results, it is noted that usually a C value between (50-100)ω_g is a suitable choice for most of the earthquakes investigated. It needs to be pointed out that the filter magnitude is manipulated according to Eq. (6.22) only to study the sensitivity of variation in T_p. It is noted that for a known T_p, a better control effectiveness can also be realized by carefully adjusting the magnitude. The damping factor, ζ_p, and the order of the filter, n, are chosen as 0.15 and 1, respectively, in investigating the influence of T_p.

Fig. 6.6 shows the response quantities of the controlled structure subjected to the El Centro (1940), Turkey (1992), Kobe (1995) and Northridge (1994) earthquakes. The actual pulse periods, T_g, for these earthquakes are 1.0s, 1.8, 1.2s, and 1.0s, respectively. In numerical simulations, controller design is carried out for each pulse period, T_{pi}, for individual earthquakes. In Fig. 6.6, curves corresponding to $T_p = T_g$ are shown by solid lines without symbols.

It is observed from Fig. 6.6 that the base displacement does not change significantly with variations in T_p when it is under-estimated or over-estimated by approximately 20%, for all the four earthquakes. However, if T_p is over-estimated beyond 20%, the base displacement becomes quite sensitive to variations in T_p. For example, the base displacement for Turkey earthquake (T_g = 1.8 sec) doesn't change even if the T_g is under-estimated as 1.0s or over-estimated as 2.2s. However, it increases significantly compared to that for T_p = 1.8 s if T_p is over-estimated as 2.6 sec. For inter-story drift and absolute accelerations of the base and the superstructure, the controller is robust if the T_p is not over-estimated more than 20% for a control force level of

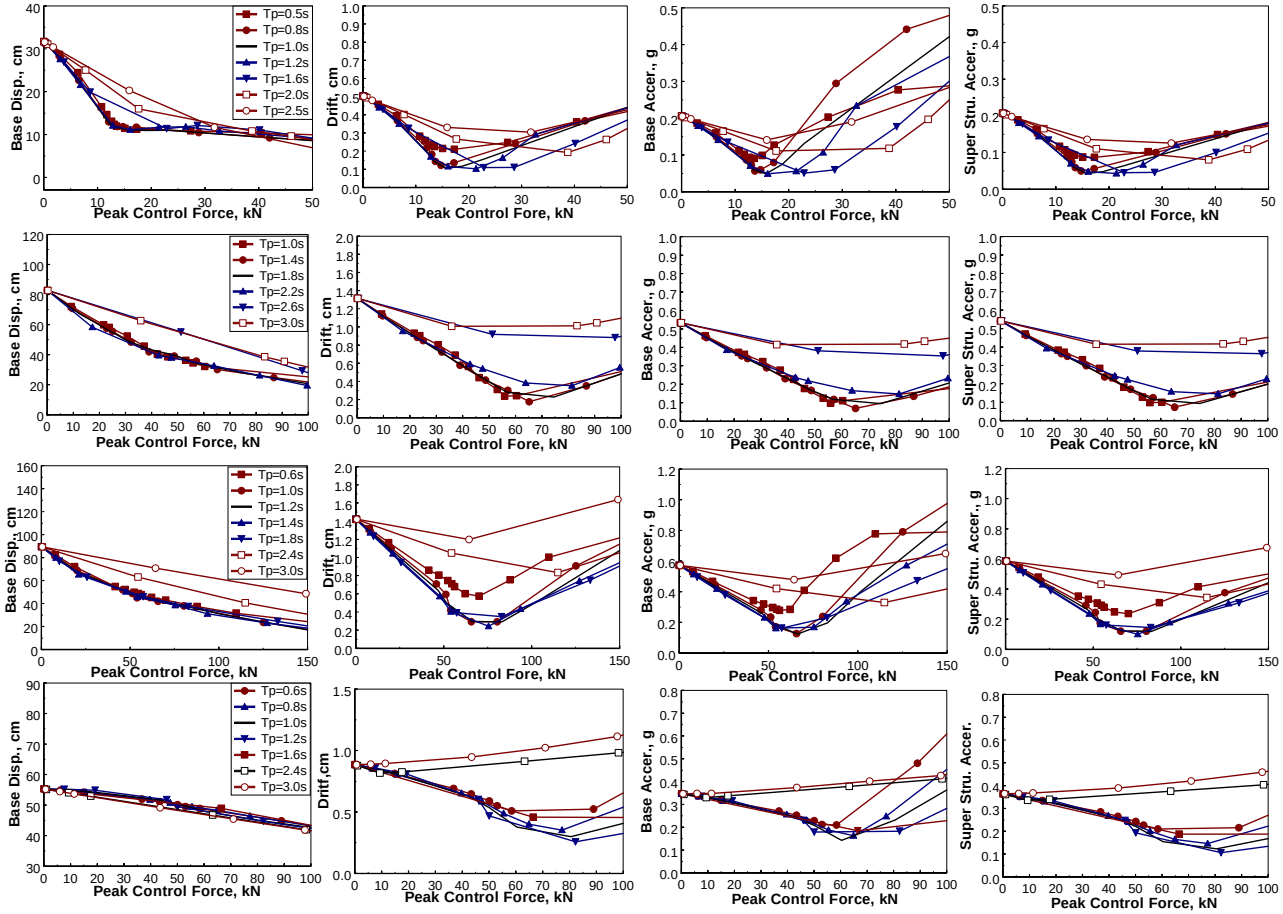

Figure 6.6: Influence of pulse period, T_p, on the performance of Active Pulse Filter (APF) controller subjected to (from Top): El Centro (1940); Turkey (1992); Kobe (1995) and Northridge (1994) earthquake.

approximately 20% of the corresponding peak ground excitation force (inertia force, $m\ddot{x}_g$) during these earthquakes. For higher control forces, these quantities increase. For practical applications, a control force of 20% maximum peak inertia force during an earthquake is already very high. Hence, the proposed Active Pulse Filter (APF) controller is robust with respect to uncertainties in the pulse period, if the pulse period is underestimated or overestimated by up to 20 % within practical range of control force.

6.7.2 Influence of the Damping Factor, ζ_p

The influence of the damping factor is investigated by varying the value of ζ_p in the filter model. Fig. 6.7 shows the plots of different response quantities as a function of control force for ζ_p =0.15, 0.35, 0.55 and 0.85. The magnitude and the period of the pulse for each earthquake are kept constant during the analysis. The design pulse period, T_p, is taken to be equal to actual pulse period, T_g, for each earthquake and the magnitude C is chosen according to Eq. (6.22) and (6.23). The order of filter, n is chosen as 1.

It is observed from Fig. 6.7 that the base displacement response doesn't change significantly for ζ_p = 0.15, 0.35 and 0.55. For a peak control force less than 20% of the peak inertia force during each earthquake, the influence of ζ_p is insignificant on all quantities. More reduction in the base displacement is achieved as ζ_p increases from 0.15 to 0.55. For inter-story drift and absolute accelerations of the base and the superstructure, lower value of ζ_p results in better reduction in these quantities. In this sense, ζ_p of the pulse model has similar effect as the supplemental damping for base-isolators. Overall, it is observed that a ζ_p between 0.15 and 0.35 is reasonable for reduction in all the response quantities.

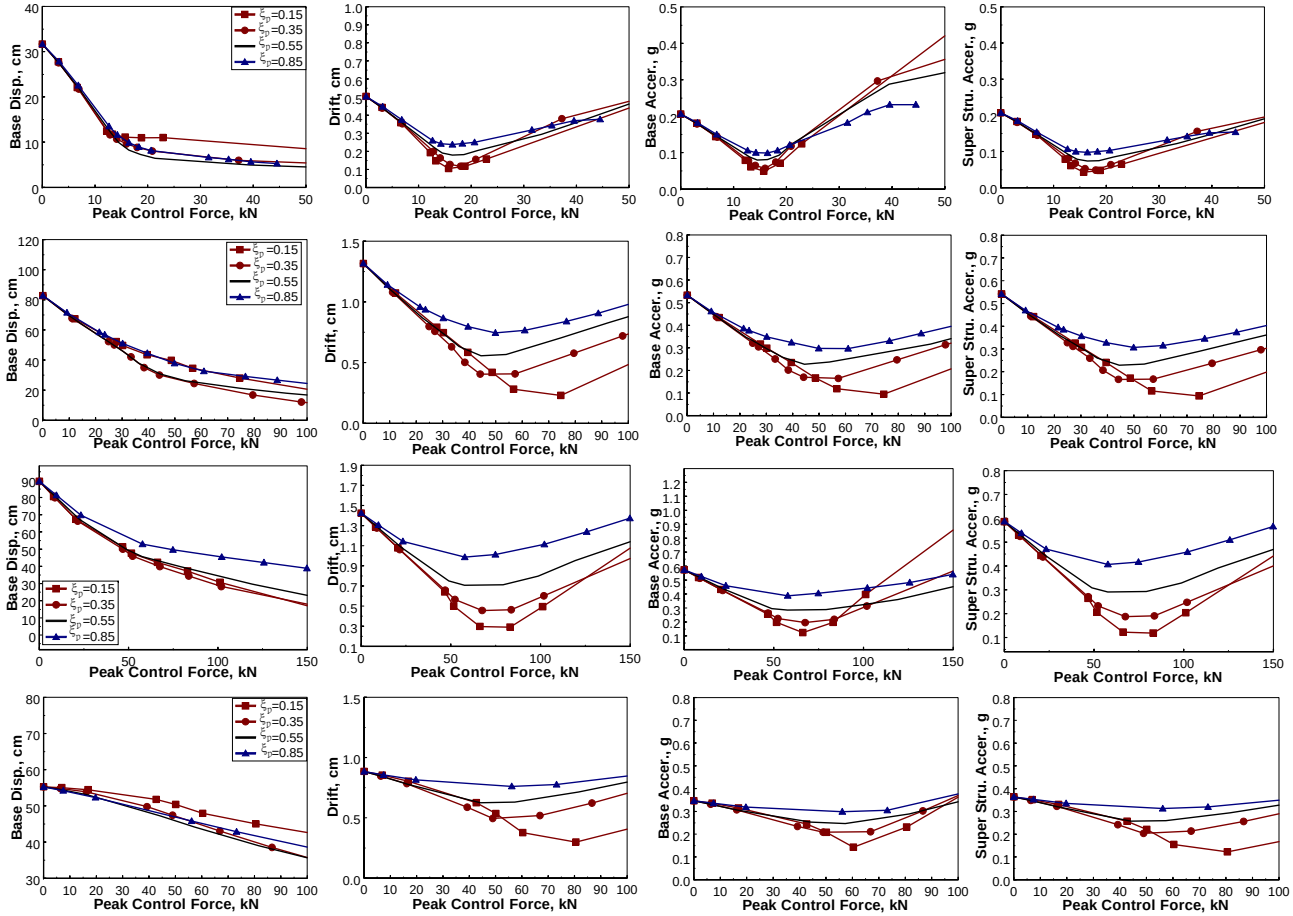

Figure 6.7: Influence of ground damping factor, ζ_p, on the performance of Active Pulse Filter (APF) Controller subjected to (from Top): El Centro (1940); Turkey (1992); Kobe (1995) and Northridge (1994) Earthquake.

6.7.3 Influence of the Order of the Filter, *n*

In the pulse model, *n* is an important parameter that affects the rate of increase in the beginning of the pulse and the shape of pulse. As an example, time-history plots of displacement, velocity and acceleration pulses for *n*=0, 1, 2 and 3, have been presented in Fig. 3.3 of Chapter 3.

Fig. 6.8 shows the plots of peak response quantities as a function of control force for different values of *n* using the four earthquakes. The design pulse period is taken as 1.5 sec for all the four earthquakes and the pulse damping factor, ζ_p is taken as 0.30 for simplicity. It is observed from Fig. 6.8 that the maximum reduction in base displacement is obtained for $n = 0$, and base displacement increases slightly for higher values of *n*, except for the case of Kobe earthquake, of which the base displacement is reduced most for $n = 3$. Difference in base displacement for different values of *n* is very small for control force up to 20% of the peak inertia force of the building during these earthquakes. For all these earthquakes, the peak base displacement always decreases as the increase of peak control force. Likewise, drift and accelerations of the base and superstructure decrease and are also insensitive to variations in *n* when the control force is less than 20% of the peak inertia force.

Hence, for control force less than 20% of the peak inertia force, any value of *n* is acceptable. And a larger value of *n* can be selected for overall best performance if super-structure drift and accelerations are more concerned.

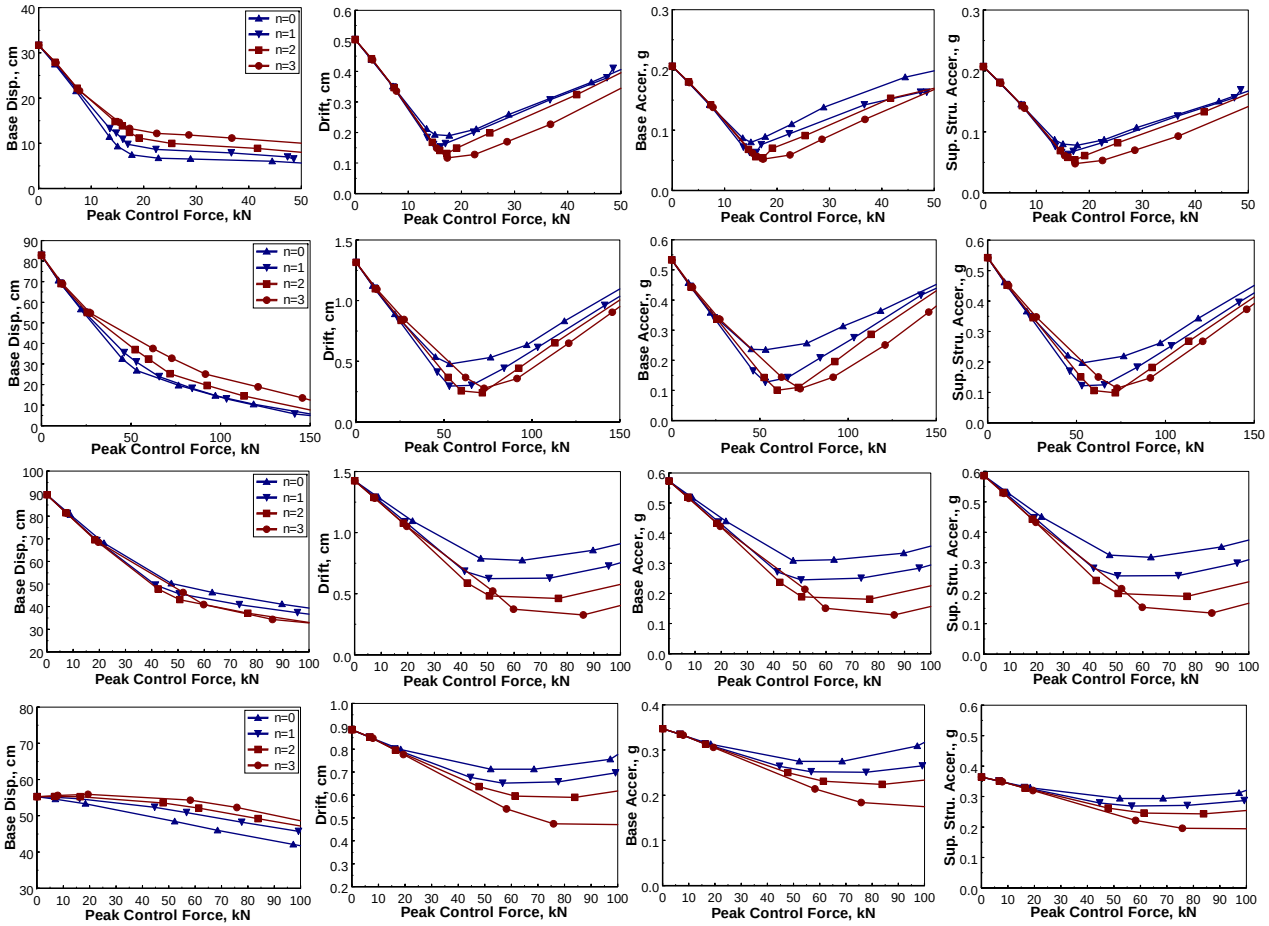

Figure 6.8: Influence of pulse shape factor, *n*, on the performance of Active Pulse Filter (APF) controller subjected to (from Top): El Centro (1940); Turkey (1992); Kobe (1995) and Northridge (1994) Earthquake.

6.8 PERFORMANCE EVALUATION USING 24 RECORDED NEAR-FIELD EARTHQUAKES

An ensemble of 24 recorded near-field ground motions is used to compare the average performance of the proposed APF and SACPF controllers with other control strategies. The detailed information of these records is presented in Table A-2 of the appendix. The properties of these earthquakes are quite different. Hence, the average results of these controllers can represent the general efficiency of these controllers during near-field excitations. For the sake of simplicity, the period and the damping factor, of the filter are taken as 1.5 sec and 0.3, respectively. The order of the pulse filter is taken as 1. The magnitude of the filter is chosen for different earthquakes in order to obtain reasonable control force level. The frequency and damping factor, of the Kanai-Tajimi filter are taken to be the same as the pulse filter, i.e., T_g=1.5 s and ξ_g =0.3.

Fig. 6.9 shows the average peak response reduction factors of the controlled model using Linear Viscous Damper (LVD), LQR, LQG, Active Kanai-Tajimi Filter (AKTF) controller, Active Pulse Filter (APF) controller and Semi-Active Continuous Pulse Friction (SAPF) controller. It is observed from Fig. 6.9 that the proposed APF controller has much better overall performance than other controllers in simultaneously reducing these response quantities. Although the efficiency in reducing the peak base displacement response is similar for all these controllers, the proposed APF controller can achieve 20~30% more reduction than other controllers in terms of superstructure drift, and absolute accelerations of the base and the superstructure. The performance of the SACPF controller is similar to the Linear Viscous Damper. However, it is interesting to see that these two controllers are even more effective than the LQR, LQG and AKTF controllers

in terms of achieving larger amount of response reductions with similar control force levels, even though these three controllers are fully active systems. These three active controllers have a similar average effectiveness regardless of the AKTF is designed using an augmented system. This indicates that design of active controllers by incorporating earthquake excitations as white noise modeled by the Kanai-Tajimi filter is not effective for near-field earthquakes.

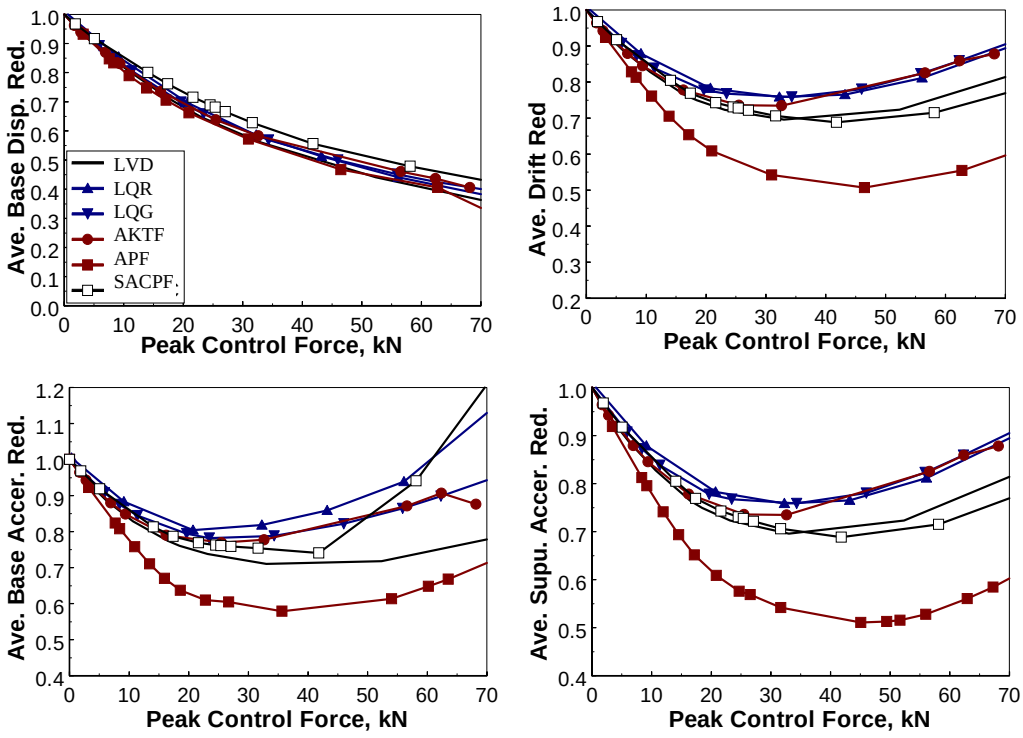

Figure 6.9: Average reduction of peak response quantities by various controllers subjected to the 24 near-field earthquakes.

Fig. 6.10 shows the average RMS response quantities of different controllers using the 24 near-field earthquakes. Similar to the peak response quantities, the RMS response quantities are also normalized by the corresponding uncontrolled RMS responses for each earthquake. It is observed that the APF controller is much better than other approaches in

the reducing all four RMS response quantities. The active controllers, i.e., LQR, LQG, AKTF and APF, are slightly better than the SACPF controller and the LVD in reducing the RMS base displacement. However, the SACPF controller and the LVD could exert larger control force without causing the increase in other RMS quantities compared to the LQR, LQG and AKTF, which is similar to the peak control results.

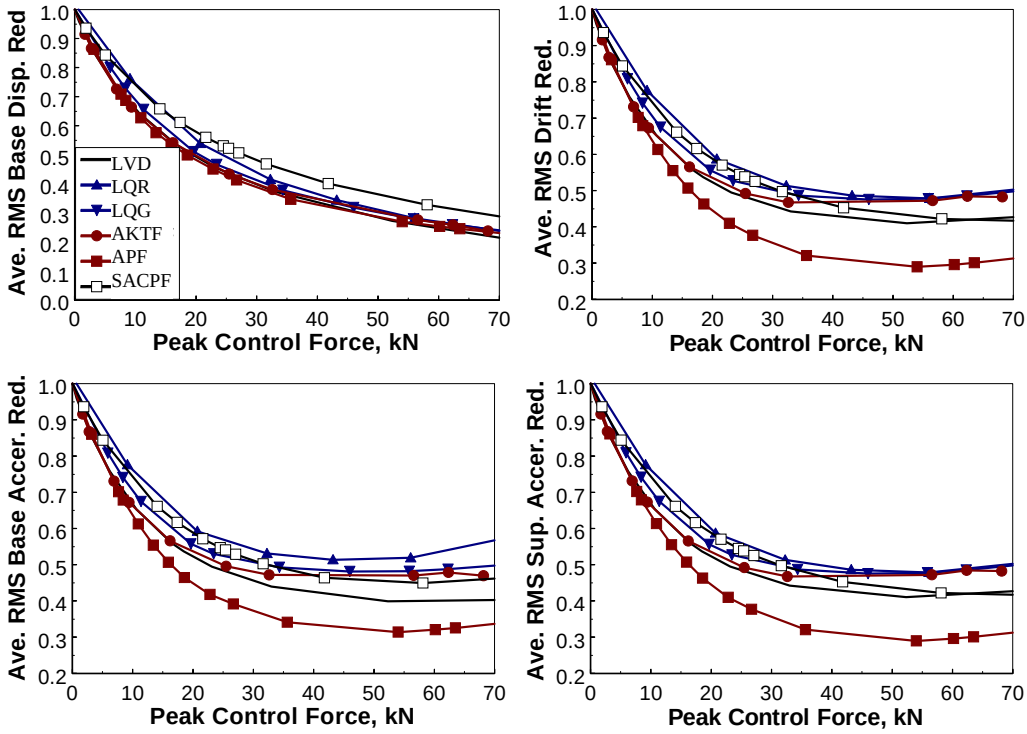

Figure 6.10: Average reduction of RMS response quantities by various controllers subjected to the 24 near-field earthquakes.

Fig. 6.11 shows time-history plots of base displacement, superstructure drift and absolute accelerations of the base and the superstructure for the structure subjected to the Kobe earthquake. Plots in Fig. 6.11 correspond to the peak control force of 60 kN in Fig. 6.9. It can be observed from the time history plots also that the peak response quantities corresponding to the APF controller are much smaller than those of the LQG and the

SACPF controllers. And the response quantities corresponding to the SACPF controller are also smaller than those of the LQG controller. It can also be observed that the response quantities corresponding to the APF controller are mitigated in a much faster manner than the LQG controller.

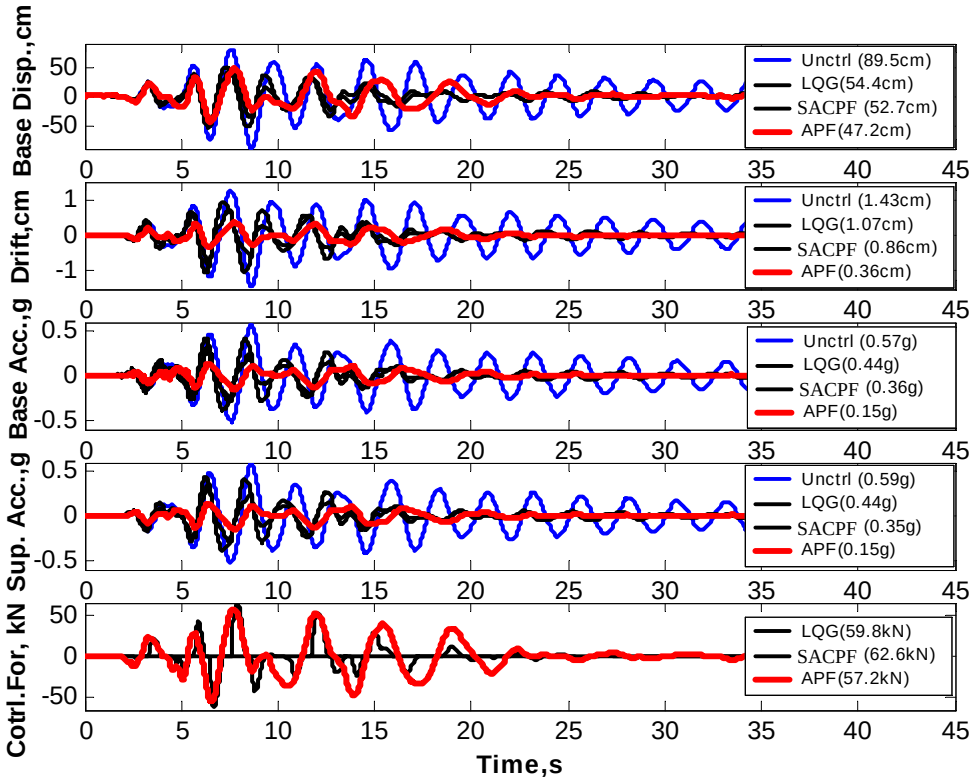

Figure 6.11: Time-history plots of response quantities using active and semi-active controllers.

In the design of APF and SACPF controllers above, pulse parameters are the same for all earthquakes. Although values of ζ_g and n are within reasonable range for all earthquakes to obtain good performance, the pulse period, T_p, is likely to vary more than 20% from the recorded ground velocity pulse period T_g, for quite amount of the earthquakes considered, resulting in inferior performance of APF and SACPF controllers

for those particular earthquakes. A much better performance can be obtained by choosing pulse period for each earthquake considering the actual dominant period of the record. In that case, average performance will be much better than those shown in Fig. 6.9 and 6.10.

6.9 CONCLUSIONS

In this chapter, a state-space model of near-field ground motion pulses is presented based on a near-field ground motion pulse model filter. The pulse filter is combined with the structural system dynamic equation to form the augmented system. This augmented system can be used to design active and semi-active controllers for base-isolated buildings using any of the modern control theories. Using Linear quadratic Gaussian (LQG) approach, Active Pulse Filter (APF) and Semi-Active Continuous Pulse Filter (SACPF) controllers are investigated in reducing response quantities of a base-isolated building model. For comparison, other active controllers, e.g., Linear Quadratic Regulator (LQR), Linear Quadratic Gaussian (LQG) and Active Kanai-Tajimi Filter (AKTF) controller, and passive linear viscous dampers are also investigated. It is observed that the APF controller performs significantly better than other controllers by reducing the peak values of base displacement, superstructure drift and absolute accelerations of the base and the superstructure simultaneously and more significantly. Other controllers can reduce the peak base displacement to the same level as the APF controller. However, other response quantities start increasing significantly after certain level of control force. The pulse filter used for the APF depends on the pulse period, damping factor and pulse shape factor. Based on sensitivity analysis, it is shown that the performance of the APF controller doesn't change significantly when the pulse period in the pulse filter is underestimated or overestimated by 20% with respect to the actual

ground pulse period, the damping factor is in the range of 0.15 to 0.35 and the shape factor is between 1 and 3, for a peak control force not exceeding 20% of the peak inertia force. Performance of APF and SACPF controllers is demonstrated through specific analysis using 4 individual earthquakes and the average results of an ensemble of 24 near-field earthquakes.

CHAPTER 7

ACTIVE AND SEMI-ACTIVE CONTROL OF A BASE-ISOLATED BENCHMARK BUILDING STRUCTUE

7.1 INTRODUCTION

Different thanconventional earthquake-resistant design which focuses on increasing the strength capacity of structures to resist ground shakings without collapse at the expense of allowing damage during extreme events, seismic isolation mitigates the earthquake-induced damage through reduced inertia load by shifting the fundamental frequency of the structure out of resonance range and concentrating the deformation and energy dissipation at the isolators [Skinner et al (1993), Kelly (1997), Naeim and Kelly (1999), Komodromos (2000)]. In addition to adequate vertical load-carrying capacity, a practical base-isolation system should be flexible enough in horizontal direction so that fundamental period of the total system is lengthened sufficiently to reduce the acceleration response. At the same time, these systems should also be capable of resisting low load levels such as wind and minor earthquakes. In addition, they should also contain adequate energy dissipation capacity, which could either be directly provided by isolation devices or by supplemental dampers. The following three types of isolation systems are typically used in practice (Fig. 7.1).

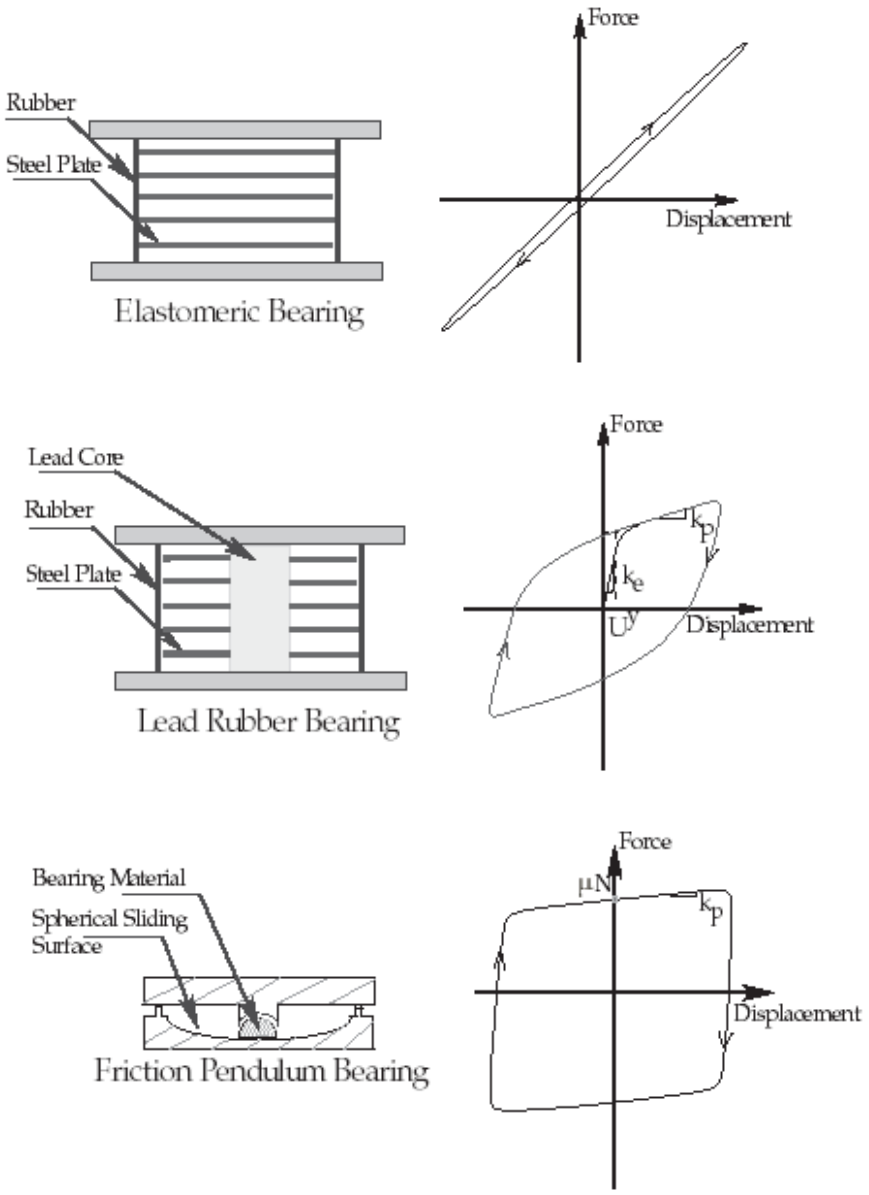

Figure 7.1 Base-isolation systems and the corresponding force-displacement relationships [Narasimhan et al (2005)].

Elastomeric base isolation system: The bearings consist of alternate layers of vulcanized rubber sheets bonded with thin steel plates. The steel plates provide the vertical load capacity and prevent lateral bulging of rubbers and rubber layers

provide horizontal flexibility. High damping rubber can be used in elastomeric bearings to effectively dissipate input seismic energy.

Lead-rubber bearing system: Lead-core can be inserted into the elastomeric or high-damping rubber bearing systems to improve vertical bearing capacity and energy-dissipation capacity. Since lead has large initial shear stiffness with low shear strength, it provides excellent energy dissipation through shear deformation. The compressive strength of lead is also strong enough for the purpose of supporting superstructure load.

Sliding/friction pendulum system: The lateral-resistant ability of sliding systems is provided by the friction developed at the contact surface, such as teflon and stainless steel. When the earthquake force is beyond the friction force, the superstructure starts sliding. A restoring force can be provided to eliminate the permanent offset of the superstructure through optimal design of geometry of the contact surface, e.g., friction pendulum system (FPS).

Recent studies have shown that although base isolation systems can significantly reduce the super-structure response, base displacements may be excessive, especially during near-fault ground motions [Heaton et al (1995), Nagarajaiah and Ferrell (1999), Makris and Chang (1998, 2000)]. Current practice is to provide non-linear passive dampers to limit bearing displacements. However, protection of base isolated buildings from strong and long-period pulses during near-field ground motions is challenging. A study by Heaton et al (1995) showed that a base-isolated building subjected to a near-field M_w 7.0 earthquake could result in large isolator drifts in excess of 50 cm, even when

damped at 25% critical damping. Large displacements at the isolation interface during a strong earthquake can lead to buckling or rupture of the isolation bearings [Nagarajaiah and Ferrell (1999)]. Although, large levels of damping reduce isolator displacements in the fundamental mode, they impart forces into the structure which can increase structural accelerations and deformations in higher modes, and can increase inter-story displacements [Kelly (1997)]. To address the need for high damping to limit the isolation drift and low damping to improve the isolation effectiveness at high frequencies, various types of active and semi-active systems have been proposed.

In active structural control, control force based on certain algorithm using response measurements or state estimation is applied directly to the structure using direct actuation devices (e.g., hydraulic actuators) to achieve certain response control objectives. The performance and applications of active control systems for base-isolated structures have been investigated in the past by Luo et al (1998), Yang et al (1995a, 1996c), Nagarajaiah (1994), Nagarajaiah et al (1993), etc. The advantages of semi-active systems include their reliability during earthquakes, adaptability to the random nature of ground motions, lesser power requirement and instantaneous local or partial response measurements required for feedback. The applications of active and semi-active systems or hybrid control systems (active or semi-active systems combined with passive systems) have been conducted in new and existing structures [Spencer and Nagarajaiah (2003)].

However, developments of new and novel active and semi-active control algorithms that can reduce both base and superstructure response quantities of base-isolated structures simultaneously are challenging for a widespread adoption of structural control technologies in practice. Traditional LQR/LQG controller design neglects the seismic

excitations. Recently, researchers have started designing controllers based on augmented systems with the assumption of excitation as white noise input through Kanai-Tajimi filter [e.g., Yang (1975, 1994), Yoshioka et al (2002), and Ramallo et al (2002)]. Although using Kanai-Tajimi based filter to model input excitation is beneficial to overall performance, these filters overestimate the energy in the low frequency range, which affects the response of long period structures. Nagarajaiah and Narasimhan (2005) have proposed a modified form of Kanai-Tajimi filter and have used it for the design of sample controllers for the base-isolated benchmark building. The modified Kanai-Tajimi filter has lower overestimation of energy in low frequency range, as compared to the original Kanai-Tajimi filter.

In this chapter, the frequency-domain pulse filter developed by converting the analytical pulse model proposed by He (2003) in Laplace domain is used in the design of active and semi-active control systems for the application to the base-isolated model. Details of the pulse filter have been introduced in Chapter 6 of this dissertation. The active controller based on the augmented structural and pulse filter model, termed as Active Pulse Filter (APF) controller, and two semi-active friction-type controllers that are based on the APF controller designed for fully active systems and are applied to the benchmark base-isolated building model. The performance of these active and semi-active systems is thoroughly investigated through comparison with the sample controllers and other existing controllers.

7.2 THE BENCHMARK BASE-ISOLATED BUILDING MODEL

The benchmark base isolated building model developed by Narasimhan et al (2005) is based on an existing building in Los Angles, California. The super-structure has eight stories and is considered to be a linear elastic system with lateral-torsional behavior. Three kinds of base isolation systems are considered for control design purpose, e.g., linear elastomeric system with low damping, nonlinear friction isolation representing friction pendulum system and bilinear elastomeric isolation system representing lead-rubber system.

Total of 92 isolators are connected between drop panels under the column locations and the footings. The superstructure and the isolation system are modeled by three master degrees of freedom (DOFs). Hence, total 27 DOFs are considered. The schematic presentation of the base isolation plan, FEM model and the elevation view is shown in Fig. 7.2. The first three periods of the fixed base model in three directions are: 0.78 sec, 0.27 sec, and 0.15 sec in north-south direction, 0.89 sec, 0.28 sec, and 0.15 sec in east-west direction and 0.66 sec, 0.21 sec, and 0.12 sec in rotation.

Seven earthquake records each consisting of fault parallel (FP) and fault normal (FN) components are provided in the benchmark package to compare the performance of different controllers. These ground motions are: Newhall (Northridge 1994), Sylmar (Northridge 1994), El Centro (1940), Rinaldi (Northridge 1994), Kobe (1995), JiJi (1999) and Erzinkan (1999). Nine evaluation criteria, J_1 to J_9, are prescribed to evaluate the effectiveness of different control systems and algorithms. These evaluation criteria are J_1=Peak base shear (isolation-level); J_2= Peak structure shear (at first story level); J_3=Peak base displacement or isolator deformation; J_4=Peak inter-story drift; J_5=Peak

absolute floor acceleration; J_6= Peak force generated by all control devices; J_7=RMS base displacement in the controlled structure; J_8=RMS absolute floor acceleration; J_9= Total energy absorbed by all control devices. Evaluation criteria J_1 to J_5, J_7 and J_8 are normalized with respect to corresponding response quantities for the uncontrolled building. The evaluation criterion J6 for peak control force is normalized by the peak base shear of the controlled building. More detailed information about the base-isolated building can be found in Narasimhan et al (2005).

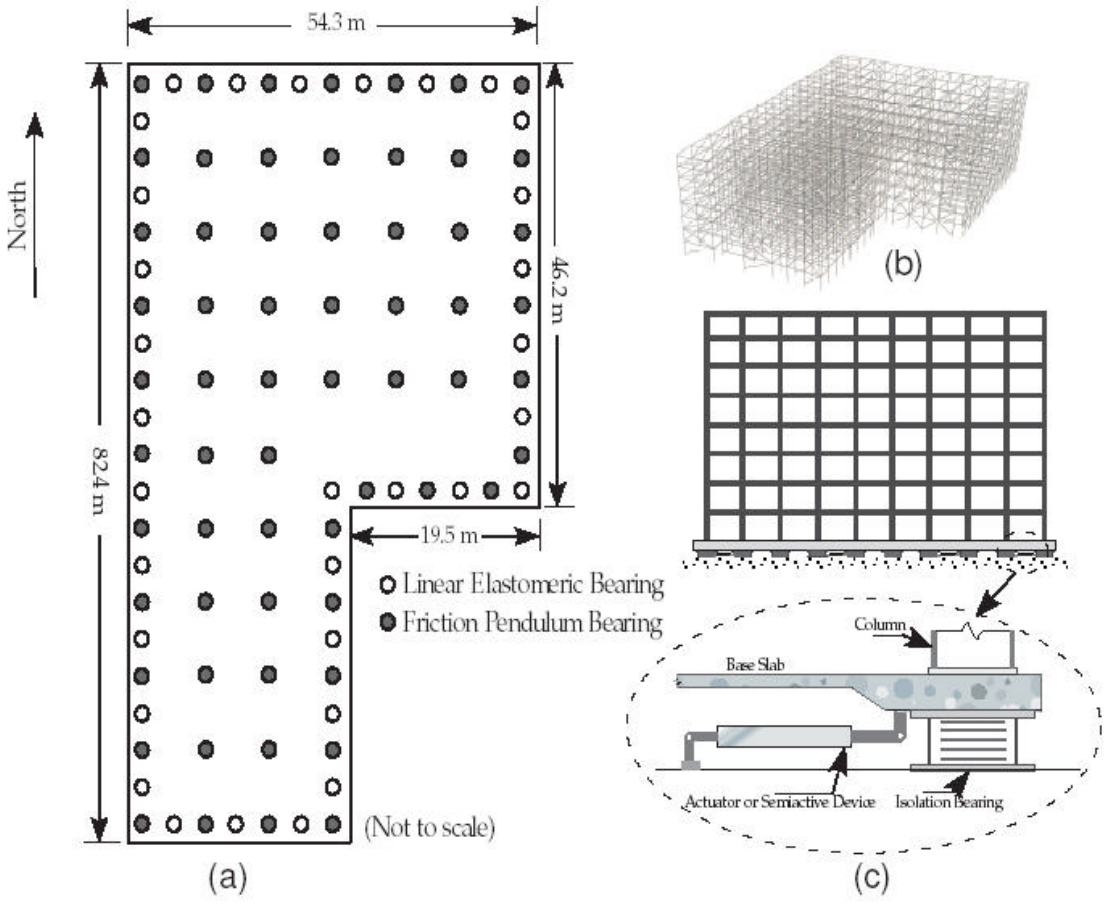

Figure 7.2 Information of the benchmark building model [Narasimhan et al (2003)]: a) Isolation plan, b) FEM model of superstructure and (c) Elevation view with devices.

7.3 GROUND MOTION PULSE-BASED ACTIVE CONTROLLER DESIGN

The analytical pulse model described in Chapter 3 has been used to develop a pulse-type ground motion filter. Details of the pulse filter can be found in Chapter 6. Design of active pulse filter controller for the application to the base-isolated building model is described in this section.

It is noted from Chapter 6 that the frequency domain model of the analytical pulse model can be obtained through Laplace Transform as,

$$\mathrm{F(s)} = (-1)^n \cdot Cb \cdot s \cdot \left[\frac{1}{(s+a)^2 + b^2}\right]^{(n)} \tag{7.1}$$

In Eq.(7.1), exponent n represents n^{th} derivation of the function in square brackets with respect to s. In order to use Eq.(7.1) in the design of seismic protective systems, it is assumed that the function F(s) represents a transfer function with white-noise W as input and earthquake ground acceleration as output. Then, the transfer function F(s) in Eq.(7.1) can be transformed into state-space form as

$$\begin{aligned} \dot{\boldsymbol{x}}_f &= \boldsymbol{A}_f \boldsymbol{x}_f + \boldsymbol{B}_f W \\ \ddot{U}_g &= \boldsymbol{C}_f \boldsymbol{x}_f \end{aligned} \tag{7.2}$$

where W is the white noise excitation and $\boldsymbol{x}_f$ is the state variable of the pulse filter F(s) in Eq.(7.1). The coefficient matrices $\boldsymbol{A}_f$, $\boldsymbol{B}_f$ and $\boldsymbol{C}_f$ depend on the order of the transfer function F(s) in Eq.(7.1).

The full-state three dimensional finite element model developed by Narasimhan et al (2005) consists of 54 states. For the purpose of controller design, the 54 states are further reduced to 24 states using the state-order reduction method [Nagarajaiah and

Narasimhan (2005), Yang et al (2004)]. The equation of the reduced order system in state-space is expressed as,

$$\begin{aligned} \dot{\boldsymbol{X}}_r &= \boldsymbol{A}_r \boldsymbol{X}_r + \boldsymbol{B}_r \boldsymbol{u} + \boldsymbol{E}_r \ddot{U}_g \\ \boldsymbol{Z}_r &= \boldsymbol{C}_{zr} \boldsymbol{X}_r + \boldsymbol{D}_{zr} \boldsymbol{u} + \boldsymbol{F}_{zr} \ddot{U}_g \\ \boldsymbol{Y}_{mr} &= \boldsymbol{C}_{mr} \boldsymbol{X}_r + \boldsymbol{D}_{mr} \boldsymbol{u} + \boldsymbol{F}_{mr} \ddot{U}_g + \boldsymbol{v}_r \end{aligned} \tag{7.3}$$

where $\boldsymbol{A}_r$, $\boldsymbol{B}_r$ and $?_r$ are reduced order system matrices, $\boldsymbol{Z}_r$ is the regulated output vector, which is obtained by choosing the appropriate mapping matrices $\boldsymbol{C}_{zr}$, $\boldsymbol{D}_{zr}$ and $\boldsymbol{F}_{zr}$. Vector $\boldsymbol{Y}_{mr}$ is the measurement vector and $?_r$ is the measurement noise vector. Eqs. (7.2) and (7.3) can be combined to obtain the augmented system as

$$\begin{aligned} \dot{\boldsymbol{X}}_a &= \boldsymbol{A}_a \boldsymbol{X}_a + \boldsymbol{B}_a \boldsymbol{u} + \boldsymbol{E}_a \boldsymbol{W} \\ \boldsymbol{Z}_a &= \boldsymbol{C}_{za} \boldsymbol{X}_a + \boldsymbol{D}_{za} \boldsymbol{u} + \boldsymbol{F}_{za} \ddot{\boldsymbol{U}}_g \\ \boldsymbol{Y}_a &= \boldsymbol{C}_{ya} \boldsymbol{X}_a + \boldsymbol{D}_{ya} \boldsymbol{u} + \boldsymbol{F}_{ya} \ddot{\boldsymbol{U}}_g + \boldsymbol{v}_a \end{aligned} \tag{7.4}$$

where $\boldsymbol{X}_a = [\, \boldsymbol{X}_r^T \;\; \boldsymbol{X}_f^T \,]^T$ is the augmented state vector. Augmented matrices in Eq.(7.4) are obtained as

$$\boldsymbol{A}_a = \begin{bmatrix} \boldsymbol{A}_r & \boldsymbol{E}_r \boldsymbol{C}_f \\ \boldsymbol{0} & \boldsymbol{A}_f \end{bmatrix}; \; \boldsymbol{B}_a = \begin{bmatrix} \boldsymbol{B}_r \\ \boldsymbol{0} \end{bmatrix}; \; \boldsymbol{E}_a = \begin{bmatrix} \boldsymbol{0} \\ \boldsymbol{B}_f \end{bmatrix} \tag{7.5}$$

in which $\boldsymbol{C}_{ya}$, $\boldsymbol{D}_{ya}$, $\boldsymbol{F}_{ya}$, $\boldsymbol{C}_{za}$, $\boldsymbol{D}_{za}$ and $\boldsymbol{F}_{za}$ are appropriate mapping matrices to obtain desired measured and regulated outputs.

For a direct comparison with sample controllers, measured and regulated outputs are taken to be the same as those for the sample controller in Nagarajaiah and Narasimhan (2005), i.e., the measurement outputs are absolute accelerations of the eighth floor, base and ground denoted by $\boldsymbol{Y}_{mr} = [\ddot{\boldsymbol{X}}_{8ax} \; \ddot{\boldsymbol{X}}_{8ay} \; \ddot{\boldsymbol{X}}_{8a?} \; \ddot{\boldsymbol{X}}_{bax} \; \ddot{\boldsymbol{X}}_{bay} \; \ddot{\boldsymbol{X}}_{ba?} \; \ddot{\boldsymbol{U}}_{gx} \; \ddot{\boldsymbol{U}}_{gy}]^T$, and the outputs to be regulated are the inter-story drifts and base displacements at the farthest

corner of the building and absolute accelerations for all degrees of freedom given by $\boldsymbol{Z}_r = [\boldsymbol{X}_b \ \boldsymbol{X}_i - \boldsymbol{X}_{i-1} \ \ddot{\boldsymbol{X}}_{ba} \ \ddot{\boldsymbol{X}}_{ia}]^T$, i = 1, 2, .. 8. The measured responses contain identically distributed RMS noise of 0.14V modeled as Gaussian rectangular pulse processes with a pulse width of 0.005 seconds. The sensor gains are given by (10/9.81)[$\boldsymbol{I}$]V/(m/sec^2), where $\boldsymbol{I}$ is an identity matrix of order 8. The noise and sensor data are the same as those for the sample controller. The ground excitation and the measurement noises are assumed to be independent of each other. The optimal active control gain is then obtained by minimizing the following performance index function:

$$J = \lim_{t \to \infty} \frac{1}{t} E\left[\int_0^t (\boldsymbol{Z}_a^T \boldsymbol{Q} \boldsymbol{Z}_a + \boldsymbol{u}^T \boldsymbol{R} \boldsymbol{u})dt\right] \tag{7.6}$$

where $\boldsymbol{Q}$ and $\boldsymbol{R}$ are weighting matrices for regulated outputs and control forces, respectively. Minimization of the performance index J in Eq.(7.6) results in the optimal control force as

$$\boldsymbol{u} = -\boldsymbol{K}\boldsymbol{X}_a \tag{7.7}$$

where $\boldsymbol{K}$ is the control gain matrix. The augmented state vector $\boldsymbol{X_a}$ is estimated as $\hat{\boldsymbol{X}}_a$ through the Kalman-Bucy filter,

$$\dot{\hat{\boldsymbol{X}}}_a = (\boldsymbol{A}_a - \boldsymbol{L}\boldsymbol{C}_y)\hat{\boldsymbol{X}}_a + (\boldsymbol{B}_a - \boldsymbol{L}\boldsymbol{D}_y)\boldsymbol{u} + \boldsymbol{L}\boldsymbol{Y} \tag{7.8}$$

where $\boldsymbol{L}$ is the observer gain matrix.

To have a direct comparison with other active control methods, active controllers such as Linear Quadratic Gaussian (LQG,), active control with Kanai-Tajimi shaping filter are also investigated in addition to the proposed active pulse filter (APF) controller and the sample active controller. The transfer function of the Kanai-Tajimi shaping filter is expressed as,

$$F(s)=\frac{2z_g w_g s + w_g^2}{s^2 + 2z_g w_g s + w_g^2} \tag{7.9}$$

where the z_g and w_g are the ground decay factor and ground frequency, respectively. Design procedure for controllers by incorporating the input ground excitation as filtered white noise modeled by the Kanai-Tajimi filter is similar to that of the APF controller.

For the design of sample active controller, Nagarajaiah and Narasimhan (2005) have proposed a modified form of Kanai-Tajimi filter which can approximately model the ground excitation characteristics of the set of earthquakes chosen for the benchmark study. The modified Kanai-Tajimi filter is given by

$$F(s)=\frac{4z_g w_g s}{s^2 + 2z_g w_g s + w_g^2}; w_g = 2p \text{ rad/sec}, \quad z_g = 0.3 \tag{7.10}$$

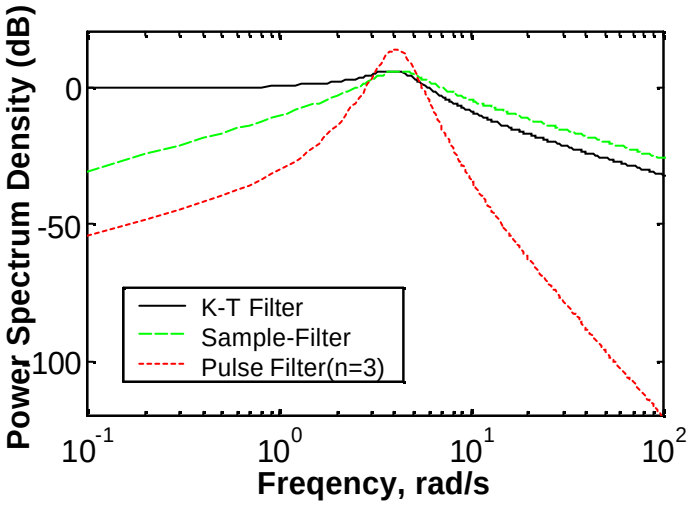

Figure 7.3: Power Spectrum Density Plots of the Kanai-Tajimi Filter, the modified Kanai-Tajimi Filter and the pulse filter.

Fig. 7.3 shows the power spectrum density (PSD) plots of the Kanai-Tajimi filter in Eq. (7.9), the modified Kanai-Tajimi filter in Eq. (7.10) and the pulse filter in Eq.(7.1).

The frequency and damping parameters for these filters are chosen as $?_g = ?_p = 4.2$ rad/s (T_p = 1.5 sec) and z_p=0.3. For the pulse filter, C is equal to 1 and n is equal to 3 in Eq. (3). It is observed from Fig. 4 that the pulse filter has lower PSD compared to Kanai-Tajimi models in Eqs. (7.9) and (7.10) in both low and high frequency ranges. The Kanai-Tajimi filter, Eq. (7.9), has larger PSD value in lower frequency range and the modified Kanai-Tajimi filter in Eq.(7.10) has larger PSD in higher frequency range. The pulse filter has larger PSD around $?_g = ?_p = 4.2$ rad/s.

7.4 SEMI-ACTIVE/PASSIVE CONTROL ALGORITHM/DEVICES

In addition to the active controllers described above, performance of various semi-active controllers and linear passive damper is also investigated using this benchmark model. Two of these semi-active controllers, i.e., Semi-Active Continuous Pulse Friction (SACPF) controller and Semi-Active Discontinuous Pulse Friction (SACPF) controller are designed through applying different semi-active constraints on the Active Pulse Filter (APF) controller.

Semi-Active Continuous Pulse Friction (SACPF) Controller

For semi-active implementation of the active controller in Eq. (7.7), a semi-active friction controller, termed as the Semi-Active Continuous Pulse Friction (SACPF) controller, is designed as

$$f_{SA} = -mg\left|K\hat{X}_a\right| tanh(a\ \dot{d}) \tag{7.11}$$

The controller in Eq. (7.11) is based on the semi-active friction controller proposed by He et al (2003). In this controller, friction force in the damper is regulated by the normal force $m\,g\left|K\hat{X}_a\right|$. In Eq.(7.11), m and g are the control gains, *tanh(.)* is the hyperbolic

function which assures the continuous slippage of the semi-active friction damper, a is a parameter that measures the thickness of the boundary layer, and $\dot{d}$ is the velocity across the damper. In this paper, mg is taken as unity in order to use the full amplitude of the active feedback force and a = 1, which is an appropriate choice for this problem.

Semi-Active Discontinuous Pulse Friction (SADPF) Controller

The second friction controller, termed as Semi-Active Discontinuous Pulse Friction (SADPF) controller, is proposed as

$$f_{SA} = \begin{cases} 0 & otherwise \\ u & u.\mathrm{sgn}(\dot{d}) < 0 \end{cases} \tag{7.12}$$

where u is the active force in Eq. (7.7). It is noted that both controllers in Eqs. (7.11) and (7.12) are intrinsically dissipative in nature. It is noted that controllers in Eqs. (7.11) and (7.12) can be implemented by a semi-active friction damper or MR damper [Saharabudhe and Nagarajaiah (2005)].

Semi-active Friction Damper (SAFD)

Friction dampers exhibit two phases of behavior, i.e., sticking and slipping. To increase the performance of semi-active friction dampers (SAFDs), one should maintain the dampers in their slipping phase as much as possible to continuously dissipate energy. He et al (2003) proposed a Smooth Boundary Layer Semi-Active Friction (SBLSAF) controller that guarantees the continuous slippage in the friction damper at all time instants by introducing a boundary layer to eliminate the undesirable acceleration spikes caused by high speed switching dynamics. The SBLSAF controller is expressed as [He et al (2003), Inaudi (1997)]

$$u(t) = -mg\left|P[d(t)]\right| \tanh(a\dot{d}) \tag{7.13}$$

in which m , g, a, $\dot{d}$ and $\tanh(.)$ have the same meanings as those in Eq. (7.11). The function $\left|P[d(t)]\right|$ in Eq.(9) is the absolute value of the local maximum (peak or trough) prior to the current time, t, i.e.,

$$P[d(t)] = d(t-s), \text{ where } s = \{ \min \bar{t} \geq 0 : \dot{d}(t-\bar{t}) = 0\} \tag{7.14}$$

in which s = time duration since the previous local maximum (peak or trough).

Semi-active Stiffness Damper (SASD)

The semi-active stiffness damper (SASD) consists of a cylinder-piston system with an on-off valve in the bypass pipe connecting two sides of the cylinder filled with hydraulic oil [Bobrow et al (2000), Yang et al (2000), Agrawal et al (2003), Jabbari and Bobrow (2002)]. When the valve is closed, the damper serves as a stiffness element with an effective stiffness k_e provided by the bulk modulus of the fluid inside. The semi-active stiffness damper can be operated either in the resetting mode (RSASD) or switching mode (SSASD). In the resetting mode, the value is pulsed to open and then closed quickly at appropriate time instants. Since the valve is closed most of the time, the energy is stored in the form of potential energy of the compressed oil in the damper system. At appropriate time instants, the value is opened to quickly release the energy. At this instant, the piston of the damper is reset to a new position. The control force in the damper is expressed as

$$u(t) = k_e (d - d_s) \tag{7.15}$$

where k_e is the effective stiffness of the damper, d is the relative displacement at the device location and d_s is the previous piston position at the instant of resetting. The valve in the damper is reset when [Yang et al (2000), Agrawal et al (2003)],

$$\dot{d} + gd = 0 \tag{7.16}$$

where g is a gain parameter. In this investigation, γ=0 is used so that resetting is made when the potential energy of the compressed oil in the damper is maximum.

In the resetting semi-active damper, stiffness k_e is added whenever the valve is closed. Another type of semi-active stiffness damper in which damper stiffness can be varied continuously has been investigated by Nagarajaiah and Mate (1998), Nadathur and Nagarajaiah (2004), and Narasimhan and Nagarajaiah (2005).

Visco-elastic Friction (VEF) Controller

The semi-active visco-elastic friction (VEF) controller, based on the nonlinear Reid damping and viscous damping mechanism, has been proposed by Chen and Chen (2000) to control a piezoelectric friction damper. The control force exerted by this damper is expressed as

$$f(t)=\begin{cases} m[e\dot{d}(t)+gd(t)] & d\dot{d}\geq 0 \\ m[e\dot{d}(t)-gd(t)] & d\dot{d}<0 \end{cases} \tag{7.17}$$

where m is friction coefficient, e and g are the gain coefficients of displacement and velocity, respectively, and $d(t)$ and $\dot{d}(t)$ are the displacement and velocity across the damper.

Linear Passive Viscous Damper

To compare the performance of different control strategies, linear viscous damper is also considered. The force generated by the linear passive viscous damper is expressed as

$$u(t)=C_d\dot{d} \tag{7.18}$$

where C_d is the damping coefficient and $\dot{d}$ is the velocity across the damper.

7.5 RESULTS AND DISCUSSIONS OF THE ACTIVE CONTROLLERS

The APF controller in Eq.(7.17) is designed by considering $n = 3$, $C=1$, $z_p=0.3$, and $T_p = 1.5$ sec (i.e., $\omega_g = 4.2$ rad/sec), respectively. These parameters are based on extensive numerical and parametric studies. Parameters w_g and z_g for the Kanai-Tajimi filter are taken as 17 rad/sec and 0.3, respectively. For the sample controller, parameters w_g and z_g for the modified Kanai-Tajimi filter are taken as 2π rad/sec and 0.3, respectively. Outputs to be regulated are the same as those for the sample active controller. These outputs include the inter-story drifts and absolute accelerations of the base and super-structure along all three degree of freedoms. A controller weighting matrix $\boldsymbol{Q}$ is selected by assuming diagonal elements corresponding to drift and absolute acceleration in X and Y directions are nonzero and diagonal elements corresponding to relative rotations and rotational accelerations are zero. In addition, all non-diagonal terms are zero, i.e.,

$$\boldsymbol{Q}=\begin{bmatrix} q_d \boldsymbol{I}_D & \\ & q_a \boldsymbol{I}_D \end{bmatrix} \tag{7.19}$$

where I_D is a 27×27 diagonal matrix with either 1 or 0 in the diagonal. In the sample active controller design, the weighting ratio of $q_d/q_a = 8/0.2 = 40$ is used. However, the ratio of $q_d/q_a = 100$ is taken in the design of all active controllers in order to increase the weighting on displacement reduction. The $\boldsymbol{R}$ matrix is taken as a 3×3 unit matrix. Various levels of control force are achieved by adjusting the values of q_d and q_a while keeping the ratio of q_d/q_a unchanged. Active control forces are applied through 16 hydraulic actuators with 8 in each of the X and Y directions placed at same locations as the sample controller.

The capacity of these actuators is also kept the same as the sample active controller for a fair comparison. The maximum capacity of actuator is 2,200kN.

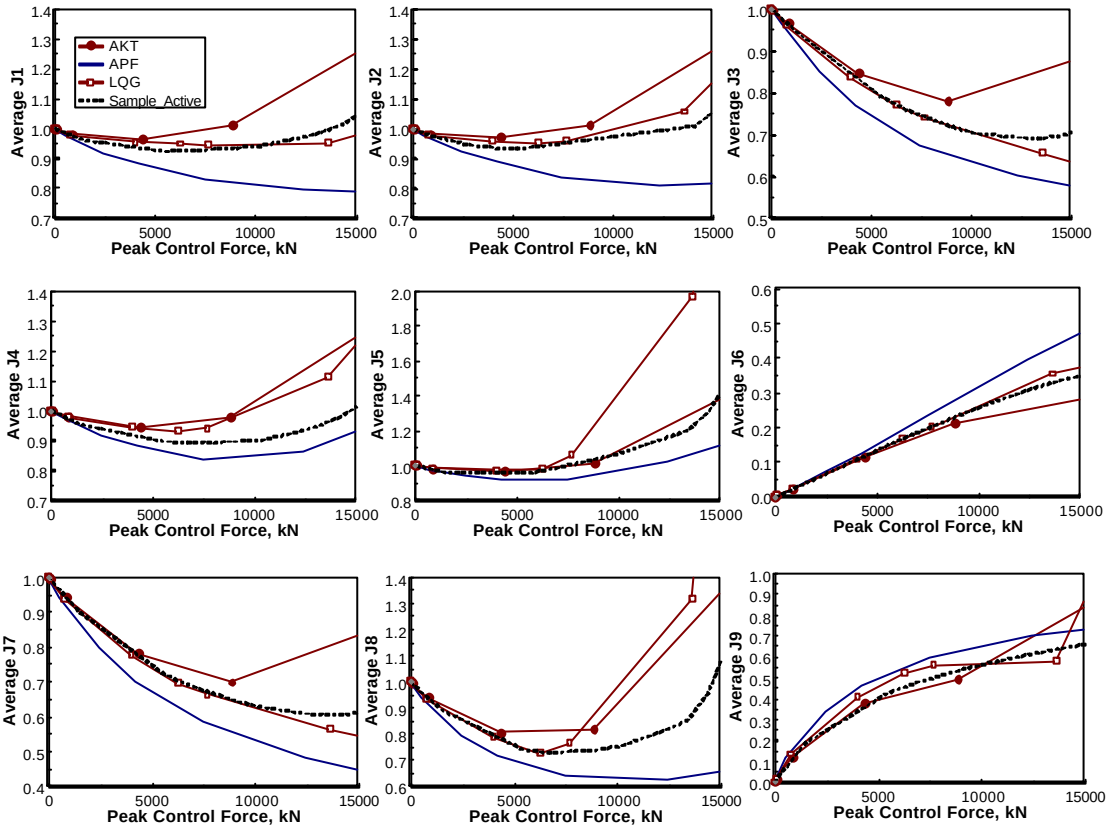

Figure 7.4: Average of performance evaluation criteria using 14-earthquake load cases as a function of applied force.

Fig. 7.4 shows the plots of the average of evaluation criteria using 7 earthquakes applied in two orthogonal directions as a function of peak control force for different active controllers. The average of evaluation criteria is obtained by calculating the evaluation criteria for each earthquake and then taking average of all of them at a particular level of control force. It is observed from Fig. 7.4 that peak base shear (J_1), peak structure shear (J_2), peak inter-story drift (J_4) and peak absolute floor acceleration (J5) start increasing for the LQG controller beyond 6000 kN control force. Evaluation

criteria J_1, J_2, J_3, J_6 and J_7 are almost the same for LQG and Sample controllers. However, the inter-story displacement (J_4), the peak (J_5) and RMS (J_8) floor accelerations for the sample active controller are superior to those of LQG controller. The performance indices J_1, J_2, J_3 and J_7 corresponding to AKT are much inferior to other three active controllers, which indicates that modeling near-field ground motion pulses as filtered white noise through Kanai-Tajimi filter is not beneficial to the control of structures against near-field ground motions. On the other hand, all the evaluation criteria decrease with increase in control force significantly for the APF controller compared to all other active controllers, while the required normalized control forces (J_6) and total dissipated energy are only slightly higher than other active controllers. This shows that the APF controller is more effective than other active controllers in reducing response quantities of the benchmark base-isolated building.

Table 7.1 presents the average results of the 9 performance indices for the peak control force of 10,000 kN. In table 7.1, "Sample" represents sample active controller, "LQG" represents the results obtained by using pure LQG active controller, "AKT" represents the results obtained by using LQG with Kanai-Tajimi filter, "APF" represents the results obtained by using the Active Pulse Filter controller. It is observed from Table 7.1 that, for the same level of control force, the performance indices J_1 to J_5, J_7 and J_8 for the APF controller are significantly smaller than those for other controllers. This again demonstrates that the APF controller is more efficient in simultaneously reducing all the response quantities, e.g., base displacement, drift, accelerations of base and super-structure. The sample controller has similar performance as that of the pure LQG algorithm for most of the performance indices, except J_4, J_5 and J_8, where the sample

controller performs much better than the LQG controller. The Active Kanai-Tajimi filter (AKT) controller is inferior to others in terms of the majority of performance indices.

Table 7.2 to 7.8 present the results of the benchmark model equipped with different active controllers subject to all 7 prescribed earthquakes. For comparison purposes, the results of the AKT controller based on the same parameters as those of the APF controller (i.e., z_g =0.3 and $w_g = \frac{2p}{T_p} = \frac{2p}{1.5} = 4.2 rad/s$) are also listed in table 2-8, designated by "AKT1". In Tables 2-8, "C.D" represents the percent corner drift and the other variables have the same meaning as those in Table 7.1. Different controllers investigated are designed by keeping the performance index, J_6 (peak control force normalized by the peak base shear in controlled case), less than 0.15, which is consistent with the sample active controller. The same design parameters are used for each control approach in obtaining the values corresponding to the 14 load cases, i.e., 7 earthquakes in FP and FN directions. It is observed from table 7.2 to 7.8 that for a similar J_6, significantly better reduction of J_1 to J_5, J_7, J_8 and corner drift (C.D) can be achieved for the APF controller compared to the others.

To show a comparison between different controllers in Table 7.2 to 7.8, minimum values of J_1-J_5, J_7-J_8 and corner drift among the 5 controllers is highlighted by bold. It is observed from Table 7.2-7.8 that the response quantity evaluation criteria J_1-J_5, J_7-J_8 using the APF controller are significantly smaller than all other controllers, except for J_4 and J_5 for Newhall earthquake (J_4=0.88, J_5=0.89 for APF versus J_4=0.84, J_5=0.87 for sample in FP-X, FN-Y direction and J_4=0.92, J_5=0.95 for APF versus J_4=0.85, J_5=0.84 for sample in FN-X, FP-Y direction), J_5 for Sylmar component of Northridge earthquake in FP-X, FN-Y direction (J_5=0.97 for APF versus J_5=0.95 for sample), J_4 and J_5 for Rinaldi

Component of Northridge Earthquake (J_4=0.95 for APF versus J_4=0.94 for sample in FP-X, FN-Y direction and J_4=0.97, J_5=0.99 versus J_4=0.95, J_5=0.94 for sample in FN-X ,FP-Y direction), J_5 for Kobe earthquake (J_5=0.98 for APF versus J_5=0.90 for FP-X, FN-Y direction and J_5=0.97 for APF versus J_5=0.94 for sample in FN-X, FP-Y direction), and J_3 for JiJi earthquake in FN-X, FP-Y direction (J3=0. 84 for APF versus J_3=0.79 for sample). The overall performances of AKT and AKT1 are similar, which indicates that the active controller based on LQG with Kanai-Tajimi filter is robust to the parameter $?_g$. However, the AKT1 is slightly better than AKT for some earthquakes in reducing J_1, J_2, J_3 and J_4.

It is noted that the same controller is used to evaluate performance during all 14 cases of earthquake response. For APF controller, this has been done by assuming the same ground motion pulse parameters in the controller design for all earthquakes. A significantly better performance can be achieved by designing the APF controller for a specific site using site specific ground motion pulse parameters [Agrawal et al (2006)].

Fig. 7.5 shows the time history plots of building response quantities using Kobe earthquake in FP-X and FN-Y direction for the uncontrolled, sample active and APF cases. It is observed that the controlled response quantities for both the sample controller and APF are much smaller than those of the uncontrolled case. For the same control force level, the base displacement, drift at 8th floor and base acceleration for the APF are much less than those of the sample controller, although the maximum acceleration at 8th floor using APF controller is larger than that of the sample controller and is almost the same as the uncontrolled case. It is also observed that the amplitudes of the response quantities using the APF controller decrease much faster than those of the sample controller.

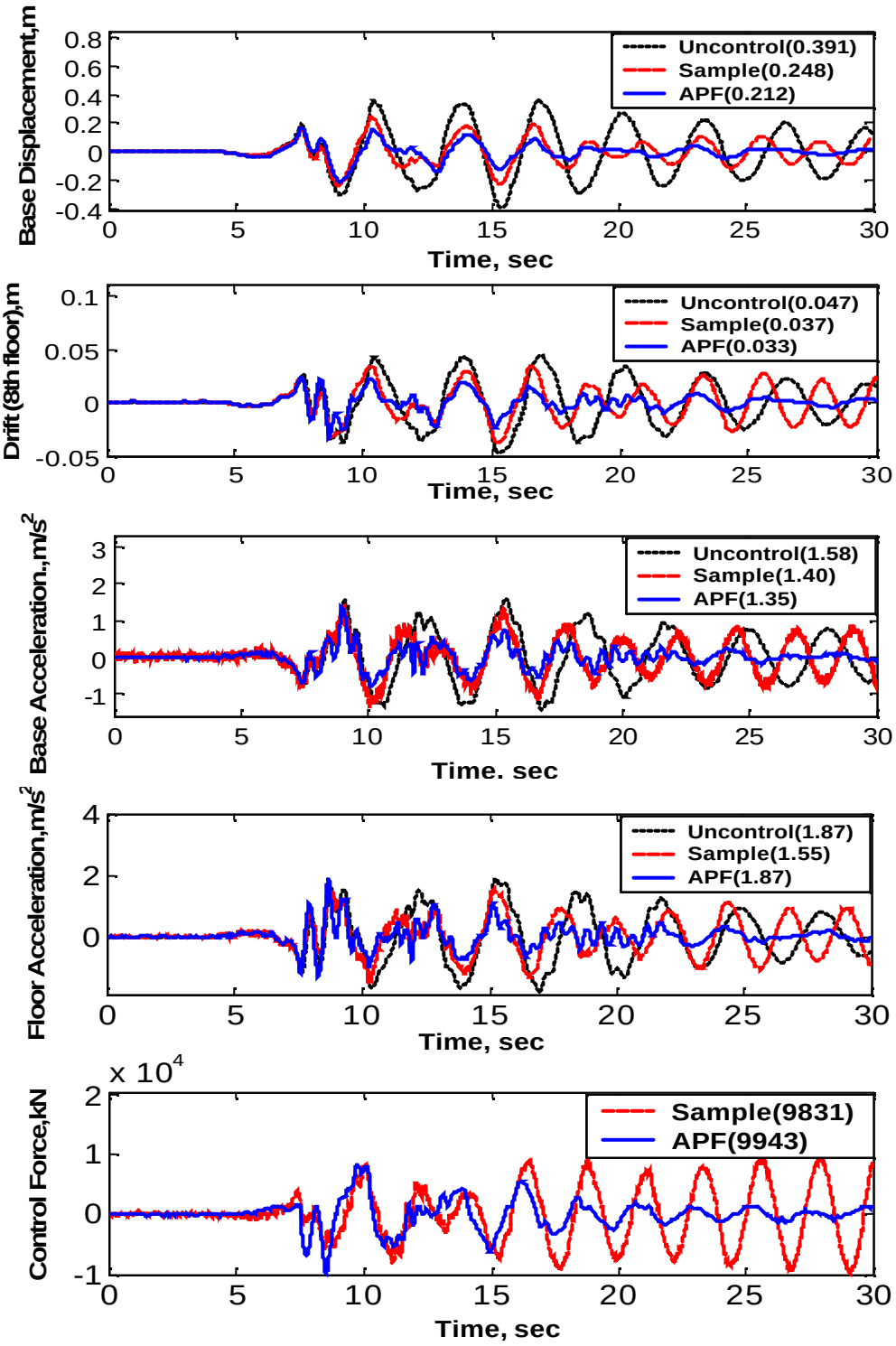

Figure 7.5 Time history plots of Kobe earthquake in FP-X and FN-Y direction. The response quantities are for X-direction. From above: Base displacement at the center of mass, Drift at 8th floor, Base acceleration at the center of mass, Acceleration at 8th floor, Control force.

7.6 RESULTS AND DISCUSSIONS OF THE SEMI-ACTIVE AND PASSIVE CONTROLLERS

In this study, the hardware locations and the number of the control devices are again taken to be the same as the sample controllers in order to compare the results with that of the sample controllers.

Tables 7.9 to 7.15 present the results of the benchmark model equipped with different controllers subject to all 7 prescribed earthquakes. In these tables, column 1 presents the evaluation criteria J_1 through J_9, percent Corner Drift (C.D) and control force normalized by the structure weight (F/W). Column 2 to 9 in Tables 7.9 through 7.15 present the corresponding quantities for all eight controllers, i.e., sample passive controller, Linear Passive Viscous (LPV) damper, sample semi-active controller, Smooth Boundary Layer Semi-Active Friction (SBLSAF) controller, Resetting Semi-Active Stiffness Damper (RSASD), Visco-Elastic Friction (VEF) damper, Semi-Active Continuous Pulse Friction (SACPF) controller and Semi-Active Discontinuous Pulse Friction (SADPF) controller.

In Tables 7.9 through 7.15, the same design parameters are used for a particular controller for all 14 earthquake cases, i.e., 7 earthquakes in each of the FP and FN directions. In order to have a direct comparison with the sample controllers, the parameters for each controller are chosen so that the peak control force of that controller is almost the same as the corresponding sample controller during the Erzinkan earthquake with FP-X and FN-Y. In other words, the peak control force of the Linear Passive Viscous damper is almost the same as the sample passive controller, and the peak control forces of the five semi-active controllers are almost the same as that of the sample semi-

active controller, see the last row of Table 7.15a. The parameters for different controllers are: damping coefficient C = 1400 kN.s/m for linear passive viscous damper; a=1, m=0.2 and g=20000 for SBLSAF; k_e=1500 kN/m for RSASD; m=0.2, e=6000 and g=2000 for VEF. Also, $q=3.5\times10^6$ for SACPF and $q=1.9\times10^6$ for SADPF are used in the design of active controller using LQG in Eq. (7.19). For SACPF and SADPF controllers, mg=1 and a = 1 are chosen. The active controller in Eq.(7.7) is designed by considering n = 3 for the transfer function in Eq. (7.1). The coefficient of the magnitude of the pulse filter, C, is taken as 1 in the controller design and the damping factor z_p and the period T_p are taken as 0.3 and 1.5 sec.

In Tables 7.9 to 7.15, the performance indices larger than 1 indicate that the response of the controlled structure is larger than that of the uncontrolled structure. These quantities are highlighted in bold. In order to present a systematic comparison for the performance of different controllers, a detailed analysis of the capability of a controller in reducing different response quantities are presented in the following.

a) Controller Performance in reducing a Particular Response Quantity

A detailed analysis of the results presented in Table 7.9-7.15 is carried out to characterize the performance of a controller in reducing a particular response quantity. Only evaluation criteria J_1 to J_5 are considered, since J_7 and J_8 are RMS response quantities corresponding to the peak response quantities. The evaluation criterion J9 is the total energy dissipated by dampers normalized by the energy input into the controlled structure. The value of J_9 varies with the earthquake ground motion, since both the energy dissipated and the input energy to the structure depend on the behavior of controllers. Likewise, the evaluation criterion J6 is the peak control force normalized by

the peak base shear, and it varies with different earthquakes. In order to show the comparison between the peak control forces required by different controllers, the last row of Tables 7.9-7.15 shows the ratio of the peak control force to the building weight, F/W. As mentioned previously, all controllers are designed for similar levels of peak control forces during the Erzinkan earthquake with FP-X and FN-Y. It is observed from Table 7.15a that passive and semi-active controllers require maximum control force of 6.3% and 5.9% of the building weight, respectively.

Peak Base Shear (J_1): It is observed from Tables 7.9 to 7.15 that the best performance in reducing the peak base shear (J_1) to 0.66 is obtained by SACPF controllers during the JiJi FN-X, FY-Y earthquake. The peak base shear increases by 25% (i.e., J_1 = 1.25) during the El Centro earthquake for the sample semi-active controller. Peak base shear using RSASD increases during the Sylmar FP-X, FN-Y, El Centro, Rinaldi, Kobe FN-X, FP-Y, and Erzinkan FP-X, FN-Y earthquakes, with maximum increase being 17% during the Kobe FN-X, FP-Y earthquake. Table 7.16 presents average of the evaluation criteria for 14 earthquakes considered. It is observed from Table 7.16 that LPV, SACPF and SADPF have the best average performance in reducing the peak base shear by 18%. Performance of all other controllers is superior to the sample semi-active and RSASD controllers, in which the sample semi-active controller only has 3% average reduction and RSASD does not reduce the average peak base shear (J_1=1.0).

Peak Structure Shear (J_2): The minimum (best) value of J_2 is obtained as 0.65 for the JiJi FN-X, FN-Y earthquake for the SACPF controller and the worst value is obtained as 1.24 during the El Centro earthquake for the sample semi-active controller. It is observed that J_2 increases during several earthquakes for the RSASD and sample semi-active

controllers. The value of J_2 increases for LPV and VEF controllers only during the Rinaldi earthquake. It is observed from Table 7.16 that the LPV, SACPF, SADPF, SBLSAF and VEF controllers are the most effective in achieving the best average J_2 and the RSASD controller has the worst performance.

Peak Base Displacement (J_3): The reduction on the peak base displacement of the base-isolated building is one of the most important criteria during strong earthquakes. The minimum (best) value of $J_3 = 0.14$ is obtained for the El Centro FP-X, FN-Y earthquake for the sample passive case, although the peak base shear, peak interstory drift and peak absolute acceleration increase drastically for this case during several earthquakes. Compared to this case, $J_3 = 0.39$ is obtained by the LPV for the El Centro FP-X, FN-Y earthquake, with relatively lesser increase in the peak base shear, peak interstory drift and peak absolute acceleration during different earthquakes, as compared to the sample passive case. For semi-active controllers, best value of $J_3 = 0.40$ is obtained by the VEF during the El Centro FP-X, FN-Y earthquake, and the worst value of $J_3 = 0.89$ is obtained for the RSASD during the Sylmar FP-X, FN-Y earthquake. It is further observed from Table 7.16 that among semi-active controllers, the VEF controller performs the best in reducing peak base displacement, followed by the sample semi-active, SBLSAF, SADPF, SACPF and RSASD controllers. The two passive controllers have better performance than other six semi-active controllers, in which 52% and 44% reductions can be achieved by the sample passive controller and LPV respectively. However, other response quantities start to increase because of the use of sample passive and LPV dampers.

Peak Superstructure Drift (J_4): The minimum (best) value of $J_4 = 0.62$ is obtained for the SACPF controller during the JiJi FN-X, FP-Y earthquake. The worst values are 2.18

and 1.37 for the sample passive and sample semi-active controllers, respectively, during the El Centro FN-X, FP-Y earthquake. It is observed from Tables 7.9 to 7.15 that this response quantity increases beyond 1.0 frequently for the sample semi-active and RSASD controllers during several earthquakes because of the addition of controllers/dampers. The peak superstructure drift for SACPF increases during the Newhall earthquake, and that for the VEF controller increases during the Newhall FN-X, FP-Y earthquake and Rinaldi earthquake. For the base-isolated buildings, superstructure drifts are reduced significantly compared to the corresponding fixed-base building because of the isolation from the ground motion. Hence, a controller that reduces or doesn't increase the peak superstructure drift, while reducing the base displacement significantly, is desirable for practical applications. In this respect, all controllers, except the sample passive and sample semi-active controllers, have been observed to perform well. This fact can also be observed from Table 7.16.

Peak Superstructure Acceleration (J_5): It is well known that the peak absolute floor acceleration of a base-isolated building with supplemental dampers installed in parallel with isolators decreases with an increase of damping in the supplemental damper up to a certain level of the damper force, and it starts to increase beyond that force. For the sample passive damper, it is observed from Tables 7.9-7.15 that the evaluation criterion J_5 increases drastically for all earthquakes, except the JiJi earthquake. In fact, the peak absolute floor acceleration for the El Centro FN-X, FP-Y earthquake increases by a factor of 3.45 for the sample passive damper (i.e., J_5 = 3.45). This typically happens when the level of supplemental damping is high. For semi-active controllers, the minimum (best) value of J_5 = 0.70 is obtained for SBLSAF and SADPF controllers during the JiJi FN-X,

FP-Y, and the worst value of 2.08 is obtained for sample semi-active controller during the El Centro FN-X, FP-Y earthquake. It is observed from Tables 7.9-7.15 that the performance for J_5 is the worst for the sample passive, sample semi-active and RSASD controllers. It is observed from Table 7.16 that SBLSAF and SADPF have the best average performance in reducing J_5.

***Corner Drift (C.D.)*:** The percent corner drift is different for different earthquakes and it doesn't vary significantly for different controllers with the same earthquake.

Average of Peak Response Quantities: The last column of Table 7.16 shows the average of peak evaluation criteria J_1 to J_5 for different controllers. It is observed that the LPV, SBLSAF, VEF, SACPF and SADPF have the best capability to reduce all response quantities simultaneously. The performances of the RSASD and sample semi-active controllers are inferior to these controllers.

b) Evaluation Criteria versus Peak Control Force

To evaluate the relationship between the evaluation criteria and the peak control forces, Fig. 7.6 and 7.7 show plots of peak evaluation criteria J_1 to J_5, as a function of peak control force for controllers discussed in Tables 7.9 to 7.15 for El Centro and Rinaldi earthquakes. Both earthquakes are applied with fault-parallel (FP) component in X direction and fault-normal (FN) component in Y direction. It has been observed from Tables 7.9-7.15 that the overall performance of controllers for the Rinaldi earthquake is inferior to that for the El Centro earthquake.

Different control force levels in Fig. 7.6 to 7.7 are achieved by varying the characteristic parameters for each controller, e.g., the damping coefficient C for LPV, control gain g for SBLSAF with friction coefficient $m = 0.2$ and boundary layer thickness

parameter a=1, damper stiffness k_e for RSASD, the displacement and velocity gain coefficients (e and g) for VEF, the weighting coefficient q for SACPF and SADPF with mg = 1 and a = 1. For the sample semi-active controller, data corresponding to only certain range of control forces could be obtained for different earthquakes by varying the controller and state weighting coefficients.

It is observed from Fig. 7.6 and 7.7 that the normalized peak base displacement, J_3, always decreases with an increase of the peak control force, where almost 70% reduction can be achieved for the El Centro Earthquake and only 30% reduction can be achieved for the Rinaldi earthquake for most of the controllers using approximately 12,000 kN control force. However, increasing the control force results in the amplification of other criteria for some controllers during different earthquakes. It is observed that the performance of SADPF is better than other controllers in reducing J_1, J_2, J_4 and J_5 during these two earthquakes. The performance of the sample semi-active controller is worse than all other controllers in reducing the peak base displacement (J_3) during both the El Centro and Rinaldi Earthquakes, as indicated by scattered square points in Fig. 7.6 and 7.7. For the El Centro earthquake, it is observed from Fig. 7.6 that the sample semi-active controller is only slightly better than the RSASD and is inferior to all other controllers in reducing the evaluation criteria J_1, J_2, J_4 and J_5 when the control force is less than a certain level. For higher control force levels, evaluation criteria J_1, J_2, J_4 and J_5 increase rapidly for the sample semi-active controller and the RSASD while these evaluation criteria decrease continuously for a significant range of control forces for the SADPF and other controllers. For the Rinaldi earthquake in Fig. 7.7, evaluation criteria J_1, J_2, J_4 and J_5 for the sample semi-active controller are superior to those for the RSASD,

comparable to those for the SBLSAF, but inferior to those for the SACPF and SADPF controllers.

Fig. 7.8 presents the average of evaluation criteria for the 6 controllers as a function of the control force. Average of evaluation criteria is calculated for all 14 cases of earthquakes considered. It is observed from Fig. 7.8 that the overall performance of RSASD in controlling J_1, J_2, J_3, J_4 and J_5 is worse than other controllers. The performances of other controllers in reducing the peak response quantities are comparable to each other. It can be further observed from Fig. 7.8 that the LPV and SADPF are slightly better than others in reducing J_1 and J_2, VEF and LPV are slightly better in reducing J_3, and the SBLSAF is slightly better in reducing J_4 and J_5.

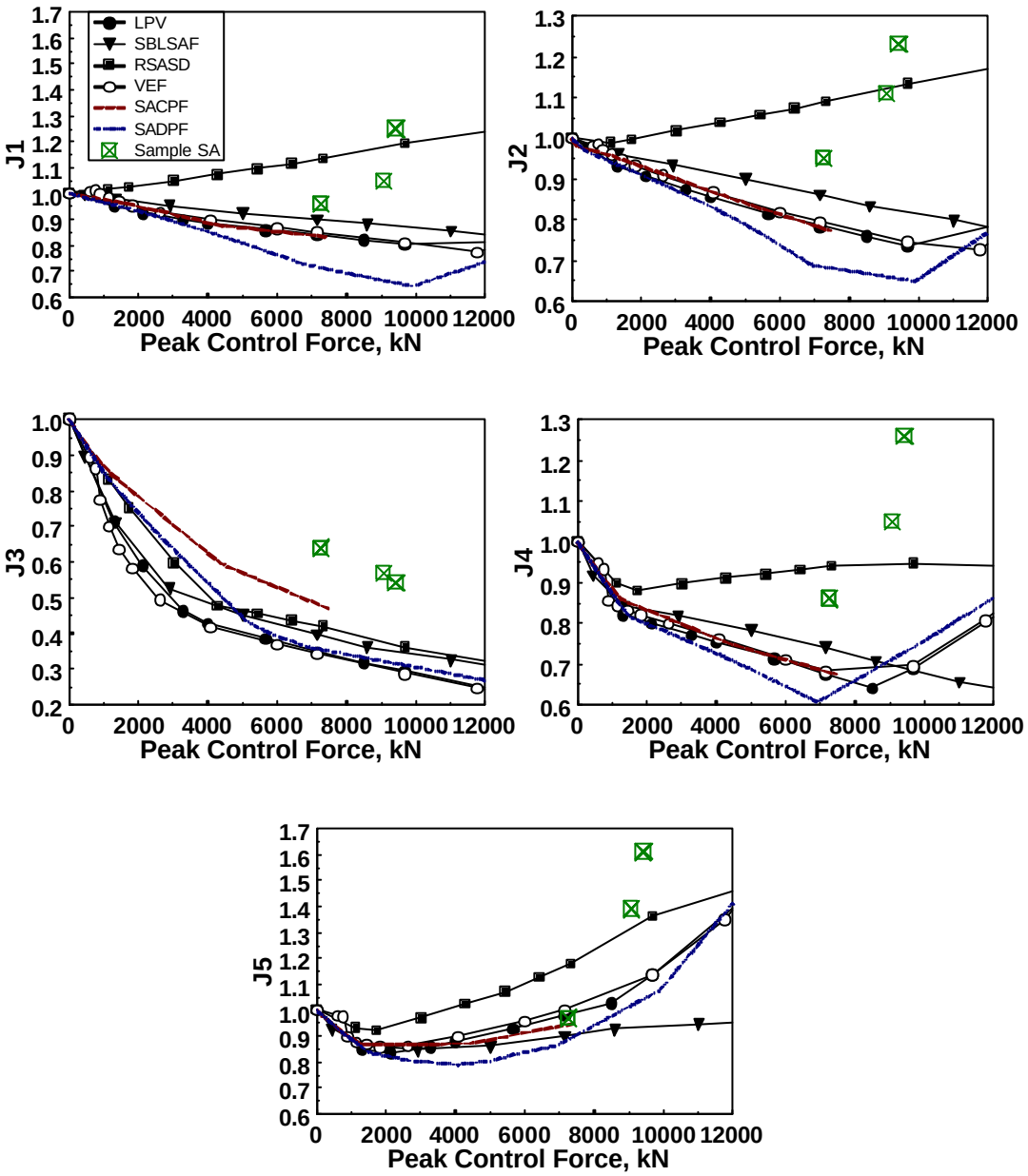

Figure 7.6: Peak Evaluation Criteria as a Function of Peak Control Force during El Centro Earthquake in FP-X, FN-Y Direction.

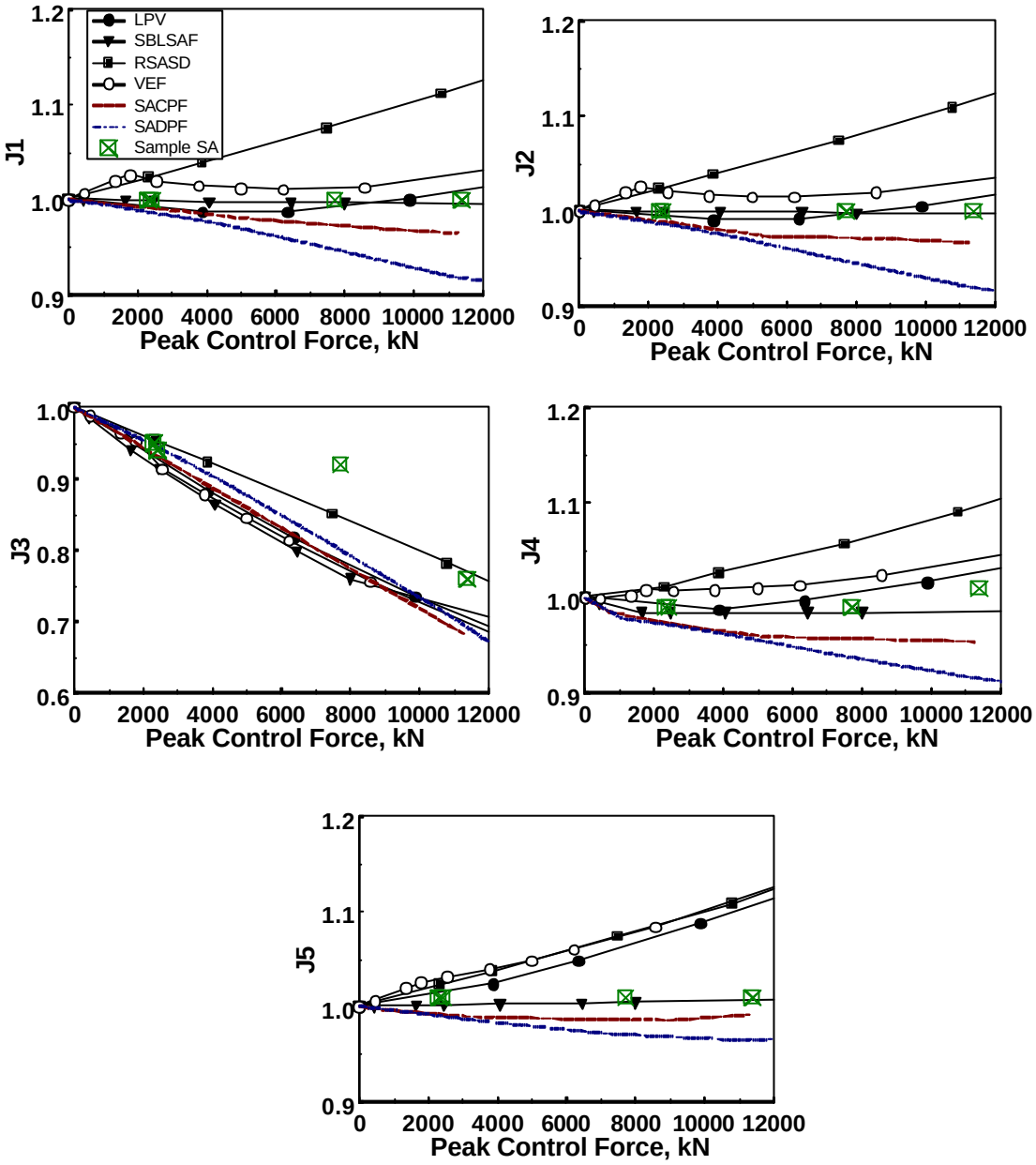

Figure 7.7: Peak Evaluation Criteria as a Function of Peak Control Force during Rinaldi Earthquake in FP-X, FN-Y direction.

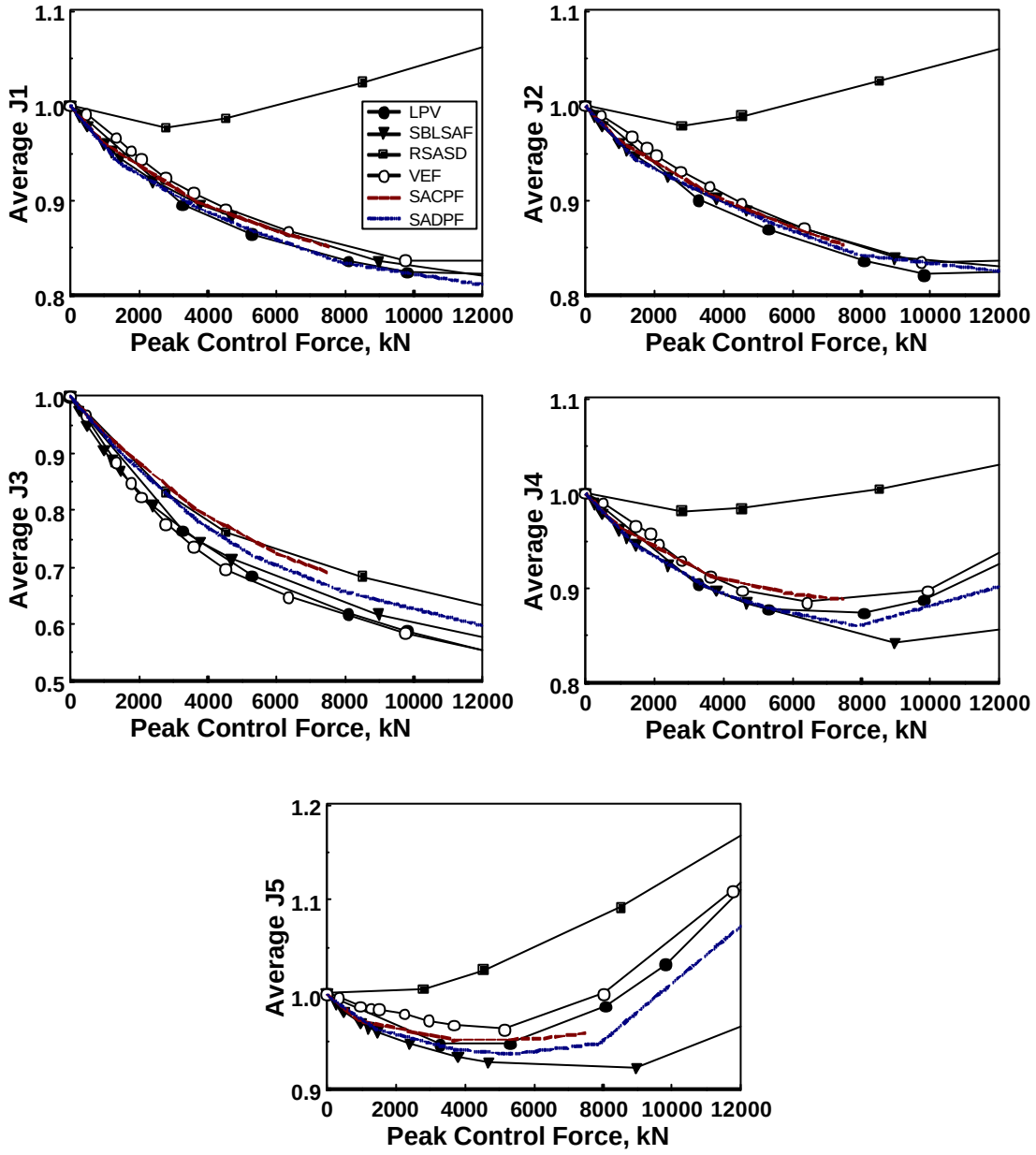

Figure 7.8: Average Peak Evaluation Criteria Using 14 earthquake cases as a Function of Peak Control Force.

c) Time History Plots

Fig. 7.9 and 7.10 show the time-history plots of various response quantities for the uncontrolled building, and the building with SACPF, SADPF and Sample controllers in Tables 7.9-7.15 using Erzinkan FP-X, FN-Y earthquake.

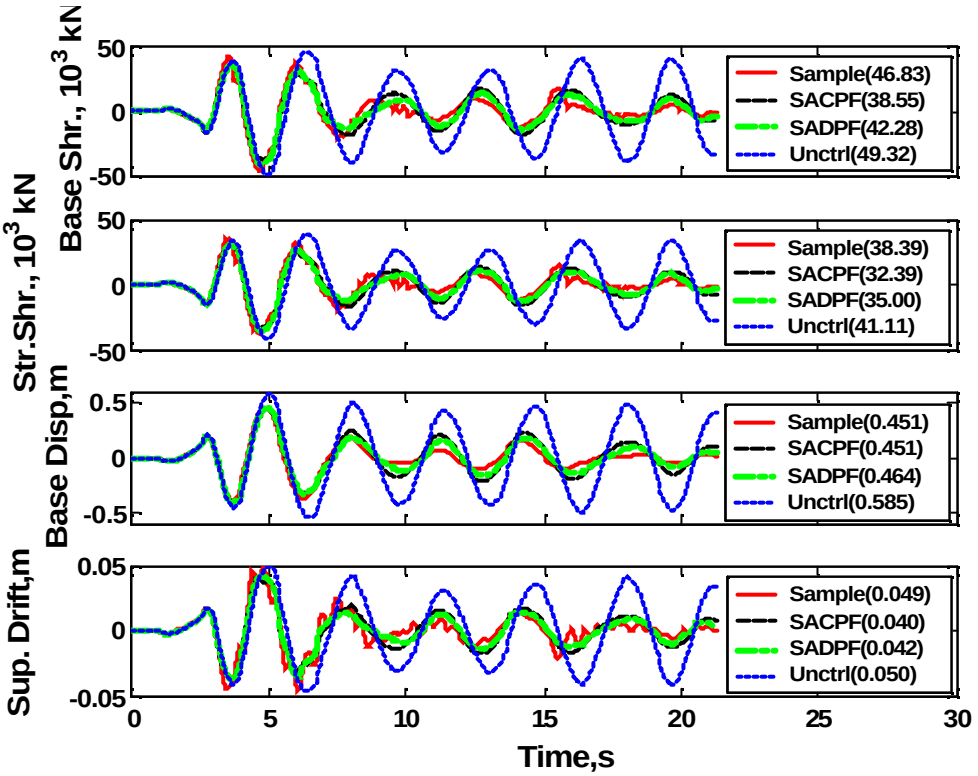

Figure 7.9: Time history plots of Base shear, Super-structure shear, Base displacement at the center of mass, and Drift at 8th floor using Erzinkan earthquake in FP-X and FN-Y direction.

Fig. 7.9 presents the plots for the base shear, structure shear, base displacement (the Center of Mass) and super-structure drift between 7th and 8th floor. The plotted quantities in Fig. 7.10 are the 8th floor acceleration, control force, total energy dissipated by the controllers and the total input energy. All the quantities plotted in Fig. 7.9 and 7.10 are for the response quantities in Y-direction of the building, except the energy plots which

are the summation of both X and Y directions. The control forces of the three controllers are kept at a same level as shown in Fig. 7.10 in order to have a fair comparison for different quantities.

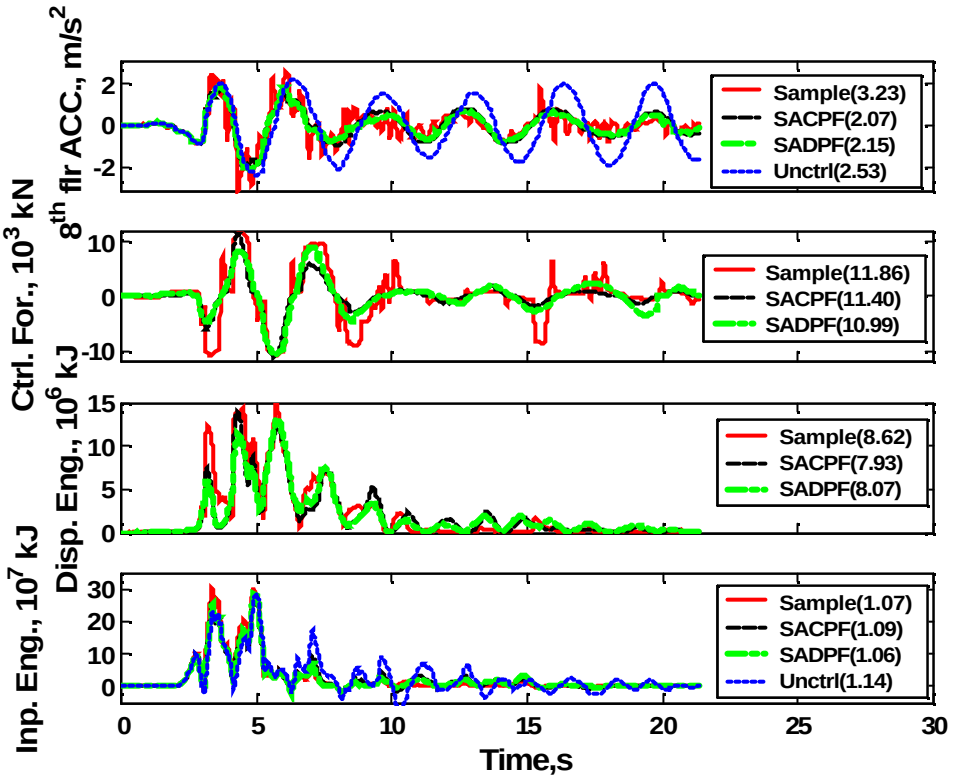

Figure 7.10: Time history plots of 8th floor acceleration, Control force, Dissipated energy and Input energy using Erzinkan earthquake in FP-X and FN-Y direction.

It is observed from Fig. 7.9 and 7.10 that the controlled response quantities can be effectively reduced as compared to the uncontrolled case with the only exception of the 8th floor acceleration. It is observed that the peak acceleration of the 8th floor is increased from 2.53 m/s^2 to 3.23 m/s^2 for the sample semi-active controller. The peak base shear, peak structure shear, peak super-structure drift and peak 8th floor acceleration for the SACPF and SADPF are smaller than those for the sample semi-active controller, while

the peak base displacements at the center of mass are almost the same for the three controlled cases. This again demonstrates that the proposed semi-active controllers based on the active algorithm with pulse filter (APF) are more effective in controlling different response quantities of a base-isolated building simultaneously. The total input energy does not change significantly for the controlled cases compared to the uncontrolled case, and the total energy dissipated by the sample semi-active controller is only slightly larger than that for the SACPF and SADPF controllers.

d) Performance Difference of Controllers

It is observed from Fig. 7.8 that the performance of all controllers in reducing base-displacement (J_3) is quite similar. The performance of RSASD is quite inferior to other controllers in reducing base shear (J_1), structure shear (J_2), inter-story drift (J_4) and floor acceleration (J_5) since RSASD adds force to the base-isolators by adding stiffness, thereby, reducing the isolation effect (i.e., higher acceleration, base-shear and inter-story drifts). All other controllers are primarily dissipative in nature and reduce all response quantities by dissipating energy simultaneously in the practical range of control forces (i.e., less than 6% of building weight as see from last row of Table 7.16).

7.7 CONCLUSIONS

The performance of different active (e.g., Active Pulse Filter (APF) controller, sample controller, Active Kania-Tajimi filter (AKF) controller and LQG), semi-active (e.g., Semi-Active Continuous Pulse Friction (SACPF), Semi-Active Discontinuous Pulse Friction (SADPF), and Smooth Boundary Layer Semi-Active Friction (SBLSAF) and Visco-Elastic Friction (VEF) controllers) and passive controllers are investigated for their

effectiveness in reducing response quantities of the benchmark base-isolated building model.

Among active controllers, the APF controller is designed by augmenting the structural system with a state-space model of near-field ground motion pulses. Comparison of various active controllers demonstrates that the APF controller is capable of reducing base displacement (drift of isolators), super structure drift and absolute accelerations of all floors simultaneously. Performance indices using 7 near-field earthquakes in two directions show that the APF controller is significantly more effective than other active controllers for the same level of control force. Besides the peak response quantities, the amplitude of different response quantities also decreases much faster than those of sample controller with time. This shows that the APF controller is more effective in suppression of vibration, compared to other active controllers.

Among semi-active controllers, SACPF and SADPF are designed by augmenting the structure with a pulse filter model. Detailed numerical results indicate the performance of a particular controller varies from one earthquake to another and all semi-active controllers considered are quite effective in reducing the base displacement of the building. Average results of the performance indices J_1 to J_5 indicate that approximately 20% reduction can be achieved by SACPF, SADPF, LPV, VEF and SBLSAF controllers for the 5 peak response criteria, only 4% reduction can be achieved for the sample semi-active controller and 6% reduction is achieved for the RSASD. The average of J_1 to J_5 increases by 1% for the sample passive controller, although it has the best overall performance in reducing the base displacement response compared to other controllers. Overall, SACPF and SADPF controllers have better capability of reducing all response

quantities compared to other semi-active controllers.

Table 7.1: Average result of performance indices at 10,000kN Control Force

	Sample	LQG	AKT	APF
J1 (Base Shear)	0.95	0.95	1.06	0.81
J2 (Struct. Shear)	0.98	1.00	1.07	0.82
J3 (Base Disp.)	0.71	0.71	0.80	0.64
J4 (Drift)	0.90	1.00	1.20	0.85
J5 (Floor Acc.)	1.07	1.41	1.08	0.97
J6 (Control Force)	0.25	0.25	0.23	0.32
J7 (RMS Base Disp.)	0.65	0.64	0.72	0.52
J8 (RMS Floor Acc.)	0.75	0.99	0.91	0.63
J9 (Device Energy)	0.55	0.55	0.55	0.61

Table 7.2: Evaluation criteria for the building subject to Newhall earthquake.

	FP-X, FN-Y					FN-X, FP-Y				
	Sample	LQG	AKT	AKT1	APF	Sample	LQG	AKT	AKT1	APF
J1	0.86	0.92	0.89	0.89	**0.84**	0.80	0.84	0.82	0.82	**0.76**
J2	0.88	0.94	0.91	0.91	**0.86**	0.86	0.88	0.89	0.87	**0.79**
J3	0.80	0.82	0.79	0.79	**0.75**	0.75	0.75	0.71	0.71	**0.64**
J4	**0.84**	0.91	0.87	0.90	0.88	**0.85**	0.99	0.90	0.77	0.92
J5	**0.87**	0.97	0.90	1.01	0.89	**0.84**	1.02	0.89	0.84	0.95
J6	0.14	0.12	0.14	0.21	0.12	0.15	0.14	0.15	0.25	0.16
J7	0.68	0.72	0.70	0.69	**0.62**	0.72	0.72	0.72	0.71	**0.69**
J8	0.79	0.85	0.82	0.82	**0.77**	0.72	0.77	0.73	0.71	**0.68**
J9	0.44	0.46	0.45	0.46	0.54	0.43	0.50	0.46	0.48	0.56
C. D	**0.17**	0.18	**0.17**	0.18	**0.17**	0.24	0.29	0.26	**0.22**	0.27

Note: Minimum of each evaluation criteria indicated by bold.

Table 7.3: Evaluation criteria for the building subject to Sylmar earthquake

	FP-X, FN-Y					FN-X, FP-Y				
	Sample	LQG	AKT	AKT1	APF	Sample	LQG	AKT	AKT1	APF
J1	0.93	0.92	0.99	0.95	**0.86**	0.96	0.89	1.02	0.99	**0.85**
J2	0.94	0.94	1.00	0.96	**0.89**	0.94	0.88	1.01	0.98	**0.84**
J3	0.93	0.91	0.95	0.93	**0.87**	0.91	0.88	0.93	0.91	**0.81**
J4	0.95	0.95	1.02	0.98	**0.90**	0.92	0.83	0.95	0.94	**0.81**
J5	**0.95**	0.99	1.01	1.07	0.97	0.92	0.84	0.94	0.98	**0.82**
J6	0.13	0.12	0.20	0.19	0.15	0.13	0.13	0.19	0.19	0.15
J7	0.72	0.72	0.73	0.70	**0.65**	0.71	0.69	0.68	0.67	**0.62**
J8	0.84	0.81	0.87	0.83	**0.75**	0.73	0.71	0.76	0.73	**0.64**
J9	0.45	0.51	0.55	0.56	0.54	0.54	0.59	0.61	0.62	0.61
C. D	0.33	0.34	0.38	0.36	**0.32**	0.37	0.34	0.38	0.37	**0.33**

Note: Minimum of each evaluation criteria indicated by bold.

Table 7.4: Evaluation criteria for the building subject to El Centro earthquake

	FP-X, FN-Y					FN-X, FP-Y				
	Sample	LQG	AKT	AKT1	APF	Sample	LQG	AKT	AKT1	APF
J1	0.97	1.00	1.01	0.97	**0.92**	0.99	1.01	1.02	0.97	**0.94**
J2	0.95	0.97	0.98	0.95	**0.90**	0.98	1.01	1.02	0.99	**0.94**
J3	0.83	0.81	0.81	0.80	**0.73**	0.93	0.89	0.85	0.84	**0.77**
J4	0.81	0.85	0.84	0.83	**0.80**	0.97	1.01	1.01	0.97	**0.94**
J5	**0.82**	0.87	0.85	0.93	**0.82**	1.02	1.01	1.06	1.04	**0.95**
J6	0.10	0.09	0.12	0.15	0.12	0.09	0.11	0.12	0.13	0.12
J7	0.78	0.77	0.76	0.75	**0.68**	0.80	0.77	0.75	0.74	**0.67**
J8	0.70	0.71	0.72	0.71	**0.63**	0.77	0.76	0.77	0.77	**0.69**
J9	0.37	0.41	0.42	0.43	0.46	0.37	0.42	0.41	0.43	0.46
C. D	0.17	0.16	0.16	0.16	**0.15**	0.11	0.11	0.11	**0.10**	**0.10**

Note: Minimum of each evaluation criteria indicated by bold.

Table 7.5: Evaluation criteria for the building subject to Rinaldi earthquake

	FP-X, FN-Y					FN-X, FP-Y				
	Sample	LQG	AKT	AKT1	APF	Sample	LQG	AKT	AKT1	APF
J1	0.97	1.06	1.02	0.99	**0.96**	0.90	0.99	0.96	0.88	**0.89**
J2	0.96	1.06	1.01	0.94	**0.96**	**0.94**	1.04	1.00	0.91	**0.94**
J3	0.95	0.92	0.95	0.93	**0.86**	0.74	0.74	0.75	0.73	**0.71**
J4	**0.94**	1.04	0.98	0.94	0.95	**0.95**	1.07	1.00	0.94	0.97
J5	**0.97**	1.06	1.01	1.05	**0.97**	**0.94**	1.07	0.98	1.02	0.99
J6	0.13	0.11	0.19	0.18	0.13	0.10	0.11	0.14	0.15	0.12
J7	0.73	0.71	0.69	0.68	**0.61**	0.67	0.66	0.60	0.60	**0.55**
J8	0.74	0.74	0.73	0.72	**0.66**	0.63	0.65	0.61	0.60	**0.55**
J9	0.46	0.49	0.53	0.53	0.54	0.48	0.52	0.55	0.55	0.58
C. D	0.35	0.34	0.35	0.35	**0.31**	0.36	0.39	0.37	**0.35**	0.36

Note: Minimum of each evaluation criteria indicated by bold.

Table 7.6: Evaluation criteria for the building subject to Kobe earthquake

	FP-X, FN-Y					FN-X, FP-Y				
	Sample	LQG	AKT	AKT1	APF	Sample	LQG	AKT	AKT1	APF
J1	0.90	0.89	0.91	0.90	**0.87**	0.86	0.83	0.86	0.83	**0.78**
J2	0.89	0.89	0.91	0.90	**0.87**	0.85	0.82	0.85	0.83	**0.78**
J3	0.85	0.83	0.81	0.80	**0.82**	**0.79**	0.81	0.79	0.79	0.84
J4	0.89	0.90	0.91	0.89	**0.88**	0.84	0.81	0.83	0.81	**0.77**
J5	0.90	0.91	0.92	0.90	**0.89**	0.84	0.81	0.83	0.81	**0.78**
J6	0.09	0.08	0.12	0.12	0.14	0.12	0.10	0.15	0.14	0.15
J7	0.81	0.79	0.73	0.73	**0.68**	0.78	0.77	0.74	0.74	**0.72**
J8	0.87	0.84	0.86	0.84	**0.77**	0.75	0.73	0.74	0.73	**0.67**
J9	0.34	0.36	0.38	0.38	0.44	0.41	0.42	0.45	0.45	0.49
C. D	0.44	0.44	0.43	0.42	**0.41**	0.56	0.53	0.57	0.55	**0.52**

Note: Minimum of each evaluation criteria indicated by bold.

Table 7.7: Evaluation criteria for the building subject to JiJi earthquake

	FP-X, FN-Y					FN-X, FP-Y				
	Sample	LQG	AKT	AKT1	APF	Sample	LQG	AKT	AKT1	APF
J1	0.84	0.90	0.90	0.88	**0.81**	0.98	1.05	1.04	1.00	**0.94**
J2	0.85	0.90	0.91	0.88	**0.81**	0.98	1.04	1.03	0.98	**0.95**
J3	0.79	0.80	0.78	0.78	**0.72**	0.83	0.86	0.84	0.84	**0.77**
J4	0.82	0.83	0.86	0.79	**0.74**	0.96	1.04	1.01	0.95	**0.96**
J5	**0.90**	0.96	0.94	1.04	0.98	**0.94**	1.03	0.99	0.98	0.97
J6	0.10	0.10	0.12	0.16	0.11	0.10	0.10	0.11	0.16	0.11
J7	0.75	0.75	0.73	0.73	**0.66**	0.87	0.88	0.88	0.87	**0.81**
J8	0.69	0.70	0.67	0.66	**0.60**	0.79	0.83	0.80	0.80	**0.74**
J9	0.41	0.44	0.43	0.45	0.50	0.27	0.31	0.28	0.32	0.38
C. D	0.21	0.21	0.21	0.21	**0.19**	0.24	0.24	0.23	**0.22**	0.23

Note: Minimum of each evaluation criteria indicated by bold.

Table 7.8 : Evaluation criteria for the building subject to Erzinkan earthquake

	FP-X, FN-Y					FN-X, FP-Y				
	Sample	LQG	AKT	AKT1	APF	Sample	LQG	AKT	AKT1	APF
J1	0.99	0.95	1.06	1.04	**0.91**	0.90	0.86	0.97	0.95	**0.83**
J2	1.02	0.97	1.09	1.08	**0.93**	0.90	0.86	0.97	0.96	**0.82**
J3	0.79	0.77	0.75	0.73	**0.66**	0.74	0.75	0.72	0.70	**0.63**
J4	0.85	0.82	0.91	0.89	**0.77**	0.91	0.86	1.02	0.96	**0.82**
J5	0.99	0.94	1.05	1.10	**0.88**	0.92	0.89	1.02	1.01	**0.82**
J6	0.11	0.11	0.16	0.16	0.17	0.12	0.12	0.16	0.15	0.14
J7	0.80	0.77	0.73	0.72	**0.66**	0.73	0.73	0.70	0.70	**0.63**
J8	0.78	0.76	0.79	0.77	**0.68**	0.71	0.71	0.71	0.69	**0.62**
J9	0.45	0.49	0.50	0.51	0.55	0.52	0.54	0.58	0.58	0.61
C. D	0.29	0.29	0.30	0.28	**0.25**	0.31	0.30	0.34	0.32	**0.27**

Note: Minimum of each eva luation criteria indicated by bold.

Table 7.9a: Evaluation criteria for the base-isolated building subject to Newhall earthquake in FP-X, FN-Y directions.

	FP-X, FN-Y							
	Sample Passive	LPV	Sample Semi active	SBLSAF	RSASD	VEF	SACPF	SADPF
J_1	0.91	0.85	0.97	0.87	0.97	0.87	0.84	0.82
J_2	0.95	0.85	**1.02**	0.89	0.99	0.87	0.86	0.85
J_3	0.51	0.57	0.56	0.69	0.68	0.58	0.69	0.68
J_4	**1.30**	**1.02**	**1.04**	0.91	0.94	0.99	**1.01**	0.94
J_5	**2.49**	**1.05**	**1.49**	**1.02**	0.96	**1.03**	**1.08**	1.00
J_6	0.34	0.34	0.30	0.29	0.19	0.30	0.29	0.24
J_7	0.25	0.36	0.33	0.47	0.42	0.37	0.51	0.44
J_8	**1.07**	0.70	0.89	0.73	0.73	0.70	0.77	0.70
J_9	0.89	0.80	0.79	0.69	0.67	0.79	0.64	0.71
C.D	0.25	0.19	0.21	0.18	0.18	0.18	0.19	0.17
F/W	0.056	0.053	0.053	0.045	0.034	0.046	0.044	0.036

Table 7.9b. Evaluation criteria for the base-isolated building subject to Newhall earthquake in FN-X, FP-Y directions.

	FN-X, FP-Y							
	Sample Passive	LPV	Sample Semiactive	SBLSAF	RSASD	VEF	SACPF	SADPF
J_1	0.83	0.78	0.88	0.78	0.87	0.79	0.76	0.74
J_2	0.93	0.79	0.92	0.81	0.90	0.81	0.81	0.77
J_3	0.51	0.56	0.55	0.67	0.67	0.57	0.63	0.60
J_4	**1.32**	**1.08**	**1.24**	0.82	**1.05**	**1.07**	**1.11**	1.00
J_5	**1.85**	**1.19**	**1.40**	0.85	**1.09**	**1.18**	**1.19**	**1.03**
J_6	0.33	0.34	0.30	0.29	0.19	0.30	0.35	0.29
J_7	0.34	0.46	0.42	0.59	0.58	0.48	0.61	0.54
J_8	**1.05**	0.71	0.84	0.73	0.78	0.71	0.77	0.67
J_9	0.89	0.79	0.80	0.68	0.65	0.78	0.66	0.72
C.D	0.40	0.32	0.37	0.26	0.31	0.32	0.32	0.31
F/W	0.056	0.053	0.053	0.045	0.033	0.047	0.053	0.043

Table 7.10a. Evaluation criteria for the base-isolated building subject to Sylmar earthquake in FP-X, FN-Y directions.

	FP-X, FN-Y							
	Sample Passive	LPV	Sample Semiactive	SBLSAF	RSASD	VEF	SACPF	SADPF
J_1	0.90	0.78	0.90	0.79	**1.01**	0.80	0.81	0.83
J_2	0.93	0.79	0.91	0.82	**1.02**	0.82	0.82	0.85
J_3	0.66	0.71	0.73	0.72	0.89	0.73	0.76	0.78
J_4	0.81	0.80	0.87	0.84	0.96	0.81	0.89	0.82
J_5	**1.48**	1.00	**1.16**	0.95	**1.13**	**1.02**	0.97	0.97
J_6	0.25	0.34	0.24	0.27	0.20	0.30	0.30	0.27
J_7	0.40	0.44	0.45	0.45	0.56	0.46	0.47	0.48
J_8	0.82	0.63	0.74	0.60	0.78	0.64	0.63	0.62
J_9	0.86	0.80	0.81	0.76	0.69	0.79	0.75	0.74
C.D	0.27	0.29	0.35	0.30	0.37	0.30	0.32	0.30
F/W	0.062	0.072	0.059	0.058	0.055	0.065	0.065	0.061

Table 7.10b. Evaluation criteria for the base-isolated building subject to Sylmar earthquake in FN-X, FP-Y directions.

	FN-X, FP-Y							
	Sample Passive	LPV	Sample Semiactive	SBLSAF	RSASD	VEF	SACPF	SADPF
J_1	0.79	0.70	0.80	0.70	0.94	0.72	0.73	0.77
J_2	0.78	0.67	0.79	0.69	0.92	0.69	0.71	0.76
J_3	0.68	0.65	0.74	0.64	0.86	0.66	0.68	0.70
J_4	0.80	0.73	0.79	0.73	0.88	0.73	0.70	0.76
J_5	**1.25**	0.89	0.92	0.76	0.95	0.87	0.78	0.80
J_6	0.25	0.33	0.23	0.26	0.20	0.29	0.30	0.29
J_7	0.46	0.47	0.51	0.46	0.61	0.48	0.49	0.50
J_8	0.67	0.49	0.61	0.48	0.67	0.50	0.54	0.55
J_9	0.85	0.80	0.81	0.76	0.69	0.79	0.74	0.76
C.D	0.33	0.30	0.34	0.30	0.38	0.30	0.29	0.31
F/W	0.061	0.073	0.059	0.057	0.061	0.066	0.070	0.069

Table 7.11a. Evaluation criteria for the base-isolated building subject to El Centro earthquake in FP-X, FN-Y directions.

	FP-X, FN-Y							
	Sample Passive	LPV	Sample Semiactive	SBLSAF	RSASD	VEF	SACPF	SADPF
J_1	0.73	0.86	**1.25**	0.95	**1.07**	0.89	0.93	0.86
J_2	0.87	0.82	**1.24**	0.93	**1.04**	0.85	0.91	0.83
J_3	0.14	0.39	0.54	0.53	0.48	0.40	0.71	0.55
J_4	**1.22**	0.72	**1.26**	0.82	0.91	0.74	0.80	0.73
J_5	**2.86**	0.92	**1.61**	0.84	**1.02**	0.92	0.82	0.79
J_6	0.67	0.31	0.38	0.15	0.20	0.27	0.15	0.23
J_7	0.09	0.29	0.42	0.50	0.42	0.30	0.67	0.49
J_8	**1.61**	0.47	0.76	0.59	0.61	0.47	0.69	0.53
J_9	0.82	0.79	0.65	0.59	0.69	0.78	0.48	0.66
C.D	0.21	0.11	0.18	0.13	0.13	0.11	0.14	0.11
F/W	0.048	0.026	0.047	0.014	0.021	0.023	0.014	0.020

Table 7.11b. Evaluation criteria for the base-isolated building subject to El Centro earthquake in FN-X, FP-Y directions.

	FN-X, FP-Y							
	Sample Passive	LPV	Sample Semiactive	SBLSAF	RSASD	VEF	SACPF	SADPF
J_1	0.73	0.86	**1.25**	0.95	**1.07**	0.88	0.93	0.88
J_2	0.93	0.85	**1.24**	0.96	**1.07**	0.87	0.94	0.89
J_3	0.19	0.58	0.65	0.71	0.67	0.59	0.71	0.65
J_4	**2.18**	0.87	**1.37**	0.97	**1.07**	0.89	0.95	0.91
J_5	**3.45**	0.96	**2.08**	0.98	**1.07**	0.95	0.97	0.92
J_6	0.69	0.30	0.37	0.15	0.20	0.27	0.15	0.24
J_7	0.12	0.39	0.42	0.61	0.50	0.41	0.67	0.47
J_8	**2.00**	0.60	0.92	0.70	0.77	0.61	0.73	0.58
J_9	0.81	0.79	0.69	0.56	0.68	0.78	0.49	0.68
C.D	0.24	0.10	0.15	0.10	0.12	0.10	0.10	0.09
F/W	0.048	0.025	0.044	0.014	0.020	0.022	0.013	0.020

Table 7.12a. Evaluation criteria for the base-isolated building subject to Rinaldi earthquake in FP-X, FN-Y directions.

	FP-X, FN-Y							
	Sample Passive	LPV	Sample Semiactive	SBLSAF	RSASD	VEF	SACPF	SADPF
J_1	0.95	**1.05**	**1.04**	1.00	**1.11**	**1.05**	0.95	0.92
J_2	0.96	**1.05**	**1.02**	1.00	**1.11**	**1.05**	0.95	0.92
J_3	0.50	0.61	0.60	0.66	0.78	0.62	0.68	0.71
J_4	0.97	**1.07**	0.96	0.99	**1.09**	**1.07**	0.96	0.92
J_5	**1.12**	**1.17**	**1.01**	**1.01**	**1.11**	**1.16**	**1.03**	0.96
J_6	0.29	0.34	0.27	0.32	0.20	0.30	0.25	0.24
J_7	0.27	0.39	0.38	0.42	0.53	0.40	0.47	0.45
J_8	0.83	0.58	0.71	0.59	0.72	0.58	0.63	0.57
J_9	0.86	0.80	0.77	0.72	0.68	0.78	0.70	0.71
C.D	0.31	0.35	0.31	0.31	0.36	0.34	0.31	0.29
F/W	0.065	0.084	0.067	0.077	0.054	0.076	0.056	0.053

Table 7.12b. Evaluation criteria for the base-isolated building subject to Rinaldi earthquake in FN-X, FP-Y directions.

	FN-X, FP-Y							
	Sample Passive	LPV	Sample Semiactive	SBLSAF	RSASD	VEF	SACP F	SADPF
J_1	0.88	0.97	0.98	0.92	**1.03**	0.97	0.89	0.87
J_2	0.93	**1.02**	**1.01**	0.97	**1.08**	**1.02**	0.94	0.92
J_3	0.53	0.62	0.62	0.72	0.70	0.62	0.69	0.68
J_4	0.93	**1.08**	0.99	1.00	**1.11**	**1.09**	1.00	0.96
J_5	**1.12**	**1.17**	**1.02**	**1.01**	**1.11**	**1.17**	**1.07**	1.00
J_6	0.28	0.32	0.26	0.33	0.20	0.30	0.22	0.21
J_7	0.24	0.37	0.30	0.42	0.50	0.38	0.43	0.37
J_8	0.58	0.43	0.47	0.46	0.54	0.44	0.49	0.42
J_9	0.87	0.80	0.78	0.72	0.68	0.78	0.71	0.73
C.D	0.34	0.40	0.36	0.37	0.40	0.40	0.38	0.36
F/W	0.064	0.081	0.067	0.076	0.052	0.075	0.050	0.048

Table 7.13a. Evaluation criteria for the base-isolated building subject to Kobe earthquake in FP-X, FN-Y directions.

	FP-X, FN-Y							
	Sample Passive	LPV	Sample Semiactive	SBLSAF	RSASD	VEF	SACPF	SADPF
J_1	0.84	0.78	**1.04**	0.78	0.97	0.80	0.78	0.80
J_2	0.84	0.77	**1.03**	0.78	0.95	0.79	0.78	0.79
J_3	0.36	0.44	0.52	0.49	0.51	0.45	0.57	0.51
J_4	**1.19**	0.93	1.00	0.78	0.92	0.88	0.84	0.74
J_5	**2.34**	**1.31**	**1.63**	1.00	**1.06**	**1.22**	**1.09**	**1.05**
J_6	0.39	0.33	0.28	0.21	0.20	0.28	0.24	0.20
J_7	0.16	0.31	0.26	0.45	0.45	0.33	0.54	0.46
J_8	**1.14**	0.55	0.73	0.59	0.66	0.54	0.62	0.50
J_9	0.87	0.79	0.73	0.66	0.65	0.78	0.60	0.66
C.D	0.28	0.23	0.25	0.19	0.22	0.22	0.20	0.19
F/W	0.056	0.044	0.051	0.028	0.033	0.038	0.032	0.028

Table 7.13b. Evaluation criteria for the base-isolated building subject to Kobe earthquake in FN-X, FP-Y directions.

	FN-X, FP-Y							
	Sample Passive	LPV	Sample Semiactive	SBLSAF	RSASD	VEF	SACPF	SADPF
J_1	0.96	0.94	**1.15**	0.95	**1.17**	0.96	0.92	0.91
J_2	1.00	0.94	**1.20**	0.94	**1.16**	0.96	0.92	0.92
J_3	0.40	0.46	0.52	0.54	0.58	0.47	0.63	0.58
J_4	**1.30**	0.96	**1.33**	0.97	**1.16**	0.98	0.95	0.95
J_5	**2.24**	0.99	**1.47**	1.00	**1.21**	1.00	0.98	0.95
J_6	0.41	0.34	0.30	0.19	0.20	0.29	0.28	0.24
J_7	0.20	0.35	0.38	0.47	0.49	0.36	0.62	0.59
J_8	**1.44**	0.74	0.98	0.68	0.76	0.72	0.74	0.65
J_9	0.87	0.79	0.72	0.65	0.65	0.78	0.56	0.61
C.D	0.28	0.21	0.30	0.23	0.25	0.22	0.22	0.22
F/W	0.055	0.045	0.050	0.026	0.033	0.039	0.037	0.031

Table 7.14a. Evaluation criteria for the base-isolated building subject to JiJi earthquake in FP-X, FN-Y directions.

	FP-X, FN-Y							
	Sample Passive	LPV	Sample Semiactive	SBLSAF	RSASD	VEF	SACPF	SADPF
J_1	0.83	0.76	0.84	0.78	0.90	0.79	0.74	0.77
J_2	0.82	0.77	0.84	0.79	0.91	0.79	0.73	0.76
J_3	0.65	0.66	0.65	0.63	0.67	0.66	0.68	0.73
J_4	0.86	0.79	0.86	0.81	0.91	0.81	0.71	0.77
J_5	0.92	0.81	0.87	0.84	0.92	0.83	0.74	0.80
J_6	0.17	0.23	0.17	0.23	0.20	0.21	0.22	0.23
J_7	0.42	0.44	0.46	0.45	0.49	0.45	0.47	0.49
J_8	0.82	0.61	0.72	0.61	0.73	0.61	0.62	0.62
J_9	0.70	0.65	0.64	0.65	0.64	0.65	0.63	0.63
C.D	0.45	0.37	0.44	0.38	0.45	0.38	0.32	0.37
F/W	0.067	0.086	0.069	0.087	0.087	0.080	0.080	0.087

Table 7.14b. Evaluation criteria for the base-isolated building subject to JiJi earthquake in FN-X, FP-Y directions.

	FN-X, FP-Y							
	Sample Passive	LPV	Sample Semiactive	SBLSAF	RSASD	VEF	SACPF	SADPF
J_1	0.74	0.68	0.74	0.68	0.83	0.70	0.66	0.71
J_2	0.74	0.68	0.73	0.68	0.83	0.70	0.65	0.70
J_3	0.63	0.64	0.63	0.58	0.66	0.64	0.65	0.72
J_4	0.75	0.67	0.73	0.68	0.85	0.69	0.62	0.68
J_5	0.77	0.69	0.80	0.70	0.92	0.71	0.65	0.70
J_6	0.17	0.23	0.17	0.23	0.19	0.22	0.22	0.22
J_7	0.40	0.44	0.46	0.45	0.56	0.44	0.51	0.52
J_8	0.74	0.52	0.61	0.52	0.71	0.52	0.54	0.55
J_9	0.70	0.65	0.64	0.65	0.59	0.65	0.62	0.63
C.D	0.53	0.48	0.51	0.48	0.57	0.49	0.43	0.48
F/W	0.068	0.087	0.069	0.087	0.087	0.084	0.082	0.087

Table 7.15a. Evaluation criteria for the base-isolated building subject to Erzinkan earthquake in FP-X, FN-Y directions.

	FP-X, FN-Y							
	Sample Passive	LPV	Sample Semiactive	SBLSAF	RSASD	VEF	SACPF	SADPF
J_1	0.94	0.76	0.93	0.74	**1.05**	0.78	0.76	0.84
J_2	0.95	0.78	0.93	0.77	**1.06**	0.80	0.78	0.85
J_3	0.49	0.45	0.47	0.46	0.58	0.46	0.49	0.51
J_4	0.85	0.76	0.86	0.73	0.92	0.77	0.81	0.79
J_5	**1.21**	0.84	**1.23**	0.78	**1.10**	0.84	0.89	0.82
J_6	0.26	0.33	0.25	0.29	0.21	0.29	0.30	0.28
J_7	0.32	0.38	0.34	0.41	0.53	0.40	0.42	0.40
J_8	0.60	0.51	0.63	0.54	0.70	0.53	0.57	0.53
J_9	0.87	0.80	0.80	0.74	0.70	0.79	0.72	0.76
C.D	0.27	0.24	0.27	0.23	0.30	0.24	0.24	0.25
F/W	0.061	0.063	0.059	0.055	0.055	0.056	0.056	0.058

Table 7.15b. Evaluation criteria for the base-isolated building subject to Erzinkan earthquake in FN-X, FP-Y directions.

	FN-X, FP-Y							
	Sample Passive	LPV	Sample Semiactive	SBLSAF	RSASD	VEF	SACPF	SADPF
J_1	0.85	0.68	0.84	0.68	0.97	0.70	0.72	0.80
J_2	0.85	0.69	0.83	0.68	0.96	0.71	0.72	0.80
J_3	0.51	0.46	0.50	0.45	0.58	0.47	0.52	0.53
J_4	0.95	0.71	0.89	0.72	0.95	0.74	0.73	0.79
J_5	**1.13**	0.73	**1.14**	0.76	**1.07**	0.77	0.77	0.83
J_6	0.25	0.33	0.24	0.28	0.21	0.28	0.30	0.25
J_7	0.29	0.34	0.32	0.37	0.46	0.35	0.45	0.42
J_8	0.48	0.42	0.52	0.44	0.60	0.43	0.50	0.48
J_9	0.87	0.81	0.79	0.74	0.72	0.80	0.72	0.76
C.D	0.33	0.24	0.34	0.25	0.31	0.25	0.25	0.27
F/W	0.061	0.064	0.059	0.055	0.056	0.057	0.061	0.058

Table 7.16 Average Evaluation Criteria for the base-isolated building using average of the 14 cases in Tables 1-7.

	FN-X, FP-Y							
	Sample Passive	LPV	Sample Semiactive	SBLSAF	RSASD	VEF	SACPF	SADPF
J_1	0.85	0.82	0.97	0.83	1.00	0.84	0.82	0.82
J_2	0.89	0.82	0.98	0.84	1.00	0.84	0.82	0.83
J_3	0.48	0.56	0.59	0.61	0.67	0.57	0.65	0.64
J_4	**1.10**	0.87	**1.01**	0.84	0.98	0.88	0.86	0.84
J_5	**1.73**	0.98	**1.27**	0.89	**1.05**	0.98	0.93	0.90
J_6	0.34	0.32	0.27	0.25	0.20	0.28	0.26	0.25
J_7	0.28	0.39	0.39	0.47	0.51	0.40	0.52	0.47
J_8	0.99	0.57	0.72	0.59	0.70	0.57	0.63	0.57
J_9	0.84	0.78	0.74	0.68	0.67	0.77	0.64	0.70
C.D	0.32	0.27	0.31	0.27	0.31	0.28	0.27	0.27
F/W	0.059	0.061	0.058	0.052	0.049	0.055	0.051	0.050
J^*_{1-5}	1.01	0.81	0.96	0.80	0.94	0.82	0.82	0.81

CHAPTER 8

DESIGN OF HYBRID CONTROLLERS FOR DISPLACEMENT CONTROL OF FLEXIBLE STRUCTURES SUBJECT TO LONG-PERIOD EXCITATIONS

8.1 INTRODUCTION

It has been observed from historic earthquakes that some near-field earthquake records contain distinct long-period pulses. For example, the 1999 Chi-Chi earthquake has pulse type components with period in the range of 10 seconds. The long-period pulses may impose very large displacement demands, especially on long-period flexible structures such as nonlinear base-isolated structures [He and Agrawal (2005), Nagarajaiah and Ferrell (1999)]. On the other hand, acceleration responses are usually smaller for flexible structures compared to rigid and intermediate structures. Hence, mitigation of displacement responses during long-period pulse-type excitations is the main objective in designing seismic protective systems.

Effectiveness of most of the existing structural control strategies is attained through adjusting damping and/or stiffness property of the target structural systems. Performance of supplemental stiffness and damping varies significantly depending on the structures being controlled as well as the excitations they might be subjected to. It is noted from the

results presented in Chapter 4 and 5 that although the effectiveness of passive viscous dampers degrades when the excitation period is not in the vicinity of structural period, i.e., out of resonant region, viscous dampers are effective in reducing displacements caused by the broadband components of near-field ground motions. On the other hand, the performance of passive yielding (stiffness) dampers depends on the ratio of structural and pulse-type excitation periods and they are not effective for long-period structures [Xu et al (2006)].

Some recent investigations have shown that variable damping and stiffness mechanisms could have better control effects than their passive counterparts [Nagarajaiah and Mate (1998), Nasu et al (2001)]. In this chapter, a hybrid semi-active stiffness controller is proposed based on a combined mechanism of viscous damping and variable stiffness. The viscous damping term in the hybrid controller aims at reducing the displacement responses caused by the broadband components of earthquakes while the semi-active stiffness term is designed to mitigate displacement responses caused by dominant pulse components of earthquakes. The stiffness of the proposed controller varies with respect to the displacement across the damper, and the stiffness force is only triggered when the displacement is greater than certain preset value. Hence, the operation of the hybrid control system is divided in two different stages: (i) the control system behaves as passive viscous damper for small and moderate earthquakes (ii) the semi-active stiffness controller is triggered when structural response exceeds certain preset value. During the second stage, stiffness and damping properties of semi-active system

are adjusted depending on instantaneous response. Following this approach, both the damping and stiffness mechanisms are designed to be always energy-dissipative during the operation to guarantee unconditional stability of the system. In this chapter, the behavior of the proposed controller is investigated through parametric study and spectrum analysis using nonlinear SDOF systems followed by an investigation using a benchmark base-isolated highway bridge model developed recently by Agrawal et al (2005) and Tan and Agrawal (2005).

8.2. DESIGN OF OPTIMAL STIFFNESS DAMPER BEHAVIOR

Passive and semi-active dampers reduce structural responses by dissipating the input energy. Besides, nonlinear energy dissipative mechanism consisting of a combination of different hysteretic behaviors such as viscous, yielding and friction, etc., has been shown to be more effective than pure displacement or velocity dependent mechanisms. A dissipative nonlinear behavior can be obtained by a suitable combination of viscous, nonlinear stiffness and hysteretic damping components expressed by the following equation,

$$F = F(x,\dot{x},p) = Viscous\ mechanism + Stiffness\ mechanism + Hysteresis\ mechanism \quad (8.1)$$

where p represents an ensemble of characteristic parameters, e.g., damping, stiffness, etc., and x and $\dot{x}$ are respectively the displacement and velocity across the device. The nonlinear damping in Eq.(8.1) can be modeled by a hysteretic model, e.g., Bouc-Wen model, with selected parameters to shape the loop for a desired form of force. The

combined nonlinear behavior of the controller can be realized by driving hysteretic dampers such as ER or MR damper with command current and applied selectively to various structures.

For a generalized design problem, an example of stiffness force can be obtained through a combination of polynomial functions such as

$$f = \ldots + k_{15}x^{1/5} + k_{13}x^{1/3} + k_1 x + k_3 x^3 + k_5 x^5 + \ldots \tag{8.2}$$

where k_{15}, k_{13}, k_1, k_3 and k_5 are the coefficients controlling the shape of stiffness shaping function in Eq.(8.2), where hardening (i.e., adding stiffness) or softening (i.e., positive secant stiffness and negative tangential stiffness) damper behavior can be obtained by choosing appropriate values of these coefficients. Exponents in Eq.(8.2) control the rate of force variation and they can be chosen according to practical design requirement and damper capacity. In this investigation, the following type of nonlinear stiffness shaping function is chosen to model stiffness force applied by dampers,

$$F(x) = \begin{cases} k_1 x & |x| \le X_1 & \text{Stage ①, linear increase} \\ F_{10} + k_2 (x - X_1)^3 & X_1 < |x| \le X_2 & \text{Stage ②, rapid increase} \\ F_{20} + k_3 (x - X_2)^{1/3} & X_2 < |x| \le X_3 & \text{Stage ③, mild increase} \\ F_{30} - k_4 (x - X_3)^3 & X_3 < |x| \le X_4 & \text{Stage ④, damper softening} \\ 0 & |x| > X_4 & \text{Stage ⑤, no damper force} \end{cases} \tag{8.3}$$

where X_1, X_2, X_3 and X_4 are threshold displacements for different stages, k_1, k_2, k_3 and k_4 are corresponding damper stiffness coefficients which have the units of N/m, N/m^3,

$N/m^{1/3}$ and N/m^3, respectively. In Eq.(8.3), F_{10}, F_{20} and F_{30} are forces at the corresponding threshold displacement X_1, X_2 and X_3, respectively, i.e.,

$$F_{10} = k_1 X_1$$

$$F_{20} = k_1 X_1 + k_2 (X_2 - X_1)^3 \tag{8.4}$$

$$F_{30} = k_1 X_1 + k_2 (X_2 - X_1)^3 + k_3 (X_3 - X_2)^{1/3}$$

Eq. (8.3) indicates that the instantaneous stiffness of the nonlinear stiffness damper varies with displacement. The damper behavior is controlled by the threshold displacement X_1 to X_4 and stiffness k_1 to k_3. By adjusting these parameters, the stiffness damper can emulate different types of behavior with increase in displacement.

Fig. 8.1 illustrates the application of the proposed stiffness damper to a SDOF system possessing bilinear behavior. It is observed from Fig. 8.1 that the damper shows different force-displacement characteristics during different stages. When the displacement is less than the threshold displacement X_1, damper force increases linearly with displacement. When displacement increases beyond X_1, the damper force is a cubic function of displacement increment since it is pre-assumed that the structure is likely to undergo excessive displacement during this stage. The damper force increases in a milder way beyond X_2, considering the practical capacity limit. The displacement X_3 corresponds to the maximum capacity of the damper. If the displacement continues to increase beyond X_3, the damper can either take a softening type behavior or be saturated. It is noted from Fig. 8.1 that saturation behavior is equivalent to the case of setting up a very large threshold displacement X_4.

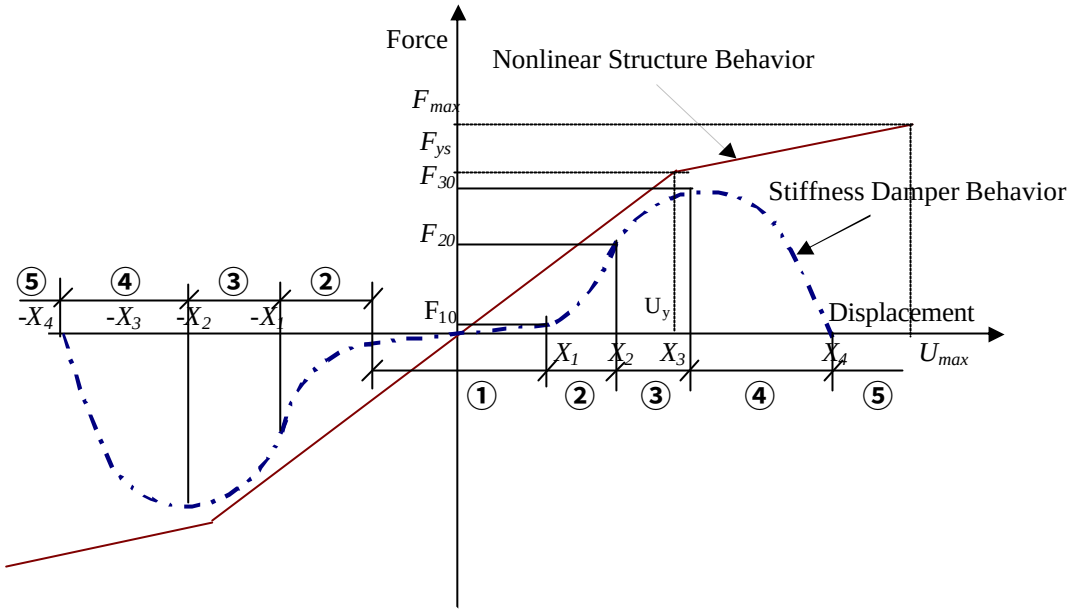

Figure 8.1: Force-displacement Relationship of Nonlinear Structure and Proposed Stiffness Damper

By deriving the damper force with respect to the displacement across it, the instantaneous stiffness of the damper can be obtained as,

$$\frac{dF(x)}{dx}=\begin{cases} k_1 & |x|\le X_1 \quad \text{Stage ①} \\ 3k_2(x-X_1)^2 & X_1<|x|\le X_2 \quad \text{Stage ②} \\ \frac{1}{3}k_3(x-X_2)^{-2/3} & X_2<|x|\le X_3 \quad \text{Stage ③} \\ -3k_4(x-X_3)^2 & X_3<|x|\le X_4 \quad \text{Stage ④} \\ 0 & |x|>X_4 \quad \text{Stage ⑤} \end{cases} \tag{8.5}$$

Eq. (8.5) shows that the instantaneous stiffness of damper is a function of the initial stiffness, instantaneous displacement and the preset threshold displacements. The damper stiffness is constant in stage 1. In stage 2, damper stiffness is quadratic function of

displacement across the damper. In stage 3, the instantaneous damper stiffness is still positive but starts decreasing with further increase in displacement beyond X_2. When the damper reaches its saturation point (maximum force capacity, corresponding to X_3), instantaneous stiffness starts decreasing into negative values, which accounts for softening behavior of the damper.

The behavior of damper during different stages can be adjusted by setting the threshold displacements X_i (i=1, 2, 3, 4) appropriately. The following procedure can be used to preset damper parameters:

1. Determine the threshold displacement X_1, X_2, X_3, and X_4 of the damper according to the property of the target structure. If the damper is to be applied in a nonlinear structure, threshold displacements should be determined according to yielding displacement and maximum allowable displacement of the structure. For a base-isolated structure, the characteristic displacements can be set according to the maximum allowable isolator deformation.
2. Assume a reasonable/practical damper force capacity, F_{dmax}, which is F_{30} at displacement X_3 as shown in Fig. 8.1.
3. Determine the reference stiffness by

$$k_{ref} = \frac{F_{30}}{X_3} \tag{8.6}$$

4. Assuming that points (0,0), (X_2, F_{20}) and (X_3, F_{30}) are collinear, stiffness k_2, k_3 and k_4 are determined as:

$$k_{ref} X_2 = F_{10} + k_2 (X_2 - X_1)^3 \rightarrow k_2 = \frac{(k_{ref} X_2 - F_{10})}{(X_2 - X_1)^3}$$

$$k_{ref} X_3 = F_{20} + k_3 (X_3 - X_2)^{1/3} \rightarrow k_3 = \frac{k_{ref} X_3 - F_{20}}{(X_3 - X_2)^{1/3}} \tag{8.7}$$

$$0 = -k_4 (X_4 - X_3)^3 + F_{30} \rightarrow k_4 = \frac{F_{30}}{(X_4 - X_3)^3}.$$

The stiffness k_1 can be set equal to zero or it can be provided by a small elastic spring for the purpose of providing restoring force.

8.3 PARAMETRIC STUDY OF THE PROPOSED CONTROLLER

The proposed polynomial stiffness function contains an ensemble of parameters and it can emulate different forms of linear and nonlinear behavior through an appropriate selection of damper parameters. For example, by setting X_1 equals to a sufficiently large value, the expression in Eq. (8.4) represents a linear stiffness damper; by setting $X_1 = X_2 = X_3$ and a sufficiently large X_4, the function represents an elasto-plastic friction or yielding damper.

To investigate the influence of these parameters, a nonlinear SDOF structure with constant displacement ductility factor μ = 4, and stiffness corresponding to a linear structural period of T_n = 0.6 seconds (which results in effective period T_e = 1 second) is used. The nonlinear SDOF structure is modeled using Bouc-Wen model with the parameters A_s = 1.0, $a_s = 0.1$, $b_s = g_s = 0.5$, n_s = 3.0. Details of the Bouc-Wen model and the parameters can be found in Chapter 4. The proposed stiffness damper is applied to the nonlinear structure to determine various parameters by subjecting the structure to the

pulse-type excitation in Fig. 4.1 of Chapter 4. The nonlinear structure is assumed to have unit mass and the corresponding elastic stiffness, k_e, is 109.66 N/m. The maximum uncontrolled displacement of the nonlinear structure is 0.201m (U_{max}=0.201m) and the yielding displacement limit is 0.05m (U_{ys}=0.05m for μ= 4) under the pulse excitation.

Fig. 8.2 shows the influence of the damper parameters on the displacement and acceleration responses as well as the damper hysteretic behavior. One parameter is investigated in each case, where Fig. 8.2a, 8.2b, 8.2c, 8.2d, 8.2e and 8.2f show the results for parameter X_1, X_2, X_3, X_4, k_1 and F_d/F_y, respectively. The damper parameters are determined according to the procedure described previously.

It is observed from Fig. 8.2 that the displacement responses are significantly reduced after adding the stiffness damper in all cases. In Fig. 8.2(a), the controlled case of X_1=0 significantly reduces the peak displacement responses from 0.201m to 0.059m with an increase of acceleration from 0.758g to 1.135g compared with the uncontrolled case. For the controlled cases, as the X_1 increases from 0 to 0.8U_{ys}, the displacement response increases from 0.069m to 0.08m and the acceleration response increases from 1.135 to 1.165g. The variations are small compared with that of the uncontrolled case. This indicates that the action of the damper starting from small structural deformation is not significantly helpful in overall control effect. Hence, stiffness damper force only needs to be applied when the structure deformation is larger than certain safety limit.

It is observed from Fig. 8.2b that displacement increases from 0.061m to 0.086m and acceleration response also increases from 1.108g to 1.176g as X_2 is increased from

$0.5U_y$ to 1.0 U_y. Hence, a smaller X2 is more beneficial in terms of displacement mitigation. As a result, when structural deformation exceeds the critical displacement X_1, the control force should be applied as quickly as possible.

It is observed from Fig. 8.2(c) that both the maximum displacement and acceleration decrease with increase in X_3. It is noted from the force-displacement plot in Fig. 8.2c that X_3 corresponds to the peak value of the control force. Hence, a smaller X_3 implies that the damper reaches its full capacity at a smaller deformation. This fact indicates that the full damper capacity should be reached soon after the displacement exceeds the critical value X_2 in order to effectively limit the buildup of excessive displacement thereafter.

The parameter X_4 controls the post-yielding behavior of the damper. As it is observed from the force-displacement plot of Fig. 8.2(d), the damper shows elastic-plastic behavior (i.e., saturation) for a very large X_4 (e.g., X_4=10U_{ys} in this case). For the case of X_4 = 1.5U_{ys} and X_4=1.8U_{ys}, the damper exhibits softening-type behavior. However, it is seen that a softening-type behavior is not effective in reducing displacement, since the peak displacement increases with decrease in X_4.

A larger initial stiffness k_1 can only slightly decrease the maximum displacement and acceleration compared to k_1=0 as seen in Fig. 8.2e. This indicates that initial stiffness of supplemental damper does not affect the overall control effect. However, nonzero elastic spring k_1 is helpful in reducing permanent displacement, as shown in displacement plot of Fig. 8.2e.

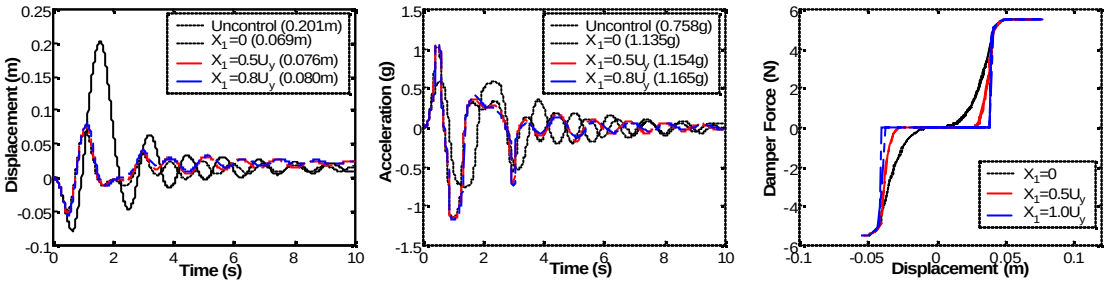

a) Influence of parameter X_1 (X_2=0.8U_y, X_3=1.0U_y, X_4=100U_y, k_1=0, F_d=F_y)

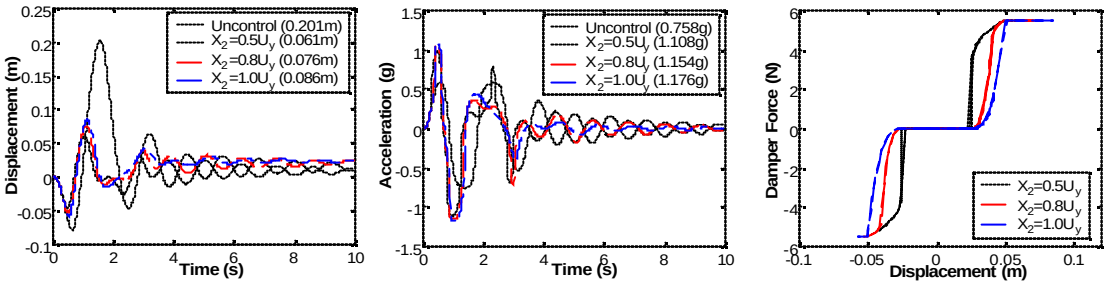

b) Influence of parameter X_2 (X_1=0.5U_y, X_3=1.0U_y, X_4=100U_y, k_1=0, F_d=F_y)

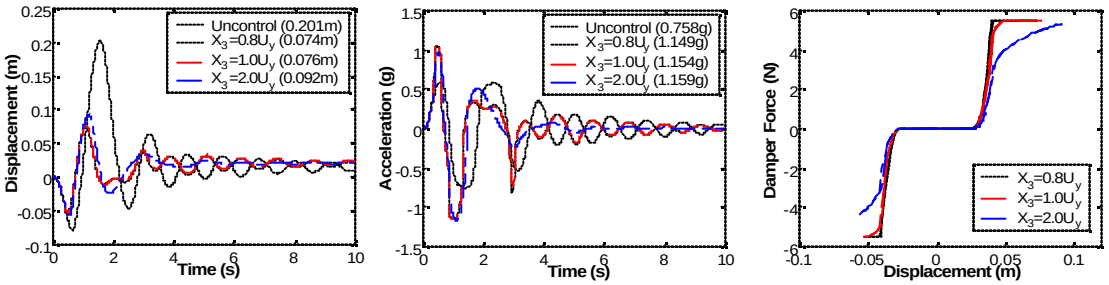

c) Influence of parameter X_3 (X_1=0.5U_y, X_2=0.8U_y, X_4=100U_y, k_1=0, F_d=F_y)

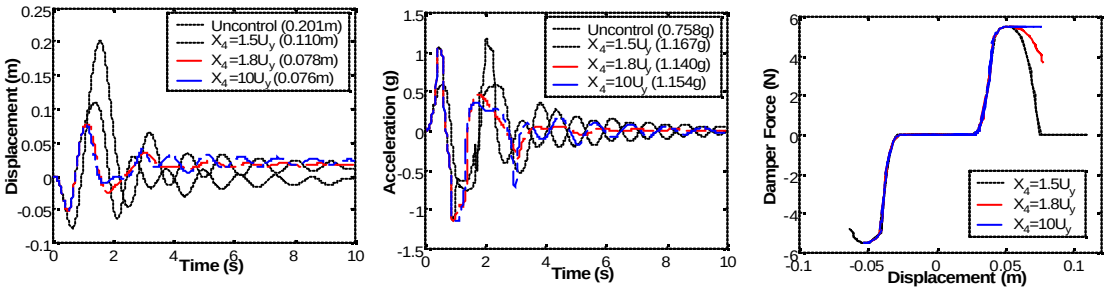

d) Influence of parameter X_4 (X_1=0.5U_y, X_2=0.8U_y, X_3=1.0U_y, k_1=0, F_d=F_y)

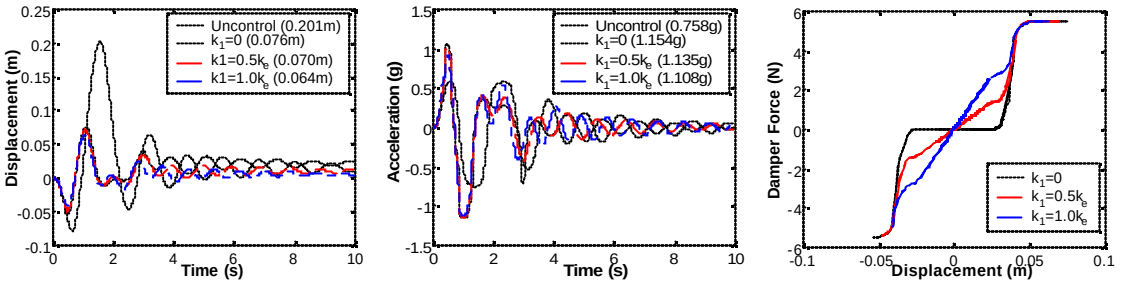

e) Influence of parameter k_1 (X_1=0.5U_y, X_2=0.8U_y, X_3=1.0U_y, X_4=100U_y, F_d=F_y)

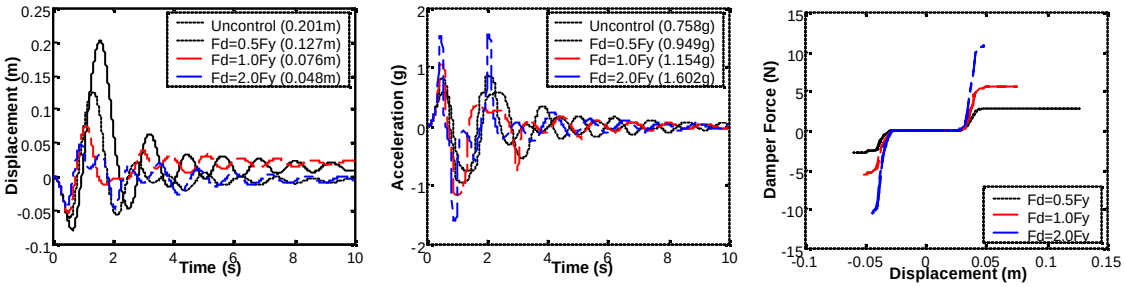

f) Influence of parameter F_d/F_y (X_1=0.5U_y, X_2=0.8U_y, X_3=1.0U_y, X_4=100U_y, k_1=0)

Figure 8.2 Parametric analysis of the proposed nonlinear stiffness damper

Plots in Fig. 8.2f show that the maximum damper capacity significantly affects the displacement and acceleration responses. An F_d increasing from 0.5F_y to 2F_y results in a significant reduction in displacement from 0.127m to 0.048m. However, acceleration also increases from 0.949g to 1.602g. Generally, a larger damper capacity can achieve better displacement reduction. However, this is accompanied by the amplification in acceleration response.

8.4. INFLUENCE OF EXCITATION FREQUENCY ON THE PROPOSED CONTROLLER PERFORMANCE

Fig. 8.3 shows ductility, displacement and acceleration responses as a function of excitation period for a nonlinear SDOF system with elastic period T_n=0.6s, μ=4. The parameters of the nonlinear stiffness damper are: k_1=0; X_1=0.5U_y; X_2=0.8U_y; X_3=1.0U_y; X_4=100U_y and F_d=F_y. The pulse excitation period is in the range of 0.1 and 5 sec.

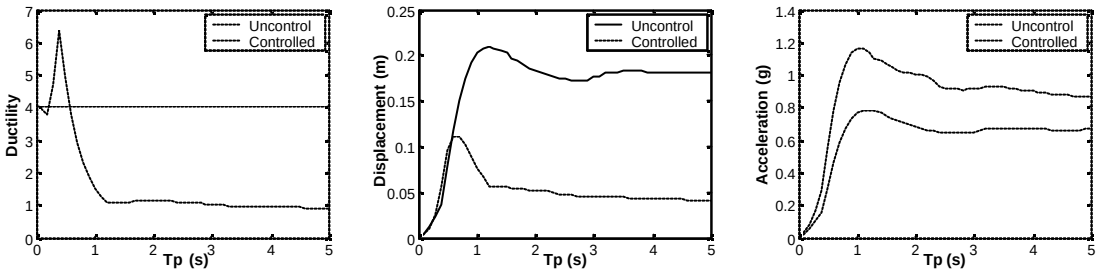

Figure 8.3 Ductility, displacement and acceleration spectrum versus pulse period: a) Ductility; b) Displacement; c) Acceleration.

It is observed from Fig. 8.3a that the ductility factor of the controlled system can be effectively reduced to 1 (i.e., without inelastic deformation) when T_p = 1 second. The reduction in ductility is consistent with displacement spectra in Fig. 8.3b. However, the acceleration response is amplified by 20 to 30% after adding the stiffness damper, as shown in Fig. 8.3c.

8.5. HYBRID SEMI-ACTIVE STIFFNESS DAMPER

It is noted that the stiffness of the proposed stiffness damper is a function of the displacement across it. To increase the energy-dissipation capacity, a secondary semi-active constraint is applied as the following,

$$f_{SA} = \begin{cases} f_s & x\dot{x} \geq 0 \\ -f_s & x\dot{x} < 0 \end{cases} \tag{8.8}$$

in which the f_s is the stiffness damper force given by Eq. (8.3), and x and $\dot{x}$ are respectively the displacement and velocity across the damper. Since the damper force obtained from Eq. (8.2) is the odd function of x, the semi-active damper force in Eq. (8.8) is always dissipative.

A viscous damping term can also be added to increase the energy-dissipation capacity of the proposed semi-active stiffness damper in Eq. (8.8). A hybrid controller is then obtained as,

$$u = \begin{cases} f_v + f_s & x\dot{x} \geq 0 \\ f_v - f_s & x\dot{x} < 0 \end{cases} \tag{8.9}$$

in which f_v is the force applied by viscous damper. It is noted from the parametric analysis in Fig. 8.2 that the parameter X_1 does not obviously influence on the total stiffness of the stiffness damper. Hence, the hybrid controller can also be expressed as

$$u = \begin{cases} f_v, & |x| \leq X_1 \\ f_v + f_s, & |x| > X_1 \text{ and } x\dot{x} > 0 \\ f_v - f_s, & |x| > X_1 \text{ and } x\dot{x} < 0 \end{cases} \tag{8.10}$$

Viscous damping force is applied at all time instants to dissipate input energy through cyclic motions. The damper behavior described by Eq.(8.10) is designated as Hybrid Semi-Active Stiffness Damper (HSASD). It is noted that the HSASD is a combination of stiffness, damping and hysteretic mechanisms.

8.6. PERFORMANCE OF PROPOSED HYBRID STIFFNESS DAMPER DURING RECORDED GROUND MOTIONS

The effectiveness of the proposed hybrid stiffness damper described in Eq. (8.10) is investigated by subjecting a nonlinear SDOF structure with ductility factor of 4 and elastic period of 2.5 sec. to 25 recorded near-field ground motions. For simplicity, the structure is assumed to have a unit mass. Detailed information of the 25 records is listed in Table 3 of Appendix. The characteristic parameters of the stiffness damper are taken as:

$$X_1=0.5U_y;\ X_2=0.8U_y,\ X_3=1.0U_y,\ X_4=100U_y,\ k_1=0,\ Fd_{max}=0.8F_y \qquad (8.11)$$

in which U_y and F_y are yielding displacement and initial yielding force of the structure, respectively. The stiffness k_1 = 0 indicates that no stiffness force is applied when the structural displacement is less than $0.5U_y$. Preset displacement X_4 =$100U_y$ indicates that the damper force saturates at F_{dmax} when the displacement across the damper exceeds X_3. The stiffness k_2, k_3 and k_4 are determined according to the procedure described in section 8.2. The viscous force of the hybrid damper is obtained by linear viscous dampers capable of adding 15% equivalent damping.

8.6.1 Peak Responses

Fig. 8.4 shows displacement, ductility and acceleration spectra of the SDOF structure with and without the damper and subjected to the 25 recorded ground motions. It is observed from Fig. 8.4a that proposed hybrid stiffness damper is capable of reducing displacement responses significantly. Average displacement of the structure without dampers is 0.571m for 25 earthquakes and it is reduced to 0.313m using the proposed

approach. Similarly, the reduction is also obvious in the ductility plot of Fig. 8.4b. In particular, it is noted that the ductility reduction for long-period excitations is much more significant than that for short period excitations. This is a distinct characteristic of the proposed stiffness damper.

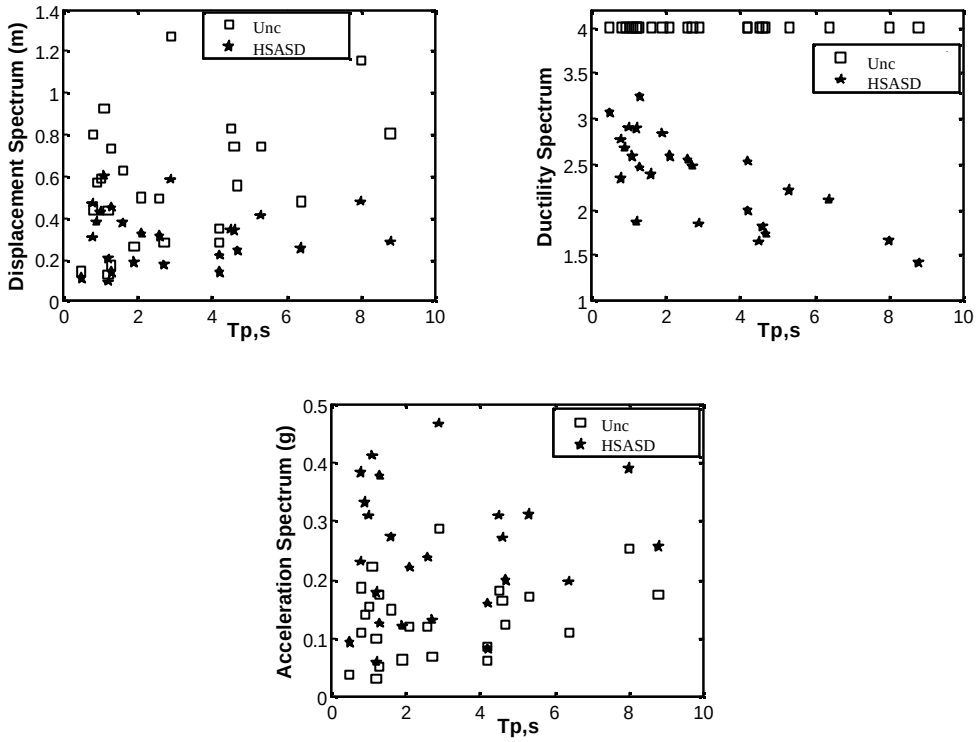

Figure 8.4 Controlled and uncontrolled displacement, ductility and acceleration spectrum for a SDOF structure (T_n=2.5s) subject to 25 recorded near-field ground motions

8.6.2. Response Time-history Characteristics

Fig. 8.5 shows the displacement, acceleration and force time history plots of the SDOF inelastic structure subjected to the TCU068-NS record of 1999 Taiwan earthquake. The dominant period of this record is 8.0s.

It is observed that proposed HSASD reduces the peak displacement significantly compared with the uncontrolled case. Peak acceleration in Fig. 8.5 by the HSASD is amplified due to the addition of stiffness force. The control force applied by the stiffness mechanism is only triggered at a few time instants while the viscous damping force is always active as long as the vibration does not stop.

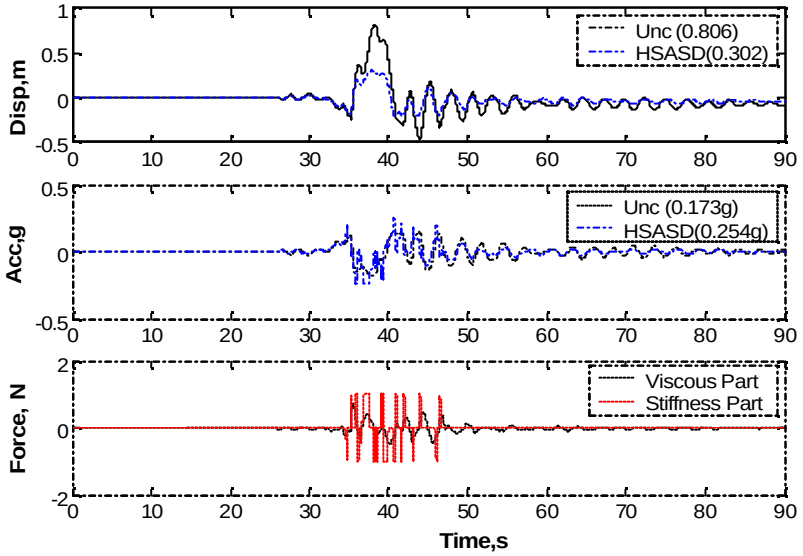

Figure 8.5 Time history plots of the nonlinear SDOF structure subjected to the NS component of the 1999 Chi-Chi earthquake recorded at TCU068 station with and without control.

8.6.3. Hysteretic Behavior

Fig. 8.6 shows the hysteretic loop of the HSASD during the TCU068-NS record of 1999 Taiwan earthquake. It is observed from Fig. 8.6 that the hysteretic loop takes a dumbbell shape: when displacement is within ± 0.12m (which equals to $0.5U_y$ for this case), the damper force is generated by viscous damping mechanism. As the displacement increases beyond 0.12m, the stiffness mechanism rapidly produces large control force to limit peak dynamic response.

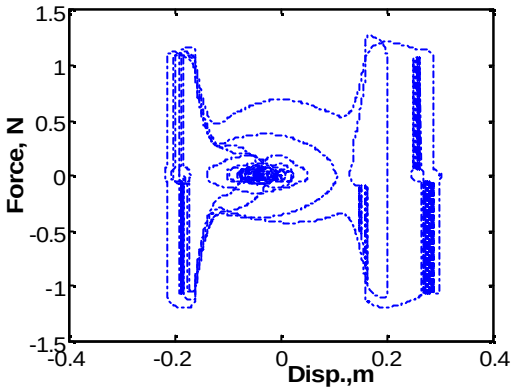

Figure 8.6 Hysteretic behavior of the proposed SAHSD damper

8.6.4 Average Control Effects of the HSASD Controller

It is shown that structural responses are significantly influenced by the ratio of the structural period to the excitation period, i.e., T_n/T_p. A control system that works very well for one structure may perform much different for another structure due to the variation of structural property. Likewise, the effectiveness of the same controller may vary significantly in protecting structures against different excitations. To evaluate the performance of the proposed hybrid controller, the average ductility and acceleration spectra of the 25 recorded near-field ground motions are shown in Fig. 8.7 as the function of T_n/T_p. It is observed from Fig. 8.8 that the ductility demand of the structures with SAHSD is significantly reduced over the entire T_n/T_p range compared to the uncontrolled case. The largest reduction occurs when $0.5<T_n/T_p<1$, where the ductility factor is reduced to 1.9 for the SAHSD. Generally, the ductility demand in the region of $T_n/T_p<1$ is reduced more significantly than that of $T_n/T_p>1$.

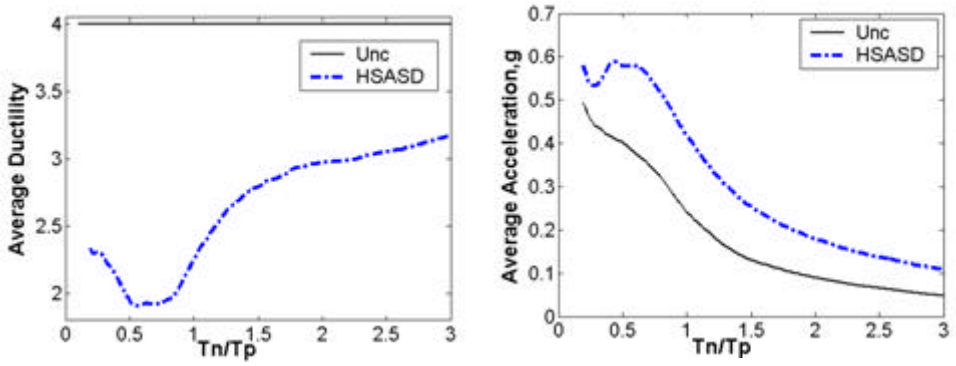

Figure 8.7: Average controlled and uncontrolled response spectra of SDOF structures subject to 25 recorded near-fault ground motions: a) Average ductility spectrum; b) Average acceleration spectrum

The decrease in displacement is accompanied by an increase in acceleration, as shown in Fig. 8.7. The amplification caused by the HSASD is largest in the region of $0.5<T_n/T_p<1$ also. Generally, the controlled acceleration is amplified in the amount of (0.05~0.2)g compared with the uncontrolled case, depending on the value of T_n/T_p.

8.7 APPLICATION OF THE HYBRID SEMI-ACTIVE STIFFNESS CONTROLLER TO THE BENCHMARK BASE-ISOLATED NONLINEAR BRIDGE MODEL

8.7.1 The Benchmark Bridge Model

Highway bridges are key nodes in transportation network connecting major transportation routes. A higher level of performance with less structural damage is required for the bridges for continual functioning after an earthquake. To increase the performance of highway bridges against strong earthquakes, various seismic protective systems have been proposed for the application in bridge structures [e.g., Yang et al.

1995, Nagarajaiah et al. 1993, Saharabudhe et al. 2004, Saiidi et al 1999]. Recently, a benchmark structural control problem for seismically excited highway bridge was developed by Agrawal et al (2004) for the evaluation of various control strategies, including devices, algorithms and sensors, for base-isolated bridge structures.

The benchmark problem is based on the newly constructed 91/5 highway over-crossing in Orange County Southern California. The schematic elevation and plan view of the bridge model is shown in Fig. 8.8. It is a continuous two-span, cast-in-place prestressed concrete box-girder bridge with four lanes. Each span is 58.5 m long and skews at 33^0 with respect to end abutments. The width of the deck along east span is 12.95 m and that of the west span is 15 m. The deck is supported by a 31.4 m long and 6.9 m high prestressed outrigger resting on two pile groups, each consisting of 49 driven concrete friction piles. The bridge deck is isolated using four traditional non-seismic elastomeric pads at each abutment, and the total eight fluid dampers are installed between the end abutments and deck (four dampers at each end) to reduce seismic responses.

A 3-D finite element model, shown in Fig. 8.9, has been developed by Agrawal et al (2005). In the FEM model, the superstructure components of the bridge, including the deck and the bent beam, are assumed to be elastic. Both the abutments and deck-ends are assumed to be rigid and have a skew angle of 33^0. Structural member nonlinearities are included to capture the inelastic moment-curvature behavior of columns and shear-displacement relationship of bearings. Moreover, lead rubber bearings are used to replace eight traditional non-seismic elastomeric pads for increasing seismic performance. The

finite element model has a total of 108 nodes, 4 rigid links, 70 beam elements, 24 springs, 27 dashpots and 8 user-defined bearing elements. The full nonlinear model of the bridge has 430 degree of freedoms.

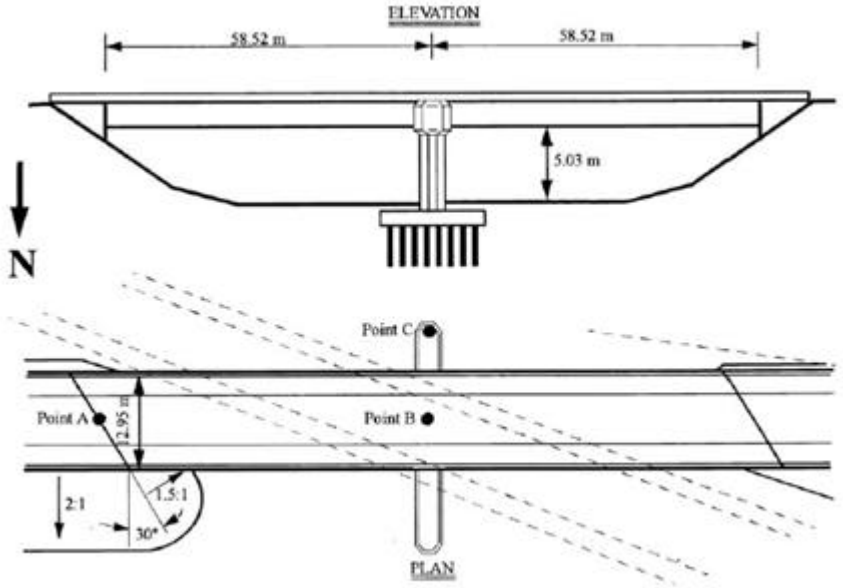

Figure 8.8 Schematic elevation and plan view of the bridge model

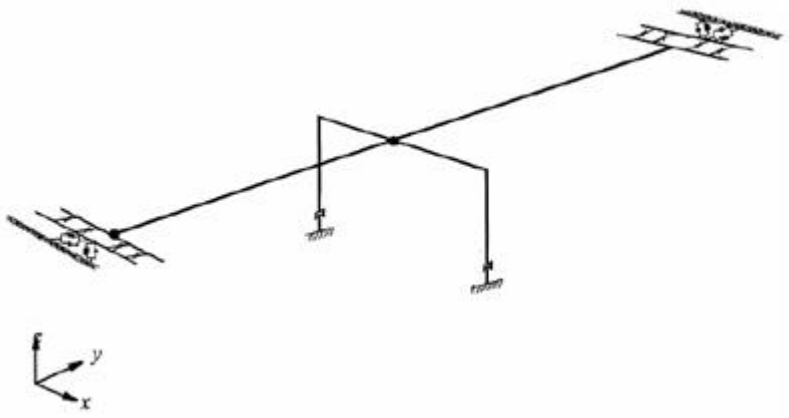

Figure 8.9 FEM model of the bridge

The first 6 natural frequencies of the bridge model and the mode descriptions are displayed in Table 8.1. The inherent damping of the superstructure is assumed to be Raleigh damping, i.e., a linear combination the mass and initial elastic stiffness matrix of the superstructure. The damping parameters are computed by assuming a 5% modal damping ratio in the first and second modes.

Table 8.1 Natural Frequencies of the FEM Model

Mode	Frequency (Hz)	Mode Description
1	1.23	Torsional
2	1.28	Torsional+Vertical
3	1.55	Vertical
4	1.69	Transverse
5	1.77	2nd Vertical
6	3.26	2nd Transverse

Six earthquake ground motions in two orthogonal directions covering the soil types from A to D based on NEHRP classification are selected for the benchmark investigation. These earthquakes are: North Palm Springs (1986), TCU084 component of Chi-Chi earthquake, Taiwan (1999), El Centro component of 1940 Imperial Valley earthquake, Rinaldi component of Northridge (1994) earthquake, Bolu component of Duzce, Turkey (1999) earthquake and Nishi-Akashi component of Kobe (1995) earthquakes.

Three types of sample control systems, namely nonlinear viscous dampers, ideal hydraulic actuators and magnetorheological (MR) fluid dampers, are designed for illustrating the implementation of various controllers by Tan and Agrawal (2004). In addition, a semi-active Lyapunov Controller is also developed for the phase II study by

Nagarajaiah et al (2004). A reduced-order model of the system retaining the dominant characteristics of the full-order evaluation system is developed for the design of sample active and semi-active controllers. Details of the sample controllers, system modeling, and the requirements of sensors can be found in Tan and Agrawal (2005) and Nagarajaiah et al (2004).

A set of 21 evaluation criteria in 3 categories is defined to evaluate the effectiveness of different control devices and algorithms, where J1 to J7 are the peak controlled responses normalized by the corresponding uncontrolled responses, including the peak base shear force (J1), peak overturning moment (J2), peak middle-span displacement (J3), peak middle-span acceleration (J4), peak deformation of bearings (J5), peak curvature at the bent column (J6), and peak dissipated energy of curvature at the bent column (J7). Evaluation criterion J8 is the number of controlled plastic connections normalized by the corresponding uncontrolled number. Evaluation criterion J9 to J14 are controlled normal responses normalized by the corresponding uncontrolled responses, including the normal base shear force (J9), normal overturning moment (J10), normal middle-span displacement (J11), normal middle-span acceleration (J12), normal deformation of bearings (J13), normal curvature at the bent column(J14). J15~J21 are the control requirements, including the peak control force generated by the control device(s) normalized by the seismic weight of the bridge based on the mass of superstructure (J15), peak stroke of the control device(s) normalized by the maximum deformation of bearings in the uncontrolled structure (J16), peak instantaneous power required by the control

device(s) normalized by the product of the weight and the maximum velocity of bearing in the uncontrolled structure (J17), peak total power required for the control of the bridge normalized by the product of weight and maximum deformation of bearings in the uncontrolled structure (J18), number of control devices (J19), number of sensors (J20) and dimension of the discrete state vector required for the control algorithm (J21).

The benchmark bridge model has been developed into two phases. In Phase I, the bridge deck is fixed to the outrigger. In Phase II, the deck is isolated from outrigger through elastomeric bearings. As a result, the period of first fundamental mode of the bridge is elongated to approximately 3.0s, which is a flexible structure. In this study, Phase II model of the benchmark bridge problem has been used.

8.7.2 Effectiveness of the Hybrid Semi-active Stiffness Controller in Controlling the Bridge Model subjected to the Prescribed Earthquakes

The proposed hybrid stiffness controller is applied to the Phase II model in this investigation. The same controller is designed for all six earthquakes. In order to develop an appropriate stiffness shaping function, the reference stiffness k_{ref} is determined according to the following expression:

$$k_{ref} = b \frac{\sum_{i=1}^{6} V_{b0i}}{\sum_{i=1}^{6} D_i} \tag{8.12}$$

where V_{b0i} is the peak uncontrolled base shear and D_i is the peak displacement response of the bridge subjected to all six prescribed earthquakes. The coefficient ß is taken as 1.5.

Through numerical simulation of response quantities of the bridge subject to all six earthquakes, the resulting stiffness k_{ref}, is obtained as 4.265×10^6 N/m. The threshold displacement X_3 is taken as 50% of the average uncontrolled peak displacements over all six earthquakes (0.34m), i.e., X_3 = 0.17m. The stiffness k_1 is taken as 10% of the reference stiffness. The threshold displacement X_1 is taken as $0.2X_3$. The threshold displacement X_2 is taken as $0.8X_3$ and any number of $X_4 >> X_3$ can be taken as long as the saturation of the damper is obtained when the deformation is larger than X_3. Other parameters are derived according to Eq. 8.7.

The linear viscous damping force in Eq.8.10 is generated by assigning damper coefficient $c_d=1.5\times10^5$ N.s/m. In addition, a boundary layer is introduced to eliminate the chattering effect caused by the switching of the semi-active stiffness damper:

$$u = \begin{cases} f_s & x\dot{x} \geq d \\ -f_s & x\dot{x} \leq -d \\ f_s \tanh(ax\dot{x}) & -d < x\dot{x} < d \end{cases} \tag{8.13}$$

The parameters a and d determining the thickness of the boundary layer are taken as 10 and 0.05, respectively.

To apply the controller, total of forty measurements are used to measure the displacement and velocity at the isolation bearings for the controller implementation in two directions. It is noted that the displacement and velocity can also be obtained by measuring acceleration data and passing the measured data through filters (integrators). Twenty devices are installed in parallel with isolation bearings for the response control of

the bridge in two directions, as shown in Fig. 8.10. The SIMULINK® block of the hybrid controller implemented is shown in Fig.8.11. The simulations are performed within the control implementation framework set forth in the benchmark definition papers.

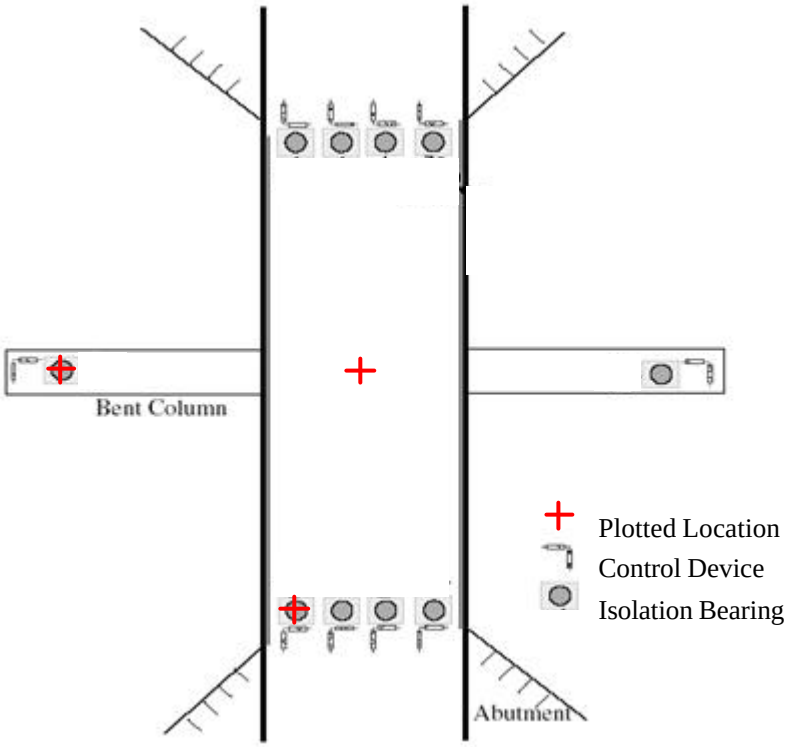

Figure 8.10 Locations of Control Devices on the Bridge

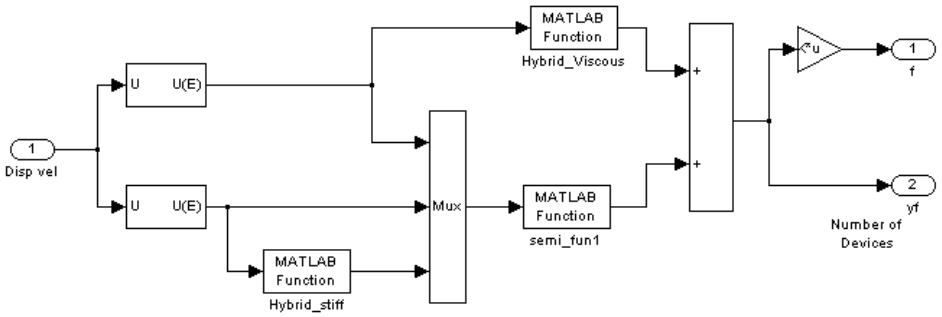

Figure 8.11 SIMULINK block of the hybrid controller

Table 8.2 shows the results of numerical simulations for the bridge subjected to the precribed earthquakes. Results for the proposed hybrid stiffness damper are indicated by "HB" in this table. For comparison purposes, the results of the sample active ("S.AC") and sample passive ("S.PA") controllers are also shown. The minimum values of evaluation criteria J3 and J5 for each earthquake are marked in bold. It is observed that the proposed hybrid stiffness damper is significantly more effective than sample active and sample passive controllers in reducing peak mid-span displacement (J3) and peak bearing displacement (J5). Compared with the sample passive controller, the hybrid stiffness damper can achieve 14% more reductions for both J3 and J5; while this value is about 48% in case of sample active controller.

Reductions in mid-span and bearing displacements are accompanied by the amplification of base shear and mid-span acceleration responses during some earthquakes, such as TCU084 component of Chichi and Rinaldi earthquakes. It is also observed that the reduction in displacement and increase in acceleration are proportional to the peak control force applied (J15) for most of the earthquakes, except for the Kobe-NIS earthquake. For this earthquake, significant more reduction in J3 and J5 can be achieved by the hybrid controller for the same amount of control force applied by sample controllers, while other quantities remain comparable. The peak dissipated energy of curvature (J7) and the number of plastic hinges (J8) are zero during all earthquakes, which indicates that the bent column does not experience plastic deformation, even though the peak bent column curvature (J6) increases for the hybrid controller during

some earthquakes. It is also seen that the normalized response quantities, J10 through J14, follow the trend of corresponding peak response quantities.

Fig. 8.12 presents response time history plots in transverse direction of the bridge subjected to Rinaldi earthquake for the cases of uncontrolled, controlled with the hybrid stiffness damper and with the sample passive controller. The locations on bridge at which these response quantities are measured are marked in Fig.8.10. It is observed that the mid-span displacement (Fig. 8.12a) and end-bearing displacement (Fig. 8.12b) are significantly reduced by the hybrid controller compared with those using sample passive controllers. The mid-span acceleration is increased at some time instants as shown in Fig. 8.12c because of the high spikes in control forces. On the other hand, both the peak displacement and peak shear force at the end bearing are significantly reduced by the hybrid stiffness damper controller as shown in Fig. 8.13d. As a result, the lead-rubber bearing experiences a much smaller bilinear hysteretic deformation in the case of the proposed hybrid stiffness damper.

It is noted that the results presented herein are for a particular form of stiffness shaping function. Much better results can be obtained using optimal form of stiffness shaping function. The objective of the current work on the proposed hybrid stiffness damper is to show the feasibility of concept for long-period flexible structures.

Table 8.2 Performance indices for the hybrid, sample active and sample passive controllers

	NPalmspr			ChiChi			El Centro			Rinaldi			TurkBolu			Kobe-NIS		
	HB	S.AC	S.PA	HB	S.AC	S.PA	HB	S.AC	S.PA	HB	S.AC	S.PA	HB	S.AC	S.PA	HB	S.AC	S.PA
J1: Pk. Base Shear	1.00	0.94	1.06	2.08	1.05	0.91	0.67	0.74	0.62	1.39	0.86	1.07	1.15	0.96	0.78	0.93	0.89	0.91
J2: Pk.Over.Mom.	1.03	0.92	1.10	1.75	0.97	0.95	0.66	0.77	0.61	1.40	0.96	1.04	1.19	0.97	0.70	0.93	0.88	0.90
J3:Pk.Mid.Disp.	**0.85**	1.01	0.87	**0.58**	1.09	0.76	0.54	0.69	**0.50**	**0.65**	0.96	0.90	**0.56**	0.93	0.59	**0.64**	0.96	0.83
J4:Pk.Mid.Acc.	1.10	1.13	1.17	2.45	0.95	1.13	0.89	0.79	1.09	2.06	0.93	1.05	1.49	0.82	0.92	1.13	0.93	1.16
J5:Pk.Bear.Def.	**0.87**	1.01	0.88	**0.56**	1.09	0.76	0.57	0.73	**0.49**	**0.63**	0.99	0.90	**0.53**	0.93	0.56	**0.65**	0.96	0.83
J6:Pk.Ductility	1.03	0.92	1.10	1.75	0.97	0.95	0.66	0.77	0.61	1.40	0.96	1.04	1.19	0.97	0.70	0.93	0.88	0.90
J7:Dis.Energy	0	0	0	0	0	0	0	0	0	0	0	0	0	0	0	0	0	0
J8:Plas.Connect.	0	0	0	0	0	0	0	0	0	0	0	0	0	0	0	0	0	0
J9:Nor.BaseShear	1.12	0.97	1.19	0.72	1.11	0.98	0.81	0.92	0.61	1.27	0.79	0.84	0.34	0.96	0.58	0.90	0.91	0.97
J10:Nor.Over.Mom	1.14	0.97	1.21	0.66	1.10	0.98	0.80	0.91	0.60	1.24	0.79	0.82	0.34	0.96	0.58	0.89	0.91	0.96
J11:Nor. Mid. Disp.	0.99	0.94	1.02	0.44	1.27	0.98	0.75	0.92	0.59	1.06	0.80	0.76	0.31	0.92	0.52	0.91	0.94	0.96
J12:Nor.Mid.Acc.	0.91	0.91	0.91	2.10	1.01	1.19	0.95	0.90	0.95	1.40	0.89	0.98	0.95	0.85	0.87	1.01	0.91	0.99
J13:Nor.Bear.Def.	0.99	0.94	1.03	0.44	1.31	0.98	0.78	0.96	0.62	1.09	0.79	0.76	0.32	0.92	0.52	0.90	0.94	0.96
J14:Nor.Ductility	1.14	0.97	1.21	0.66	1.10	0.98	0.80	0.91	0.60	1.24	0.79	0.82	0.34	0.96	0.58	0.89	0.91	0.96
J15*:Pk.Con.Force	0.00	0.00	0.00	0.02	0.00	0.00	0.00	0.00	0.00	0.02	0.00	0.00	0.02	0.00	0.00	0.00	0.00	0.00
J16:Pk.Stroke	0.87	1.01	0.88	0.56	1.09	0.76	0.57	0.73	0.49	0.63	0.99	0.90	0.53	0.93	0.56	0.65	0.96	0.83
J17:Pk.Power	0	0.01	0	0	0.02	0	0	0.01	0	0	0.02	0	0	0.01	0	0	0.01	0
J18:Total power	0	0.00	0	0	0.00	0	0	0.00	0	0	0.00	0	0	0.00	0	0	0.00	0
J19:No.Con.Dev.	20	20	20	20	20	20	20	20	20	20	20	20	20	20	20	20	20	20
J20:No.Sensors	40	16	0	40	16	0	40	16	0	40	16	0	40	16	0	40	16	0
J21:Comp.Res.s	0	28	0	0	28	0	0	28	0	0	28	0	0	28	0	0	28	0

* Value 0.00 indicates that the peak control force is less than 0.005.

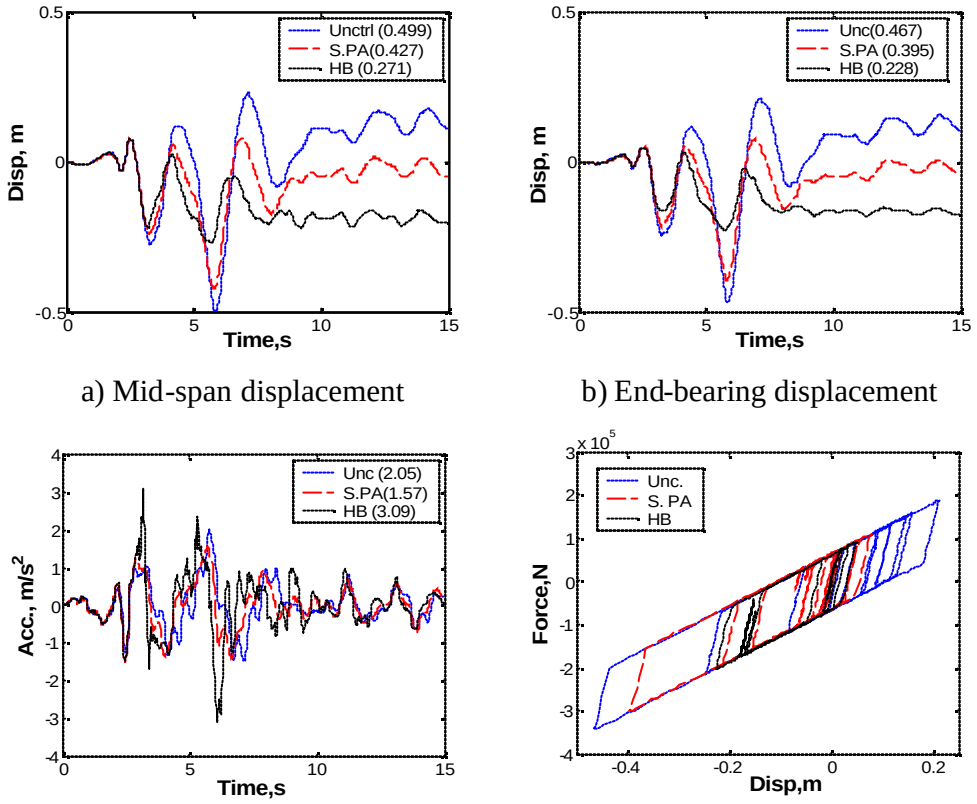

a) Mid-span displacement

b) End-bearing displacement

c) Mid-span acceleration response

d) End lead-rubber-bearing behavior

Figure 8.12 Response quantities of the bridge in transverse direction subject to Rinaldi earthquake for the uncontrolled and controlled cases with hybrid stiffness damper (HB) and sample nonlinear passive damper (S. PA).

8.7.3 Effectiveness of the Hybrid Semi-active Stiffness Controller in Controlling the Bridge Model subjected to Long-period Pulse-type Excitations.

It is shown that the proposed hybrid stiffness damper can reduce peak structural displacements effectively during long-period excitations. Dominant periods of the prescribed earthquakes in the benchmark problem are less than or equal to 1.1s; except for that of the EW component of El Centro record, which is 2.1s. To investigate the performance of the proposed hybrid stiffness damper for the benchmark bridge model during long period excitations, TCU068-NS component of 1999 Chichi earthquake and

its dominant pulse component, which is expressed by the pulse model as shown in Chapter 3 are used. The dominant period of the TCU068-NS record is 8.0s and the period of its pulse component is approximately 10s, as described in Chapter 3.

Table 8.3 presents the peak uncontrolled responses of the bridge during these two excitations. Tables 8.4 and 8.5 present evaluation criteria for the hybrid and sample controllers during these two excitations, respectively, where "HB", "S.AC", "S.SA" and "S.PA" represent the hybrid stiffness controller, the sample active controller, the sample semi-active controller and the sample passive controller, respectively. The parameters of these controllers are the same as before. It is observed from Tables 8.4 and 8.5 that the peak mid-span displacement (J3) and the peak base displacement (J5) for the proposed hybrid stiffness controller are significantly smaller than those for other controllers/dampers. Best values of J3 and J5 among sample controllers are achieved by the sample semi-active controller. However, they are much larger than those for the hybrid controller. Most of the evaluation criteria for the sample active controller are larger than 1. The sample passive damper can reduce all response quantities simultaneously. However, the percent reduction is quite small for all the important quantities. Although the reduction in displacement by the hybrid stiffness damper is accompanied by amplifications in base shear, moment and acceleration, percent increase in these quantities is comparable for different controllers. Hence, the hybrid stiffness damper is superior to sample controllers in terms of achieving better displacement reduction with similar level of amplification in base shear and accelerations.

Table 8.3 Peak uncontrolled response quantities subjected to the TCU068NS and the pulse excitations

	Pk. Base Shear (N)	Pk. Over. Mom. (N/m)	Pk. Mid. Disp. (m)	Pk. Mid. Acc. (m/s^2)	Pk. Bear. Def. (m)	Pk. Curv. (rad)
TCU068-NS	1.25×10^{6}	8.74×10^{6}	0.89	2.46	0.88	0.42×10^{-3}
Pulse	9.92×10^{5}	6.93×10^{6}	0.64	1.80	0.63	0.33×10^{-2}

Table 8.4 Performance indices for various controllers subjected to the TCU068-NS earthquake

	HB	S.AC	S.SA	S.PA
J1: Pk. Base Shear	1.21	1.01	0.95	0.93
J2: Pk. Over.Mom.	1.19	1.01	0.95	0.93
J3:Pk.Mid.Disp.	0.41	1.06	0.77	0.86
J4:Pk.Mid.Acc.	1.49	0.97	1.44	0.91
J5:Pk.Bear.Def.	0.41	1.06	0.77	0.86
J6:Pk.Ductility	1.19	1.01	0.95	0.93
J7:Dis.Energy	0	0	0	0
J8:Plas.Connect.	0	0	0	0
J9:Nor.BaseShear	1.08	1.03	0.97	0.95
J10:Nor.Over.Mom	1.07	1.03	0.96	0.95
J11:Nor. Mid. Disp.	0.51	1.07	0.82	0.89
J12:Nor.Mid.Acc.	1.09	0.99	1.09	0.97
J13:Nor.Bear.Def.	0.51	1.07	0.82	0.89
J14:Nor.Ductility	1.07	1.03	0.96	0.95
J15:Pk.Con.Force	0.02	0.00	0.01	0.00
J16:Pk.Stroke	0.40	1.04	0.76	0.85
J17:Pk.Power	-	0.02	-	0
J18:Totalower	-	0.00	-	0
J19:No.Con.Dev.	20	20	20	20
J20:No.Sensors	40	16	40	0
J21:Comp.Res.	0	28	28	0

Table 8.5 Performance indices for various controllers subjected to the pulse excitation

	HB	S.AC	S.SA	S.PA
J1: Pk. Base Shear	1.32	1.03	1.08	0.90
J2: Pk.Over.Mom.	1.29	1.03	1.05	0.90
J3:Pk.Mid.Disp.	0.46	1.07	0.59	0.83
J4:Pk.Mid.Acc.	1.44	0.99	1.35	0.91
J5:Pk.Bear.Def.	0.47	1.07	0.60	0.83
J6:Pk.Ductility	1.29	1.03	1.05	0.90
J7:Dis.Energy	0	0	0	0
J8:Plas.Connect.	0	0	0	0
J9:Nor.BaseShear	0.93	1.04	0.96	0.94
J10:Nor.Over.Mom	0.93	1.04	0.96	0.94
J11:Nor. Mid. Disp.	0.66	1.08	0.71	0.92
J12:Nor.Mid.Acc.	0.92	1.01	0.92	0.95
J13:Nor.Bear.Def.	0.66	1.08	0.72	0.92
J14:Nor.Ductility	0.93	1.04	0.96	0.94
J15:Pk.Con.Force	0.02	0.00	0.00	0.00
J16:Pk.Stroke	0.46	1.06	0.59	0.82
J17:Pk.Power	-	0.01	-	0
J18:Totalower	-	0.00	-	0
J19:No.Con.Dev.	20	20	20	20
J20:No.Sensors	40	16	40	0
J21:Comp.Res.	0	28	28	0

Fig. 8.13 presents response quantities for the bridge in longitudinal direction during TCU068-NS earthquake. It is observed from Fig. 8.13a that the mid-span displacement using hybrid stiffness damper is reduced to 0.321m, compared with 0.565m and 0.895m using sample semi-active and sample active controllers, respectively. On the other hand, peak mid-span acceleration and peak base (bearing) shear using hybrid stiffness damper are larger than those for other controllers, see Fig. 8.13b and 8.13c. The shear response of mid-span bearings is significantly reduced as shown in 8.13d for the hybrid stiffness damper. On the other hand, end bearing shear in Fig.8.13c is only slightly increased compared with that for the sample active controller.

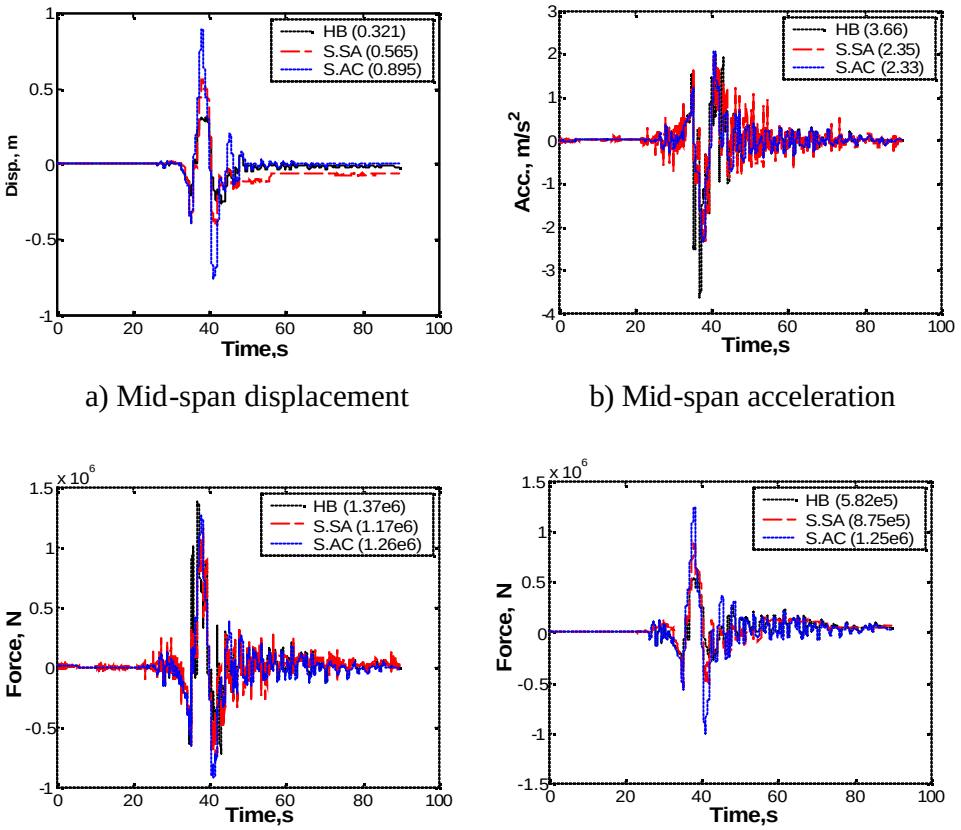

a) Mid-span displacement

b) Mid-span acceleration

c) End base shear

d) Mid-bearing shear

Figure 8.13 Longitudinal (Y-direction) response information for the cases of hybrid stiffness controller (HB), sample semi-active controller (S.SA) and sample active controller (S.AC), subjected to the TCU068-NS excitation.

8.8 CONCLUSIONS

A stiffness-based hybrid semi-active controller, termed as Semi-Active Hybrid Stiffness Damper, is proposed for displacement reduction of flexible structures subjected to long-period pulse-type near-field ground motions. It is known that displacement reduction of short and intermediate structures subjected to pulse type and broadband excitations can be realized using existing protective/damping systems. However, it has

been observed that these systems are not effective during flexible structures subjected to long-period pulse-type excitations.

The hybrid controller proposed in this investigation operates in two stages. The viscous damping force is the only force applied when structural deformation is small. As displacement exceeds a preset threshold value, variable stiffness force is built up rapidly to limit peak dynamic responses. The stiffness of the damper is a nonlinear function of displacement across it. A friction-type constraint is applied to make the proposed controller dissipative in nature.

Detailed parametric analysis is performed to investigate the characteristics of the proposed hybrid stiffness damper. Effectiveness of the hybrid stiffness damper is evaluated using nonlinear SDOF systems as well as the nonlinear base-isolated highway bridge benchmark model. Results indicate that the proposed hybrid stiffness damper is very effective in reducing structural displacement and ductility demands during long-period pulse-type excitations. The reduction in displacement is accompanied by the increase in acceleration caused by the application of stiffness force. It is observed that the performance of hybrid stiffness damper is superior to those of sample controllers in terms of better displacement reduction with similar amplification of shear and acceleration for the benchmark bridge model.

Effective stiffness of structures decreases significantly because of nonlinear deformation. Hence, the effects of stiffness variations by the proposed hybrid stiffness damper for nonlinear structures are more obvious than those for linear structures. Stiffness variation mechanism works effectively in reducing displacement caused by static-like long-period pulse-type excitations. The variable stiffness mechanism in the

proposed hybrid stiffness damper can automatically adjust the incremental rate of applied force in real time manner.

It is noted that the stiffness shape function used in this investigation is a group of polynomial functions. However, other type of functions can also be used to realize the continuous variation of stiffness. The hybrid stiffness damper can be realized by typically used damper devices, such as MR dampers, ER dampers, variable orifice dampers, etc. Further work need to be carried out for the practical application of the hybrid stiffness damper as well as developing different types of stiffness shape functions.

CHAPTER 9

CONCLUSIONS AND RECOMMENDATIONS FOR FUTURE RESEARCH

9.1 CONCLUSIONS

The objective of this research is to investigate the effectiveness of various seismic structure protective systems susceptible to disastrous earthquakes.. This objective is achieved through: a) investigations of the effects of near-field ground motion pulses on the performance of various control systems installed in linear and nonlinear structures; b) development of innovative semi-active and active control systems by incorporating dynamic pulse behavior in controller design; c) verification of performance of these controllers using models of a base-isolated benchmark building and a base-isolated benchmark highway bridge; and d) development of novel stiffness shape concept for nonlinear flexible structures.

Typically, near-field ground motions consist of dominant pulse components and broadband frequency components. Characteristics of near-field ground motions and effects of pulse, broadband, long-period and high-frequency components of near-field ground motions on the responses of linear and nonlinear structures are investigated extensively. Using a combination of the analytical pulse model proposed by He (2003) and Empirical Mode Decomposition (EMD) method used by Huang et al (2001), recorded acceleration histories are decomposed into dominant pulse components and

broadband frequency components. Through this decomposition it is demonstrated that the analytical pulse model proposed by He (2003) matches very well with the pulse components obtained through the EMD method. Response quantities and time history plots obtained by the two forms of pulse components are almost the same. It is observed that pulse components are the major sources causing displacement responses of linear and nonlinear structures and they are responsible for pushing nonlinear structures to the elastic limit or beyond this limit within a short period of ground shaking. This is found to be the case for short, intermediate and long-period structures. Although broadband frequency components alone can cause significant amount of displacement responses, these responses occur at different time instants than those of the pulse components and thus they are not the cause of overall peak responses. However, the combined effects of these two components during the same time period cause the overall inelastic structural deformation. Hence, all types of structures (short period, intermediate period and long-period) develop permanent displacement during near-field ground motions with predominant pulse components. The analytical pulse model can be used for systematic study of various seismic protective systems, since the pulse components of recorded earthquakes are responsible for causing major structural deformation during earthquake events.

Performance of passive energy dissipation systems (PEDS) during near-field ground motions is investigated systematically using the analytical pulse model. These results are verified using various recorded near-field ground motions. It is found that the degradation in the effectiveness of viscous dampers during near-field ground motions is due to the presence of distinct pulse-type components. When the ratio of structural and

predominant ground motion periods, T_n/T_p, is close to 1, the effectiveness of viscous dampers during recorded near-field ground motions is similar to their effectiveness observed when subjected to pulse components only and the viscous dampers perform the best under this situation. However, when the T_n/T_p ratio is much different than 1, viscous dampers can only effectively reduce the displacement caused by broadband frequency components and they are much less effective in reducing displacement caused by the pulse components. Yielding dampers are effective in reducing displacement, acceleration and input energy only when T_n/T_p <1, and may amplify these quantities otherwise. It is also observed that the performance of PEDS depends on their absorbability of instantaneous input energy. If a PEDS cannot dissipate the input energy instantaneously, even though it may have an excellent ability to dissipate the total input energy at the end of excitation, the structure may still undergo damage due to the instantaneous accumulation of input energy during the course of an earthquake.

To investigate the inelastic behavior of structures during near-field ground motions, the response of nonlinear structures subjected to 50 recorded near-field ground motions as well as pulse-type excitations is studied. It is noted that the level of structural damage not only depends on the maximum response quantities, but also on the cumulative effects of numerous inelastic hysteretic cycles during an earthquake. For this reason, both strength and energy related response quantities are investigated. Inelastic behavior of structures is investigated in detail by deriving *R-m* relationships as a function of T_n/T_p based on extensive simulations of nonlinear structures with various levels of displacement ductility factors and subjected to both recorded ground motions and pulse-type excitations. It is observed that the Newmark-Hall's relationship is applicable for the

design of inelastic structures if its parameters are adjusted in terms of T_n/T_p using the results obtained from 50 recorded near-field ground motions. A pulse model based R-μ relationship is also developed and proposed for the inelastic design of structures. The proposed R-μ relationship matches very well with the lower bound values (mean minus one sigma) of the R-μ envelope obtained for recorded ground motions for $T_n/T_p < (T_n/T_p)_c$ and it is more conservative than Newmark-Hall's relationship for the case of short period structures subjected to relatively longer period pulse-type ground motions. For $T_n/T_p > (T_n/T_p)_c$, the proposed R-m relationship yields similar results to those in the Newmark-Hall formula.

The energy-related properties of inelastic structures are also investigated. It is noted that the energy-related properties can be used to characterize the cumulative damage of structures and they can be used effectively for performance-based design. Input energy spectra, hysteretic energy spectra, ratio of hysteretic to input energy spectra as well as spectra for damper dissipated energy for pulse-type and near-field ground motions are thoroughly investigated. Numerical results demonstrate the evolution process of seismic energy in inelastic structures with and without supplemental passive energy dissipation devices.

Performance of passive energy dissipation systems for nonlinear structures is also investigated systematically for both pulse-type and recorded ground motions. Because of significant nonlinearity inherent in inelastic structures, performance of energy dissipation devices in nonlinear structures is inferior to that in linear structures, since a significant portion of input energy may be dissipated through hysteretic structural behavior. As a result, energy dissipated by supplemental dampers decreases with increase in structural

nonlinearity (ductility). However, for a given structure, supplemental energy dissipation devices still significantly dissipate the energy input to the structure and thus effectively reduce excessive damage during strong earthquakes.

Traditional design methods for active and semi-active systems do not consider the characteristics of the seismic excitations or assume these to be white noise.. Hence, the effectiveness of these controllers cannot be guaranteed in the presence of seismic excitations with dominant pulse behavior. To address this issue, an approach to design novel active and semi-active controllers by including the dynamics of pulse behavior in ground motion design is proposed. Previously, He (2003) had proposed a pulse filter in frequency domain, which can be converted to state-space form using MATLAB subroutines. The pulse filter is combined with the structural system dynamic equation to form the augmented system. This augmented system is utilized to design active and semi-active controllers for base-isolated buildings using any of the modern control theories. Using a Linear Quadratic Gaussian (LQG) approach, Active Pulse Filter (APF) and Semi-Active Pulse Filter (SAPF) controllers are designed and their effectiveness is investigated using a 2DOF based isolated building model and an eight story base-isolated benchmark building model. It is observed that the APF controller performs significantly better than other controllers by reducing the peak values of base displacement, superstructure drift and absolute accelerations of the base and the superstructure simultaneously and more significantly. The pulse filter used for APF depends on ground pulse period, ground damping factor and pulse shape factor. Based on a sensitivity analysis, it is shown that the performance of the APF controller doesn't change significantly when pulse period in the pulse filter is underestimated or overestimated by

up to 20% with respect to actual ground motion period, the damping factor is in the range of 0.15 to 0.35 and the pulse shape factor is between 1 and 3, for a practical range of control force.

A stiffness-based hybrid semi-active controller is proposed for displacement reduction of flexible structures subjected to long-period pulse-type near-field ground motions. It is known that displacement reduction of short and intermediate structures subjected to pulse-type and broadband frequency excitations can be obtained using existing protective/damping systems. However, it is observed that these systems are not effective during flexible structures subjected to long-period pulse-type excitations. The hybrid stiffness damper operates in two stages: only a viscous damping force is applied when structural deformation is small; and as the displacement exceeds a preset threshold value, a variable stiffness force is built up rapidly to limit peak dynamic response. The stiffness of the damper is a nonlinear function of its displacement.. A friction-type constraint is applied to make the proposed controller dissipative in nature.

Applications of the damper to nonlinear SDOF structures and a nonlinear base-isolated highway bridge model demonstrate that the proposed hybrid stiffness damper is very effective in reducing structural displacement and ductility demands during long-period pulse-type excitations. The reduction in displacement is accompanied by an increase in the acceleration caused by the application of stiffness control force. It is observed that the performance of the hybrid stiffness damper is superior to that of sample controllers in terms of better displacement reduction with similar amplification of shear and acceleration of the benchmark bridge model. Stiffness variation mechanism works

effectively in reducing displacement caused by static-like long-period pulse-type excitations.

9.2 FUTURE RESEARCH

There are still many issues that need to be addressed and further explored in the area of response control of structures. These may include a) the development of highly efficient and reliable control systems, b) large scale testing of various control devices, c) applications in the design and retrofit of structures, d) code adoption of seismic protective systems in future design guidelines. In terms of the application of seismic protective systems in earthquake engineering, ground motion characteristics need to be specifically considered in the future design and application of various control systems.

It is noted that advanced seismic protective systems are yet to be fully utilized in practice, particularly in the U.S., although passive devices have been recommended in many documents, such as UBC97, FEMA273 (1997), FEMA 368 (2000) and FEMA 356 (2000). Moreover, the design and analysis of structures with passive devices are still based on code provisions developed for far-field earthquakes, even though a generalized near-source factor is recommended to account for the near-fault effects in some of these documents. This could result in a significant under-prediction of inelastic structural demand during near-field ground motions and the near-source effects on the performance of seismic protective systems may not be accurately estimated. Hence, a systematic evaluation and revision of current design and analysis methods considering near-field excitation effects should be taken for increased safety and reliability of both the structure and seismic protective systems. Interaction between structures and control devices should

be properly addressed in the design and analysis of structures equipped with seismic protective systems.

The development of more efficient, reliable and applicable semi-active and hybrid control systems is always a challenging topic. Although controllers designed based on traditional algorithms, such as LQR/LQG, could achieve favorable control effects, they require accurate estimation of model parameters and response quantities, which is a challenging task for nonlinear structures. To this end, experimental verification of controller design by augmenting structural models with pulse filters is essential and should be carried out in future research. The concept of utilizing a stiffness shape function to control stiffness deterioration due to nonlinear behavior (hysteretic, degrading, pinching) is novel and needs to be investigated using different forms of the stiffness shape functions. The research presented in this dissertation shows that the hybrid stiffness damper can reduce displacements and ductility, although there is an increase in peak base shear forces and accelerations. This issue can be resolved by designing stiffness shape functions suitable for a particular form of inherent nonlinearity of the structure.

APPENDIX-Ground Motion Records Used in this Dissertation Research

Table A-1. 50 Near-field Ground Motion Records Used in Chapter 5

NO.	ID	Description	Period (s)	PGA (g)	PGV (cm/s)	PGD (cm)	Magnitude (ML)	USGS Soil Class	Distance to fault (km)
1	NORTHR/PUL104	Northridge, 1994/01/07	0.5	1.585	55.7	6.06	6.7	A	8.0
2	NORTHR/PUL194	Northridge, 1994/01/07	0.9	1.285	103.9	23.80	6.7	A	8.0
3	CAPEMEND/CPM000	Cape Mendocino 1992/04/25	0.9	1.497	127.4	41.01	7.1	A	8.5
4	CAPEMEND/CPM090	Cape Mendocino 1992/04/25	2.4	1.039	42.0	12.39	7.1	A	8.5
5	LANDERS/LCN275	Landers 1992/06/28	4.2	0.721	97.6	70.31	7.3	A	1.1
6	LANDERS/LCN000	Landers 1992/06/28	3.4	0.785	31.9	16.42	7.3	A	1.1
7	PALMSPR/WWT180	N. Palm Springs 1986/07/08	0.5	0.492	34.7	6.38	6.0	A	7.3
8	PALMSPR/WWT270	N. Palm Springs 1986/07/08	0.4	0.612	31.5	4.58	6.0	A	7.3
9	MORGAN/AND250	Morgan Hill 1984/04/24	0.5	0.423	25.3	4.58	6.2	B	2.6
10	MORGAN/AND340	Morgan Hill 1984/04/24	0.8	0.289	27.6	6.33	6.2	B	2.6
11	NORTHR/ARL090	Northridge 1994/01/17	1.0	0.344	40.6	15.04	6.7	B	9.2
12	NORTHR/ARL360	Northridge 1994/01/17	3.0	0.308	23.2	10.75	6.7	B	9.2
13	NORTHR/PKC090	Northridge 1994/01/17	0.9	0.301	31.4	10.87	6.7	B	8.2
14	NORTHR/PKC360	Northridge 1994/01/17	0.7	0.433	51.5	7.21	6.7	B	8.2
15	NORTHR/WPI046	Northridge 1994/01/17	2.2	0.455	92.8	56.64	6.7	B	7.1
16	NORTHR/WPI316	Northridge 1994/01/17	2.0	0.325	67.4	16.11	6.7	B	7.1
17	CHICHI/CHY028-N	Chi-Chi, Taiwan 1999/09/20	0.8	0.821	67.0	23.28	7.6	C	7.31
18	CHICHI/CHY028-W	Chi-Chi, Taiwan 1999/09/20	1.9	0.653	72.8	14.68	7.6	C	7.31
19	CHICHI/TCU076-N	Chi-Chi, Taiwan 1999/09/20	1.2	0.416	64.2	35.37	7.6	C	1.95
20	CHICHI/TCU076-W	Chi-Chi, Taiwan 1999/09/20	3.2	0.303	62.6	31.47	7.6	C	1.95
21	CHICHI/TCU129-N	Chi-Chi, Taiwan 1999/09/20	0.9	0.634	36.1	28.87	7.6	C	1.18
22	CHICHI/TCU129-W	Chi-Chi, Taiwan 1999/09/20	4.1	1.01	60.0	50.15	7.6	C	1.18
23	DUZCE/DZC180	Duzce, Turkey 1999/11/12	5.5	0.348	60.0	42.09	7.1	C	8.2
24	DUZCE/DZC270	Duzce, Turkey 1999/11/12	5.0	0.535	83.5	51.59	7.1	C	8.2
25	IMPVALL/H-EMO000	Imperial Valley 1979/10/15	3.0	0.314	71.7	25.53	6.5	C	0.5
26	IMPVALL/H-EMO270	Imperial Valley 1979/10/15	3.0	0.296	90.5	31.71	6.5	C	0.5

27	IMPVALL/H-E04140	Imperial Valley 1979/10/15	0.9	0.485	37.4	20.23	6.5	C	4.2
28	IMPVALL/H-E04230	Imperial Valley 1979/10/15	3.6	0.36	76.6	59.02	6.5	C	4.2
29	IMPVALL/H-E06140	Imperial Valley 1979/10/15	2.8	0.41	64.9	27.69	6.5	C	1.0
30	IMPVALL/H-E06230	Imperial Valley 1979/10/15	3.4	0.439	109.8	65.89	6.5	C	1.0
31	IMPVALL/H-E07140	Imperial Valley 1979/10/15	1.5	0.338	47.6	24.68	6.5	C	0.6
32	IMPVALL/H-E07230	Imperial Valley 1979/10/15	3.2	0.463	109.3	44.74	6.5	C	0.6
33	IMPVALL/H-E08140	Imperial Valley 1979/10/15	1.4	0.602	54.3	32.32	6.5	C	3.8
34	IMPVALL/H-E08230	Imperial Valley 1979/10/15	4.2	0.454	49.1	35.59	6.5	C	3.8
35	IMPVALL/H-EDA270	Imperial Valley 1979/10/15	2.6	0.352	71.2	45.8	6.5	C	5.3
36	IMPVALL/H-EDA360	Imperial Valley 1979/10/15	1.4	0.48	40.8	14.04	6.5	C	5.3
37	NORTHR/NWH090	Northridge 1994/01/17	1.3	0.583	75.5	17.57	6.7	C	4.5
38	NORTHR/NWH360	Northridge 1994/01/17	1.3	0.59	97.2	38.05	6.7	C	4.5
39	NORTHR/SYL090	Northridge 1994/01/17	2.4	0.604	78.2	16.05	6.7	C	6.4
40	NORTHR/SYL360	Northridge 1994/01/17	2.6	0.843	129.6	32.68	6.7	C	6.4
41	NORTHR/JEN022	Northridge 1994/01/17	2.8	0.424	106.2	43.06	6.7	C	6.2
42	NORTHR/JEN292	Northridge 1994/01/17	1.1	0.593	99.3	24.0	6.7	C	6.2
43	NORTHR/RRS228	Northridge 1994/01/17	1.0	0.838	166.1	28.78	6.7	C	7.1
44	NORTHR/RRS318	Northridge 1994/01/17	2.4	0.472	73.0	19.76	6.7	C	7.1
45	NORTHR/SPV270	Northridge 1994/01/17	0.8	0.753	84.8	18.68	6.7	C	8.9
46	NORTHR/SPV360	Northridge 1994/01/17	0.9	0.939	76.6	14.95	6.7	C	8.9
47	NORTHR/SCS052	Northridge 1994/01/17	3.0	0.612	117.4	53.47	6.7	C	6.2
48	NORTHR/SCS142	Northridge 1994/01/17	1.6	0.897	102.8	46.99	6.7	C	6.2
49	NORTHR/SCE018	Northridge 1994/01/17	2.2	0.828	117.5	34.22	6.7	C	6.1
50	NORTHR/SCE288	Northridge 1994/01/17	0.9	0.493	74.6	28.69	6.7	C	6.1

General properties: Magnitude (ML)>5.5, Distance <10KM, PGA>0.25g, PGV>25cm/s

USGS soil classification: A: Vs>750 m/s, B: 360<Vs<750m/s, C: 180<Vs<360m/s

Table A-2. 24 Ground Motions Used in Chapter 6

No.	Description of earthquakes	Period (s)	PGA (g)
1	FN Elcentro, 1979	1.0	0.313
2	FP Elcentro, 1979	2.1	0.215
3	EW Erzikan, 1992	2.0	0.496
4	NS Erzikan, 1992	1.8	0.515
5	EW Kobe JMA, 1995	0.8	0.631
6	NS Kobe JMA, 1995	0.9	0.841
7	FN Northridge Newhall, 1994	1.3	0.736
8	FP Northridge Newhall, 1994	0.3	0.655
9	FN Northridge Rinaldi, RRS228, 1994	1.0	0.840
10	FP Northridge Rinaldi, RRS228, 1994	2.3	0.476
11	FN Northridge Sylmar, 1994	2.6	0.875
12	FP Northridge Sylmar, 1994	2.4	0.604
13	FN Tabas, 1978	5.3	0.900
14	FN Loma Prieta, Los Gatos, 1989	2.9	0.717
15	FP Loma Prieta, Los Gatos, 1989	1.5	0.458
16	FN Loma Prieta, Lex. Dam, 1989	1.1	0.686
17	FP Loma Prieta, Lex. Dam, 1989	4.2	0.370
18	FN C. Mendocino, Petrolia, 1992	0.8	0.638
19	FP C. Mendocino, Petrolia, 1992	0.8	0.655
20	FN Northridge Olive View, 1994	2.6	0.732
21	FP Northridge Olive View, 1994	0.5	0.595
22	FN Kobe Takatori, 1995	1.3	0.786
23	FP Kobe Takatori, 1995	1.2	0.424
24	NS Chi-chi TCU065, 1999	6.4	0.603

Table A-3. 25 Near-field ground motion records used in Chapter 8

No.	Description	Magnitude	Period, s	PGA, g
1	FN Tabas, 1978	7.4	5.3	0.90
2	FP Tabas, 1978	7.4	4.7	0.98
3	FN Loma Prieta, 1989, Los Gatos	7.0	2.9	0.72
4	FP Loma Prieta, 1989, Los Gatos	7.0	1.6	0.46
5	FN Loma Prieta, 1989, Lex. Dam	7.0	1.1	0.69
6	FP Loma Prieta, 1989, Lex. Dam	7.0	4.2	0.37
7	FN C. Mendocino, 1992, Petrolia	7.1	0.8	0.64
8	FP C. Mendocino, 1992, Petrolia	7.1	0.8	0.65
9	FN Erzincan, 1992	6.7	2.1	0.43
10	FP Erzincan, 1992	6.7	1.9	0.46
11	FN Landers, 1992	7.3	4.6	0.71
12	FP Landers, 1992	7.3	1.2	0.80
13	FN Nothridge, 1994, Rinaldi	6.7	1.0	0.89
14	FP Nothridge, 1994, Rinaldi	6.7	2.7	0.39
15	FN Nothridge, 1994, Olive View	6.7	2.6	0.73
16	FP Nothridge, 1994, Olive View	6.7	0.5	0.60
17	FN Kobe, 1995	6.9	0.9	1.09
18	FP Kobe, 1995	6.9	1.3	0.57
19	FN Kobe, 1995, Takatori	6.9	1.3	0.79
20	FP Kobe, 1995, Takatori	6.9	1.2	0.42
21	Turkey Earthquake, 1999,Gebze	7.4	4.5	0.27
22	EW of TCU065, 1999,Chichi	7.6	4.6	0.81
23	NS of TCU065, 1999, Chichi	7.6	1.8	0.60
24	EW of TCU068, 1999, Chichi	7.6	8.9	0.57
25	NS of TCU068, 1999, Chichi	7.6	8.0	0.46

Note: first 20 records were used by the SAC project.

REFERENCES

1. Abe, M. and Igusa, T. (1996). "Semi-active Dynamic Vibration Absorbers for Controlling Transient Response". *Journal of Sound & Vibration*, 198:547–569.
2. Agrawal A. K., Tan P., Nagarajaiah S., Zhang J. (2005), Benchmark Structural Control Problem for a Seismically Excited Highway Bridge, Part I: Problem Definition, *http://www-ce.engr.ccny.cuny.edu/People/Agrawal*
3. Agrawal, A. K., Yang, J. N, and He, W. L (2003), "Applications of Some Semiactive Control Systems to Benchmark Cable-stayed Bridge", *Journal Structural Engineering*, 129(7): 884-894
4. Agrawal, A.K. and He, W. L. (2004), "Pulse Strength Reduction Factor for Structures Subject to Near-field Earthquakes", *Proc. ASCE Structure Congress 2004*, CD-ROM.
5. Agrawal, A.K. and Yang, J.N. (1995), "Nonlinear Optimal Polynomial Control for Linear and Nonlinear Structures", Technical Report NCEER-95-0019. National Center for Earthquake Engineering Research, December 11, 1995.
6. Agrawal, A.K. and Yang, J.N. (1996), "Optimal Polynomial Control of Seismic-Excited Linear Structures", *Journal of Engineering Mechanics*, 122 (8):753-761.
7. Agrawal, A.K. and Yang, J.N. (1999). Design of Passive Energy Dissipation Systems Based on LQR Methods. *J. of Intelli. Mat. Sys. & Structures*, 10 (12):933-944.
8. Agrawal, A.K. and Yang, J.N. (2000a), "Semi-Active Control Strategies For Buildings Subject to Near-Field Earthquakes", *Proc. SPIE, in Smart Structures and Materials 2000: Smart Systems for Bridges, Structures, and Highways*; 3988: 359-370, March 6-8, Newport Beach, CA.
9. Agrawal, A.K. and Yang, J.N. (2000b), "A Semi-active Electromagnetic Friction Damper for Response Control of Structures", *Advanced Technology in Structural Engineering (CD-ROM), Proc., ASCE 2000 Structures Congress and Exposition*, Chap. 2, Philadelphia
10. Agrawal, A.K., Xu, Z. and He, W.L. (2005). "Ground Motion Pulse Based Active Control of a Linear Base-isolated Benchmark Building", 2005; *J. Struct. Cont. Health Monit.*, Vol.13 (2-3): 792-808.
11. Agrawal, A.K., Xu, Z. and He, W.L. (2006). "Novel Active and Semi-Active Controller Design Considering Near-Field Ground Motion Pulse Components", to appear at the *Proceedings of the 4th World Conference on Structural Control and Health Monitoring (4WCSCM)*, University of California at San Diego, CA, 2006.
12. Aiken, I.D., Kelly, J.M. (1992), "Comparative Study of Four Passive Energy Dissipation Systems". *Bull. NZ Nat. Soc. Earthquake Engineering*, 25(3):175–92.

13. Akbay, Z. and Aktan, H.M., (1991). Actively Regulated Friction Slip Braces, *Proc. 6th Canadian Conf. Earthq. Engrg.*, Univ. of Toronto Press, Toronto.

14. Akbay, Z. and Aktan, H.M., (1995). Abating Earthquake Effects on Buildings by Active Slip Brace Devices, *Shock Vibration*, **2**: 133-142.

15. Akiyama, H. (1998), "A Prospect for Future Earthquake-Resistant Design. *Engineering Structures*", 20 (4-6): 447-451

16. Alavi, B and Krawinkler, H. (2001), "Effects of Near-Fault Ground Motions on Frames Structures", John A. Blume Earthquake Engineering Center Research Report No. 138, Feb. 2001.

17. Anderson, J.C. and Bertero, V.V. (1987). "Uncertainties in Establishing Design Earthquakes". *Journal of Structural Engineering*. 113(8): 1709-1724.

18. Antsaklis, P.J. and Passino, K.M (1992). *An Introduction to Intelligent and Autonomous Control*, Kluwer Academic Publishers Group, Boston, MA

19. ATC-40: Applied Technology Council, Seismic Evaluation and Retrofit of Concrete Buildings, 1996

20. Battaini, M., Casciati, F. and Faravelli, L. (1999), "Fuzzy Control of Structural Vibration: An Active Mass System Driven by a Fuzzy Controller", Earthquake Engineering & Structural Dynamics, 27(11):1267-1276

21. Bazzurro, P. and Luco, N. (2003). "Parameterization of Non-stationary Acceleration Time Histories" , Report for Pacific Earthquake Engineering Research (PEER) Center Lifelines Program Project 1G00.

22. Benioff, H., (1955). "Mechanism And Strain Characteristics of the White Wolf Fault as Indicated by Aftershock Sequence", Earthquakes in Kern County, California, during 1952, *California Division of Mines Bulletin*, No. 171, 199-202.

23. Bergman, D. M., and Goel, S. C. (1987), "Evaluation of Cyclic Testing of Steel-plate Devices for Added Damping and Stiffness" , Rep. No. UMCE 87-10, Univ. of Michigan, Ann Arbor, Michigan

24. Bertero V. V., Mahin, S. A. and Herrera, R. A. (1978). "A Seismic Design Implications of Near-Fault San Fernando Earthquake Records", *Earthquake Engineering and Structural Dynamics*, 6:31-42.

25. Bertero, V.V., Anderson, J.C., Krawinkler, H., and Miranda, E (1991). "Design Guidelines for Ductility and Drift Limits: Review of State-of-the-Practice and State-of-the-Art in Ductility and Drift-Based Earthquake-Resistant Design of Tall Buildings". Berkeley, California: Earthquake Engineering Research Center, University of California at Berkeley. UCB/EERC-91/15.

26. Bobrow, JE, Jabbari, F, and Thai, K (2000). "A New Approach to Shock Isolation and Vibration Suppression Using a Resettable Actuator". *ASME Trans., Dynamic Systems, Measurement and Control.* 122: 570-573.

27. Bozorgnia, Y. and Mahin, S. A. (1998). "Ductility and strength demands of near-fault ground motions of the Northridge earthquake", *Proceedings of the 6th U.S. National Conference on Earthquake Engineering*, EERI, Seattle.

28. Brown, A.A.G and Harris, C. (1994), *Neurofuzzy Adaptive Modeling and Control*, Prentice-Hall, Inc., NJ

29. Carlson, J. D., and Spencer, B. F., Jr. (1996), "Magneto-Rheological Fluid Dampers for Semi-Active Seismic Protection.'' *Proc., 3rd Int. Conf. on Motion and Vibration Control*, Chiba, Japan, 3:35–40.

30. Chen, G.D. and Chen, C.C. (2000). "Behavior of Piezoelectric Friction Dampers Under Dynamic Loading". *Proc. SPIE Symp. on Smart Structures and Materials: Smart Systems for Bridges, Structures and Highways*, Newport Beach, CA 2000. 3988: 54-63.

31. Chopra, A. K (2001), *Dynamics of Structures: Theory and applications to earthquake engineering*, 2nd edition. ISBN:0130869732,

32. Chopra, A. K., Chintanapakdee, C. (2001), "Comparing Response of SDOF Systems to Near-fault and Far-fault Earthquake Motions in the Context of Spectral Regions", *Earthquake Engineering and Structural Dynamics*, 30: 1769-1789

33. Climent, A.B., Pujades L.G. and Almansa F.L. (2002), Design Energy Input Spectra for Moderate-Seismicity Regions. *Earthquake Engineering and Structural Dynamics*, 31:1151-1172.

34. Cohen, L. (1995), *Time-frequency analysis*. Englewood Cliffs, NJ: Prentice-Hall.

35. Connor, J. J. (2003), *Introduction to Structural Motion Control*, Published by Pearson Education, Inc., New Jersey, ISBN 0-13-009138-3.

36. Constantinou, M.C. and Symans, M.D. (1992). ''Experimental and Analytical Investigation of Seismic Response of Structures with Supplemental Fluid Viscous Dampers.'' *Tech. Rep. NCEER-92-0032*, National Center for Earthquake Engineering Research, Buffalo, N.Y.

37. Constantinou, M.C., Soong, T.T. and Dargush, G.F. (1998). "Passive Energy Dissipation Systems for Structural Design and Retrofit", Multidisciplinary Center for Earthquake Engineering Research, Buffalo, N.Y.

38. Cuesta, I. and Aschheim, M.A (2004), "The Use of Simple Pulses to Estimate Inelastic Response Spectra", *Journal of Earthquake Engineering*, 8(6), pp 865-893.

39. Cuesta, I. and Aschheim, M.A. (2001a), "Inelastic Response Spectra Using Conventional and Pulse R-Factors". *Journal of Structural Engineering*, 127 (9):1013-1020.

40. Cuesta, I. and Aschheim M.A. (2001b), "Isoductile Strengths and Strength Reduction Factors of Elasto-Plastic SDOF Systems Subjected to Simple Waveforms", *Earthquake Engineering and Structural Dynamics*, 30:1043-1059.

41. Decanini, L.D. and Mollaioli, F. (2001), "An Energy-Based Methodology for the Assessment of Seismic Demand", *Soil Dynamics and Earthquake Engineering*, 21(2):113-137

42. Dyke, S.J., Caicedo, J.M., Turan, G., Bergman, L.A. and Hague, S. (2003). "Phase I Benchmark Control Problem for Seismic Response Of Cable-Stayed Bridges". *Journal of Structural Engineering*, 129(7):857-872

43. Dyke S. J, Spencer B. F. Jr., Sain, M.K. and Carlson, J.D. (1996a), "Experimental Verification of Semi-active Structural Control Strategies Using Acceleration Feedback". *Proceedings of Third International Conference on Motion and Vibration Control*, Vol. III, Chiba, Japan, 291-296

44. Dyke, S. J. and Spencer, B. F., Jr., (1997). ''A Comparison of Semi-active Control Strategies for the MR damper.'' *Proc., IASTED Int. Conf., Intelligent Information Systems*, the Bahamas.

45. Dyke, S. J., Spencer, B. F., Jr., Sain, M. K. and Carlson, J. D. (1996b). ''Modeling and Control of Magnetorheological Dampers for Seismic Response Reduction.'' *Smart Mater. Struct.*, 5:565–575.

46. Ehrgott, R. C. and Masri, S. F. (1993), "Structural Control Applications of an Electrorheological Device", *Proc., Int. Workshop on Structural Control*, Honolulu, 115–129.

47. Erdik, M. and Durukal, E. (2001), " A Hybrid Procedure for the Assessment of Design Basis Earthquake Ground Motions for the Near-fault Conditions", *Soil Dynamics and Earthquake Engineering*, 21:431-443

48. Fajar, P and Vidic T. (1994). "Consistent Inelastic Design Spectra: Hysteretic and Input Energy". *Earthquake Engineering and Structural Dynamics*, 23:523-532

49. Fu, Y. and Kasai, K. (1998), "Comparative Study of Frames Using Viscoelastic and Viscous Dampers" , *Journal Structural Engineering*, 124(5):513-552

50. Gavin, H. P., Hanson, R. D. and McClamroch, N. H. (1996a), "Control of Structures Using Electrorehological Dampers", *Proc., 11th World Conf. on Earthquake Engineering*, Acapulco, Mexico, Pergaman, CD-ROM Proceedings.

51. Gavin, H., Cenk, A. and Natasha, O. (2003), "Fault Tolerance of Semiactive Seismic Isolation", *Journal of Structural Engineering*, 129(7):922-932.

52. Gavin, H.P., Hanson, R.D. and Filisko, F.E. (1996b), "Electrorheological Dampers, Part I: Analysis and Design" ,*Journal of Applied Mechanics*, ASME, 63(3): 669-675.

53. Gavin, H.P., Ortiz, D.S and Hanson, R.D.(1993), "Testing and Modeling of a Proto-type ER Damper for Seismic Structural Response Control", *Proceedings of International Workshop on Structural Control*, Honolulu, HI, 166-180

54. Goel, R. K. (1997), "Seismic Response of Asymmetric Systems: Energy based Approach" , *Journal Structural Engineering*, 123(11): 1444-1453

55. He W.L. (2003). *Smart energy dissipation systems for protection of civil infrastructures from near-field earthquakes*. Ph.D. Dissertation, The City University of New York.

56. He W.L. and Agrawal A.K. (2006). "An Analytical Model for Ground Motion Pulses during Near-Field Earthquakes for the Design of Smart Protective Systems". Accepted for publication in the *Journal of Structural Engineering.*

57. He W.L. and Agrawal AK. (2005) "Effects of Near-Field Ground Motion Pulses on Performance of Supplemental Viscous Dampers in Flexible Structures". Accepted for publication in the *Journal of Structural Engineering.*

58. He, W. L., Agrawal, A. K. and Yang, J. N. (2003), "Novel Semiactive Friction Controller for Llinear Structures Against Earthquakes", *Journal Structural Engineering*, 129(7): 941-950

59. He, W.L. and Agrawal, A. K. (2005), "Passive and Hybrid Control Systems for Seismic Protection of a Benchmark Cable-Stayed Bridge", Journal of Structural Control and Health Monitoring, published online at May 4, 2005.

60. Heaton T.H., Hall J.F., Wald D.J. and Halling M.W. (1995). "Response of High-Rise and Base-Isolated Buildings to a Hypothetical *Mw*7.0 Blind Trust Earthquake". *Science*. 267: 206–211.

61. Hirai, J., Naruse, M. and Abiru, H. (1996), "Structural control with variable friction damper for seismic response", *Proc. 11th World Conf. on Earthquake Engineering*, Acapulco, Mexico, Pergamon, CD-ROM.

62. Housner, G.W. (1959). "Behavior of Structures during Earthquake". *Journal of Engineering Mechanics.* 85(4): 109–129.

63. Housner, G.W., Bergman, L.A., Caughey, T.K., Chassiakos, A.G., Claus, R.O., Masri, S.F., Skelton, R.E., Soong, T.T., Spencer, B.F. Jr and Yao, T.P. (1997). "Structural Control: Past, Present, and Future". *Journal of Engineering Mechanics*, 123(9): 897–971.

64. Hrovat, D., Barak P. and Rabins, M. (1983). "Semi-Active Versus Passive or Active Tuned Mass Dampers for Structural Control". *Journal of Engineering Mechanics*; 109(3):691–705.

65. Huang, N.E., Chern, C.C., Huang, K., Salvino L.W., Long, S.R. and Fan K.L. (2001), "A New Spectral Representation of Earthquake Data: Hilbert Spectral Analysis of Station TCU129, Chi-Chi, Taiwan, 21 September 1999", *Bulletion of the Seismological Society of America*, 91 (5):1310-1338

66. Huang, NE., Shen, Z. and Long SR. (1999), "A New View of Nonlinear Water Waves: The Hilbert Spectrum". *Annu. Rev. Fluid Mech.*, 31: 417-457

67. Huang, NE., Shen, Z., Long, SR., Wu, MC., Shih, HH., Zheng, Q., Yen, N.C., Tung, CC. and Liu, HH. (1998), "The Empirical Mode Decomposition and the Hilbert Spectrum for Nonlinear and Non-Stationary Time Series Analysis". *Proc. R. Soc. Lond. A*, pp 903-995,

68. Huang, N.E., Wu, M.L.C, Long, S.R., Shen, SP, Qu, W.D., Gloersen, P. and Fan K.L. (2003), "A Confidence Limit for the Empirical Mode Decomposition and Hilbert Spectral Analysis". *Proc. R. Soc. Lond.* A 459, pp2317-2345

69. Inaudi, J. A. (1997), "Modulated Homogeneous Friction: A Novel Semiactive Damping Strategy." *Earthquake Engineering and Structure Dynamics*, 26:361-376

70. Iwan, W. D (1980), "Estimating Inelastic Response Spectra from Elastic Spectra," *Earthquake and structural Dynamics*, 8:375-388

71. Jabbari, F., and Bobrow, J. E (2002), Vibration Suppression with Resettable Device", *Journal of Engineering Mechanics*, 128(9):916-924

72. FEMA 274: *NEHRP Commentary on the Guidelines for the Seismic Rehabilitation of Buildings*, 1997.

73. FEMA 352: *Recommended Postearthquake Evaluation and Repair Criteria for Welded Steel Moment-Frame Buildings*, 2000.

74. FEMA 356: *Prestandard and Commentary for the Seismic Rehabilitation of Buildings*, 2000

75. FEMA368: *NEHRP Recommended Provisions for Seismic Regulations for New Buildings and Other Structures*, 2000

76. Feng Q. and Shinozuka M. (1990). Use of a Variable Damper for Hybrid Control of Bridge Response under Earthquake. Proceedings of U.S. National Workshop on Structural Control Research, Los Angeles, CA, 1990: 107–112.

77. Gilmore, A.T. (1997), "Energy Concepts and Damage Indices" , EERC-CUREe Symposium in Honor of Vitelmo V. Bertero, January 31 - February 1, 1997, Berkeley, California, http://nisee.berkeley.edu/lessons/teran-gilmore.html

78. Hall, J., Heaton, T., Halling, M. and Wald, D., (1995), "Near-Source Ground Motion and Its Effect on Flexible Buildings" , *Earthquake Spectra*, 11 (4):569-605.

79. Huang, C.T. (2001), "Considerations of Multimode Structural Response for Near-Field Earthquakes", *Journal of Structural Engineering*, 129 (4):458-467.

80. Jalili, N. (2002), "A Comparative Study and Analysis of Semi-Active Vibration-Control Systems", *Journal of Vibration and Acoustics*, 124(4): 593-605.

81. Jung, H.J., Park, K.-S., Spencer, B.F. Jr and Lee, I. W. (2004), "Hybrid Seismic Protection of Cable-Stayed Bridges", *Earthquake Engineering & Structural Dynamics*, 33(7):795-820.

82. Kamagata, S. and Kobori, T. (1994), "Autonomous Adaptive Control of Active Variable Stiffness Systems for Seismic Ground Motion". *Proc. of 1st World Conference on Structural. Control*, 2, TA4-23, Pasadena, LA

83. Kannan. S., Uras, H.M., and Aktan, H.M. (1995). "Active Control of Building Seismic Response by Energy Dissipation," *Earthquake Engineering and Structural Dynamics*, 24:747-759.

84. Kasai, K., Munshi, J. A., Lai, M. L., Maison, B. F. (1993), "Viscoelastic Damper Hysteretic Model: Theory, Experiment and Application" , *Proc., ATC 17-1 on Seismic Isolation, Energy Dissipation and Active Control*, 2:521-532

85. Kawashima, K. and Unjoh, S. (1993), "Variable Dampers and Variable Stiffness for Seismic Control of Bridges" , *Preceedings of International Workshop on Structural Control*, Honolulu, HI, 283-297

86. Kawashima, K. Unjoh S, Iida, H., and Mukai, H. (1992), "Effectiveness of the Variable Damper for Reducing Seismic Response of Highway Bridges". *Proceedings of second US-Japan Workshop on Earthquake Protective Systems for Bridges*, PWRI, Tsukuba Science City, Japan. 479-493

87. Kelly, J. M. (1999), "The Role of Damping in Seismic Isolation" , *Earthquake Engineering and Structural Dynamics*, 28: 3–20.

88. Kelly, J. M., Skinner, R.I., and Heine, A.J (1972), "Mechanisms of Energy Absorption in Special Devices for Use in Earthquake Resistant Structures" , *Bull. N. Z. Soc. Earthquake Engrg*., 5(3):63-88

89. Kelly, J.M. (1997). *Earthquake-Resistant Design with Rubber*, 2nd edition, published by Springer-Verlag, New York, ISBN: 3540761314.

90. Kim S, Spencer B.F. Jr and Yun C.B. (2004). "Sliding Mode Fuzzy Control for Smart Base Isolated Building". *Proc. ASCE Engineering Mechanics Conference*, June 16-16, 2004, Newark, DE, CD-ROM.

91. Kobori, T., Takahashi, M., Nasu T., Niwa, N. and Ogasawara K. (1993), "Seismic Response Controlled Structure with Active Variable Stiffness System". *Earthquake Engineering and Structural Dynamics*. 22(12):925-941.

92. Komodromos, P. (2000), *Seismic Isolation for Earthquake Resistant Structures*. WIT Press, UK

93. Kurata, N, Kobori, T, Takahahi, M, Niwa, N. and Kurino, H (1992), "Shaking Table Experiment of Active Variable Damping System" , *Proceedings of First World Conference on Structural Control*, Pasadena, CA, TP2:108-117

94. Li. C. and Reinhorn, A.M (1995), "Experimental and Analytical Investigation of Seismic Retrofit of Structures with Supplemental Damping: Part 2- Friction Devices", NCEER Rep. 95-0009, State Univ. of New York at Buffalo, Buffalo, NY

95. Lin, W. H. and Chopra, A. K. (2002), " Earthquake Response of Elastic SDOF Systems with Nonlinear Fluid Viscous Dampers" , *Earthquake Engineering and Structural Dynamics*, 31:1623-1642

96. Lin, Y.K. and Cai, G.Q. (1995), *Probabilistic Structural Dynamics: Advanced Theory and Applications*, New York, McGraw-Hill.

97. Luo N., Rodellar J. and De Le Sen M. (1998). "Composite Robust Active Control of Seismically Excited Structures with Actuator Dynamics". *Earthquake Engineering & Structural Dynamics*. 27(3): 301-311.

98. MacRae, G.A., Morrow D.V. and Roeder C.W. (2001). "Near-Fault Ground Motion Effects on Simple Structures", *Journal of structural engineering*, 127 (9): 996-1004.

99. Madden, G.J., Symans, M. D. and Wongprasert, M. (2003), "Experimental Verification of Seismic Response of Building Frame with Adaptive Sliding Base-Isolation System" ,*Journal of Structural Engineering*, 128(8):1037-1045.

100. Makris N, Burton SA., Hill D., Jordan M. (1996), "Analysis and Design of ER Damper for Seismic Protection of Structures". *Journal of Engineering Mechanics* 1996; 122(10): 1003–11.

101. Makris, N. (1997), "Rigidity-plasticity-viscosity: Can Electrorheological Dampers Protect Base-isolated Structures fom Near-source Ground Motions?" *Earthquake Engineering and Structural Dynamics*, 26: 571-591.

102. Makris, N. and Chang, S. P (2000), "Effective of Viscous, Viscoplastic and Friction Damping on the Response of Seismic Isolated Structures" , *Earthquake Engineering and Structural Dynamics*, 29(1): 85-107

103. Makris, N. and Chang, S.P. (1998), "Effect of Damping Mechanisms on the Response of Seismically Isolated Structures". *PEER Report 1998/06*, Pacific Earthquake Engineering Research Center, University of California, Berkeley, November 1998.

104. Makris, N. and Chang, S.P. (2000). "Effect of Viscous, Viscoplastic and Fiction Damping on the Response of Seismic Isolated Structures". *Earthquake Engineering and Structural Dynamics*, 29: 85-107.

105. Makris, N. and Constantinous, M. C. (1991), "Fractional-derivative Maxwell Model for Viscous Dampers" , *Journal of Structural Engineering*, 117(9), 2708-2724

106. Makris, N. Constantinous, M. C. and Dargush, G. F. (1993), "Analytical Model of Viscoelastic Liquid Dampers", *Journal Structural Engineering*, 119(11): 3310-3325

107. Malhotra, P.K.(1999), "Response of Buildings to Near-Field Pulse-Like Ground Motions", *Earthquake Engineering & Structural Dynamics*, 28(11):1309-1326

108. Mavroeidis, G.P., Dong, G. and Papageorgiou, A.S. (2004), "Near-Fault Ground Motions and the Response of Elastic and Inelastic Single-Degree-Of-Freedom (SDOF) Systems", Earthquake Engineering and Structural Dynamics, 33(9):1023-1049.

109. Menum, C. and Fu, Q. (2002). "An Analytical Model for Near-Field Ground Motions and the Response Of SDOF Systems", *7th US National Conference on Earthquake Engineering (7NCEE)*, Earthquake Engineering Research Institute, Oakland, CA.

110. Miranda, E. (1993). "Site-Dependent Strength Reduction Factors", *Journal of Structural Engineering*, 119 (12): 3505-3519.

111. Moon, S.J., Bergman, L.A. and Voulgaris, P.G. (2003), "Sliding Mode Control of Cable-Stayed Bridge Subjected to Seismic Excitation" , *Journal of Engineering Mechanics*, 129(1):71-78.

112. Nadathur, V. and Nagarajaiah, S. (2004). "Wind Response Control of Building with Variable Stiffness Tuned Mass Damper Using Empirical Mode Decomposition and Hilbert Transform," *Journal of Engineering Mechanics*, 130(4), 451-458.

113. Naeim, F. and Anderson, J.C. (1993). *Classification and Evaluation of Earthquake Records for Design*, A report to EERI and FEMA, Report No. 93-08, Department of Civil Engineering, University of Southern California, June 1993.

114. Naeim, F. and Kelly, J.M. (1999). *Design of Seismic Isolated Structures: From Theory to Practice*, published by John Wiley & Sons, ISBN: 0471149217.

115. Nagarajaiah, S. (1994). "Fuzzy Controller for Structures with Hybrid Isolation System" , Proc., *First World Conf. Struct. Control*, TA2.67-76

116. Nagarajaiah, S. and Ferrell, K. (1999). "Stability of Elastomeric Seismic Isolation Bearings", *Journal of Structural Engineering*, 125(9): 946–954.

117. Nagarajaiah, S. and Mate, D. (1998), "Semi-Active Control of Continuously Variable Stiffness System", *Proc., 2nd World Conf. Structural Control*, Vol. 1, Wiley, New York, 397–405.

118. Nagarajaiah, S. and Narasimhan, S. (2005). "Smart Base Isolated Benchmark Building Part II: Sample Controllers For Linear and Friction Isolation". *Journal Structural Control and Structural Health Monitoring*, 13(2-3):589-604.

119. Nagarajaiah, S. and Varadarajan, N (2000). ''Novel Semiactive Variable Stiffness Tuned Mass Damper with Real Time Tuning Capability'', *Proceedings of 13th Engineering Mechanics Conference*, CD ROM, Reston, Va.

120. Nagarajaiah, S., Riley, M. A. and Reinhorn, A. M. (1993), "Control of Sliding Isolated Bridges with Absolute Acceleration Feedback," *Journal of Engineering Mechanics*, 119(11):2317-2332.

121. Nagarajaiah, S., Sahasrabudhe, S. and Iyer, R. (2000), "Seismic Response of Sliding Isolated Bridges with Smart Dampers Subjected to Near Source Ground Motions". *Proc. Structures Congress*, ASCE, Philadelphia

122. Narasimhan S., Nagarajaiah S, Johnson E.A. and Gavin H. P. (2005). "Smart Base Isolated Benchmark Building Part I: Problem Definition". *Journal Structural Control and Structural Health Monitoring*, 13(2-3):573-588.

123. Narasimhan, S., and Nagarajaiah, S(2005). "STFT Algorithm for Semiactive Control of Base Isolated Buildings with Variable Stiffness Isolation Systems Subjected to Near Fault Earthquakes", *Engineering Structures*, 27, 514-523.

124. Nasu, T., Kobori, T., Takahashi, M., Niwa, N., and Ogasawara, K. (2001). "Active Variable Stiffness System with Non-resonant Control", *Earthquake Engineering and Structural Dynamics*, 30(11):1597-1614.

125. Newmark, N.M. and Hall, W.J. (1982). "Earthquake Spectra and Design", *Engineering Monograph*, Earthquake Engineering Research Institute, Berkeley, CA

126. Ohtori, Y., Christenson, R.E., Spencer, B.F., and Dyke, S.J. (2004). "Benchmark Problems in Seismically Excited Nonlinear Buildings". *Journal of Engineering Mechanics*. 130(4): 366-385.

127. Ou, J (2004). "Recent Advances on Structural Control in Mainland China". *Proceedings of the 4th International Workshop on Structural Control*, pp 13-17, June10-11, 2004, Columbia University, New York.

128. Pall, A. S., Marsh, C. (1982), "Response of Friction Damped Braced Frames", *Journal Structural Division*, 108(6):1313-1323

129. Panariello, G.F. and Betti, R. (1997). "Optimal Structural Control via Training on Ensemble of Earthquakes". *Journal of Engineering Mechanics*. 123(11):1170-1179.

130. Park, Y.J., Ang, A.H. and Wen, Y.K. (1987). "Damage-Limiting Aseismic Design of Buildings", *Earthquake Spectra*, 3(1):1-26

131. Pattern, W.N. (1998). "The I-35 Walnut Creek Bridge: an Intelligent Highway Bridge via Semi-active Structural Control". *Proceedings of the 2nd World Conference on Structural Control*, 1:427-436, Kyoto, Japan.

132. Pavlou, E.A. and Constantinou, M.C. (2004). "Response of Elastic And Inelastic Structures with Damping Systems to Near-Field and Soft-Soil Ground Motions", Engineering structures, published online at http://www.elsevier.como/locate/engstruct

133. Pekcan, G., Mander, J. B. and Chen, S. S. (1999). "Fundamental Considerations for the Design of Non-linear Viscous Dampers" , *Earthquake Engineering and Structural Dynamics*, 28:1405-1425

134. Perry, C. L., Fierro, E. A., Sedarat, H. and Scholl R. E. (1993). "Seismic Upgrade in San Francisco Using Energy Dissipation Devices". *Earthquake Spectra*, 9(3): 559-579

135. Priestley, M.B. (1965). "Evolutionary Spectra and Nonstationary Process". *J. R .Statist. Soc.* B27, pp 204-237.

136. Priestley, M.B. (1988). "*Nonlinear and Nonstationary Time Series Analysis*". Academic Press, London.

137. Ramallo, J.C., Johnson, E.A. and Spencer, B.F. Jr.(2002). "Smart Base Isolation Systems". *Journal of Engineering Mechanics*. 128(10): 1088–1099.

138. Sadek, F., Mhraz, B., Taylor, A. W., and Chung, R.W. (1996), "Passive Energy Devices for Seismic Applications" , NISTIR 5923, *National Institute of Standards and Technology*, Maryland

139. Saharabudhe, S. and Nagarajaiah, S. (2005). "Seismic Response Control of Sliding Isolated Bridges with MR Dampers: Experimental Study," *Earthquake Engineering and Structural Dynamics Journal*, 34, Published online 31 January 2005.

140. Sahasrabudhe S and Nagarajaiah S (2005), "Semi-active Control of Sliding Isolated Bridges using MR Dampers: An Experimental and Numerical Study", *Earthquake Engineering and Structural Dynamics*, 34(8):965-983.

141. Saiidi, M, Maragakis E. and Griffin G., (1999), "Effect of Base Isolation on Seismic Response of Multi-column Bridges" ,*Struct Engng Mech,* 8:411-419.

142. Sato, T., Sato, M., Tanaka, S., and Toki, K. (1996). "Modeling of a Variable Damper and its Application", *Proceedings of Second International Workshop on Structural Control*, Hong Kong, 482-489

143. Shames, I.H. and Cozzarelli F.A. (1992). *Elastic and Inelastic Stress Analysis.* Prentice–Hall, Englewood Cliffs, NJ.

144. Shen, K. L., Soong, T. T. (1995), "Modeling of Visccoelastic Dampers for Structural Application" ,*Journal of Engineering Mechanics*, 121(6), 694-701

145. Shinner, R. I., Kelly, J. M., and Heinre, A. J. (1975), "Hysteresis Dampers for Earthquake-Resistant Structures". *Earthquake Engineering and Structural Dynamics*, 3:287-296

146. Singh, J.P. (1995). Lecture notes for "Seismic Loading: Code Versus Site Specific" presented at a "Portland Regional Seminar on Seismic Engineering Issues" in September, 1995. http://nisee.ce.berkeley.edu/lessons/singh.html

147. Skinner, R.I., McVerry, G.H. and Robinson, W.H.(1993), *An Introduction to Seismic Isolation*, Published by John Wiley & Sons Inc, ISBN: 047193433.

148. Somerville, P. G. and Graves, R. W. (1993). "Conditions That Give Rise to Unusually Large Long Period Ground Motions", *The Structural Design of Tall Buildings*, **2**: 211-232.

149. Somerville, P., Saikia, C.K., Wald, D. and Graves, R. (1995). "Implications of the Northridge Earthquake for Strong Ground Motions from Thrust Faults", *Bull. Seism. Soc. Am.*, 86, S115- S125.

150. Somerville, P.G., Irikura, K., Graves, R., Sawada, S., Wald, D., Abrahamson, N., Iwasaki, Y., Kagawa, T., Smith, N.F. and Kowada, A. (1998). "Characterizing Earthquake Slip Models for the Prediction of Strong Ground Motion", *Seismological Research Letters*, 70, 59-80.

151. Somerville, P.G., Smith, N.F., Graves, R.W. and Abrahamson, N.A. (1997). "Modification of Empirical Strong Ground Motion Attenuation Relations to Include the Amplitude and Duration Effects of Rupture Directivity", *Seismological Research Letters*, 68, 180-203.

152. Soong, T. T. (1990), *Active Structural Control: Theory and Practice*, Published by John Wiley & Sons, Inc, New York, ISBN 0-470-21670-0, 1990.

153. Soong, T.T. and Constantinou, M.C. (1994). *Passive and Active Structural Vibration Control in Civil Engineering*, Springer, New York.

154. Soong, T.T., Dargush, G.F. (1997). *Passive Energy Dissipating Systems in Structural Engineering*. Chichester, UK: John Wiley and Sons Ltd.

155. Soong,T.T. and Grigoriu, M.(1993), *Random Vibration of Mechanical and Structural Systems*, Prentice Hall, Englewood Cliffs, New Jersey 1993.

156. Soong,T.T. and Spencer, B.F. Jr (2002). "Supplemental Energy Dissipation: Sate-of-the-art and State-of-the-practice". *Engineering Structures*, 24: 243-259.

157. Spencer, B. F., Dyke, S. J. and Deoskar, H.S. (1998a). "Benchmark Problems in Structural Control: Part 1 - Active Mass Driver System." *Earthquake Engineering and Structural Dynamics*, 27(11):1127–1139.

158. Spencer, B. F., Dyke, S. J., and Deoskar, H.S. (1998b). "Benchmark Problems in Structural Control: part 2 - Active Tendon System." *Earthquake Engineering and Structural Dynamics*, 27(11):1141–1147.

159. Spencer, B. F., Dyke, S. J., Sain, M. K., and Quast, P. (1993). "Acceleration Feedback Control Strategies for Aseismic Protection." *Journal of Engineering Mechanics*, 120(1):135–158.

160. Spencer, B. F., Jr., and Sain, M. K. (1997b), ''Controlling Buildings: A new Frontier in Feedback'', *IEEE Control Syst. Mag.*, 17(6):19–35.

161. Spencer, B. F., Jr., Dyke, S. J., and Sain, M. K. (1996), "Magnetorheological Dampers: A New Approach to Seismic Protection of Structures", *Proc. IEEE Conf. on Decision and Control*, Chiba, Japan.

162. Spencer, B.F, Dyke, S.J, Sain, M.K, Carlson, J.D. (1997a), "Phenomenological Model for Magnetorheological Dampers". *Journal of Engineering Mechanics*; 123(3): 230–8.

163. Spencer, B.F. and Yang G. (2004). "Recent Developments in Structural Control Research in the U.S.", *Proceedings of the 4th International Workshop on Structural Control*, pp 3-12, June10-11, 2004, Columbia University, New York.

164. Spencer, B.F. Jr and Nagarajaiah, S. (2003). "State of the Art of Structural Control. *Journal of Structural Engineering"*, 129(7): 845-856.

165. Spencer, B.F. Jr, Johnson, E.A., and Ramallo, J.C.(2000). "Smart Isolation for Seismic Control". *JSME Int. J. Ser. C: Special Issue on Frontiers of Motion and Vibration Control*. 43(3): 704–711.

166. Stammers, C.W. and Sireteanu, T. (1998), "Vibration Control of Machines by use of Semi-active Dry Friction Damper". *Journal of Sound and Vibration*, 209(4): 671-684.

167. Suhardjo, J., Spencer, B.F. Jr, Sain, M.K. (1990), "Feedback–Feedforward Control of Structures under Seismic Excitation", *Structural Safety*, 8:69–89.

168. Symans, M. D., and Constantinou, M. C. (1997b), "Experimental Testing and Analytical Modeling of Semi-Active Fluid Dampers for Seismic Protection", *J. Intell. Mater. Syst. Struct.*, 8(8):644–657.

169. Symans, M. D., and Kelly, S. W. (1999). "Fuzzy Logic Control of Bridge Structures Using Intelligent Semiactive Seismic Isolation Systems." *Earthquake Engineering and Structural Dynamics*, 28:37–60.

170. Symans, M.D. and Constantino, M.C. (1997a), "Seismic Testing of a Building Structure with a Semi-active Fluid Damper Control System". *Earthquake Engineering and Structural Dynamics*, 26(7):759-77

171. Symans, M.D. and Constantinou, M.C. (1999), "Semi-Active Control Systems for Seismic Protection of Structures: A State-Of-The-Art Review". *Engineering Structures*, 21(6): 469–487.

172. Symans, M.D., Constantinous, M.C., Taylor D.P. and Garnjost, K.D. (1995), "Development and Experimental Study of Semi-active Fluid Damping Devices for Seismic Protection of Structures". Report No: NCEER 95-0011, National Center for Earthquake Engineering Research, Buffalo, NY

173. Tan P., Agrawal A. K.(2005), "Benchmark Structural Control Problem for a Seismi-cally Excited Highway Bridge, Part II: Sample Control Designs", *http://www-ce.engr.ccny.cuny.edu/People/Agrawal*.

174. Tan, P., Agrawal, A.K and Pan, Y. (2005). "Near-field Effects on Seismically Excited Highway Bridge with Nonlinear Viscous Dampers", accepted for publication in *Journal of Bridge Structures*.

175. Terenzi, G. (1999). "Dynamics of SDOF Systems with Nonlinear Viscous Damping", *Journal of Engineering Mechanics*, 125(8):956-963

176. Tirca, L.-D., Foti, D and Diaferio, M. (2003). "Response of Middle-rise Steel Frames with and without Passive Dampers to Near-field Ground Motions", *Engineering Structures*, 25:169-179.

177. Tsai, C. S., and Tsai, K. C (1995), "TPEA Devices as Seismic Damper for High-rise Buildings", *Journal Engineering Mechanics*, 121(10):1075-1081

178. Tsai, K. C., Chen, H. W., Hong, C. P. and Su, Y. F. (1993). " Design of Steel Triangular Plate Energy Absorbers for Seismic-resistant Construction." *Earthquake Spectra*, 9(3):505-528

179. Uang, C. M. and Bertero, V. V. (1988), "Use of Energy as a Design Criterion in Earthquake Resistant Design" , Report No. UCB/EERC-88/18, Earthquake Engineering Research Center, Berkeley, CA

180. Uang, C.M. and Bertero V.V. (1988). "Implications of Recorded Earthquake Ground Motion on Seismic Design of Building Structures". Berkeley, CA: Earthquake Engineering, Research Center, University of California, Berkeley. UCB/EERC-88/13.

181. Uang, C.M. and Bertero, V.V. (1990). "Evaluation of seismic energy in structures", *Earthquake engineering and structural dynamics*, 19:77-90

182. UBC 97: *Uniform Building Code*, International Code of Building Officials (ICBO) 1997

183. Utkin, V.I. (1992). *Sliding Modes in Optimization and Control Problems*, Springer Verlag, New York.

184. Veletsos, A.S. and Newmark, N.M. (1960), "Effects of inelastic behavior on the response of simple systems to earthquake motions," *Proceedings of 2nd World Conference on Earthquake Engineering*, 2:895-912, Tokyo, Japan.

185. Veletsos, A.S., Newmark, N.M. and Chelepati, C.V. (1965), "Deformation Spectra for Elastic and Elastoplastic Systems Subjected to Ground Shock and Earthquake Motions," *Proceeding of 3rd World Conference on Earthquake Engineering*, Vol. 2, pp 663-682, Wellington, New Zealand.

186. Verbruggen, H. B. and Babuska, R (1999), *Fuzzy Logic Control: Advances in Applications*, World Scientific Publishing Company, ISBN: 9810238258

187. Vidic, T., Fajfar, P. and Fischinger, M. (1994). "Consistent Inelastic Design Spectra: Strength and Displacement". *Earthquake engineering and structural dynamics*. 23: 507-521

188. Wang, L.X.(1994). *Adaptive Fuzzy systems and Control: Design and Stability Analysis*, Prentice-Hall, NJ

189. Wang, Y., McFarland, D.M., Vakakis, A.F., and Bergman, L.A. (2002), "Efficacy of A Nonlinear Base-Isolation System Subjected To Near-Field Earthquake Motions", Proc. International Conf. on Advances and Challenges in Earthquake Engineering Research, August 15-17, 2002, Harbin, China.

190. Wen, Y.K. (1988), "Equivalent Linearization for Hysteretic Systems under Random Excitations". *Journal of Engineering Mechanics*, 20(8): 685-91.

191. Whittaker, A. S., Bertero, V. V., Thompson, C. L., and Alonso, L. J. (1991), "Seismic Testing of Steel Plate Energy dissipation devices." , *Earthquake Spectra*, 7(4):563-604

192. Wong, K. K. F. and Yang, Y. M. (2001), "Energy-based Damage Assessment on Structures during Earthquakes" , *The Structure Design of Tall Buildings*, 10:135-154

193. Wong, K.F. and Yang, R (2002). "Earthquake Response and Energy Evaluation of Inelastic Structures, *Journal of Engineering Mechanics*", 128(3): 308-317

194. Wu, J.C. and Yang, J.N. (2004), "Modified Sliding Mode Control for Wind-Excited Benchmark Problem" , *Journal of Engineering Mechanics*, 130(4):499-504.

195. Wu, J.C.(2003), "Experiments on a Full-scale Building Model Using Modified Sliding Mode Control" , *Journal of Engineering Mechanics*, 129(4):363-372

196. Xia, C., Hason, R. D. (1992), "Influence Of ADAS Element Parameters on Building Seismic Response" ,*Journal Structural Engineering*, 118(7):1903-1918

197. Xu, Z. and Agrawal A.K. (2004). "Applications of Several Semi-Active Control Systems to the Benchmark Base Isolated Building". *Proc. ASCE Engineering Mechanics Conference*, June 16-16, 2004, Newark, DE, CD-ROM.

198. Xu, Z., Agrawal, A.K. and Yang, J.N. (2005), "Semi-Active and Passive Control Of The Phase I Linear Base-Isolated Benchmark Building Model", *Journal of Structural Control and Health Monitoring*, 13 (2-3):626-648.

199. Xu, Z., Agrawal, A.K., He, W.L. and Tan, P. (2006), "Performance of Passive Energy Dissipation Systems during Near-Fault Ground Motion Type Pulses", Published online by *Engineering Structures*.

200. Yamaguchi, H and El-Abd, A (2003), "Effect of Earthquake Energy Input Characteristics on Hysteretic Damper Efficiency", *Earthquake Engineering and Structural Dynamics*, 32:827-843.

201. Yang, J. N., Wu, J. C. and Agrawal, A. K. (1995a), "Sliding Mode Control of Nonlinear and Hysteretic Structures", Journal of *Engineering Mechanics*. 121(12): 1330-1339.

202. Yang, J. N., Wu, J. C. and Agrawal, A. K. (1995b), "Sliding Mode Control of Seismically Excited Linear Structures" , *Journal of Engineering Mechanics*. 121(12): 1386-1390.

203. Yang, J. N., Wu, J. C., and Li, Z. (1996a), "Control of Seismic-excited Buildings Using Active Variable Stiffness Systems." *Journal of Engineering Mechanics*, 18(8):589-596

204. Yang, J. N., Wu, J. C., Kawashima, K. and Unjoh, S. (1995), "Hybrid Control of Seismic Excited Bridge Structures" , *Earthquake Engineering Structural Dynamics*, 24:1437-1451

205. Yang, J.N and Akbarpour, A. (1990), "Effect of System Uncertainty on Control of Seismic-Excited Buildings" , *Journal of Engineering Mechanics*, 116(2):462-478.

206. Yang, J.N. (1975). "Application of Optimal Control Theory to Civil Engineering Structures". *Journal of the Engineering Mechanics Division*, 101(6): 819-838.

207. Yang, J.N. and Agrawal, A.K. (2002), "Semi-Active Hybrid Control Systems for Nonlinear Buildings against Near-Field Earthquakes". *Engineering Structures*. 24(3): 271–280.

208. Yang, J.N., Agrawal, A.K., Samali, B. and Wu, J.C. (2004). "A Benchmark Problem for Response Control of Wind Excited Tall Buildings". *Journal of Engineering Mechanics*, 130(4): 437-446.

209. Yang, J.N., Kim, J.H. and Agrawal, A.K.(2000), "A Resetting Semiactive Stiffness Damper for Seismic Responses Control". *Journal of Structural Engineering*. 126(12): 1427-1433.

210. Yang, J.N., Li, Z and Vongchavalitkul, S (1994a), "Stochastic Hybrid Control of Hysteretic Structures" , *Journal of Probabilistic Engineering Mechanics*, 9:125-133

211. Yang, J.N., Li, Z. and Vongchavalitkul, S. (1994b), "Generalization of Optimal Control Theory: Linear and Nonlinear Control ", *Journal of Engineering Mechanics*, 120(2):266-283.

212. Yang, J.N., Wu, J.C, Reinhorn, A.M. and Riley, M. (1996c), "Control of Sliding-Isolated Buildings Using Sliding Mode Control". *Journal of Structural Engineering*. 122(2): 83-91.

213. Yang, J.N., Wu, J.C., Agrawal, A.K. and Li, Z.(1994c), "Sliding Mode Control for Seismic-Excited Linear and Nonlinear Civil Engineering Structures", Technical Report NCEER 94-0017, National Center for Earthquake Engineering Research, State University of New York at Buffalo, NY

214. Yang, J.N., Wu, J.C., Kawashima, K. and Unjoh, S.(1995c). "Hybrid Control of Seismic-Excited Bridge Structures". *Earthquake Engineering and Structural Dynamics*, 24: 1437-1451.

215. Yang, J.N., Wu, J.C., Reinhorn, A.M., Riley, M. Schmitendorf, W.E. and Jabbari, F. (1996b), "Experimental Verifications of H_8 and Sliding Mode Control for Seismically Excited Buildings", *Journal of Structural Engineering*, 122(1):69-75.

216. Yoshioka, H., Ramallo, J. C. and Spencer, B. F. (2002), "'Smart' Base Isolation Strategies Employing Magnetorheological Dampers", *Journal of engineering Mechanics*, 128(5): 540-551.

217. Zhang, R. H., Soong, T. T., Mahmoodi, P. (1989), "Seismic Response of Steel Frame Structures with Added Viscoelastic Dampers", *Earthquake Engineering and Structural Dynamics*, 8:389-396

218. Zhang, Y.F. and Iwan, W.D. (2002), "Protecting Base-Isolated Structures from Near-Field Ground Motion by Tuned Interaction Damper", *Journal of Engineering Mechanics*, 128(3):287-295.

219. Zhou, F.L. (2001). "Seismic Isolation of Civil Buildings in P. R. China", *Progress in Structural Engineering and Materials*, Vol. 3, No. 3, Published by WILEY.

220. Zhou, K.M., Doyle, J.C. and Glover, K. (1996). *Robust and Optimal Control*, Published by Prentice Hall, NJ, ISBN 0-13-456567-3.